Dynamics of Blood Drop Formation and Flight

Natalia Kabaliuk

A thesis presented for the degree of Doctor of Philosophy
in Mechanical Engineering
at the University of Canterbury,
Christchurch, New Zealand
2014

To the women of my family - my
grandmother, mother, sister and daughter -
for highly appreciated support,
understanding and
inspiration

Acknowledgments

Foremost, I would like to acknowledge the support of my supervisors during the course of this study. Special thank you goes to my senior supervisor, Associate Professor Mark Jermy, for the valued opportunity to undertake this PhD study, expertise, guidance and proofreading of this thesis. I would like to acknowledge the practical expertise, guidance, encouragement and interest in the research provided by my ESR-based supervisor, Dr. Michael Taylor. Support and encouragement provided by Dr. Mathieu Sellier have been highly appreciated as well.

The technical staff of the Mechanical Engineering workshop, Eric Cox, Julian Phillips, Kevin Stobbs, Scott Amies and Garry Cotton, contributed essential work, advice and encouragement throughout this study. Special thanks go to Dr. Patrick Geoghegan for presenting some of the material from this thesis at the 2013 Training IABPA conference. Much credit goes to Dr. Michael Taylor, Bart Epstein and Terry Laber for allowing me to include some of their experimental data on the blood drop falling velocity and to Elisabeth Williams for the data on cast-off spatter, both presented in Chapter 7. I thank to the University of Canterbury for the financial support in a form of a UC Doctoral Scholarship.

I expend my thanks to the fellow students at the ESR and University of Canterbury, Liz, Theresa, Therese, Rebecca, Gulraiz, Prateek and Milad, for the valued friendship, useful discussions and encouragement throughout these three years.

I would also like to thank the Sinclairs, Linda, Chris, Jamey, Carissa and Luke, for making me and my family feel in Christchurch at home and taking such a good care of Veronika while I was working towards this PhD. This has been much appreciated.

I would also like to acknowledge Pavlo Kokhanenko for the highly appreciated encouragement to undertake this research, useful practical discussions and the amount of time spent with Veronika, allowing me to finish my PhD.

I thank to my mother Liudmila, sister Anna and brother-in-law Alexander for invaluable support, understanding and encouragement throughout my life and PhD. I express my gratitude to Alexander and Pavlo, without whom my academic journey wouldn’t have started.

Abstract

Violent crimes involving bloodshed may result in the formation of a number of blood drops that move through air and impact onto a surface producing a bloodstain pattern. Bloodstain Pattern Analysis (BPA), the analysis of the position, distribution, size and morphology of the stains within the pattern present at the crime scene, may provide information about the events that gave rise to the bloodshed. The location of blood origin, i.e. victim's position at the moment of wounding and (or) wound location, determination is of major interest. This may be estimated if the size, velocity and directionality of a drop that produced a particular stain, as well as forces acting on a drop and its behavior during flight, are known. The latter is hard to achieve in practice.

This study investigated the dynamics of formation and flight of blood drops commonly found at a crime scene with the aim to facilitate blood origin determination.

Features of blood drop formation at passive dripping with correlation to dripping surface characteristics were studied experimentally. Passive blood drop volume was found to decrease for sharper dripping objects. Higher number of accompanying droplets was produced with dripping blood than water. Surface roughness influenced drop size and number of accompanying droplets only weakly over the hydrophobicity and the range of roughnesses studied.

Principal classes of blood drops (passive, cast-off, impact and gunshot) were characterized by typical sizes, velocities, levels of in-flight deformation and disintegration possibility. Passive blood drops were found to travel at velocities lower than terminal in typical crime scene conditions and possess low deformation levels. Impact-generated blood drops and gunshot blood drops larger than 0.5 mm in diameter were found to undergo significant levels of in-flight deformation with a possibility of disintegration. Smaller gunshot drops (with diameters less than 0.1-0.5 mm) may be treated as spherical during flight if travelling at velocities less than 30 m/s.

These factors may affect blood origin determination through the effects on blood drop flight and were investigated in this study. The effects of in-flight blood drop oscillations on its trajectory were also considered.

A numerical scheme for accurate blood drop flight characteristics, including oscillations, deformation and disintegration, modeling was developed and validated against a number of analytical and experimental cases with special attention to the passive blood drop oscillations and ultimate deformation at terminal velocity, cast-off and impact blood drop deformation and breakup features. This provided an efficient and accurate method for typical blood drop flight reconstruction from blood origin to impact as well as from the bloodstain location to the possible blood origin.

Factors affecting blood drop trajectory and blood origin estimation were studied using the developed scheme. These included effects of drop deformation and oscillations, air currents and in-flight drop evaporation

The effects of blood **drop deformation** and drop breakup possibility were considered. Blood drops of 0.2-1 mm in diameter travelling at velocities higher than about 10-20 m/s and drops larger than 1 mm at around 15 m/s were found to undergo significant deformation that should to be taken into account when speculating about the possible trajectory of the drop. At velocities higher critical drop deformation may be reached leading to consequent **drop disintegration**. Considerations regarding time and travel distance for a blood drop to breakup were provided. Drops smaller than 0.2 mm in diameter required velocities much higher than 30 m/s to significantly deform and breakup during flight. Such velocities are rarely achieved in crime-scene wounding scenarios, with the possible exception of wounding with high speed rifle bullets. Drop in-flight deformation was shown to lead to drop flight trajectory curving earlier in flight, possibly altering impact angle and velocity towards blood origin height overestimation, for drops larger than 0.5 mm in diameter, and, thus, should be considered for blood drop flight reconstruction. For drops smaller than 0.5 mm and for fast-moving drop trajectories shorter than 1 m the deformation may be ignored when drop flight is considered.

It was found that for blood drop flight reconstruction purposes (from blood origin to impact and vice versa) **drop oscillations** may be ignored. The effect of the initial passive and cast-off drop oscillation on the evolution of blood drop flight velocity and distance was found to be negligibly small. Time and travel distance of a blood drop for its oscillation to decay was studied in relation to its possible effects on drop spreading upon impact and, thus, on resultant bloodstain appearance.

The effects of **air movement** and in-flight blood **drop evaporation** on its flight were considered as well. Blood drops smaller than about 0.5-1 mm were found to be the most susceptible to the effects of air currents and winds. The possibility of air motion during bloodstain generation should be taken into account when drop flight and blood origin being

reconstructed. It was suggested that for the majority of measurable bloodstains resulted from drops of 0.5-1 mm in diameter, the effect of in-flight drop evaporation on its trajectory is expected to be negligible for typical crime scene conditions.

Additionally, maximum possible **travel distance** and **straight-line drop trajectory** length were estimated for typical blood drops.

A maximum drop flight range was of 30 cm for a 0.1 mm blood drop at 30 m/s and as much as ~3 and 6 m for a 2 mm drop at 5 and 17 m/s (maximum velocity without drop disintegration) respectively in idealized crime scene conditions. Cast-off and impact spatter drops representatives with diameters of 0.5-1 mm at 5-30 m/s were found to travel on average a maximum of 2-3 m if not intercepted by a wall, or any other object, or subject. Mist-like drops smaller than 0.5 mm travelled less than 1 m. The latter had straight-line trajectories only over the first 25 cm of flight or less. Whereas, larger fast (at > 10 m/s) upward-moving (at > 70º to horizontal) blood drops could travel at least 1-3.5 m in straight paths. Drops travelled within 20° to horizontal had straight-line trajectory lengths of no more than 1-1.5 m. Relevant stain selection recommendations were drawn as well.

The developed scheme for accurate blood drop trajectory and the presented research findings may aid in accurate bloodstain pattern analysis and blood origin determination.

Publications Arising from this Research

Journal Papers

1. **Kabaliuk, N.**, M.C. Jermy, K. Morrison, T. Stotesbury, M.C. Taylor and E. Williams, Blood drop size in passive dripping from weapons. Forensic Science International, 2013. 228: p. 75-82.

2. **Kabaliuk, N.**, M.C. Jermy, E. Williams, B.P. Epstein, T.L. Laber and M.C. Taylor, Accurate Blood Drop Flight Modelling. Forensic Science International, 2014 (**current**).

3. **Kabaliuk, N.**, M.C. Jermy and M.C. Taylor, Factors Affecting Blood Drop Trajectory in Typical Crime Scene Conditions. Forensic Science International, 2014 (**current**).

Conference Proceedings

1. **Kabaliuk N.**, M.C. Jermy, M.C. Taylor, and P.H. Geoghegan, Does the non-spherical shape of a spatter drop affect its trajectory? IABPA Training Conference: The Science Behind Bloodstain Pattern Analysis, San Diego, USA, 2013.

2. Williams E., M.C. Taylor, E. Huang, P.H. Geoghegan, J. Spinola-Fernandez, L. Young, **N. Kabaliuk**, T. de Castro and S. Walt, Man vs Machine: Combining Blood Fluid Dynamics and 3D Human Biomechanics with Cast-off Pattern Creation and Reconstruction... in a Cage. IABPA Training Conference: The Science Behind Bloodstain Pattern Analysis, San Diego, USA, 2013.

3. **Kabaliuk N.**, M.C. Jermy, M.C. Taylor and M. Sellier, Computational Modelling of Blood Drop Flight or Does Deformation of a spatter Drop Affect Trajectory? 3nd Annual Forensic Biology Symposium, Dunedin, New Zealand, March 2013.

4. **Kabaliuk N.**, T. Stotesbury, E. Williams, K. Morison, M.C. Taylor and M.C. Jermy, Blood Droplet Size in Passive Dripping, 21st International Symposium on the Forensic Sciences ANZFSS 2012, Hobart, Tasmania, Australia, September 2012.

5. **Kabaliuk N.**, M.C. Jermy, M.C. Taylor, Passive Dripping of Blood from Weapons. 2nd Annual Forensic Biology Symposium, Dunedin, New Zealand, February 2012.

6. Geoghegan P.H., C.J.T. Spence, **N. Kabaliuk**, M.C. Taylor, M.C. Jermy, The Flow Field External to the Human Nose and the Acceleration of Blood Drops from the Nasal Cavity During Violent Assault. 17th International Symposia on Applications of Laser Techniques to Fluid Mechanics, Lisbon, Portugal, 2014 (**in review**).

Table of Contents

List of Figures

List of Tables

1 Fluid dynamics of drop formation and flight

1.1 Drop formation

1.1.1 **Periodic dripping**

The most elementary drop formation mechanism is dripping of a liquid from an orifice or nozzle into an immiscible ambient fluid, such as, for example, water or blood dripping into ambient air.

In dripping of liquid at relatively low flow rates, when inertial and drag forces are small, the force balance is mainly between interfacial tension and gravitational forces. This results in the formation of relatively large (> 1 mm) (Lane and Green, 1956) and uniform drops which periodically detach from the orifice. This type or mode of drop formation is called **dripping mode** or **periodic dripping**. The same physics applies to dripping from an object wetted by a liquid.

The following general stages of this drop formation process can be distinguished. The static stage of dripping is characterised by slow growth of the mass of a liquid adhering to the orifice due to interfacial tension forces. As soon as the weight of a hanging drop exceed interfacial tension forces hanging drop starts to elongate mowing downward forming a liquid neck (see Figure 1.1a). Under gravity the neck further elongates into an almost cylindrical column/bridge or so called ligament (Figure 1.1b) (Rayleigh, 1891) which eventually becomes narrow enough and breaks in one or several (Figure 1.1c) places as a consequence of the instability of a liquid cylinder when its length exceeds circumference (Rayleigh, 1878). In most cases it breaks at the lower end near the detaching drop, so called ‘end-pinching’, and the main or primary drop is formed and it continues to move downward experiencing large amplitude shape oscillations which eventually damp by the liquid viscosity. After this, the ligament contracts vertically and experiences spatial oscillations due to capillary waves (Figure 1.1d). In some cases it may break in several places forming smaller, satellite or accompanying droplets (Figure 1.1e). These oscillate in shape and may move upwards and merge or bounce from the residual mass adhered to the source, collide or bounce from each other (Qian and Law, 1997) and may move with different velocities and trajectories.

Similar description of the ligament breakup, recoil and wave propagation with more details can be found in (Peregrine, 1990).

It should be noted that the described drop formation process is similar for a wide range of dripping liquids; however, it depends on liquid properties, size of the orifice and environmental conditions.

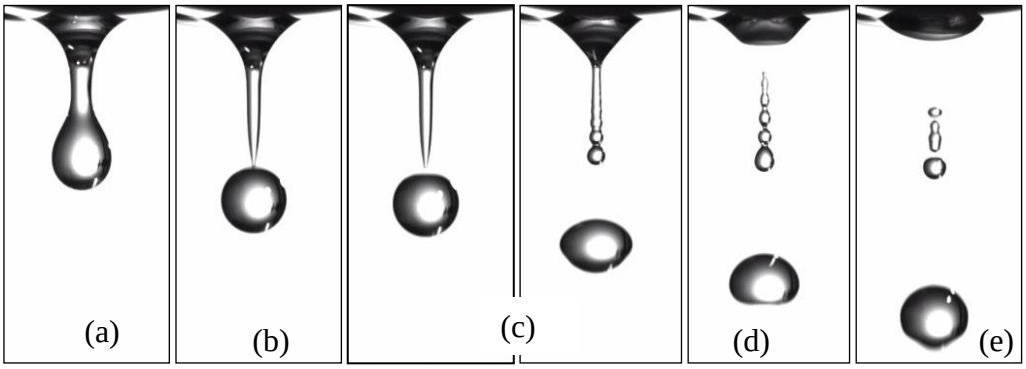

Figure 1.1. Dripping of distilled water (from the curved stainless steel surface): neck (a) and ligament (b) formation; ligament 'end-pinching' and contraction (c); consequent ligament breakup (c) and satellite formation (e).

A number of theoretical and experimental studies were dedicated to dynamics of drop formation at dripping mode.

In particular, Tate (1864) was interested in the weight W of the main drop and satellite droplets fallen from the orifice of radius R and diameter D) studied the influence of the orifice radius R on the **weight** W of the **resulting (main) drop including satellite droplets** and stated that $W = 2\pi R\sigma$, where σ is the liquid surface tension. This is correct only if the liquid surface makes right angle of contact with the orifice walls and all hanging drop actually detaches. However, some curvature of the drop surface near the wetted perimeter exists in reality and a small fraction of Tate's 'ideal' drop volume remains attached to the nozzle after the main drop detachment.

From dimensional analysis Rayleigh (1899 and 1915) proposed that $W = R\sigma f\left(R/a\right)$, where $a = \sqrt{\dfrac{2\sigma}{\rho g}}$ is the capillary length, ρ is the dripping liquid density, g is the gravitational acceleration. Function $f\left(R/a\right)$ was approximated as a constant and experimentally found to be equal to 3.8.

Harkins and Brown (1919) in the study of the drop-weight method for the determination of liquid surface tension recognized that the weight of a drop is also a function

of the drop shape which depends on the ratio of R to linear dimension of the pendant drop l proportional to the square root of the volume V of the detached drop. The shape of the drop in turn determines the fraction of the 'ideal' drop that actually falls $\psi\left(R/V^{1/3}\right)$. These led to the expression for the weight of the detached drop such as $W = 2\pi R\sigma\psi\left(R/V^{1/3}\right)$. The authors experimentally observed that the correction $\psi\left(R/V^{1/3}\right)$ is relatively unaffected by dripping liquid density ρ over a wide range and has a distinct minimum followed by a maximum.

This gives $V = \dfrac{2\pi R\sigma f\left(R/l\right)}{g\rho}$ and the main drop radius $r = \sqrt{\dfrac{3R\sigma f\left(R/l\right)}{2g\rho}}$ which depend on orifice size, liquid surface tension and density. It can be inferred from these correlations that the bigger the radius of the orifice the bigger the size of the falling primary drop.

Edgerton et al. (1937) studied the process of drop detachment from a range of orifices using high-speed motion camera. The authors experimentally explained the behaviour of the Harkins and Brown correction factor curve $\psi\left(R/V^{1/3}\right)$ Harkins and Brown (1919). For relatively small orifices the volume of the detached drop is a large fraction of the 'ideal' drop. Further along the curve the size of the formed drop decreases relative to the orifice size. Close to the maximum of $\psi\left(R/V^{1/3}\right)$ the ligament length and thickness increases along with the detached drop size. At the maximum of the curve the biggest portion of the 'ideal' drop falls. With further increase in orifice size the increase in the size of satellite drops formed from it is small compared to the increase in its radius and the curve falls.

Clift, Grace and Weber (1978) provide fitted equations for ψ as a function of $D/V^{1/3}$ with references on Heertjes et al. (1974) and Lando and Oakley (1967):

$$\psi\left(D/V^{1/3}\right) = 1 - 0.66023\frac{D}{V^{1/3}} + 0.33936\left(\frac{D}{V^{1/3}}\right)^2 \text{ for } 0 \le D/V^{1/3} \le 0.6;$$

$$\psi\left(D/V^{1/3}\right) = \left[0.92878 + 0.87638\frac{D}{V^{1/3}} - 0.261\left(\frac{D}{V^{1/3}}\right)^2\right]^{-1} \text{ for } 0.6 < D/V^{1/3} < 2.4.$$

The effect of the **thickness of the orifice walls**, for example a capillary tube, **liquid flow rate** *Q*, **viscosity** μ, **surface tension** and **density** on the dynamics of drop formation was studied by Zhang and Basaran (1995). It was found that as the ratio of the inner R_i to outer radius R of the orifice decreases the volume of the primary drop decreases. However when some critical value of this ratio, in particular when $R_i/R > 0.2$ is reached the primary drop size becomes relatively independent of this parameter. In dripping mode the primary

drop size was shown to monotonically increase with *R* and *Q*. Smaller primary drops were produces by liquids with higher density and/or lower surface tension. Newtonian liquid viscosity had only little effect on the primary drop size in support of findings by Schleele and Meister (1968) and Narasinga Rao et al. (1966). However the ligament length increased considerably with the liquid viscosity.

In particular, very viscous Newtonian fluids, for example glycerine and honey, develop very long and long-surviving stable ligaments which then break somewhere in the interior (Shi et al., 1994; Eggers and Dupont, 1994 and Eggers, 2005).

The length of the ligament was also shown to increase with the outer radius of the orifice and the liquid flow rate (Zhang and Stone, 1997). Longer ligament in turn broke into more satellite or accompanying droplets.

The effect of viscosity and density ratios, gravitational and capillary forces on drop formation (on the main drop size) in liquid-liquid systems can be found in computational and experimental works of Zhang and Stone (1997), Zhang (1999), Scheele and Meister (1968) and Narasinga Rao et al. (1966).

The solution of the Laplace equation describing the equilibrium **shape of a drop** hanging from an orifice or surface is the basis of the pendant drop method for liquid surface tension measurements (Fordham, 1948 and Stauffer, 1965). From the Yang-Laplace equation the pressure difference across the curved surface of a drop is

$\Delta p = \sigma\left(\frac{1}{R_1}+\frac{1}{R_2}\right)$, where R_1 and R_2 are principal (orthogonal) radii of curvature at a particular point on the liquid surface (Figure 1.2). Taking the origin at the bottom of the drop, the pressure difference can be represented as $\Delta p = \frac{2\sigma}{b} + \Delta\rho g z$, where b is the radius of curvature at the drop bottom where $b = R_1 = R_2$, z is the vertical coordinate with the origin at the drop bottom.

Theoretically if the two radii of curvature are known at two points on the drop surface the complete drop shape can be determined. However in practice R_1 and R_2 can hardly ever be determined.

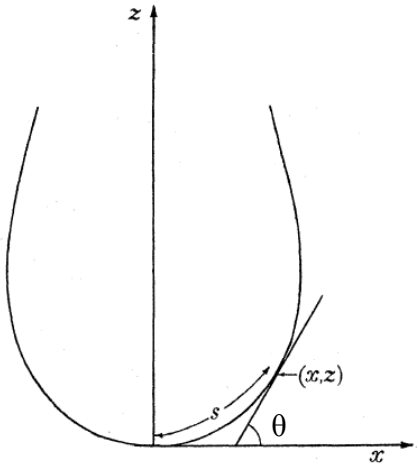

Figure 1.2. Pendant drop diagram.

Introducing cylindrical coordinates X (horizontal coordinate from drop bottom) and S (arclength of the drop surface curve from the drop bottom to a point on its surface) and based on geometrical considerations such as $\frac{1}{R_1}=\frac{d\theta}{dS}$, $R_2=\frac{\sin\theta}{X}$, $\frac{dX}{dS}=\cos\theta$, $\frac{dZ}{dS}=\sin\theta$ where θ is a slope at a point on the drop surface the Laplace equation can be rearranged as following (Thiessen and Man, 1999) $\frac{d\theta}{ds}=2+\beta z-\frac{\sin\theta}{x}$ with the change in variables to $s=\frac{S}{b}$, $x=\frac{X}{b}$, $z=\frac{Z}{b}$. This equation for the shape of a pendant drop can be solved numerically with the following initial conditions $x(0)=z(0)=\theta(0)=0$.

Experimentally obtained drop profile can be fitted to the Laplace equation solution which is the basis for modern pendant drop technique of interfacial tension and contact angle measurements (Rotenberg et al., 1983; Cheng et al., 1990 and Couper, 1993).

Equations describing the equilibrium shape of a hanging volume of liquid in terms of theoretical fluid dynamics can be found in (Batchelor, 1967). Pozrikidis (2012) analyzed the stability of a liquid drop attached to a horizontal plane and determined the limits within which a pendant or sessile drop is stable.

Tanasawa and Toyoda (1955) analyzed equilibrium forms of a hanging drop for different values of the radius of curvature at the drop tip, liquid surface tension and gravitational forces. They calculated the slow development of the pendant drop up to the first break, but their method was not capable of modeling the capillary waves which result, and so could not calculate the length of the ligament or the size of the accompanying droplets.

Lefebvre (1989) reported an equation (Equation 1.1) for the diameter *d* of a drop falling from the underside of a horizontal wetted surface, and references Lapple et al. (1957), who in turn reference Tamada and Shibaoka (1961). However this equation does not appear in Tamada and Shibaoka's paper or Hida and Nakanishi's paper (Hida and Nakanishi, 1970) and may be a correlation to their data.

$$d = 3.3\sqrt{\frac{\sigma}{\rho g}} \tag{1.1}$$

Papageorgiou (1995) investigated nonlinear dynamics of the breakup of the cylindrical liquid thread (ligament) based on the Stokes equation, i.e. neglecting the influence of inertia. The proposed model could predict the breakup conditions and satellite droplets formation for different initial conditions.

Eggers (1993) studied the breakup of liquid ligament numerically solving the Navier-Stokes equation both before and after the breakup 'singularity', where inertia can no longer be neglected due to the increasing velocity of the contracting ligament.

Dynamics of elongated ligament was studied by Tong and Wang (2007) using the finite-volume formulation of the Navier-Stokes equation. Special attention was drawn to the end-pinching mechanism of the ligament breakup. Velocity and pressure distribution near the primary drop detachment point were obtained (Figure 1.3).

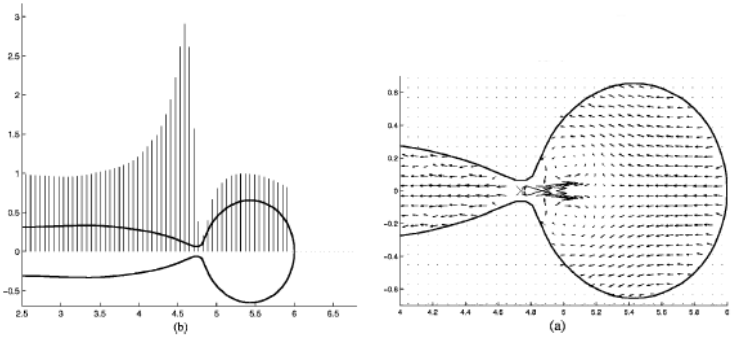

Figure 1.3. Pressure (a) and velocity (b) fields immediately prior to primary drop detachment (from Tong and Wang, 2007).

The minimum pressure was located in the region close to the detaching primary drop where the radius of the ligament is minimal. However, there was a sharp variation in pressure from the observed minimum in the middle of the ligament neck to its maximum value upstream due to the severe change in ligament surface curvature from concave to convex.

Stone and Leal (1989) in their numerical study of an initially extended drop found that a critical ligament elongation ratio exists above which its breakup will not occur.

Marmottant and Villermaux (2004) in the experimental study of the fragmentation of stretched liquid ligaments describe the dynamics of the ligaments during fast and slow elongation. For small stretching rates, the breakup occurred first on the lower end of the ligament which then contracted, in most cases, into one satellite droplet. Whereas, at large stretching rates the ligament broke up on both ends almost simultaneously. Thisfurther fragmented into the large distribution of satellite droplet sizes.

Handerson et al. (2000) investigated the motion and breakup of ligaments of liquids with different viscosities. A criterion for a ligament breakup or pinch off location based on the growth rate of disturbances with various wave numbers was proposed. In short, a ligament breaks up in one or more interior points if the wavelength of the most unstable wave mode is shorter than the ligament length. The breakup occurs at the ends when the wavelength is approximately equal to the ligament length.

As the flow rate of the liquid in the nozzle (orifice) increases the inertial effects no longer can be ignored. At these conditions there is the additional mass flow into the falling drop during necking and detachment. Relationships for the resulting drop size taking into account gravity surface tension, viscosity, inertia and volume added during necking and detachment can be found in Scheele and Meister (1968), Kumar and Kuloor (1970), Humphrey (1980).

1.1.2 **Chaotic dripping**

At certain conditions dripping process continues but the detaching drops vary in size from one to another in a quasi-periodic or chaotic way. The time between successive drops also varies in non-lineal manner and the point of drop detachment moves further from the orifice. This regime of drop formation is called the **chaotic dripping** or **dripping faucet**.

Dreyer and Hickey (1991) investigated the dynamics of dripping faucet with different radii. At higher flow rates two or more drops were observed to leave the faucet in a sequence followed by a sequence of smaller drops.

Clanet and Lasheras (1998) experimentally observed the decrease in drop detachment period with the orifice radius and liquid flow rate. The transition between periodic and chaotic dripping in terms of Weber number $We = \frac{\rho v^2 D}{\sigma}$ based on orifice diameter D and inlet velocity v were observed at We ≈ 1 for D = 4.1 mm and We = 6 for D=0.5 mm.

Theoretical and numerical studies of dripping faucet can be found in (Shaw, 1984); (Ambravaneswaran et al., 2000); (Fuchikami et al., 1999); (Kiyono and Fuchikami, 1999).

1.1.3 **Jet breakup**

With further increasing flow rate the balance between surface tension and gravitational forces is no longer can be maintained and the liquid emerges from the orifice in a form of a cylindrical jet. Perturbations and oscillations grow on the liquid free surface and under favorable conditions the jet disintegrates into drops. The detachment point of the droplets shifts downstream from the exit of the orifice. This process of drop formation is called **jet breakup** or **jet disintegration.**

A great number of studies dedicated to jet disintegration exist due to its importance in a variety of industrial processes such as ink-jet printing, fuel combustion, spray painting and so on. A comprehensive review of jet breakup mechanisms with relevant references can be found in Brodkey (1967), Liu (1981), Lefebvre (1989), McCarthy and Molloy (1974), Reitz and Bracco (1986).

The brief description of disintegration mechanisms (or regimes) of a liquid jet injected into ambient air together with different approaches in their classification is followed (provided below).

The jet disintegration was studied experimentally by Savart (1833) who correlated the continuous length of a jet to its velocity and diameter. Plateau (1873) theoretically showed that a liquid jet becomes unstable and disintegrates into drops possessing smaller possible surface area if its length larger than its perimeter.

Rayleigh (1878, 1879 and 1892) theoretical studied the stability of a non-viscous laminar liquid jet. The jet is considered to be symmetric or varicose (having straight axis and with infinitesimal rotationally symmetric perturbations or disturbances on its surface (Figure 1.4a)). Initial disturbances in the liquid (which are always present) induce local pressure fluctuations due to surface tension effects. These lead to the local fluid movement which in turn amplifies the existing disturbances leading to the eventual jet breakup.

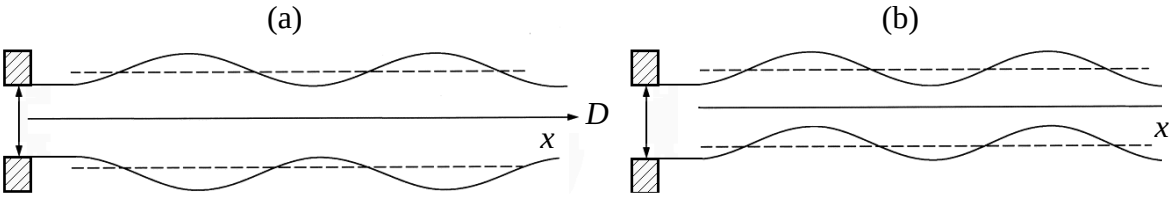

Figure 1.4. Varicose (symmetric) (a) and sinuous (anitisymmetric) (b) jets.

From Rayleigh's analysis the initial disturbances on the surface of a jet with initial diameter D having wavelengths λ greater its circumference πD grow exponentially under the influence of surface tension force. For the growth rate $q_{\max}$ and wavelength λ_{opt} of the fastest-growing disturbance Rayleigh gives the following expressions:

$$q_{\max} = 0.97\sqrt{\frac{\sigma}{\rho D^3}} \; ; \; \lambda_{opt} = 4.51D \, .$$

Eventually the jet of length $4.51D$ breaks up into drops of uniform size $d = 1.89D$ with regular spacing.

Rayleigh's theory was supported by the experimental findings of Tyler (1933) who obtained similar relationships for the fastest-growing disturbance and resulting drop size.

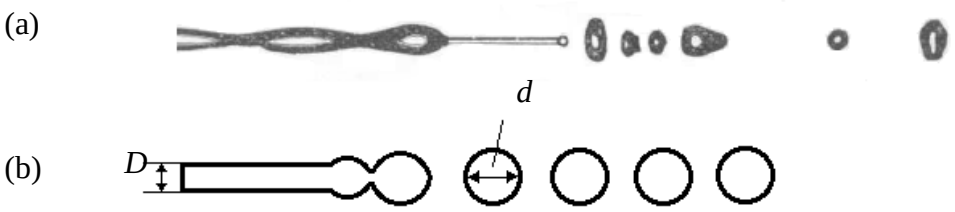

Figure 1.5. Real water jet breakup (from Rayleigh (1891)) (a) and Rayleigh's 'idealized' approach/consideration (b).

This description of the jet breakup ignores viscous, inertial and aerodynamic effects providing the upper limit for resulting drop sizes. In addition, it does not predict satellite droplets formation (Figure 1.5).

In the same paper Rayleigh considered the dynamical effects of the relative velocity and density difference across the interface and, in subsequent study, the effect of viscosity on the jet breakup.

Weber (1931) investigated the effects of liquid viscosity on the low-velocity varicose jet breakup and concluded that if the wavelength of the initial disturbance is smaller than the jet circumference $\lambda_{\min} = \pi D$ the surface tension forces tend to damp it or amplify it in the

opposite case. Viscosity was shown to have no effect on $\lambda_{\min}$. The wavelength of the most rapidly growing disturbance in terms of Ohnesorge number $Oh = \frac{\mu}{\sqrt{\rho D \sigma}}$ was represented as $\lambda_{opt} = \pi D \sqrt{2(3Oh+1)}$. For inviscid fluids ($Oh = 0$) this gives $\lambda_{opt} = 4.44D$, and for very viscous fluids ($Oh \to \infty$) $\lambda_{opt} \to \infty$ which agrees well with Rayleigh's analysis. This shows that when the liquid viscosity becomes significant a damping of the initial instabilities takes place.

The time of breakup and resulting drop diameter are represented as $t_{bup} \approx \frac{1}{\lambda_{opt}}$ and $d = \left(1.5\lambda_{opt} D^2\right)^{1/3}$ correspondingly. It is seen that high surface tension leads to more rapid breakup and smaller resulting drop. Whereas, an increase in the viscosity of a fluid increases the breakup time (and breakup length) and resulting drop size. In addition, for low viscosity fluids the drop size is independent of the surface tension and correlates only with the jet radius.

Weber also showed that the air friction causes the reduction in the minimum and the fastest-growing wavelengths and, when the relative velocity exceeds a certain value, the possibility of the distortion of the jet centerline or wave formation resulting in an antisymmetric or sinuous jet (Figure 1.4b). Thus, with the increase in the relative jet velocity there is a faster jet disintegration and resulting drop size reduction.

Levich (1962) theoretically investigated the jet breakup under the influence of aerodynamic forces. From his analysis for very high relative velocities extremely short wavelength disturbance on the jet surface become unstable producing much smaller droplets compared to low velocity jets breakup. The time of detachment of small drops is much smaller than the complete jet breakup time. Levich showed that for more viscous fluids longer wavelength disturbances lead to the breakup resulting in bigger drop. High viscosity reduces the disturbance growth rate increasing the breakup time (together with the breakup length).

Further studies were dedicated to high-velocity jet breakup and to the classification of jet breakup mechanisms by the jet appearance and forces leading to breakup.

According to (Liu, 1981) jet breakup mechanisms can be classified into four regimes by the relative importance of surface tension, inertial, viscous and aerodynamic forces.

Rayleigh or varicose jet breakup occurs where the theory of Rayleigh (and Weber) described above applies. As the relative jet velocity increases aerodynamic forces dominate over surface tension forces; sinuous wave is formed with the oscillations amplified by air resistance and damped by surface tension (first wind-induced breakup). The jet disintegrates closer to the nozzle (shifts upstream) into drops smaller than the jet diameter. Further increase in the relative velocity leads to the unstable growth of the short wavelength surface waves induced by the relative motion of the liquid in a jet and surrounding gas (second wind-induced breakup). The jet breakup occurs several jet diameters downstream generating a range of droplets much smaller than the jet diameter in size. In the next regime, called atomization or primary atomization, the breakup appears near with the nozzle exit producing conical spray of droplets. It is believed that the effect of air resistance is dominant during the atomization of high-velocity jets. This process is enforced by jet turbulence, inertial effects and surface tension initiating the disturbances on the jet surface (Chigier, 1991).

The transition between the regimes described is not sharp due to the dependence of the disintegration mechanism on the initial condition of the jet (velocity profile, level of pulsations and disturbances, turbulence etc.), nozzle geometry and wall roughness (see for example Chigier, 1991).

Tanasawa and Tyoda (1955) characterized jet breakup regimes using the Jet number $Je = \frac{v^2 \rho_a D}{\sigma}\left(\frac{\rho}{\rho_a}\right)^{0.45}$ based on the jet inlet velocity v and density ρ_a of surrounding gas (air). Dripping of a liquid from a nozzle occurs at $Je < 0.1$. For $0.1 < Je < 10$ breakup occurs due to longitudinal jet oscillations (laminar and laminar to turbulent transition breakup). At $10 < Je < 500$ jet oscillates laterally. Due to the air friction narrow membranes and/or fine ligaments are formed on the jet surface which quickly separates into drops. After this spray regime follows when the jet core breaks up into fine droplets surrounded by larger droplets produced during the ligaments and membranes shattering.

In the preceding description of the phenomenon of jet disintegration, together with the drop sizes after jet disintegration and jet disruption manner mentioned above, the continuous length of a jet before the breakup L is also of interest. So called jet stability curve (Figure 1.6) as a convenient way to represent the relationship of the breakup length and jet velocity were constructed by various authors (see for example Savart (1883) and Lefebvre (1989)).

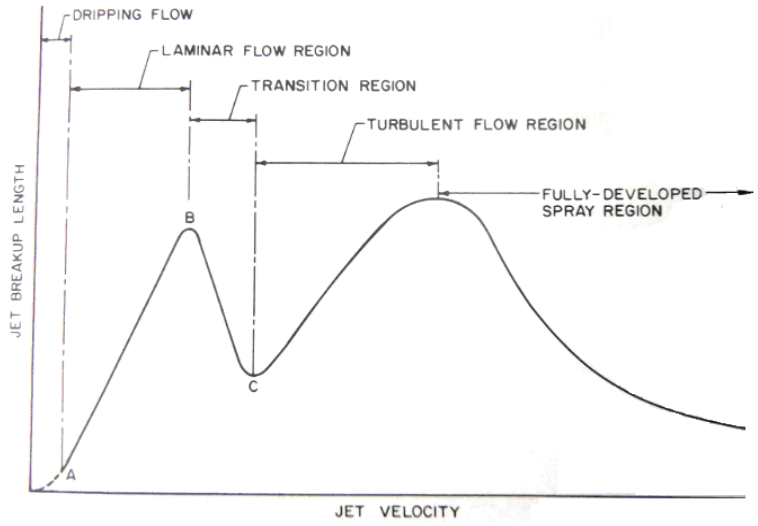

Figure 1.6. Jet stability curve (from Lefebvre (1989)).

The curve begins with a dripping region (OA) at low velocities. Once the jet is formed *L* increases with increasing jet velocity (AB) corresponding to a laminar jet described by Rayleigh and Weber. Here the breakup length also increases with the jet diameter, liquid density and viscosity and decreases with surface tension.

At some point it reaches the maximum denoting the transition between varicose to sinuous jet breakup regime (Hainlein, 1932) and/or dominance of air resistance according to Weber and/or the onset of turbulence. This transition point shifts to lower jet velocities for liquid with higher viscosity.

The breakup length decreases with further increase in jet velocity (BC) where the flow in a jet changes from laminar to turbulent de Sande and Smith (1976).

Further along the curve *L* increases with the velocity up to a maximum value after which it stats to decrease with the jet velocity.

Expressions for the jet continuous length and empirical correlations describing the transitions between various jet breakup regimes can be found in (Lefebvre, 1989 and Liu, 1981).

According to Hiroyasu et al. (1982) there is no clear trend in the effect of the nozzle diameter to length ratio on the jet breakup length at low ambient pressure.

1.1.4 **Sheet breakup**

Under certain conditions the liquid can emerge from the nozzle (or other source) in a form of a sheet which then disintegrates into droplets. The dynamics of a **liquid sheet**

depends primary on its initial velocity and the physical properties of a liquid and surrounding media (Lefebvre, 1989 and Liu, 1981) distinguish the next three modes of sheet breakup (Figure 1.7).

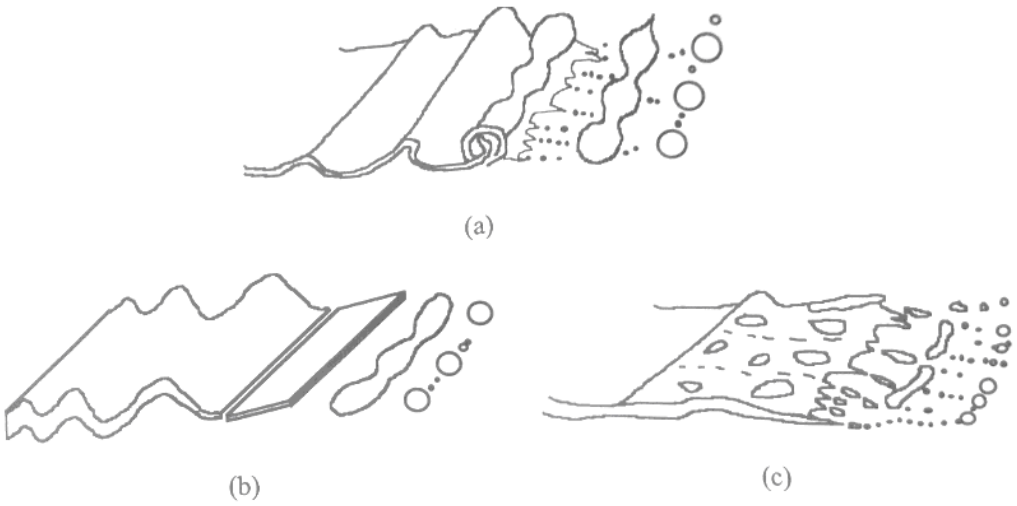

Figure 1.7. Liquid sheet/film breakup modes: rim (a), wavy-sheet (b) and perforated-sheet (c) disintegration (from Liu (1981)).

During the rim disintegration mode (Figure 1.7a) the free edge of the liquid sheet contracts into a thicker rim due to surface tension forces tending to reduce the free liquid surface. The rim subsequently disintegrates into relatively large drops similar to the breakup of a liquid jet. The drops move in the original flow direction while remaining connected to the main liquid body by thin ligaments which eventually breakup into smaller satellite droplets. This is applicable to the sheets of very viscous fluids with high surface tension.

The wave-sheet disintegration (Figure 1.7b) occurs when aerodynamic forces induce rapidly growing waves on the surface of a sheet leading to its breakup in the locations corresponding to the half or full wavelength of the oscillations (at the crests and troughs) when a critical value of the wave amplitude is reached. The detached element contracts due to surface tension effects, but can further disintegrate into drops of various sizes following the varicose instability mechanism.

Perforated sheet disintegration mode (Figure 1.7c) describes the holes formation in the body of the sheet. The holes grow in size until the mesh of thin ligament is formed which break into relatively uniform drops.

Dombrowski and Fraser (1954) showed that liquid sheet with high surface tension and viscosity are highly resistant to the breakup, whereas the liquid density has negligible effect on the breakup mechanism. Hagherty and Shea (1955) and Dombrowski and Johns (1963)

correlated the mean diameter of the resulting drops with the square root of the sheet thickness. Rizk and Lefebvre (1980) found that the thickness of a sheet depends on the liquid and surrounding air properties. Thicker sheets are formed from more viscous fluid and/or at higher flow rates with no effect of the liquid surface tension. However, the surface tension decreases the sheet breakup time. Arai and Hashimoto (1985) stated that the breakup length increases with increasing sheet inlet velocity and the decrease in liquids viscosity.

The above mentioned drop formation processes and the physics (fluid dynamics) behind them are common (frequently encountered in) for different technological applications and real life situations.

1.2 Drop in flight

1.2.1 The governing equations

The fundamental fluid dynamics equations governing motion of particles immersed in fluids (Schlichting, 1968; Clift, Grace and Weber, 1978; Zaprianov and Tabakova, 1999 and Landau and Lifshitz, 1987) are listed below.

The **continuity equation** arises from the conservation of mass:

$$\frac{\partial \rho}{\partial t} + \nabla \cdot (\rho \vec{v}) = 0 , \tag{1.2}$$

where ρ is the density of the continuous phase or the medium surrounding the particle (gas or liquid), $\vec{v} = \vec{v}(t, \vec{r}) = v_x \vec{i} + v_y \vec{j} + v_z \vec{k}$ is the continuous phase velocity vector as a function of time t and space coordinates or the radius vector $\vec{r} = x\vec{i} + y\vec{j} + z\vec{k}$, $\nabla = div = \frac{\partial}{\partial x}\vec{i} + \frac{\partial}{\partial y}\vec{j} + \frac{\partial}{\partial z}\vec{k}$ denotes, a vector operator, divergence. For incompressible fluids $\rho = const$ so that $\frac{D\rho}{Dt} = 0$ and Equation 1.2 gives $\nabla \cdot \vec{v} = 0$.

The **momentum equation** (or Navier-Stokes equation) derived from the conservation of momentum

$$\rho \frac{D\vec{v}}{Dt} = \rho \vec{f} - \nabla \cdot T , \tag{1.3}$$

where $\frac{D}{Dt} = \frac{\partial}{\partial t} + \vec{v} \cdot \nabla$ is the substantial derivative, a sum of temporal and convective derivatives, $\rho \vec{f}$ is the external body force per unit volume ($\vec{f}$ is equivalent to the

gravitational acceleration $\bar{g}$ in the gravity field), $\nabla \cdot T$ is the net surface force per unit volume with minus sign because this is a resistive force.

$T = -pI + \tau$ is the stress tensor expressed as a sum of the isotropic (the stresses due to compression of a fluid) and deviatoric (due to viscous stresses) parts. Where *p* is pressure in a fluid and τ is the symmetric viscous stress tensor.

Equation 1.3 states that that the velocity of an element of a fluid moving (or translating) with the velocity $\bar{v}$ undergoes change (acceleration) due to the external force and the gradient in the stress tensor which include the acceleration due to the gradient in the static pressure *p* ($-\frac{1}{\rho}\nabla \cdot p$) (pressure force) and due to the viscous stress ($-\frac{1}{\rho}\nabla \cdot \tau$) (shear force).

The stress tensor τ includes normal and shear stresses which correspond to the net surface forces per unit area acting perpendicularly and tangentially to the surface element in a fluid and depends on the rate of fluid deformation.

The deformation of a fluid element can be described by the deformation tensor $D_{ij} = \frac{\partial v_i}{\partial x_j}$, or velocity gradients in a fluid, that can be expressed in the form

$$\frac{\partial v_i}{\partial x_j} = \frac{1}{2}\left(\frac{\partial v_i}{\partial x_j} + \frac{\partial v_j}{\partial x_i}\right) + \frac{1}{2}\left(\frac{\partial v_i}{\partial x_j} - \frac{\partial v_j}{\partial x_i}\right) = \dot{\gamma}_{ij} + \omega_{ij}, \qquad (1.4)$$

where *i, j* are used to denote three velocity and radius vector components, $\dot{\gamma}$ is the rate of strain tensor and Ω is the vorticity tensor. The latter can be expressed as $\dot{\gamma} = \frac{1}{2}\left(\nabla \cdot \bar{v} + (\nabla \cdot \bar{v})^T\right)$, where $\left[(\nabla \cdot \bar{v})^T\right]_{il} = \left[\nabla \cdot \bar{v}\right]_{ji}$. The trace of the rate tensor *E* (the sum of diagonal elements called normal strain rates) describes the rate of the volume dilatation of a fluid element such as $\dot{\gamma}_{ii} = \nabla \cdot \bar{v}$ wich is equal to zero for incompressible fluids. The off-diagonal elements $\dot{\gamma}_{ij}$, called shear strain rates, represent the rate of the shear strain or shear rate of a liquid element.

The vorticity tensor Ω (or in the other representation $\Omega = \frac{1}{2}\left(\nabla \cdot \bar{v} - (\nabla \cdot \bar{v})^T\right)$) describes the rate of a fluid element rotation as a rigid-body without the volume change and shear deformation (or without viscous stress).

The form of the stress tensor, in particular, the relationship between its constitutive viscous shear stress tensor with the strain rate tensor (or shear rate for incompressible liquids), depends on the nature or rheology of the fluid. The equations that specify the

relationship between the shear stress and shear rate tensors are called rheological or constitutive equations.

So called Newtonian fluids (isotropic (the same in all directions) and linear) (such as most gases, water, glycerol) show linear relationship between τ and $\dot{\gamma}$: $\tau_{ij} = C_{ijlm} D_{lm} = C_{ijlm} \frac{\partial v_l}{\partial x_m}$, where a coefficient tensor for an isotropic fluid can be expressed as $C_{ijlm} = \mu\left(\delta_{ij}\delta_{jm} + \delta_{im}\delta_{jl}\right) + \lambda\delta_{ij}\delta_{lm}$, where $\delta_{ij} = \begin{cases} 0, & if\ i \neq j \\ 1, & if\ i = j \end{cases}$ is the Kronecker delta, μ and λ are viscosity coefficients and empirical functions primarily of fluid temperature. μ is the measure of a liquid resistance to shear deformation (or applied shear stress) and is called shear, dynamic or simply viscosity. The volume viscosity or the second viscosity λ describes the reaction of a fluid to the applied normal stress or volume dilatation (Tritton, 1988). The linear combination of these $k = \frac{2}{3}\mu + \lambda$ is called the bulk viscosity.

Thus $\tau_{ij} = \mu\left(\frac{\partial v_i}{\partial x_j} + \frac{\partial v_j}{\partial x_i}\right) + \lambda \frac{\partial v_l}{\partial x_l}\delta_{ij} = \mu\left(\frac{\partial v_i}{\partial x_j} + \frac{\partial v_j}{\partial x_i}\right) + \lambda\delta_{ii}\nabla\cdot\bar{v}$. So the stress tensor can be represented as $T = -pI + \lambda\left(\nabla\cdot\bar{v}\right) + 2\mu\dot{\gamma}$. For incompressible fluids the shear stress tensor is $\tau_{ij} = \mu\left(\frac{\partial v_i}{\partial x_j} + \frac{\partial v_j}{\partial x_i}\right) = 2\mu\dot{\gamma}_{ij}$ and the stress tensor $T = -pI + 2\mu\dot{\gamma}$, here $I = \begin{bmatrix} 1 & 0 & 0 \\ 0 & 1 & 0 \\ 0 & 0 & 1 \end{bmatrix}$ is the identity tensor.

However, some fluids (such as blood, toothpaste, ink, paint), called non-Newtonian, possess nonlinear relationships between the stress and strain tensors (Chhabra and Richardson, 1999; Skelland, 1967 and Brodkey, 1967).

It is convenient to define so called 'apparent viscosity' $\mu_a = \frac{\tau}{\dot{\gamma}}$ which is a function of the current shear rate value for so called purely viscous or time-independent fluids. For these fluids the constitutive equation is $\tau = f\left(\dot{\gamma}\right)$. Depending on the form of the function f this class of non-Newtonian fluids can be divided into shear-thinning, or pseudoplastic, for which the apparent viscosity decreases with the rate of the applied shear, shear-thickening, or

dilatant, with the increase in μ_a with the shear rate and viscoplastic having the characteristic yield stress τ_0 that must be exceeded to cause the fluid deformation or movement.

For so called time-dependant fluids the apparent viscosity, however, is also a function of the duration of shear and kinematic history of a fluid. A sub-class of these fluids, namely thixotropic fluids, when sheared with a constant rate shows the shear stress to decrease with time. Rheopexic fluids show the opposite behaviour or negative thixotropy.

Another class of non-Newtonian fluids which exhibit both viscous and elastic behavior is called viscoelastic fluids.

Rheological properties of blood as a time-independent (pseudoplastic) and viscoelastic fluid (Baskurt et al., 2007; Gabelnick and Litt, 1973 and Dacie and Lewis, 1995) will be discussed later in this review (in the text).

For the complete determination of the compressible flow of viscous fluid the equation for **the thermodynamic state** of the form $p = f(\rho)$ should be also specified in addition to the **energy equation** describing the balance between heat and mechanical energy for nonisothermal processes:

$$\rho \frac{De}{Dt} = \nabla \cdot (\kappa \nabla T) - \rho \nabla \cdot \vec{v} + \mu \Phi , \qquad (1.5)$$

where *e* is the absolute thermodynamic internal energy per unit mass, *T* is temperature, κ is fluid thermal conductivity (from Fourier's law the heat flux $q = -\kappa \nabla T$), μ - continuous fluid viscosity, Φ is the dissipative function correlated to heat generation due to friction. Further on only incompressible ($\rho = const$) and isothermal (*T = const*) flows of viscous fluid will be discussed.

In order to mathematically close this system of equations **boundary and initial conditions** (i.e. $\vec{v}(\vec{r} = \vec{r}_o, t = t_0)$) have be further specified.

On the surface of a **<u>rigid particle</u>** in a viscous flow there is an adherence of the fluid particles to the solid surface so that both normal and tangential velocity components are zero, so called non-lip conditions: $\vec{v} \cdot \vec{n}\big|_S = 0$; $\vec{v} \cdot \vec{\tau}\big|_S = 0$, where $\vec{n}$ and $\vec{\tau}$ are unit normal and tangential vectors on the particle surface *S*. On the surface of the rigid particle moving with $\vec{v}_p$, however, $\vec{v}\big|_S = \vec{v}_p$. Far from the particle the fluid moves with the velocity of the undisturbed flow or stream velocity U .

For **fluid particles** (drops and bubbles) immersed in an immiscible fluid kinematic and dynamic boundary conditions should be specified at the interface $\hat{S}$ between two fluids (see Figure 1.8).

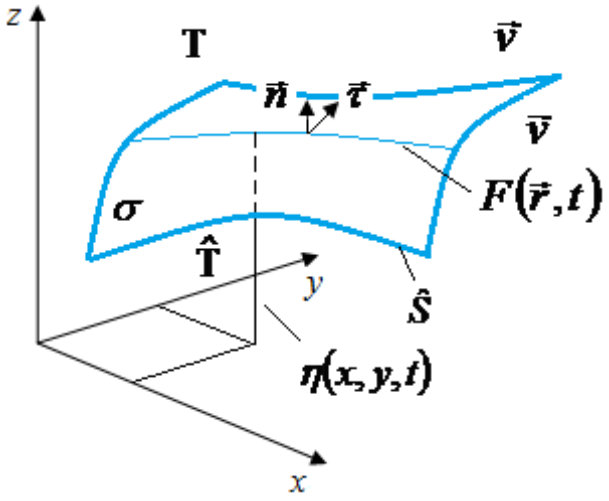

Figure 1.8. Free surface interface between two fluids.

The continuity condition for the velocities $\vec{v}$ above and $\hat{v}$ below the interface (or free surface) $\hat{S}$: $\vec{v} = \hat{v}$.

Assuming that the position of the interface can be described by the implicit function $F(\vec{r},t) = 0$ at any time *t*, such as, for example, for the elevation of the free surface above some reference plane at position x, y and time t is $z = \eta(x,y,t)$ and thus $F(\vec{r},t) = z - \eta(x,y,t)$.

∇F is normal to the free surface $\hat{S}$, so the unit normal vector to it can be defined as $\vec{n} = \pm \dfrac{\nabla F}{|\nabla F|}$ with $\vec{n} > 0$ directed outward and $\vec{n} > 0$ inward relative to $\hat{S}$.

For the impermeable boundary between two liquids (i.e. a boundary across which there is no flux of matter of the macroscopic scale) the particles remain on the free surface so that

$$\frac{DF}{Dt} = \frac{\partial F}{\partial t} + \vec{v} \cdot \nabla F = 0 . \tag{1.6}$$

This is true from above and below the interface $\hat{S}$ so that

$$\vec{v} \cdot \vec{n} = \hat{\vec{v}} \cdot \vec{n} = \frac{\partial F / \partial t}{|\nabla F|} . \tag{1.7}$$

Equation 1.7 manifests the **kinematic velocity condition** on a fluid interface and states that the normal components of the velocity on either side of the interface are equal. For the

stationary interface $\frac{\partial \eta}{\partial t} = 0$, the vector difference of velocities across the impermeable interface vanishes on the interface such as $(\vec{v} - \hat{\vec{v}}) \cdot \vec{n}\big|_S = 0$.

However, when a change of state (phase change or transformation) of the fluid occurs at the boundary (for example, evaporation) or where the boundary surface displays a selective permeability phenomenon, the condition (Equation 1.6) is no longer rigorously applicable.

The **dynamic boundary condition** implies the stress balance condition on both sides of the free surface (Scriven, 1960) such as $(\mathrm{T} \cdot \vec{n} - \hat{\mathrm{T}} \cdot \vec{n}) + \nabla_s \sigma - \sigma \vec{n} (\nabla_S \cdot \vec{n}) = 0$. (3.7)

Here σ is the surface tension on the interface that can be defined as the integral along the curve L of the force $df = \sigma dl \times \vec{n}$ exerted be one side of the liquid surface on the other through the curve element dl (see Figure 1.9) (Lautrup, 2010). $\nabla_s = (I - \vec{n}\vec{n}) \cdot \nabla$ is the surface gradient operator. $\nabla_s \cdot \vec{n} = \frac{1}{R_1} + \frac{1}{R_2}$ is the twice mean surface curvature with principal radii of curvature R_1 and R_2 (for the a sphere of radius R: $R_1 = R_2 = R$ and for the flat surface $R_1 = R_2 \to \infty$).

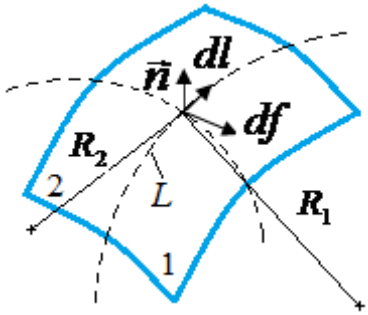

Figure 1.9. Curved free surface element and its principal radii of curvature.

The condition (3.7) describes a jump (discontinuity) in stress across the fluid interface that is balanced by the surface forces. In fact, surface tension on a curved surface creates normal stress jump across the free surface: $(\mathrm{T} \cdot \vec{n} - \mathrm{T} \cdot \vec{n}) \cdot \vec{n} = \sigma (\nabla_S \vec{n})$. The excess pressure due to the surface tension and curvature of the surface can be expressed as $\Delta p = \sigma \left(\frac{1}{R_1} + \frac{1}{R_2} \right)$ (the Young-Laplace law). Thus the pressure under a curved surface (such as in a drop or bubble) is higher than the pressure in the surrounding medium on the value of Δp.

In addition, surface tension gradients on the interface cause a jump in the tangential stress into two tangential to the interface directions: $\left(\mathrm{T}\cdot\vec{n}-\mathrm{T}\cdot\vec{n}\right)\cdot\vec{\tau}=\left(\nabla_S\sigma\right)\cdot\vec{\tau}$. This induces the movement of the movement of one or both fluids across the interface, so-called Marangoni effect (Levich, 1963).

Is should be mentioned that for the spherical Newtonian liquid particle with the radius *R* moving in air with the velocity $\vec{v}_p$ the following boundary conditions can be specified (Zaprianov and Tabakova, 1999):

– for the normal and tangential velocities on both sides of the interface:

$$\left(\vec{v}-\vec{v}_p\right)\cdot\vec{n}=0,\ \left(\hat{\vec{v}}-\vec{v}_p\right)\cdot\vec{n}=0;$$

$$\vec{v}\cdot\left(I-\vec{n}\vec{n}\right)=\hat{\vec{v}}\cdot\left(I-\vec{n}\vec{n}\right),\text{ using the identity }\vec{v}=\vec{v}\cdot\vec{n}\vec{n}+\left(I-\vec{n}\vec{n}\right)\cdot\vec{v};$$

– tangential stress balance: $\hat{p}-p+2\mu\left[\dot{\gamma}\cdot\vec{n}-\lambda\hat{\dot{\gamma}}\cdot\vec{n}\right]\cdot\vec{n}=\frac{2\sigma}{R}$, where $\hat{p}$ and *p* are the total pressure of the two fluids;

– normal stress balance: $\left(\dot{\gamma}\cdot\vec{n}\right)\cdot\left(I-\vec{n}\vec{n}\right)=\lambda\left(\hat{\dot{\gamma}}\cdot\vec{n}\right)\cdot\left(I-\vec{n}\vec{n}\right)$, where $\lambda=\frac{\hat{\mu}}{\mu}$ the viscosity ratio of the two fluids.

Movement of liquid particles, or drops, with constant surface tension ($\sigma=const$) in air as well as the behaviour of rigid particles for comparison will be considered below in this review.

1.2.2 **Drag and lift forces**

When there is relative movement between an object and a surrounding fluid the latter exerts pressure forces (pdA) normal to the surface of an object and shear forces ($\tau_A dA$, where τ_A is the viscous shear stress on a surface element *dA*) parallel to its surface along the entire surface of the object (Figure 1.10) (Yunus and Cimbala, 2005).

The resultant force $\mathrm{F_R}$ (see Figure 1.10) exerted on an object moving with relative velocity $\vec{v}$ through a fluid of density ρ and viscosity μ can be divided into parallel F_D and perpendicular $\mathrm{F_L}$ to the direction of the undisturbed flow (such as the direction of the free stream velocity far from the object or the object's velocity) components.

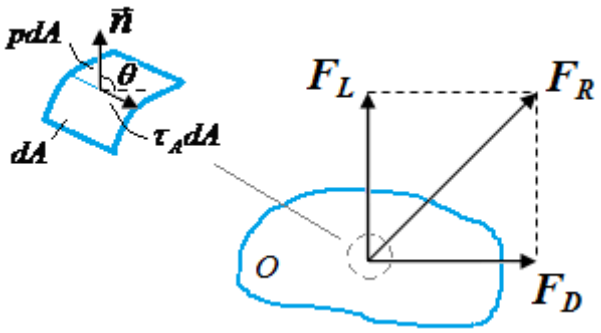

Figure 1.10. Drag and lift forces on an object.

These two forces are called the drag and lift forces correspondingly:

$$F_D = \int_A dF_D = \int_A (-p\cos\theta + \tau_A \sin\theta) dA;$$

$F_D = \int_A dF_D = \int_A (-p\cos\theta - \tau_A \sin\theta) dA$, where θ is the angle between the outer normal to dA and liquid flow direction. To calculate the net drag and lift forces on the object the detailed pressure and shear forces distribution on the surface of the object needs to be known. The latter, however, is often difficult to obtain.

From the dimensionless analysis lift and drag forces can be expressed as $F_D = -\frac{1}{2}\rho v_{rel}^2 C_D A$ and $F_L = -\frac{1}{2}\rho v_{rel}^2 C_L A$ correspondingly. Here $\vec{v}_{rel} = \vec{u} - \vec{v}$ - relative velocity based on the object's velocity $\vec{u}$ and bulk liquid (or free stream) velocity $\vec{v}$, $v_{rel} = |\vec{v}_{rel}| = \sqrt{(u_x - v_x)^2 + (u_y - v_y)^2 + (u_z - v_z)^2}$ is the relative velocity magnitude. $\frac{\rho v_{rel}^2}{2}$ is the dynamic pressure in the surrounding fluid, A is a reference projected area (frontal or planform area), $C_D = f(\mathrm{Re})$; $C_L = f'(\mathrm{Re})$ are dimensionless constants called drag and lift coefficients which represent drag and lift characteristic of the object. For incompressible fluids (i.e. Mach number $Ma = \frac{v}{a}$, where a is the speed of sound in the fluid, is small) these depend on dimensionless Reynolds number $\mathrm{Re} = \frac{\rho v d}{\mu}$ as the ratio of inertial forces (characterize fluid resistance to any change in motion) to viscous forces based on particle characteristic dimension (i.e. diameter d) and kinematic viscosity $\eta = \frac{\mu}{\rho}$ of the surrounding fluid. For free surface flows, however, other dimensionless numbers should be taken into account. These will be discussed in more details later in the text.

For an ideal fluid with no internal friction ($\mu = 0$) there is a slip of the fluid along the surface of the object moving uniformly through it and, as a result, experiencing no drag force (D'Alembert paradox). However any object in a real fluid experiences resistance as a result of the adherence of the fluid particles to the solid surface (no-slip) leading due to friction to the formation of the retarded fluid layer adjoined to the object's surface, so called boundary layer (Schlichting, 1968). Shear stresses inside the boundary layer are high due to high velocity gradients. Whereas, outside this layer, the velocity is relatively uniform and the shear stresses are small. The thickness of the boundary layer δ increases along the object's surface in the direction of flow due to an increase in the amount of the retarded fluid. δ decreases with the fluid viscosity.

Under certain conditions the boundary layer thickens downstream and eventually separates from the surface of the object. A low pressure region with flow recirculation (vortices), called wake, forms behind the object leading to a pressure distribution which differs from the case of the frictionless flow.

The portion of the **drag force** that is due to the inertia of the fluid is called the **pressure drag** (or form drag or profile drag) and arises from the pressure difference between the front and back of the immersed body (see above). It is proportional to the frontal area and depends on the form or shape of the object.

The **skin friction drag** or friction drag is the component of the shear force on the surface of an object in the direction of flow and it depends on the orientation of the object, its surface area and on the magnitude of τ_A which proportional to the fluid viscosity.

Thus, for high Re numbers flows (negligible viscous effects) the total drag on an object is due to the pressure drag, whereas, the skin friction drag is predominant at low Re numbers.

The **lift force** originates when the object orientation in the flow causes the movement of the object normal to the direction of the undisturbed flow.

1.2.3 **Rigid particles**

In the limiting case of low Reynolds numbers, Navier-Stokes equation can be simplified and approximate solutions can be found.

For the very slow motion, or creeping motion, of a rigid sphere in an infinite media when viscous forces are dominant Stokes (1851) derived one such solution. For the net (drag) force exerted on a sphere by the viscous flow with the uniform free stream velocity $\vec{v}$ Stokes obtained the next expression: $F_D = 3\pi\mu \cdot d \cdot \vec{v}$. One third of this expression is due to the

pressure drag and two thirds is due to skin friction. From here the drag coefficient is given by $C_D = \frac{24}{\mathrm{Re}}$. For such a creeping flow the flow pattern is symmetric about a plane perpendicular to the direction of flow and passing through the centre of the sphere (Figure 1.11). It is seen that the sphere entrains a large amount of the fluid over an extensive region around it.

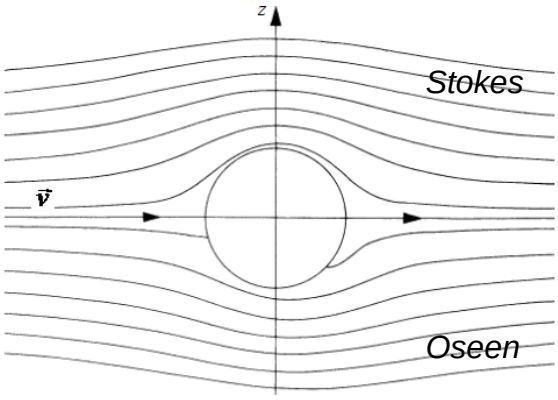

Figure 1.11. Streamlines relative to a rigid sphere immersed into a viscous fluid according to Stokes (1851) and Oseen (1910) (from Clift, Grace and Weber (1978)).

Oseen (1911) preserved one of the convective terms in the Navier-Stokes equation to include the inertial effects for low-Re flows in his calculations and received the following formulae for the drag force and dimensionless drag coefficient: $F_D = 6\pi\mu \cdot a \cdot U\left[1+\frac{3}{8}\mathrm{Re}+O(\mathrm{Re})\right]$; $C_D = \frac{24}{\mathrm{Re}}\left[1+\frac{3}{16}\mathrm{Re}\right]$. From Figure 1.11 for Oseen's solution there is an asymmetry in the flow pattern ahead and behind the sphere and the wake formation is visible.

A yet more accurate expression was given by Proudman and Pearson **(**1957): $F_D = 6\pi\mu \cdot a \cdot U\left[1+\frac{3}{8}\mathrm{Re}+\frac{9}{40}\mathrm{Re}^2 \ln \mathrm{Re}+O(\mathrm{Re}^2)\right]$. Similar expressions for low-Re numbers flows can be found in works by Goldstein (1929), Lewis and Carrier (1949), Chester and Breach (1969).

Figure 1.12 illustrates the behavior of the rigid sphere drag coefficient a function of Re number from Clift, Grace and Weber (1978) based on the critical analysis of numerous experimental data (Nguyen, 1973). Stokes' and Oseen's solutions are also plotted for comparison. Similar correlations can be found in a more recent study by (Achenbach, 1974).

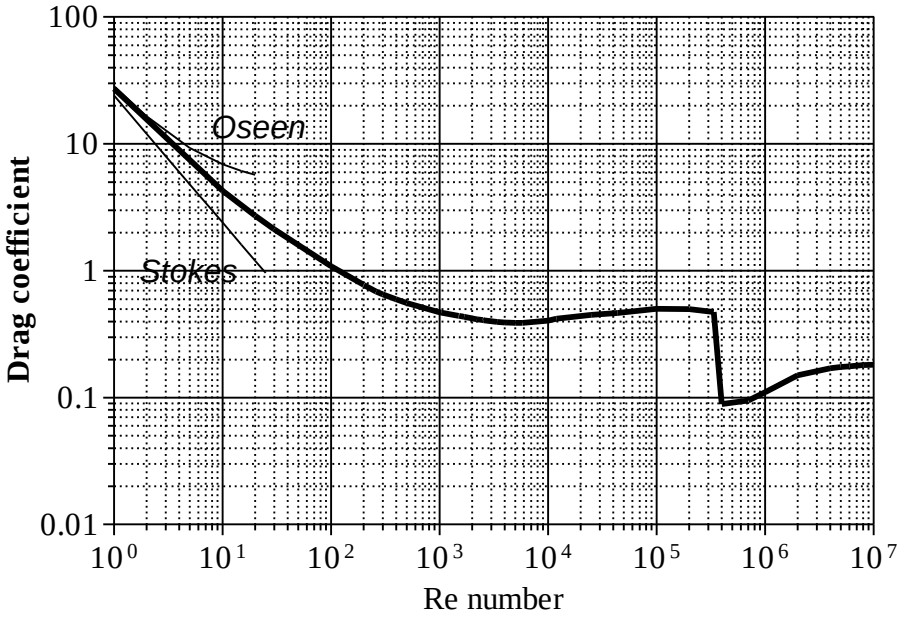

Figure 1.12. Log-log plot of the sphere drag coefficient as a function of Re number.

It is seen that Stokes' and Oseen's approaches are valid only for Re << 1 and Re < 5 correspondingly.

This dependence of the drag coefficient on Re number can be explained by examining the flow field around a rigid sphere with increasing Re number (Michaelides, 2006; Clift, Grace and Weber, 1978):

1. **Unseparated flow** (1 < Re < 20): boundary layer aligned with the body surface. Its thickness increases downstream along the sphere. Flow pattern asymmetry becomes progressively marked as Re increases.

2. **Separation** (Re ≈ 20): the flow in the boundary layer is reversed under the influence of the pressure distribution, vortices form.

3. **Steady wake** (20 < Re < 130): vortices stretch and the separation point shifts from the rear with increasing Re. As Re increases, the importance of the skin friction decreases relative to the form drag.

4. **Unsteady wake** (130 < Re < 400): onset of instability in the wake occurs at 130<Re<150 leading to vortices shedding from the sphere surface at Re > 400. Skin friction becoming inferior to pressure drag once Re > 150 causing a decrease in C_D.

5. **Subcritical regime** (400 < Re < $3{,}5\cdot10^5$): regular vortices shedding from alternate sides which may cause fluctuations in the motion of freely falling particles affecting mean drag. Shedding frequency at first increases with Re number, for $6\cdot10^3$ < Re < $3\cdot10^4$,

however, the frequency decrease significantly after this point. At Re = $6 \cdot 10^3$ boundary layer separates at a point on the solid surface which rotates around the surface with the frequency equal to the vortex shedding frequency. C_D is relatively independent of Re number. The flow in the boundary layer is laminar in this regime, but the flow in the separated region and the wake is highly turbulent.

6. **Turbulent wake** (Re ≥ $3{,}5 \cdot 10^5$): the boundary layer becomes turbulent, flow separation point shifts downstream reducing the size of the wake and the pressure drag. For Re > 10^6 C_D increases to about 0.9.

1.2.3.1 Terminal conditions

As an object falls vertically under its weight *W* (Figure 1.13), which is counter balanced by the buoyancy force F_B, the drag force is much less than the gravitational force due to the low velocity of the object. The drag force increases as it accelerates until at some point it balances object's weight so that $F_D = W - F_B$. As a result the object moves with zero acceleration and uniform velocity, called terminal velocity U_T.

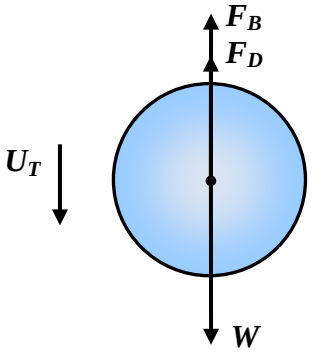

Figure 1.13. Forces acting on a falling object.

For spherical particles from the equality $F_D = \frac{1}{2}\rho U_T^2 \frac{\pi}{4} d^2 C_D = \frac{\pi d^3}{6}\Delta\rho g$ terminal velocity is $U_T = \sqrt{\frac{4}{3}\frac{\Delta\rho d g}{\rho C_D}} = \sqrt{\frac{4}{3C_D}\left(\frac{\hat{\rho}}{\rho} - 1\right) d g}$, where $\Delta\rho$ is a density difference between the object $\hat{\rho}$ and the surrounding media (ρ).

From Stokes' law at Re << 1 $U_T^{St} = \frac{\Delta\rho d^2 g}{18\mu}$. It is seen that terminal velocity increases with the object's density and size (more precisely, its projected area) and decreases with the

density of the surrounding media. Objects with lower drag coefficients have can reach higher terminal velocities.

1.2.3.2 Arbitrary shape particles

Detailed classification and drag considerations for nonspherical particles in an external viscous flow at low and high Reynolds numbers can be found in (Clift, Grace and Weber, 1978). In short, the flow patterns around these objects and thus the net drag depend on the particle orientation in the flow. The net drag is generally not parallel to the direction of motion, so that a particle moves without rotation only if it possesses certain symmetry or a specific orientation. Each particle possesses at least three orthogonal (principal) axes. For an axisymmetric particle translating with relative velocity $\vec{u}$ parallel to one of its principal axes *i*, which identical to one its axes of symmetry, the net drag is given by $F_D = -\mu c_i \vec{u}$, where c_i is called 'principal translational resistances'. For the particle to move steadily in free fall or rise F_D must be pointed vertically to balance the gravity force and must be applied to the particle's centre of mass. For an interesting example of spheroids with axial diameter *2a* and equatorial diameter *2b* (Figure 1.14) which in limiting case can reduce to a sphere (aspect ratio $AR = \frac{b}{a} = 1$), a disk ($AR \to 0$) or a needle ($AR \to \infty$) Happel and Brenner (1973) provided the following expression for the drag force in the creeping flow: $F_D = -6\pi l \mu \vec{u} K\left(\frac{a}{b}\right)$, where *a*, *b* – major and minor semiaxeses (*a*>*b*; *l*=*a* - oblate; *b*>*a*; *l*=*b* - prolate), *K* - correction coefficient that is the ratio of the hydrodynamic force for the spheroid to the force on the sphere with the same equatorial diameter *2a*. Various analytical expressions for *K* together with drag coefficient correlations at slightly higher Re numbers can be found in (Clift, Grace and Weber, 1978; Michaelides, 2006).

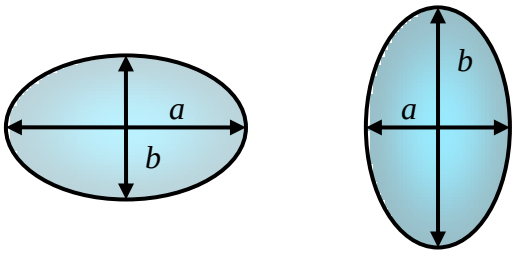

Oblate (a > b) Prolate (a < b)

Figure 1.14. Oblate and prolate spheroids.

Flow field around spheroidal particles at high Re numbers due to inertial effects shows higher asymmetry when the longer particle dimension is normal to the flow with decreasing wake for more 'streamlined' particles (Masliyah and Epstein, 1970; Michaelides, 2006; Clift, Grace and Weber, 1978). Flow separation occurs at lower Re for the particles with lower aspect ratio. Steady wakes are observed at higher Re numbers if the particle is more prolate. At high Re the flow patter around spheroids are similar to that of a sphere. For a disk, however, the flow separation is limited by its geometry so that a sharp drop in the drag coefficient (typical for a sphere) is not observed. Clift, Grace and Weber (1978) distinguished two regimes for free falling spheroidal particles when particles align to the relative flow so that their maximum dimension is normal to the flow (here C_D changes with Re less strongly than in creeping flow) and when secondary motions due to mostly vortex shedding occur (C_D is independent of Re).

1.2.4 **Unsteady flow: rigid and fluid particles**

Boussinesq (1885) and Basset (1888) studied uniform transient creeping flow $\bar{v}(t)$ past a solid sphere and derived the equation of its motion and an expression for the transient force exerted on it. The latter contained a term identical to the Stokes's drag for steady motion and two additional terms called 'added mass' and Basset force. The former is a result of the acceleration of a certain volume of the fluid around the sphere due to its movement through the media. For the transient movement of a sphere the added mass equals the mass of a volume of fluid half the volume of the sphere ($\frac{2}{3}\pi\frac{d^3}{8}\rho$, d is the diameter of the sphere). All bodies accelerating in a fluid experience added mass force, but since it is dependent on the density of the fluid it is often neglected for dense bodies moving in less dense fluids or when $\frac{\hat{\rho}}{\rho}\to\infty$, for example liquid drops moving in air (Michaelides, 2006). However, for $\hat{\rho}\approx\rho$ added mass exceed the mass of the object.

The Basset force arises as a result of the delay in boundary layer development with changing relative velocity. Liang and Michaelides (1992) found that the Basset force may be neglected in the particle equation of motion only when the fluid to particle density ratio is very high and the particle diameter is greater than 1 μm. Due to its complicated form and the difficulty of its implementation it is often neglected. However, for movement with high acceleration the Basset term can exceed the Stokes' term as much as a factor of two.

All in all, drag is higher during accelerated than during steady motion (Haghes, 1952).

A number of studies exist regarding the transient creeping flow motion. Faxen (1922) studied the transient non-uniform flow around a sphere near the boundary. Maxey and Riley (1983) investigated a non-uniform transient fluid flow field $\vec{v}(\vec{r},t)$ and considered so-called 'Faxen term' to account for the effects of the flow non-uniformities. Auton (1987), Auton et al. (1988) introduced corrections to the velocity derivatives in the 'added mass' term.

Lovalenti and Brady (1993) studied an arbitrary solid particle moving with arbitrary velocity in a viscous fluid at small but finite Re numbers and showed that the history term decays faster than in creeping motion and that the forces during acceleration and deceleration of a sphere are different. The same is true for the case of the motion of a particle from rest and for finite particle (drop or bubble) fluid viscosity due to the formation and spreading of the wake.

Odar and Hamilton (1964) elaborated a modification to the Boussinesq-Basset expression based on the empirical corrections for Re < 16000 and showed that during the movement of a particle 'added mass' term dominates initially; history term passes through a maximum and decay, whereas, steady drag increases monotonically with particle velocity. Kim et al. (1998) produced similar numerical corrections for 0 < Re < 150. Odar (1966) studied the free fall of spheres at Re < 62 and pointed that Re at which the wake separation and shedding occur higher than that during the steady flow.

Temkin (1980; 1982) and Chang and Maxey (1995) showed that the drag coefficient of a sphere decreases from the standard drag curve values during an acceleration and increases during deceleration due to, respectively, the reduction and growth of the wake.

A comprehensive review of the literature on the unsteady flow past objects of different shapes at low and high Re numbers can be found in (Michaelides, 2006; Clift, Grace and Weber, 1978 and Zapryanov and Tabakova, 1998).

Chisnell (1987) and Sy et al. (1970; 1971) investigated the uniform transient flow around a viscous spherical drop at very low Re numbers. Lovalenty and Brady (1993) studied transient arbitrary flow around a fluid particle. Michaelides and Feng (1995) included velocity slip on the surface of a sphere and effects of its finite viscosity. The studies of the unsteady flow around fluid particles at moderate and high Re are limited to intermediate Re and rising spherical and circular-cap bubbles. It is believed that the difference in drag force on fluid particles at moderate and high Re numbers is associated more with the deformation than with 'added mass' or history terms (Michaelides, 2006; Clift, Grace and Weber, 1978).

A small review of experimental studies of the effect of solid sphere acceleration on the drag coefficient can be found in (Buzzard and Nedderman, 1967).

1.2.5 **Fluid particles**

Fluid particles include both liquid drops and gas bubbles. The most attention will be dedicated to the motion of drops in gaseous media (such as water drops in air) with some comparison to bubbles in liquids and liquid-liquid systems (drops in immiscible liquids) for reference.

1.2.5.1 Circulations

The relative motion of a fluid particle with diameter *d* and viscosity $\hat{\mu}$ in a surrounding media with viscosity μ in the creeping flow regime was studied by Hadamard (1911) and Rybczynski (1911). They obtained the following expression for the hydrodynamic force exerted on the particle and its drag coefficient:

$$F_D = 3\pi\mu \cdot d \cdot v_{rel} \frac{2\mu + 3\hat{\mu}}{3\left(\mu + \hat{\mu}\right)},\ C_D = \frac{16}{\mathrm{Re}} \frac{2\mu + 3\hat{\mu}}{3\left(\mu + \hat{\mu}\right)}.$$

From the balance of the gravitational and drag forces this gives the equation for the terminal velocity as $U_T = U_T^{St} \frac{1 + \hat{\mu}/\mu}{2/3 + \hat{\mu}/\mu} \begin{cases} \hat{\mu} >> \mu \Rightarrow U_T = U_T^{St} \\ \hat{\mu} << \mu \Rightarrow U_T = \frac{3}{2} U_T^{St} \end{cases}$, which for the case of very viscous drops in a less viscous media ($\frac{\hat{\mu}}{\mu} \to \infty$) reduces to the expression for the Stokes' terminal velocity U_T^{St} of a solid sphere. In the limiting case of small viscosity ratios $\frac{\hat{\mu}}{\mu} \to 0$ (a bubble in a viscous fluid) it predict a terminal velocity one and a half times bigger than U_T^{St}. This difference arises due to the motion of the interior fluid (in a drop or bubble) under friction on the surface which results in the decrease in boundary layer thickness of the external flow compared to the case of an equivalent rigid particle (with the same weight *W*) leading to the shift of the flow separation point downstream, reduction of drag and to the increase in U_T (Levich, 1962).

Bond (1927) and Bond and Newton (1928) investigated the effect of surface tension σ on internal circulations inside a fluid particle and produced the following expression for the

terminal velocity: $U_T = U_T^{St}\phi\left(\frac{\hat{\mu}}{\mu}; \frac{a\sigma}{W}\right)$

$$\begin{cases} large\ drops \Rightarrow \frac{d\sigma}{W} \to 0 \Rightarrow Hadamard - Rybchinsky\ law \\ small\ drops \Rightarrow \frac{d\sigma}{W} \to large \Rightarrow U_T = U_T^{St} \end{cases}.$$

The authors imply that for large drops or bubbles the ratio $\frac{d\sigma}{W}$ is small and the expression for U_T approaches Hadamard-Rybczynski law. For the case of small particles ($\frac{d\sigma}{W}$ is large) the terminal velocity tends to that of a solid sphere with.

Hughes and Gilliland (1952) explained the effect of surface tension on the circulations inside a drop pointing that there is a creation of the surface at the front of the drop and a local creation of surface energy due to the action of the skin friction. The necessary energy for this is supplied by the moving internal fluid, and by the energy due to loss of the surface at the rear of the drop. There is, however, viscous dissipation of this energy inside the drop which is supposed to be overcome by skin friction forces to maintain circulation. So, the circulations only become significant when the skin friction is large enough to overcome the viscous damping inside the drop.

Considering that the skin friction drag correspond to one third of the total drag ($\frac{2}{3}\frac{\pi}{6} g d_{cr}^3 \Delta\rho$)

in creeping flow and assuming that critical condition for the onset of circulations is when it equals surface tension forces $\pi d_{cr}\sigma$ the authors give the following formula for the critical diameter of the drop: $d_{cr} = 3\sqrt{\frac{\sigma}{\Delta\rho g}}$. The transition begins at $d \approx 0.1 d_{cr}$ (Bond and Newton, 1927).

Boussinesq (1913) proposed the concept of a viscous surface layer and derived the terminal velocity of a fluid particle in a form $U_T = U_T^{St}\frac{\mu + \hat{\mu} + \frac{2e}{3a}}{2\mu + 3\hat{\mu} + \frac{2e}{a}}$, where *e* is the surface viscosity coefficient which describes the relationship between surface tension and the rate of the surface change. The latter appeared to be difficult to measure experimentally.

Levich (1962) investigated the effect of surfactants on the internal circulations. He concluded that due to the relative particle motion surfactants tend to concentrate at the rear of the particle causing the formation of surface tension gradient (and tangential stress) and as a result surface retardation. This increases the total drag and lowers terminal velocity: $U_T = U_T^{St} \frac{\mu + \hat{\mu} + \gamma}{2\mu + 3\hat{\mu} + \gamma}$ where γ is the retardation coefficient which is higher for smaller drops.

Representative photos of circulation patterns can be found in Spells (1952).

A number of experimental studies of the fluid particles motion (Lane and Green, 1956; Beard, 1976) acknowledged that for small liquid drops (d < 1 mm; Re < 300) or fluid particles with high viscosity ratios circulations are negligible leading to rigid sphere behaviour. Bigger drops or particles with low viscosity ratios experience circulations which reduce velocity gradient at the interface leading to the decrease in friction forces and cause the flow separation point to shift, in such a way that increases pressure in the separated zone lowering the form drag. All this decreases the net drag and drag coefficient and increases particle terminal velocity compare to that of an equivalent solid sphere.

Warshay et al. (1956) studied terminal velocities of liquid drops in various liquids and showed that the increase in drop viscosity reduces circulations causing the increase in shear at the surface and quicker boundary layer separation increasing the pressure drag. Similar results were found by Gillaspy and Hoffer (1983) who also showed that internal circulations do not affect drop shape considerably, but are believed to contribute to the onset of the fluid particle deformation towards an increase in its cross-sectional area which in turn causes an increase in drag. The effect of circulations on the drag of drops (such as water drops) in air was shown to be negligible compared to the effect of the drop shape distortion discussed below (Savic, 1953; McDonald, 1954; LeClair, 1972). In addition, progressive deformations were shown to decrease internal circulations velocities in a drop (Harper and Moore, 1968). The circulations die out at Re > 800 according to LeClair (1972).

1.2.5.2 Drop deformation or distortion from sphericity

Under the action of surface tension forces a drop tends to minimize its surface energy and shape of a sphere having the smallest possible surface area. However when subject to external fluid flow drops deform until normal and shear stresses balance at the fluid-fluid interface (Clift, Grace and Weber, 1978).

Fluid particle (both bubbles and drops) deformation can be characterized using Reynolds number $\mathrm{Re} = \frac{\rho U d}{\nu}$ (mentioned earlier), Bond (or Eötvös (Eo)) number $Bo = \frac{\Delta\rho g d^2}{\sigma}$ (ratio of **buoyancy** (or **gravity**) to **surface tension** forces), Weber number $We = \frac{\rho U^2 d}{\sigma}$ (measure of the relative importance of **inertial** forces compared to **surface tension** forces), Morton number $Mo = \frac{g\mu^4\Delta\rho}{\rho^2\sigma^3}$ (characterize the shape of bubbles or drops moving in a surrounding fluid), Ohnesorge number $Oh = \frac{\hat{\mu}}{\sqrt{\hat{\rho} d \sigma}}$ as the ratio of inner liquid **viscous** forces to **surface tension** forces, $\chi_E = \frac{\hat{\mu}}{\mu}$ and $\gamma = \frac{\hat{\rho}}{\rho}$ - viscosity and density ratios.

1.2.5.3 Shape classifications of fluid particles

Saito (1913) showed theoretically that a drop in the external flow deforms into either an oblate or prolate spheroid.

Taylor and Acrivos (1964) specified that the oblate shape is typical for low We numbers, whereas, drops resemble convex beans having so-called '**spherical-cap'** shape.

Hinze (1955) pointed that the extent of the deformation depends on the value of We number.

Hughes (1955) studied basic types of fluid 'globule' deformation in different types of flow and showed that flattened, torus-like shape ('lenticular') is typical for the parallel, axisymmetric hyperbolic and rotating flow. A fluid particle in a plane hyperbolic or Couette flow fattens into a long cylindrical thread ('cigar-shaped'). In irregular flow it deforms locally and bulges and protuberances occur ('bulgy' deformation).

Clift, Grace and Weber (1978) classify shapes of both drops and bubbles in free fall or rise in liquid media under gravity into three groups. **Spherical** particles are observed when the interfacial tension and/or viscous forces are much more important than inertia forces at to low Re and Bo. **Ellipsoidal** deformation is observed for relatively high Re and moderate Bo numbers. The shape differs from true ellipsoid (oblate or flattened). For bubbles wobbling may also occur. So-called 's**pherical-cap**' shape often with indentation at the front (dimpled) is observed for fluid particle movement at high Re and Bo.

Michaelides (2006) provided similar classification. He suggested that drops and bubbles can be considered spherical when the deviation between the values of axial and equatorial diameters is within 5%. Sphericity is maintained at low Re for any value of Bo number and at moderate Re numbers for Bo < 1.

Grace et al. (1976) produced a correlation between Re, Bo and Mo for drops and bubbles rising at their terminal velocities in Newtonian fluid'.

1.2.5.4 Drop deformation and drag at terminal velocity

There are many experimental studies of the movement of water drops at terminal velocities in air due to its importance for meteorological science.

Gunn and Kinzer (1949) investigated terminal velocities of distilled water falling in stagnant air. Small drops (d < 0.08 mm) were considered to obey Stokes' law. Drops of diameter d < 1 mm followed solid-like behaviour. Bigger drops tended to deform by aerodynamic forces and even oscillate and spin during free fall. Bond and Newton (1927) gave a criterion for the deviation from solid-like behavior of free falling drops in air in a form $Bo \approx 0.4$, where the transition begins at $d_{cr} = 1.8\sqrt{\frac{\sigma}{\Delta\rho g}}$. For liquid-liquid systems this criterion, according to Winnikow and Chao (1966), is $Bo \approx 0.2$. Similar results were obtained experimentally by Licht and Narasimhamurty (1956) who produced a correlation between drag coefficient and Bond number in a form: $\frac{C_D}{C_D^{St}} = 1.87Bo + 0.425$, for $Bo \geq 0.4$, where significant drop deformation begins.

For drops of 4 < d < 6 mm terminal velocity was observed to be a weak function of drop diameter and corresponded to about 9.17 m/s. Drops larger than 9 mm tended to become unstable and disintegrate (breakup) into smaller drops.

The data obtained by Gunn and Kinzer can be expressed as $U_T = 9.40\left(1 - \exp\left(-3.45 \times 10^3 (d/2)^{1.31}\right)\right)$.

Levich (1962) used the pressure difference approach to explain this phenomenon considering that drop is deformed under the pressure difference $\Delta p = \frac{\rho U^2}{2}$ in the front and rear of the drop, but capillary pressure resists the deformation. From drag and gravitational forces balance with constant drop volume condition he derived an expression for the terminal

velocity independent of the drop size $U_T \approx \sqrt[4]{\frac{4\Delta\rho g\sigma}{C_D\rho^2}}$. This predicts higher U_T (lower C_D) for particles with greater surface tension which are less deformed (or flattened).

So, the drop deformation associated with an increase in its cross-sectional (projected) area leads to an increase in drag (and drag coefficient) on the deformed drop which in turn decreases terminal velocity compared to the case of an equivalent rigid sphere movement.

Beard and Pruppacher (1969) measured the drag and terminal velocities on small water drops in air for 0.2 < Re < 200. They acknowledged that the drag on water drops at this Re number was close to that of equivalent solid spheres which imply that deformation is negligible. The ratio of the actual to Stokes' drag for these drops was given by:

$$\frac{F_D}{F_D^{St}} = 1 + (0.10 \pm 0.02)\mathrm{Re}^{(0.99\pm0.05)}, \quad for \quad 0.2 \le \mathrm{Re} \le 2,$$

$$\frac{F_D}{F_D^{St}} = 1 + (0.11 \pm 0.01)\mathrm{Re}^{(0.81\pm0.03)}, \quad for \quad 2 \le \mathrm{Re} \le 21,$$

$$\frac{F_D}{F_D^{St}} = 1 + (0.189 \pm 0.006)\mathrm{Re}^{(0.632\pm0.007)}, \quad for \quad 21 \le \mathrm{Re} \le 200.$$

For Re > 200 the drag on drops was observed to be higher than that of a solid sphere indicating their spherical shape distortion. Terminal velocities values were in good agreement with that from Gunn and Kinzer (1949).

Beard (1976) investigated terminal velocities of water drops 1 μm - 7 mm in diameter. For small droplets (1 < d < 20 μm) terminal velocity is less than 0.01 m/s. Droplets of intermediate size (20 μm < d < 1 mm) were found to be reasonably well approximated by the expressions for solid spheres with negligible effect of varying surface tension and drop viscosity. Large drops (up to 7 mm) deviated from solid-like behaviour having lower terminal velocity and, consequently, higher drag due to an increase in the projected area and drag coefficient. The aspect ratio $AR = \frac{d_{\min}}{d_{\max}}$, i.e. the ratio of polar d_{min} to equatorial d_{max} diameters of these drops (1 < d < 7 mm) was approximated as: $\frac{1}{AR} = 0.9 + 0.1d$. Relative terminal velocity constancy was observed for d > 4 mm.

Pruppacher and Beard (1970) for drops with diameters 1 ≤ d ≤ 9 mm provided the following correlations for the aspect ratios at terminal velocities: $AR = 1.030 - 0.062d$.

Analogous fitted correlations can be found in Beard and Chuang (1987):

$AR = 1.0048 + 5.7\times10^{-4} d - 2.628\times10^{-2} d^2 + 3.682\times10^{-3} d^3 - 1.677\times10^{-4} d^4$ for 1 ≤ d ≤ 7;

Andsager et al. (1999): $AR = 1.012 - 0.01445d - 1.028\times10^{-2} d^2$ for 1 ≤ d ≤ 4mm;

Goddard et al. (1994): $AR = 1.075 + 6.5\times10^{-2} d - 3.6\times10^{-3} d^2 + 4.0\times10^{-3} d^3$ for 1 ≤ d ≤ 5 mm;

Thurai and Bringi (2005): $AR = 1.055 - 0.0653d$ for for 1.5 ≤ d ≤ 8 mm;

Brandes et al. (2002):

$AR = 0.9951 + 2.51\times10^{-2} d - 3.644\times10^{-2} d^2 + 5.303\times10^{-3} d^3 - 2.492\times10^{-4} d^4$. The latter also produced an expression for the terminal velocity of water drops based on experiments by Gunn and Kizner and Beard and Pruppacher for drops up to 8 mm in diameter:

$U_T = -0.1021 + 4.932d - 0.9551d^2 + 0.07934d^3 - 0.002362d^4$.

Other authors crudely approximated the relationship between terminal velocity and water drops sizes by a power-law expression $U_T = A \cdot d^B$, where A and B are fitted constants. For drops with d > 0.4 mm Best (1950) derived that $U_T = 10.30 - 9.65e^{-0.6d}$. A similar expression was produced by Gossard et al. (1992): $U_T = 9.65\left(1 - e^{-0.53d}\right)$ and Uplingers (1977): $U_T = 4.85de^{-0.195d}$.

The shape of large water drops at terminal conditions were theoretically assessed by Green (1975). From considerations of the balance of surface and gravity forces at the drop equator and ignoring the effects internal circulations and aerodynamic pressure at the equator he derived with good agreement with previous experiments that $AR = \left[\frac{4}{17}\left(\frac{17Bo}{4} + 1\right)^{1/2} + \frac{13}{17}\right]^{-3/2}$, where Bo number is based on drop radius (d/2).

Pruppacher and Pitter (1970) and then Beard and Chuang (1987) considered the effects of aerodynamic pressure at the surface of a water drop and internal circulations in it and approximated the shape of the drop at terminal condition by a 10th order cosine distortion of the initial spherical drop of radius r_0: $r(\theta) = r_0\left(1 + \sum_{n=1}^{10} c_n \cos(n\theta)\right)$, where $c_1 ... c_{10}$ are the coefficients, called 'shape coefficients', that depend on the radius of the drop, θ is a polar angle measured from the bottom of the drop. From verification experiments the authors discovered that drops with d ≤ 0.34 mm maintain their spherical shape while moving at terminal velocity; drops with 0.34 < d < 1 mm cam be considered as oblate spheroids; large drops with 1 < d < 4 mm have asymmetric oblate form with a flat base, whereas, large drops (d > 4) mm become dimpled at the base.

The data on terminal velocities and aspect ratios of water drops from various sources are plotted below (see Figure 1.15 and 1.16).

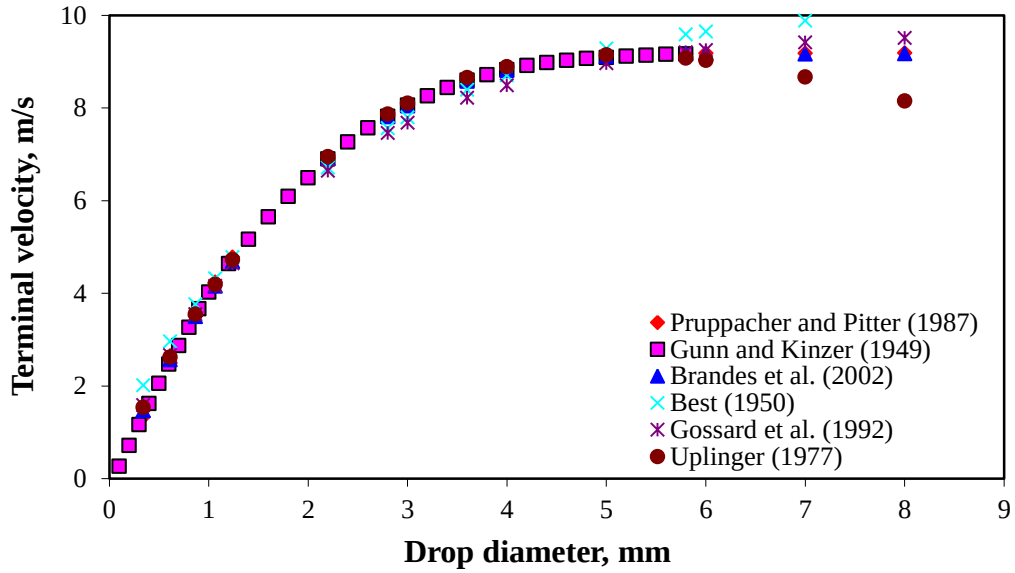

Figure 1.15. Terminal velocity of water drops in air.

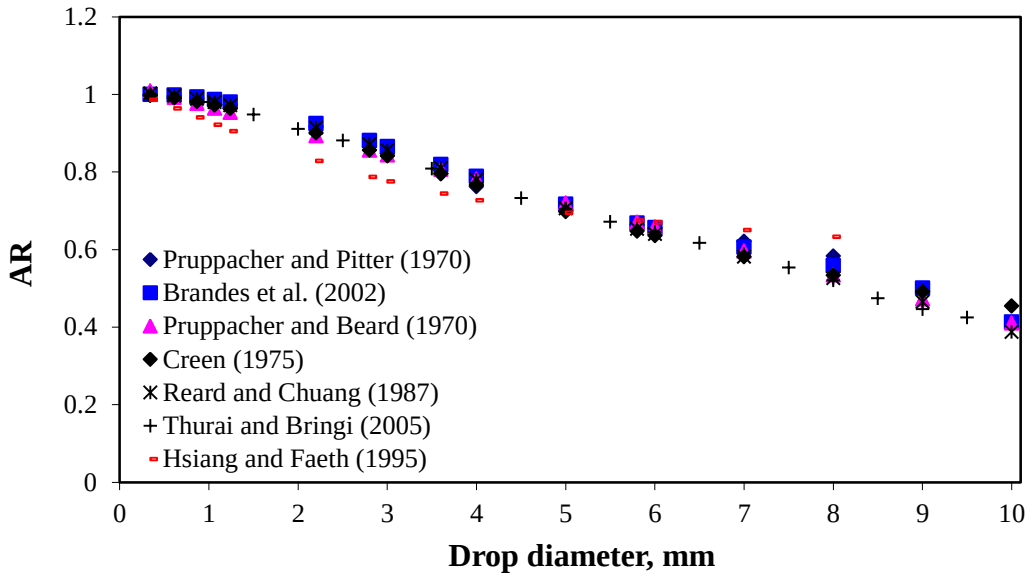

Figure 1.16. Aspect ratio of free falling water drops in stagnant air at terminal velocity.

van Boxel (1997) investigated the distance needed for water drops to reach their terminal velocities. He showed that only small drops (d < 1 mm) would reach 95% of their terminal velocities falling from rest (with zero initial velocity) less than 2 m. Larger drops needed larger distances to reach terminal conditions. For example, for 2 mm to attain 95% of its U_T = 6.49 m/s it needs to fall as much as 5.8 m. For the case of a drop with initial velocity close to its terminal velocity this distance can be expected to decrease.

1.2.5.5 Drop deformation during accelerated motion

In many applications (real life situations) accelerated drop movement in space and time occurs after the drop formation. The drag force on the drop is generally not balanced by its weight. The drop can travel with velocities both much lower and much higher than its terminal velocity depending on the conditions of its formation. The levels of the drop deformation in flight (and with it its drag properties) also can differ from those at terminal conditions.

The aerodynamic loading of the drop varies as its relative velocity changes during accelerated motion. In order to determine accelerated drop drag properties/characteristics and, consequently, to track its movement the response of the drop to the applied aerodynamic forces must be specified.

The response of the drop (and the level of drop deformation) depends both on the intensity and the rate of the change of the applied aerodynamic forces. In the case of slow, gradual loading, such as during rain drop acceleration in free fall, a drop has sufficient relaxation time to adjust itself to the deforming dynamic pressure force, so-called quasi-steady deformation (Schmehl, 2002 and 2003 and Hsiang and Faeth, 1995). Whereas, a drop responses differently during sudden or impulsive loading, for example, when a drop experiences a shock wave disturbance. At some critical conditions the drop can disintegrate or breakup into smaller droplets under the action of aerodynamic forces.

In practice, the loading mechanism is often quite complex and can rarely be determined. Not many loading scenarios have been studied. Schmehl (2003) provided a graph for the temporal evolution of the aerodynamic loading of a drop for some loading regimes in terms of We number and the time scale of the process t normalized by the characteristic time of free drop shape oscillations $t^* = \sqrt{\frac{d^3\hat{\rho}}{\sigma}}$ (Figure 1.17). It is seem that a drop in the free fall experiences relatively gradual increase in the aerodynamic load to a constant value corresponding to the terminal conditions. A drop in the shock tube, on the contrary, is subjected to a near-instantaneous jump in the loading and its relatively gradual relaxation.

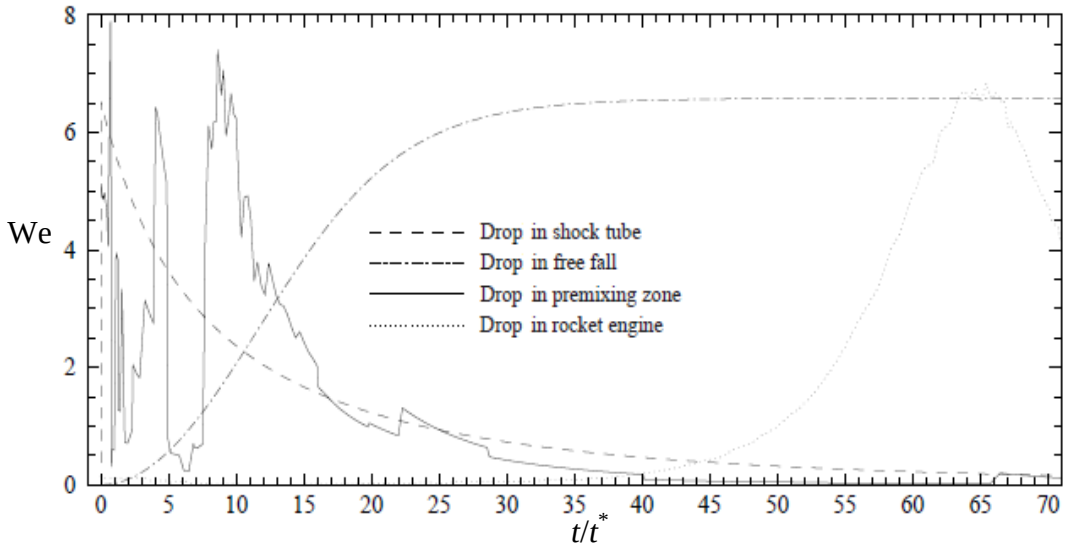

Figure 1.17. Aerodynamic loading of a drop in different applications from Schmehl (2003).

These two limiting cases of steady and sudden drop deformation were studied the most extensively.

Hsiang and Faeth (1993, 1995) studied drop deformation at both steady terminal conditions and shock wave disturbances for $\hat{\rho}/\rho$ = 1.15-12000, *Oh* = 0.0006-600, We = 0.004-700, Re = 0.03-16000.

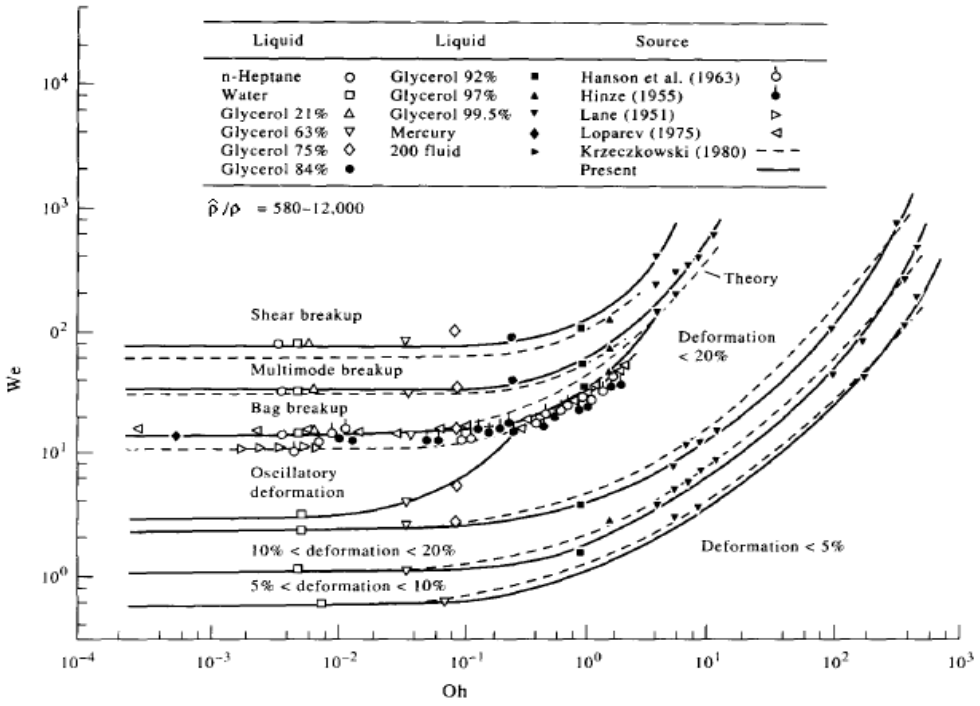

Figure 1.18. Deformation and breakup regimes for shock wave disturbance (from Hsiang and Faeth, 1995).

They produced the classification of drop deformation and breakup regimes in terms of We and *Oh* numbers (Figure 1.18) and showed that during shock wave disturbances for $Oh < 0.1$ deformation and breakup conditions are relatively constant. For $0 < We < 0.6$ drop deforms less than on 5% and for $0.6 < We < 1$ deformation is about 5-10% exists. Here the drop can be considered effectively spherical *AR≈1*. Further increase in *We* up to about 3 brings the drop distortion up to 10-20%. At $3 < We < 11$ drop oscillates during flight with a weakly damped amplitude. This regime dies away for *Oh* > 0.4.

For higher *Oh*, or higher liquid viscosity (or higher initial drop diameter), the transition regimes remain, but shift to higher We numbers. In other words, higher liquid viscosity lowers the rate of drop deformation (not altering the nature of the deformation), in turn, increasing the time for drop relative velocity reduction decreasing the deforming dynamic pressure force. Some of the regimes die out at high Oh numbers, such as the oscillatory deformation at *Oh* > 0.3 and bag breakup at Oh > 4.

Drop distortion at steady disturbance was not observed to be influenced by drop liquid viscosity.

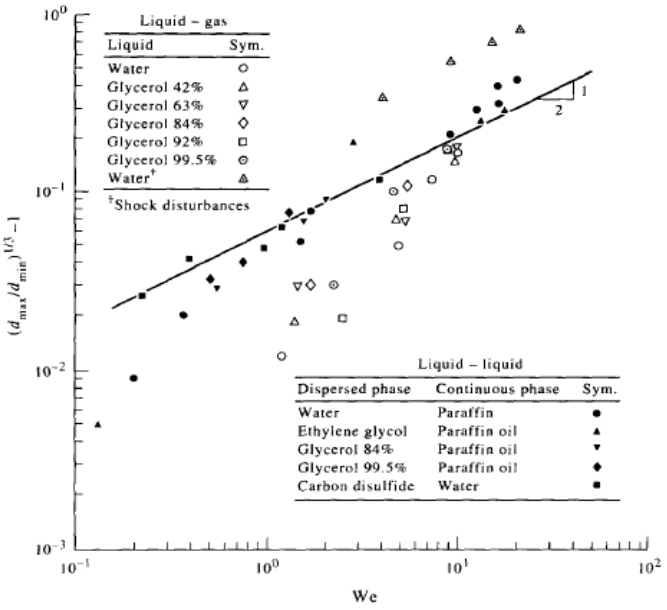

Figure 1.19. Drop deformation as a function of We for steady deformed drop (from Hsiang and Faeth (1995)).

Hsiang and Faeth (1995) for drop deformation for steady disturbances based on data for drops at terminal velocities in both gases and fluids provided the following expression for both low and high Ohnesorge number: $AR = \frac{d_{\min}}{d_{\max}} = \left(1 + 0.07We^{0.5}\right)^{-3}$, where Weber number

$We = \frac{\rho_a v_{rel}^2 d_0}{\sigma}$ based on the equivalent sphere diameter (or undisturbed initial drop diameter) d_0 and the density of surrounding air ρ_a.

However this expression was shown to overestimate the deformation during steady disturbance for liquid drops in gases for We < 10 (see Figure 1.19).

The deformations observed at shock wave disturbances were considerably higher then those at steady conditions. From Hsiang and Faeth (1992) the maximum cross-sectional drop deformation or the maximum drop equatorial diameter during shock wave disturbance is given by $\frac{d_{\max}}{d_0} = \left(1 + 0.19We^{0.5}\right)$.

The instantaneous cross stream drop distortion $d_c - d_0$ (d_c cross stream diameter) is represented as a linear function of time t when normalized by the maximum cross stream distortion $\frac{d_c - d_0}{d_{\max} - d_0} = f\left(\frac{t}{t^*}\right) = k\frac{t}{t^*}$, where t^* is characteristic time of drop breakup or characteristic deformation time (Bratz et al., 2010).

For $Oh < 0.1$ when the effect of liquid viscosity on breakup time is small $t^* = \frac{d_0}{v_{rel}}\sqrt{\frac{\rho}{\rho_a}}$, where ρ now is the density of the liquid in a drop.

For $0.1 < Oh < 3.5$ the time to reach $d_{\max}$ is delayed and $t^* = \frac{d_0}{V_{rel}}\sqrt{\frac{\rho}{\rho_a}}\left(1 - \frac{Oh}{7}\right)^{-1}$.

Both expressions are valid for $We < 10^5$ implying that the scaling of drop distortion in the early stages of deformation is relatively universal in this *We* number range.

Maximum distortion ($d_c = d_{\max}$) was found to be reached when $\frac{t}{t^*} = 1.6$.

Similar classifications of drop deformation and breakup were produced by Hinze (1955) and Krzeczkowski (1980). The latter studied deformation mechanisms and break-up duration of liquid drop in an air stream and analogously described that in the initial stages of drop deformation the drop deforms into, so called 'liquid disc' which, according to the flow conditions around the drop, may further deform leading eventually to drop disintegration.

O'Rourke and Amsden (1987) proposed so-called Taylor Analogy Breakup (TAB) model for low-Weber numbers sprays of drops. The model is based on the analogy between an oscillating and distorting drop and a spring mass system. The droplet distortion represented as a one-dimensional harmonic oscillation under the deforming aerodynamic

force, restoring surface tension force and damping viscous force. The droplet deformation in the direction of flow is expressed in terms of the dimensionless distortion $y = \frac{2\Delta d_{\min}}{d_0/2}$, where $\Delta d_{\min}$ describes the deviation of the minor drop diameter from its undisturbed value d_0. The equation of motion of the deformation is

$\frac{d^2y}{dt^2} = \frac{20\hat{\mu}}{\hat{\rho}d^2}\frac{dy}{dt} + \frac{16\sigma}{\hat{\rho}d^3}y = \frac{8\rho_a v_{rel}^2}{3\hat{\rho}d^2}$ with the solution in the form

$y(t) = We_C + e^{-t/t_D}\left\{(y_0 - We_C)\cos\omega t + \frac{1}{\omega}\left(\frac{dy_0}{dt} + \frac{y_0 - We_C}{t_D}\right)\sin\omega t\right\}$, where $We_C = We\frac{C_f}{C_k C_b}$,

$We = \frac{\rho_a v_{rel}^2 d}{2\sigma}$, $t_D = \frac{\hat{\rho}d^2}{2C_d\hat{\mu}}$, $\omega = \sqrt{\frac{8C_k\sigma}{\hat{\rho}d^3} - \frac{1}{t_D}}$ and empirical coefficients $C_b = 1/2$, $C_d = 5$,

$C_f = 1/3$, $C_k = 8$. $y_0 = y(t=0)$ and $\frac{dy_0}{dt} = \frac{dy}{dt}(t=0)$ are the initial values of distortion and distortion rate of change and are usually taken to be equal zero (Liu et al., 1993).

1.2.5.6 Dynamic drag coefficient of deformed drops

There are a number of possibilities of how to express the drag coefficient as a function of drop shape and Re number.

Haider and Levenspiel (1989) provides an expression for the drag coefficient in a form $C_D = \frac{24}{\mathrm{Re}}\left(1 + b_1\,\mathrm{Re}^{b_2}\right) + \frac{b_3\,\mathrm{Re}}{b_4 + \mathrm{Re}}$, where Re number is based on the equivalent sphere (or undisturbed drop) diameter and

$b_1 = \exp\left(2.3288 - 6.4581\phi + 2.4486\phi^2\right), b_2 = 0.0964 + 0.5565\phi$,

$b_3 = \exp\left(4.905 - 13.8944\phi + 18.422\phi^2 - 10.2599\phi^3\right)$,

$b_4 = \exp\left(1.4681 + 12.2584\phi - 20.7322\phi^2 + 15.8855\phi^3\right)$, where $\phi = \frac{s}{S}$ is the ratio of the surface area of the undisturbed drop s to that of the deformed drop S.

An initially spherical drop in the external flow deforms into a so-called 'liquid disk'. Thus the drag coefficient can be interpolated between that of a sphere $C_D^{Sph} = f(\mathrm{Re})$ and of a disk $C_D^{Disk} = f(\mathrm{Re})$ using the aspect ratio of the drop (Schmehl, 2002; Luxford, 2005):

$C_D = AR \cdot C_D^{Sph} + (1 - AR)C_D^{Disk}$.

For a sphere $AR = 1$, whereas, for a thin disk $AR \approx 0$.

TAB model uses the dimensionless drop distortion *y* to derive the drag coefficient in the form $C_D = C_D^{Sph}(1+2.632y)$ (Liu et al., 1993). For the undisturbed spherical drop $y = 0$ and the maximum deformation corresponds to $y = 1$.

1.2.5.7 Drop breakup

Lane (1951) studied the behavior of water drops in steady stream of air and in air blasts.

He observed progressive flattening of drops in steady stream of air with velocity *v*, and at a critical velocity of the air the drop blew into the 'hollow bag' with a roughly circular rim containing about 70-75% of the original drop mass (Figure 1.20). The bag at some point disintegrated into smaller droplets, whereas, the rim broke up into slightly large droplets.

Figure 1.20. Drop bag breakup mechanism (from Lane (1951)).

Lane provided an expression for the critical (for drop breakup) relative stream velocity v_{rel} in the form $v_{rel}^2 d = 1200$ considering that drop breakup occurs when deforming aerodynamic pressure force on the drop exceeds restoring surface tension force or when $C_D \frac{\rho v_{rel}^2}{2} = \frac{4\sigma}{d}$ and $C_D \approx 0.4$ for the range of Re numbers studied. However, this result was twice as much as he found experimentally: $v_{rel}^2 d = 612$ which he explained by the effects of drop deformation in flight.

From the same critical condition the expression for the critical stable drop diameter can be inferred in the form $d_{cr} = \frac{8\sigma}{C_D \rho U_{cr}^2}$ which gives critical Weber number $We_{cr} = \frac{\rho v_{rel}^2 d_{cr}}{\sigma} = \frac{8}{C_D}$ where C_D of the deformed drop is unknown, but is probably between the values for a sphere (0.45) and a disk (1) at relatively high Re numbers. The latter correspond to critical *We* numbers of 8 and 16 correspondingly.

Clift, Grace and Weber (1978) provided the maximum stable size drop size during steady disturbances as $d_{cr} \approx 4\sqrt{\sigma / g\Delta\rho}$ which implies that Bo number cannot exceed a value of approximately 16.

The behaviour of drops in air blasts when the air stream velocity exceeded critical velocity ($We >> We_{cr}$) for the bag type breakup differed greatly from that at steady disturbances. From Lane's observations the drop was deformed into a 'convex surface' to the air flow with edges in a form of a thin sheet and ligaments which breakup into droplets (Figure 1.21).

Figure 1.21. Shear drop breakup (from Lane (1951)).

Hinze (1955) defined We number and the 'viscosity group' or Ohnesorge number as the controlling dimensionless numbers of the breakup process. The critical We number was expressed as a function of Oh number:

$$We_{cr} = C\left[1+\varphi(Oh)\right] = C\left[1+\phi\left(\frac{\hat{\mu}}{\sqrt{\hat{\rho}\sigma d}}\right)\right],$$

where the function ϕ decreases to zero for $Oh \to 0$ and $C = We_{cr}\big|_{Oh\to 0}$ and are both functions of flow conditions around the drop. From here We_{cr} is higher for more viscous drops.

A review of the critical Weber numbers We_{cr} for drop breakup in a steady air stream can be found in Wierzba (1990). The author reports that We_{cr} are scattered over a wide range from 2.2 to 99.6 due to possibly different experimental methods and facilities, aerodynamic load on a drop, test liquid viscosities and the uncertainty in the definition of the critical conditions and corresponding We numbers. From experiments with water drops falling perpendicular to a horizontal stream of air it was shown that We_{cr} = 11 – 14 and that the possibility of the breakup was increased at higher We numbers.

Krzeczkowski (1980) observed that mentioned 'liquid disc', as an ultimate deformation before the breakup, may further deform into a hollow sphere or bag leding to bag breakup; a hollow sphere with a jet ('bag-jet' breakup) or exhibit more irregular ('bulgy') deformations (Figure 1.22).

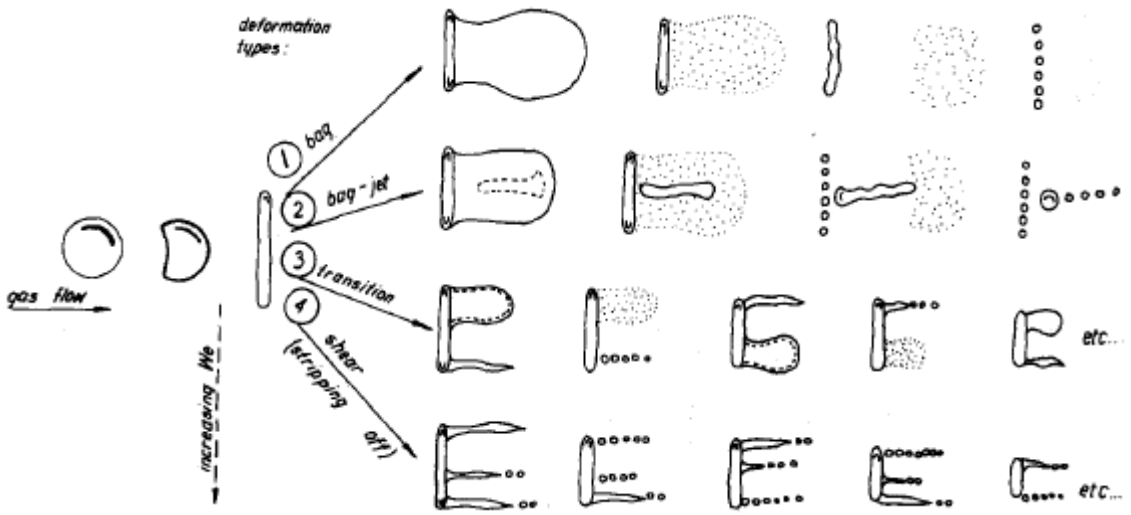

Figure 1.22. Drop deformation and breakup regimes for steady disturbances from Krzeczkowski (1980).

Krzeczkowski pointed that drop deformation and breakup mechanism and duration depend on Weber and Laplace number ($\frac{1}{La} = \frac{\mu^2}{\rho\sigma d_0}$) and the viscosity ratio (μ/μ_a). Similarity between bag and bag-jet breakup mechanisms and between transition and shear mechanisms were observed by tracking the kinematics of drop deformation till breakup.

Pilch and Erdman (1987) distinguished the following drop breakup regime and corresponding critical We number:

Vibrational breakup - $We < 12$;

Bag breakup - $12 < We < 50$;

Bag-and-stamen - $50 < We < 100$;

Sheet stripping - $100 < We < 350$;

Catastrophic - $We > 350$.

Hsiang and Faeth (1992 , 1993) produced similar classification:

Bag - $10 < We < 16$;

Multimode - $16 < We < 100$;

Shear - $We > 100$;

Catastrophic - $We > 10^4$.

Liu and Reitz (1993) proposed the next classification: bag breakup - $6 < We < 80$, shear stripping breakup - $80 < We < 350$ and catastrophic $We > 350$.

In the drop breakup model proposed by Schmehl et al. (2002) based on experimental findings of Hsiang and Faeth (1992) and Pilch and Erdman (1987) drop breakup can only occur if the droplet Weber number is larger than the critical Weber number in terms of Ohnesorge number: $We_{cr} = 12\left(1+1.077Oh^{1.6}\right)$.

As soon as the maximum drop deformation into a 'liquid disk' $d_{\max}$ is reached (Figure 1.23) drop further deforms and finally disintegrates into smaller or child drops.

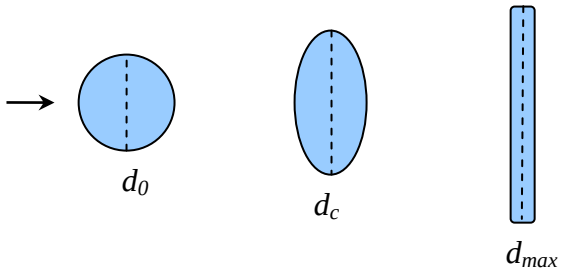

Figure 1.23. Deformation of an undisturbed drop with diameter d_0 into a 'liquid disk' with $\boldsymbol{d_{max}}$.

The time of drop breakup t_{bup} when normalized to the characteristic time of breakup t^* is represented as

$$\frac{t_{bup}}{t^*} = \begin{cases} 6\left(We-12\right)^{-0.25}, & 12 \le We < 18 \\ 2.45\left(We-12\right)^{0.25}, & 18 \le We < 45 \\ 14.1\left(We-12\right)^{-0.25}, & 45 \le We < 351 \\ 0.766\left(We-12\right)^{0.25}, & 351 \le We < 2670 \\ 5.5, & We \ge 2670 \end{cases} \quad \text{for } Oh \le 1;$$

and $\frac{t_{bup}}{t^*} = 4.5\left(1+1.2Oh^{0.74}\right)$ for $Oh > 1$ when $\frac{t_{bup}}{t^*}$ progressively increases with Oh with eventual breakup suppression at large Oh.

It is assumed that the bag breakup mechanism is possible when $12\left(1+1.077Oh^{1.6}\right) < We < 20\left(1+1.2Oh^{1.5}\right)$. The multimode regime is characterized by $20\left(1+1.077Oh^{1.5}\right) < We < 32\left(1+1.5Oh^{1.4}\right)$. For these breakup mechanisms the actual drop disintegration may occur anytime in the second half of the t_i to t_{bup} time frame or during $t \in \left(\frac{t_i + t_{bup}}{2}; t_{bup}\right)$.

The mean size of child droplets produced after the main drop disintegration can be predicted by $d_{ch} = d_o\left(1.5Oh^{0.2}\left(\frac{We}{\left(1+1.077Oh^{1.6}\right)}\right)^{-0.25}\right)$. The velocity of the child droplets is expressed as $\vec{v}_{ch} = \vec{v} + \vec{v}_{ch}^{\,n}$, where $\vec{v}$ is a parent drop velocity prior to breakup, $\left|\vec{v}_{ch}^{\,n}\right| = \frac{5d_0}{2\left(t_{bup} - t_i\right)}$ is a new velocity component with random orientation in the plane perpendicular to $\vec{v}$ direction.

The shear stripping breakup regime is characterized as $We > 32\left(1+1.5Oh^{1.4}\right)$ with breakup possibility any time between t_i and t_{bup}. For this regime $d_{ch}^{shear} = \frac{4d_{ch}d_{cr}}{5d_{cr} - d_{ch}}$, where $d_{cr} = \frac{We_{cr}\sigma}{\rho V_{rel}^2}$ is the maximum stable drop diameter from condition $We = We_{cr}$.

In TAB model the drop breakup is possible only when $y > 1$. The velocity component of the child drops normal to the parent droplet velocity is given by $\left|\vec{v}_{ch}^{\,n}\right| = \frac{d_0}{4}\frac{dy}{dt}$. The mean diameter of the child droplets is $\frac{d_0}{d_{ch}} = \left[1 + 0.4K + \frac{\rho d_0^3}{\sigma}y_0^2\left(\frac{6K-5}{120}\right)\right]$, where K=10/3 is so-called energy ratio factor.

A description of other types of drop breakup such as due to resonance with eddies shedding behind the drop; due to velocity gradients in hyperbolic, Couette and rotating flows; in turbulent flow due to eddies with the integral land scale smaller then drop size can be found in Clift, Grace and Weber (1978).

1.2.5.8 Secondary motion

The motion of a drop can be complicated by its shape oscillations and so-called 'rigid-body' type motion such as swerving, rocking, zig-zag or spiral motion (Clift, Grace and Weber, 1978) which modify the pressure distribution over the surface of the drop.

1.2.5.8.1 *Drop oscillations*

A drop can experience shape oscillations immediately after the formation depending on the mode of its formation (Schroeder and Kintner, 1965).

For small-amplitude oscillations ($A \le 0.1d_0/2$) Lamb (1932) and Rayleigh (1879) derived theoretical frequency of drop oscillations, so-called natural frequency,

$f_N = \sqrt{\frac{2n(n-1)(n+1)\sigma}{\pi^2 d_0^3 \rho}}$, where n is the order of spherical harmonic shape perturbations ($n \geq 2$). The shape of a drop is determined mostly by the fundamental (n = 2) and the first (n = 3) harmonics with a little contribution from faster damping higher harmonics. For each harmonic there are $m = n + 1$ shape modes. The fundamental frequency exhibits three shape modes, notably, axisymmetric (n=2, m=0), transverse (2, 1) and horizontal (2, 2) (Figure 1.24). Whereas the first harmonic exhibits four shape modes (see an example in Figure 1.25).

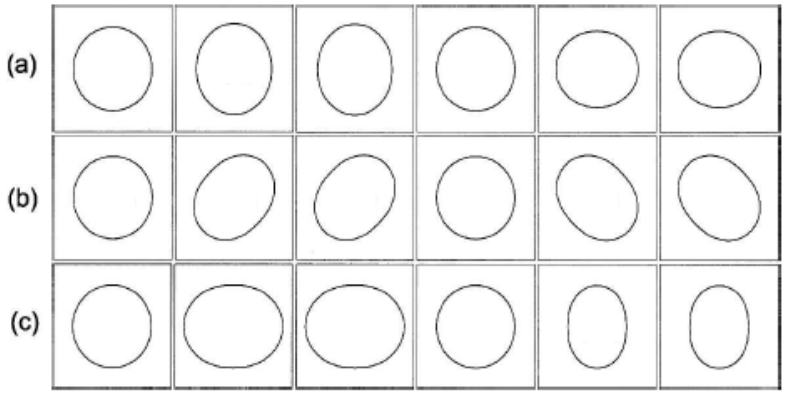

Figure 1.24. Fundamental harmonic n = 2 of drop shape oscillations: (a) axisymmetric, (b) transverse and (c) horizontal modes (from (Testik et al., 2006)).

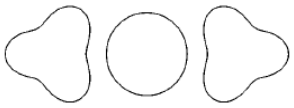

Figure 1.25. m = 1 mode of the first drop shape oscillation harmonic (from (Saylor and Jones, 2005)).

Rayleigh (1892), considering the most important mode of oscillation between an oblate and prolate spheroids (2, 0), derived the equation for the drop oscillatory motion:

$1 - \frac{d_{\max}}{d_0} = A\sin\left[8\sqrt{\frac{\sigma}{\rho d_0^3}}t + \phi\right]$, where A is the fractional amplitude, ϕ is the phase angle of the sinusoidal oscillations, d_{max} is the equatorial diameter of the oscillating drop, d_0 is the undisturbed drop diameter and t is time. Neglecting circulations in the drop the effect of drop viscosity can be represented as $A = A_0 \exp\left(-\frac{-20\mu t}{\rho d_0^2}\right)$, where $A_0 = A(t=0)$ is the initial drop oscillations amplitude as a result of its formation or other disturbance which provoked the oscillations. The amplitude of drop oscillations is believed to be a function of the

Ohnesorge number, density and viscosity ratio. Drop oscillations are dumped exponentially in time by the drop fluid and continuous media viscosities.

For the 3 mm drop the amplitude of oscillations decreases on half in about 0.35 s or after 60 cm of the free fall.

Rayleigh's frequencies of drop shape oscillations can rage from 350-30 Hz for d_0 = 1-5 mm raindrops.

These drop shape oscillations generate internal circulations. The effect of internal circulation in turn is to increase the rate of the energy dissipation and therefore to damp the oscillations (Hughes and Gilliland, 1952).

Levich (1962) showed that surfactants on the drop surface increase the damping rate of oscillations.

For larger-amplitude drop oscillations ($A \geq 0.2 - 0.25 d_0/2$ nonlinear effects such as interactions between modes may be present (multimode oscillations) (Becker et al., 1991).

In addition, drop shape deformation during flight leads to so-called frequency splitting (Feng and Beard, 1991). The characteristic frequencies for the drop oscillation modes (n, m) can be given by

$$f_{n.,m}^{FB} = \frac{\omega_{n,m}}{\pi}\left(\frac{2\sigma}{\rho d_0^3}\right)^{1/2}\left(1 - \frac{A_0^{\langle 2,1\rangle}(n,m)\varepsilon_1^2}{4\omega_{n,m}}\right),$$

where $\omega_{n,m}^2 = n(n-1)(n+1)$ and ε_1 is the effective drop fall velocity. The frequency modification factor $\frac{A_0^{\langle 2,1\rangle}(n,m)}{4\omega_{n,m}}$ equals to -0.00804, 0.0241 and 0.121 for the fundamental mode n = 2 and for m = 0, 1 and 2 respectively. This predicts an increase in the fundamental frequency of drop oscillations.

1.2.5.8.2 *Shape oscillations vs. vortex shedding*

Vortex shedding from the drop wake is associated with the onset of the drop oscillations for the critical Re ≈ 300 (corresponding to $d_0 \approx 1mm$ in free fall) (Winnikow and Chao, 1966). Indeed, the periodic detachment of eddies from the wake behind a drop causes pressure variations at the drop surface exciting drop vibrations.

The vortex shedding frequency and the frequency of the drop oscillations may differ. In liquid-liquid systems the observed vortex shedding frequency are generally less than the native frequency by about 20-40% and 10-20% for pure and surfactant-contaminated systems correspondingly.

Visualization of the flow in the wake of a free falling drop in air can be found in Saylor and Jones (2005).

Beard and Kubesh (1991) studied images of falling raindrops and suggest that certain modes are more common at particular drop sizes. 1.4-1.54 mm in diameter drops were found to oscillate in the (2,0) mode, whereas for smaller drops (1.1 and 1.3 mm in diameter) only the existence of the (2, 1) and (3, 1) modes was found.

For raindrop drop sizes 4.5-7 mm in diameter oscillations in the (2, 0) mode were always present according to (Szakall et al., 2009) in addition to (2, 1) and (2, 2) modes.

It should be noted that the average axis ratio of oscillating drops generally differs from that at equilibrium state.

From geometric analysis by Beard and Kubesh (1991) axisymmetric mode shape oscillations (2, 0) were shown to result in drop shape distortions vary equally above and below the equilibrium aspect ratio. However, for the transverse mode the distortions only vary above the quiescent drop aspect ratio.

Drops with d_0 < 1 mm exhibit scant, if any, oscillation distortion. For drops with d_0 = 1–1.3 mm, however, a distinct increase in the aspect ratio, with a data scatter only above the aspect ratio for a quiescent drop, due to the transverse mode of oscillations. Larger drops (d_0 > 1.3 mm) also have increased aspect ratios with the scatter both above and below the data for a quiescent drop, due to both transverse and axisymmetric modes.

Axis ratios of the raindrops with diameters from 2.5 to 7.5 mm was found in (Szakall et al., 2009) to fit well with the values for the quiescent drops.

The shape distortion of an oscillating drop alters drop drag. Drop shape oscillations towards an increase in its cross-sectional area lead to drop deceleration due to the increased drag and hence to the increased aerodynamic pressure that further distorts the drop and enhances its oscillations.

1.2.5.8.3 *'Rigid type' drop motion*

In addition to the drop shape oscillations in can drift laterally (transverse) due to nonlinear effects associated with large amplitude oscillations as a result of the vortex shedding behind the drop (Testik et al., 2006). This transverse drifts occur with velocities of about 20-30% of the drop terminal velocity with no preferred direction.

Swerving, rocking, 'zig-zag' or spiral motion can also occur (Gunn and Kinzer, 1949). Lindt (1972) argued that so-called secondary motion of a particle increases its drag.

1.3 Non-Newtonian drop formation and flight

Few studies have been done on non-Newtonian drop formation and flight in Newtonian continuous media (such as air).

Chhubra (2007) provides thoughtful review of the current knowledge of the features of Newtonian drops in non-Newtonian media while briefly mentioning non-Newtonian drops.

Both passive Newtonian and non-Newtonian drops were considered to form into two stages by Kumar and Kuloor (1970): by the growth of the drop attached to the orifice and breakup of the liquid neck connecting the main drop body and the orifice. The authors argued that the proposed correlation for the detached drop volume under the constant flow rate was applicable to non-Newtonian drop formation with some modifications to the drag force term.

Shore and Harrison (2005) investigated formation of visco-elastic drops in pulsed pressure nozzles. The fluid elasticity was found to suppress satellite droplet formation.

Goldin et al. (1969) observed that the breakup of visco-elastic jets differed from that of Newtonian jets, and was associated with the formation of drops connected by stable threads along the jet length, the so-called 'beads on a string' structure. The jet breakup length increased with the extensional viscosity.

Similar structures were observed by Wagner et al. (2005) during the formation of viscoelastic drops. The drop pinching was delayed, thin stable cylindrical thread with satellite bead in the middle was observed. The formation of the beads-on-string structure of viscoelastic threads was modeled by Clasen et al. (2006).

Existing non-Newtonian drop flight studies are limited to the investigation of drop motion in surrounding fluid media (typical for settling applications).

Motion of a spherical power-law drop in Newtonian fluid was studied numerically by Gurkan (1989). He found that the degree of shear-thinning of falling power-law drops had small effect on drop drag coefficient. On the contrary, drop pseudoplasticity inhibited drop oscillations. Gillaspy and Hoffer (1983) studied the effects of drop viscosity on its drag and argued that the drop fluid rheology does not affect its drag coefficient.

The shape of free-falling shear-thinning drops in viscous Newtonian fluid was shown to be controlled by viscous and interfacial tension forces, with negligible shear-thinning and inertial effects by Rodrigue (2008).

Motion and shape of a visco-elastic drop falling through viscous Newtonian fluid were investigated by Sostarecz and Belmonte (2005). An unusual dimpled falling drop shape was reported and reproduced numerically.

Several studies focused on the secondary breakup of non-Newtonian drops (viscoelastic, in the majority of cases). Due to scant reported data, however, the features of the non-Newtonian drop breakup, such as critical breakup condition, dominant forces/dimensionless groups, types and time frames of breakup, remain uncertain (Ashgriz, 2010).

The studies suggested that the initial stages of Newtonian and non-Newtonian drop deformation are similar. These deform into an oblate spheroid under aerodynamic loading. Bag, multimode and sheet-thinning non-Newtonian drop breakup regimes, similar to those of a purely viscous drop, were observed and reported. The thickness of liquid ligaments and sheets formed during breakup increased with the increase in non-Newtonian behavior (Ashgriz, 2010 cf. Arcoumanis et al., 1994). The time for a viscoelastic drop to finally disintegrate into smaller droplets was showed to increase with polymer concentration. Joseph et al. (2002) claimed that viscoelastic drops tend to break-up faster than the purely viscous ones having similar viscosity.

1.4 Physical properties of blood

1.4.1 Blood composition, specific gravity and density

Blood is called a liquid connective tissue filling the cardiovascular system in vertebrates, humans, in particular (Guyton and Hull, 2000). This is primarily due to its embryologically similar origin (mesodermal) to other connective tissues and its connective role in the transport of oxygen, nutrient, hormones etc. to other tissues and organs and in the removing of the waste products.

It consists of plasma and so-called formed elements (blood cells) which constitute 50-60% and 40-50% of the whole blood volume correspondingly.

The hematocrit (Ht) or packed cell volume (PCV) is the volume percentage of red blood cells in blood. In other words, it is the ratio of the volume of packed red blood cells to the total volume of a blood sample. It is normally about 40-50% for men and 35-45% for women.

Blood **plasma** contains 85-91% of water by volume and dissolved mineral, organic compounds and gases (oxygen and carbon dioxide). 2-3wt% of plasma are cations (Na^+, K^+, Mg^{2+}, Ca^{2+}) and anions (HCO_3^-, Cl^-, phosphates, sulphates). Organic compounds correspond to 9% of plasma by weight. These are nitrogen-bearing substances (such as proteins,

monoacids, urea, creatinine, ammonia, metabolic waste products) and anazotic or nitrogen-free (glucose (in concentration 70 - 130 mg/dl before meals and less than 180 mg/dl after meals), fatty acids, pyruvate, lactate, phospholipids, triacylglycerols, cholesterin). Proteins represent 7-8% of plasma by weight and play major role in molecules transport, osmotic pressure maintenance and blood clotting. The most abundant ones are albumins (4.5 g per 100 ml), globulins (2.5 g per 100 ml) and fibrinogen (0.3 g per 100ml). In addition, plasma contains dissolved hormones, vitamins, enzymes and mediators. It has yellow/straw color due to the presence of bilirrubin (a waste product of haem, part of hemoglobin degradation).

PH of plasma is 7.3-7.5, colloid osmotic pressure is about 330 mm H_2O and specific gravity is 1.0239 at 25/4ºC and 1.019-1.022 at 37/4ºC (Trudnowski and Rico, 1974).

The liquid remaining after blood is allowed to clot is called serum, which is in effect plasma with clotting proteins (mostly fibrinogen) removed.

Formed elements of blood are erythrocytes (red blood cells, RBCs), leukocytes (white blood cells), and thrombocytes (platelets).

The red blood cells constitute about 95-99% of the cellular component of blood. The cells develop in the bone marrow and circulate in body for about 100–120 days before they are recycled in liver and spleen.

RBCs are bereft of nucleus and most organelles biconcave-disk-shaped cells with a disk diameter of approximately 6.2-8.2 μm (Turgeon, 2004) and a thickness of about 2-2.5 μm and a minimum thickness in the centre of 0.8-1 μm, being much smaller than most other human cells. These cells have an average volume of about 90 femtoliters (fl) (McLaren et al., 1987) with a surface area of about 136 μm^2. Due to high membrane flexibility erythrocytes can squeeze through capillaries as small as 3 μm in diameter. They contain iron-containing oxygen-binding protein, hemoglobin, that comprises about a third of the total cell volume. The latter gives blood its specific red colouring.

The specific gravity of RBCs is 1.098 (at 25/4 ºC) which is higher than that of blood plasma (see above) causing it to naturally settle with time. The rate at which red blood cells settle (or sediment) in a period of an hour is called erythrocyte sedimentation rate (ESR) or just sedimentation rate. This process is governed by the combined effect of pro-sedimentation factors, mostly fibrinogen, and the factors resisting the sedimentation, in particular the negative charge of the erythrocytes. Normal ESR for men is 1-10 mm/hr and 2-15 mm/hr for women.

Platelets, or thrombocytes are small, irregularly shaped clear 2–5 μm in diameter cell fragments (without nuclei) with a life span of 5-9 days. They comprise about 4.9% of the cell volume of blood. Platelets participate in the prevention of blood loss, homeostasis.

White blood cells, or leukocytes, are immune system cells and make up about 0.1% of the cellular component of blood in a healthy adult. They live for about three to four days in human body. A number of leukocytes types can be differentiated with diameters from 7 to 20 μm.

Since platelets and leukocytes make up only about 5% of the cellular component of blood, their effect on the macroscopic properties of blood is negligible.

Whole blood volume is ~78 ml/kg of body weight; it is slightly alkaline (PH is 7.35-7.4) with specific gravity of 1.056 at 25/4ºC and 1.048-1.054 37/4 ºC (Trudnowski and Rico, 1974). Density of blood is reported to be in the range of 1.052 - 1.063 g/m^3 (Hinghofer-Szalkay and Greenleaf, 1987; Kenner, 1989).

In terms of colloidal chemistry, blood represents a highly complex suspension of polydisperse, flexible, chemically and electrostatically active cells suspended in plasma with proteins that form a colloidal solution, whereas, urea, glucose and other organic substances and salts represent a true solution. Erythrocyte sedimentation can be treated as a natural form of the sedimentation of a suspension. In this light, the physical properties of blood as a complex fluid are the result of the combined effects of all its constituents.

1.4.2 **Surface tension of serum, plasma and whole blood**

Since about 50% of blood content is water, (liquid-vapour) interfacial properties of blood may be analysed in terms of their deviation form (or relative to) that of pure water.

The most important property of liquid water that has a crucial influence on all immersed molecules, particles, cells and surfaces is its very strong energy of cohesion, which is 30% due to van der Waals attractions and 70% due to the hydrogen-bonding driven (i.e., polar) attraction of water molecules (van Oss, 2008). The polar attraction between water molecules causes strong attraction of all hydrophobic (non-polar) molecules and particles immersed in water (so-called ‘hydrophobic effect’), whereas polar attraction of water molecules and hydrophilic (polar) molecules and particles causes the repulsion between such hydrophilic entities when immersed in water (‘hydration pressure’ effect). The latter effect causes repulsion of blood cells from each other and keeps them in stable suspension in blood and prevents from clot formation. Moreover, repulsion exists between serum protein molecules which keeps them in stable solution avoiding precipitation.

It is believed that single sugars such as glucose, some of the smaller molecular weight amino acids (e.g., glycine) (Docoslis et al., 2000) and many salts (such as NaCl and KCl) (Weast 1970, 1971) decrease the surface tension of water at very low concentrations. At high concentrations, however, these solutes increase surface tension of water considerably.

In particular, dissolved glucose has high energy of cohesion (or the amount of work that is needed to be performed in a system in order to separate two unit areas of identical material (molecules) from contact to infinity) leading to a strong continuous attraction between these molecules' freely available electron-acceptors and electron-donors and so increases surface tension of water on about 32% (Docoslis et al., 2000). In aqueous solutions the molecules of simple sugars are repelled from the free interface and move to the bulk fluid.

For salts the surface tension change is proportional to the concentration of the salt and, provided the concentration is not too low, it is towards the increase in the surface tension of the solvent (water) and depends on both the anions and the cations present, but usually more strongly on the anions (Weissenborn and Pugh, 1996). Each ionic species experiences different forces near the free interface. These might be forces of attraction or repulsion, but all together they lead to an increase or decrease of concentration near the interface. It is this alteration in concentration that leads to the surface tension increment.

Moreover, the increase in the surface tension of water implies the increase in the free energy of cohesion which enhances hydrophobicity of its aqueous solution. For the case of salts, for example, this leads to the decrease in solubility of proteins and their precipitation when added to a concentrated salt solution (so-called 'salting out').

On the contrary, despite of the effects of glucose and salts dissolved in blood plasma (and/or serum) the surface tension of blood serum is much lower than that of pure water Morgan and Woodward (1913).

As mentioned above blood plasma (and serum) is also a concentrated protein solution.

Protein molecules consist of hydrophobic and hydrophilic amino acids. In aqueous solutions proteins hydrophobic amino acids usually form protected hydrophobic areas while hydrophilic amino acids interact with the molecules of the solvent and allow proteins to form hydrogen bonds with the surrounding water molecules.

A number of experimental studies suggest the controlling role of water in protein adsorption to the surface (Krishnan, 2005). It is argued that liquid-vapour interface saturates with protein adsorbed from bulk solution at a fixed weight-volume concentration (~436 mg/ml) independently of protein type or proportions in a mixture. Accordingly, blood serum is not different from plasma in terms of the observed surface tension increments.

Globular proteins such as, for example, human albumin and serum immunoglobulin-G (IgG) are attracted to the free interface when in aqueous solution. It causes a decrease of 17-18% in the apparent surface tension of the aqueous solvent (Absolom et al., 1981).

Mean surface tension of blood plasma was reported by Harkins and Harkins (1929) to be of about 52 and 48 mN/m at 20º and 37ºC correspondingly.

Zozaya (1935, 1938) found an average value of 54.2 mN/m. In more recent study Kratochvil and Hrncir (2001) reported values within 60-68 mN/m range.

The surface tension of the whole blood in healthy humans was measured by Hrncir and Rosina (1997) to be 55.9 mN/m at 22ºC with no correlation to age or sex and most of the haematological parameters.

Kratochvil and Hrncir (2001) reports average normal whole blood surface tension of 64.6 mN/m at 22°C with the linear dependence on the concentration of the anticoagulant (sodium citrate) used.

Temperature dependence of the whole blood surface tension was studied by Rosina et al. (2007). The next expression was provided for blood surface tension as a function of temperature t in the range from 20 to 40°C: $\sigma(t) = (-0.473t + 70.105)$ mN/m. Blood serum and sediment surface tension values in the same temperature range were approximated as $\sigma(t) = (-0.368t + 66.072)$ mN/m and $\sigma(t) = (-0.423t + 67.223)$ mN/m correspondingly.

1.4.3 **Rheology of blood**

Blood is a non-Newtonian fluid whose apparent viscosity (ratio of the shear stress to shear rate) varies with shear rate. Blood viscosity decreases with the increase in the shear rate (pseudoplastic or shear-thinning behaviour). For shear rates above about 100 s^{-1} (as for blood in small vessels) blood viscosity approach its asymptotic limit (Newtonian plateau) (Figure 1.26) with viscosity of about 4-6 mPa·s and 3.5-5.8 mPa·s for male and female ‘normal population (Dintenfass, 1985). However, at lower shear rate of about 10 s^{-1} it increases to as much as about 10 mPa·s.

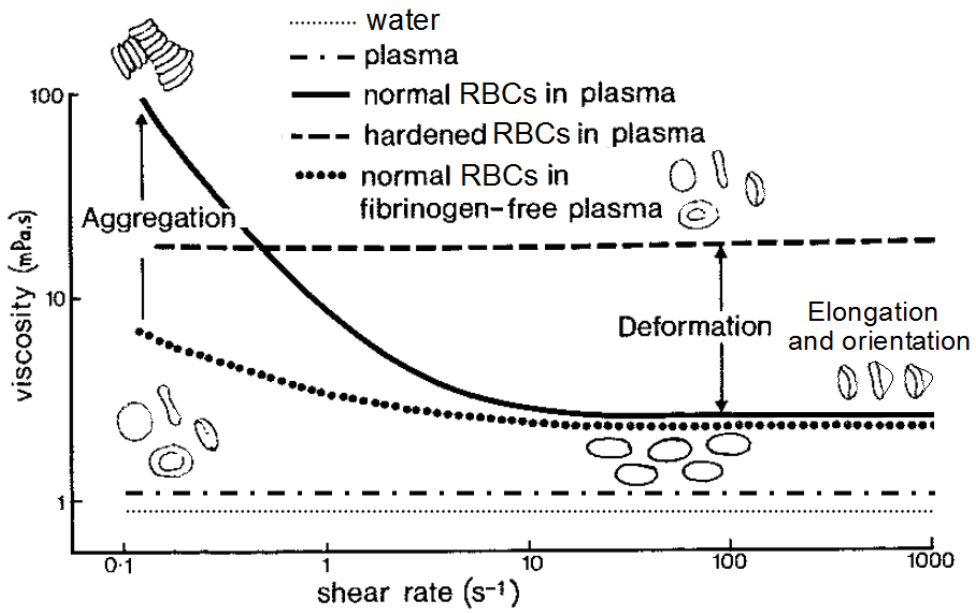

Figure 1.26. Water, plasma and whole blood viscosity (PCV 0.40) at different shear rates (modified from Lowe and Barbenel (1988) and Somer and Meiselman (1993)) at 37°C.

Blood viscosity is determined by the following parameters and mechanisms: plasma viscosity, hematocrit (PCV), RBCs aggregation and deformability and temperature. PCV and RBC aggregation are two main factors that contribute to the shear-thinning behaviour of blood. Effects of other types of blood cells (leukocytes and platelets) are considered to be minimal mostly due to their small number relative to the erythrocytes.

In this light, the rheological behaviour of blood is dependant both on composition and amount of blood cells and plasma proteins and on the shear rate values.

1.4.3.1 Plasma viscosity

Blood plasma behaves like a Newtonian fluid with viscosity independent of the shear rate. The viscosity of plasma contribution to that of the whole blood is believed to be more pronounced at high shear rates.

Viscosity of plasma is higher than that of water due to molecules suspended in it which cause additional energy dissipation during flow (Lowe and Barbenel, 1988). Its viscosity at 37°C is 1.15-1.35 mPa·s with the average of 1.25 mPa·s opposed to 0.69 mPa·s for water (Lowe and Barbenel, 1988; Dintenfass, 1985). This difference is mainly due to high molecular weight proteins with only 1-2% due to smaller molecules.

Plasma viscosity correlates to the concentration, size and length to width ratio of a particular protein class. The proteins which have the greatest effect on plasma viscosity are the serum globulins (lipoproteins, immunoglobulins etc.). Albumin due to its relatively low

molecular weight and symmetry and despite its weight percentage (3.4-5.4 g/dl; dl - decilitre) contributes only about 36% of the difference between plasma and water viscosities. On the contrary, fibrinogen which comprises only about 4wt% of plasma causes 22% difference in plasma and water viscosities due to its high molecular weight and asymmetry.

Plasma viscosity increases linearly by about 2.4% with the decrease in temperature by one degree over the range 20-40°C. At 25°C it is in the range 1.50-1.72 mPa·s, whereas at 20°C it is 1.70-1.92 mPa·s.

1.4.3.2 RBCs aggregation

Human RBCs can form clusters at low shear rates known as rouleaux. Under normal conditions erythrocytes' membranes possess negative charges and repulsive electrostatic forces act between cells (Rampling, 1988). Indeed, they show no signs of aggregation in, for example, saline solution. However, in the presence of plasma proteins, in particularly, fibrinogen and globulin, the cells tend to aggregate. It is argued in (Rampling, 1988) that the tails of these high molecular weight (150,000 or more) molecules tend to adhere to adjacent cells and link them together over such distance that the total adhesive force accedes that of repulsion. This process depends on the concentration of the proteins and increases at decreasing shear rate. This in turn increases the effective cell volume resisting the flow and hence increases blood viscosity. Upon the increase of the shear rate the aggregates tend to break up causing a decrease in blood viscosity (see Figure 1.26). Consequently, red cell aggregation is the major factor for shear-thinning or pseudoplastic behavior of blood.

1.4.3.3 RBCs deformation

At high shear rates, however, erythrocytes are dispersed and tend to deform from their normal resting shape into ellipsoids and move along flow streamlines which explains much lower normal blood viscosity compared to, for example, the suspension of hardened red cells in plasma (see Figure 1.26). In addition, it is believed that the reduction in the red cell membrane deformability inhibits rouleaux formation.

This important property of RBCs allows blood to flow even at hematocrit of 98% (Fung, 1993).

1.4.3.4 Hematocrit or PCV

Whole blood viscosity varies substantially with volume fraction of RBCs or packed cell volume with logarithmic increase in blood viscosity with linear increase in PCV over the

range of 0.2-0.6 and relatively linear dependence over the normal range for healthy human of 0.35-0.55. The effect of hematocrit on blood viscosity is more pronounced at lower shear rates (Figure 1.27).

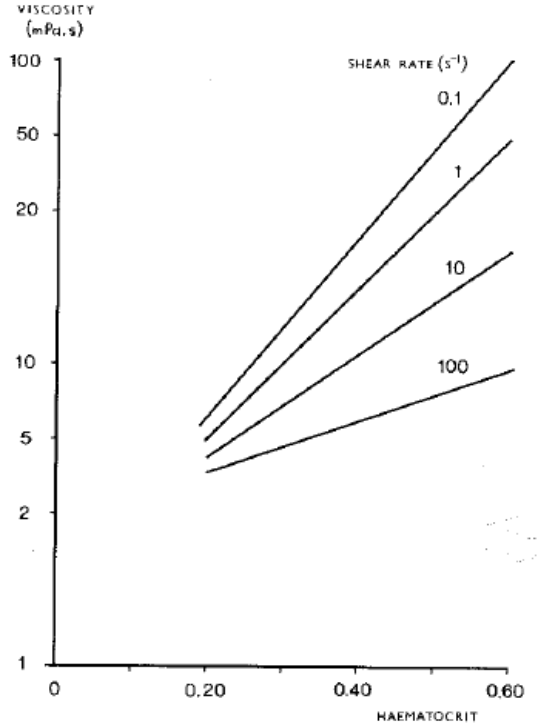

Figure 1.27. Whole blood viscosity vs. hematocrit at different shear rates from Lowe and Barbenel (1988).

This dependence of blood viscosity on Ht can be explained in terms of the increase in RBCs aggregation with the increase of their concentration. This in turn causes an increase in the effective cell volume bringing higher level of energy dissipation during flow and hence higher blood viscosity. At high shear rates, however, the increase in cells concentration stimulates cells' deformation which decreases their effective size and so balances the increase in blood viscosity (Dintenfass, 1971; Chien, 1972; Dinnar, 1981 and Guyton and Hall, 1996).

1.4.3.5 Blood viscosity vs. temperature

The temperature dependence of blood viscosity is similar to that of plasma (discussed above). However, it is believed to be slightly more pronounced with 3% change in blood viscosity with each degree of Celsius (Barbee, 1973).

1.4.3.6 Blood yield stress

Due to RBCs aggregation at low shear rates some amount of stress needs to be exerted to break the aggregates and induce some bulk movement of blood.

According to Merrill et al. (1969) the level of yield stress depends on fibrinogen concentration and hematocrit. For normal blood it is about 4-5 mPa and is relatively independent of temperature in the range of 10-37°C (Barbee, 1973).

1.4.3.7 Blood Thixotropy

Blood viscosity was shown to decrease with time during shearing at a constant rate (Huang et al., 1975; Dintenfass, 1985). In particular it was found that blood viscosity decreased over about 20 seconds during shearing at 10 s^{-1}, whereas upon the increase in the shear rate to 100 s^{-1} no time was needed to reach an equilibrium viscosity value. This is primarily due to the breakdown of RBC aggregates at low shear rates with more rapid structural changes at high shear rates.

In addition, Gaspar-Rosas and Thurston (1988) found that about 50 seconds is needed to restore this internal structure at low shear rates compared to relatively instant disaggregation at high shear rates.

1.4.3.8 Viscoelasticity of blood

Human blood also shows viscoelasticity in periodic or transient flow (Thurson, 1972; Stoltz et al., 1999) exhibiting time dependent strain when a stress is applied.

It was observed that the aggregates of red blood cells deform elastically under stress (Schmid-Schonbein et al. 1968, 1969). In addition, viscoelasticity of human RBCs (or elasticity of their deformation) was also recognized (see, for example, Puig-de-Morales-Marinkovic et al. (2007)). Moreover, Wells and Schmid-Schijnbein (1969) claimed that RBCs behave like a fluid drop in flow with the shear stress transmitted across the membrane, exciting the flow in the interior of a cell. These factors may be considered as primary contributors to the viscoelastic behaviour of blood.

Moreover, the elastic behaviour of blood increases significantly with increasing hematocrit due to the increased number of the interactions between the cells.

At low shear rates the viscoelasticity is primarily due to the aggregation of RBCs. At intermediate shear rates, however, the progressive breakdown of the aggregates occurs together with the alignment and deformation of distinct cells. The latter becomes predominant cause of the viscoelasticity of blood at high shear rates.

Thurston (1960) considered complex blood viscosity in the form $\mu^* = \tau/\dot{\gamma} = \mu' - i\mu'' = \mu e^{-i\phi}$, where τ and $\dot{\gamma}$ are the stress and rate of strain correspondingly, μ' and μ'' are real (connected with energy dissipation) and imaginary (associated with the

energy storage in the elastic deformation of blood) parts of viscosity, μ and ϕ are the magnitude and phase of μ^*.

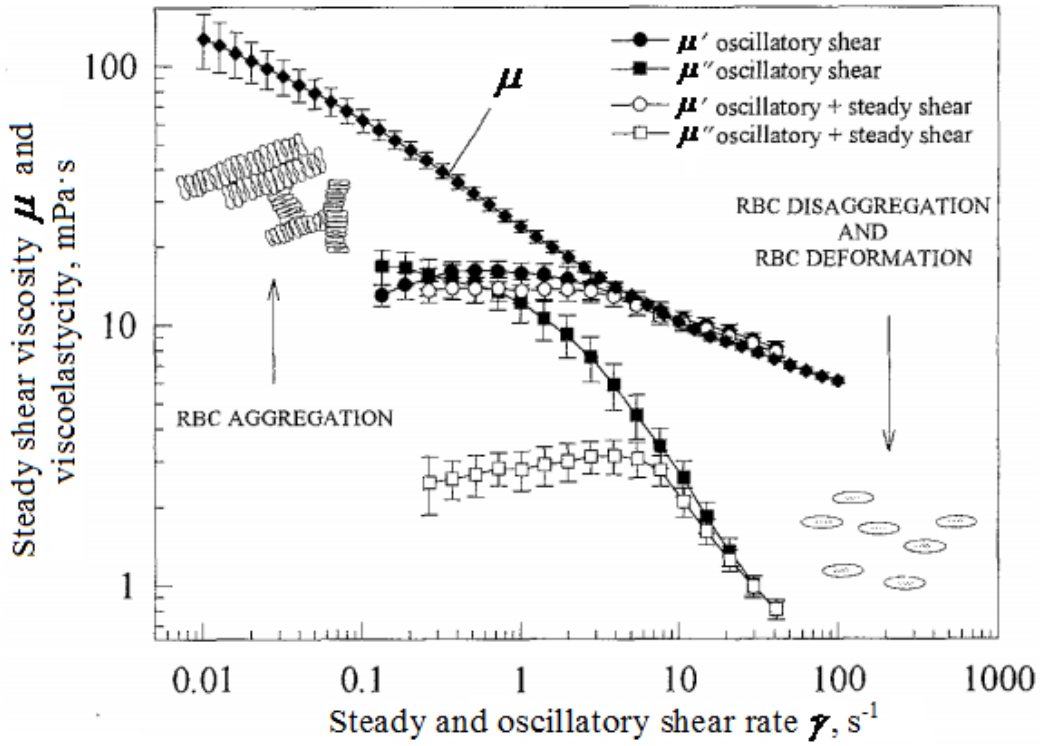

Figure 1.28. Steady shear rate dependence of steady blood viscosity and oscillatory shear rate dependence of blood viscoelasticity with and without a superimposed steady shear rate $\dot{\gamma}_{sup} = 2\ s^{-1}$ at PCV of 0.45, T = 25°C, flow frequency of 0.5 Hz (from Vlastos et al. (1997)).

It is seen from Figure 1.28 that at low shear rates the viscous component of complex viscosity μ' is lower than the steady shear viscosity, however at higher shear rates (above 8 s^{-1}) these two align. The latter implies that the energy dissipation levels in these two flows are identical. An analogous tendency is observed for μ' when a constant superimposed steady shear rate of 2 s^{-1} is induced.

The elastic component of complex viscosity μ'' starts to decrease with $\dot{\gamma}$ at about 1 s^{-1} due to the RBC disaggregation which is complete by $\dot{\gamma} = 30\ s^{-1}$ resulting in a sharp drop in the elastic viscosity component. A superimposed steady shear rate delays aggregation at low shear rates and disaggregation causing a mild decrease in μ' and relatively sharp exponential decrease of μ''.

2 Blood drop formation and flight in Bloodstain Pattern Analysis (BPA)

Blood is one of the most common types of physical evidence found at scenes of violent crime (James et al., 2005; Bevel and Gardner, 2008). When analysed it can help to identify the individual involved in a crime (DNA profiling), as well as to reconstruct the circumstances of blood deposition. The amount, location and pattern of blood deposition, when analysed accurately, may provide valuable information for crime investigation.

Bloodstain Pattern Analysis (BPA) is a forensic technique that focuses on the analysis of the bloodstain evidence present at crime scenes. The technique is based on the knowledge of a variety of scientific disciplines, such as biology, chemistry, medicine, forensic pathology, physics, biophysics and ballistics.

BPA originated over hundred years ago with early works (see, for example, Balthazard et al., 1939 and MacDonell and Bialousz, 1971) dedicated to establish a scientific principles and methodology of the technique date back to the first decade of the 20th century.

Position, distribution, size and morphology of the bloodstains found are inspected by crime scene investigators using of BPA principles. The typical methods of bloodstain assessment include visual inspection, basic photography and simple geometric measurements. The analysis is aimed to extract information about the position of an assailant and a victim during an assault, their movement through a crime scene, people involved and character of the wounding inflicted, such as the weapon used, force applied and number of wounding incidents. The chronological sequence of events that led to bloodstain formation is of importance overall.

BPA experts are often asked to report their findings to the court and to comment on particular scenarios of the evidence interpretation of relevance to defence or prosecution of a defendant with a high level of reliability and expertise required. The findings may potentially help to incriminate or exculpate a suspect and support or dispute witness' statements.

The determination of the source blood found at a crime scene in a form of bloodstains is one of the major problems in BPA. This chapter aims to provide an overview of the main principles relevant blood origin determination.

Bloodstain interpretation is based on the understanding of the natural laws that govern formation of bloodstains. Bloodstain formation may be viewed as a sequence of events from blood drop generation and drop flight to its deposition on a surface. Bloodstains available for examination represent the end product of this sequence and implicitly contain the information about the events that led to its formation. At certain conditions this information can be extracted from the stain analysis in a form of the drop impact conditions estimates, such as, for example, the volume and velocity of the blood drop resulted in this bloodstain. If the phenomena involved in drop flight prior to impact on a surface as well as the characteristics of blood drop formation mechanisms relevant to BPA are known, the blood drop of the estimated size and velocity may, subsequently, be traced back to its possible origin.

The correlation between the bloodstain characteristics, blood drop formation, flight and origin is discussed below in more details.

2.1 Bloodstain and blood drop formation correlation

Violent crimes involving bloodshed may result in the formation of a number of blood drops that move through air and eventually impact onto a surface producing a group of bloodstains (or bloodstain pattern). This is termed blood spatter (SWGSTAIN terminology, 2009).

BPA analysts examine the spatter patterns present at a crime scene to reveal the information about the possible mechanism and conditions of the spatter generation from spatter drop formation and flight to the drop impact with a surface.

There are several bloodstain pattern classifications reported in the BPA literature.

Bloodstains can be classified by their appearance and possible spatter generation mechanism. There are three main bloodstain classes or types according to James et al., 2005 and Bevel and Gardner, 2008: passive stains (formed under the action of gravity only), projected stains (created when an additional force other than gravity is applied) and transfer stains (originated from the transfer of blood from one object to another). Passive stains can be subdivided into drip stain, drip pattern, flow pattern, splash pattern and pool. Swipe, wipe, pattern transfer, absorbed stains belong to the transfer stain patterns. Projected stains may be formed as a result of centripetal acceleration (cast-off), blunt force impact (impact pattern), bullet impact (gunshot pattern), as well as due to expiration of blood (expiration pattern) and arterial damage (arterial spurt).

Based on the momentum or energy of the spatter generation event the bloodstain patterns can be divided into “low”, “medium and “high”-energy spatter (MacDonell and Bialous, 1971; Laber, 1985). The average stain size within a pattern is believed to decrease with the velocity of the generation event.

Bloodstain pattern classifications may facilitate recognition of the event that lead to the pattern formation overall.

Additionally, the characteristics of a single stain within a pattern, such as its size and morphology, may be correlated to the volume and impact velocity of the drop that produced a stain (Laber, 1985; Wonder, 2001; Parker, 1985; Ross, 2006 and MacDonell and DeLije, 1989).

MacDonell and de Lige (1989) sought to develop a relationship that would enable the volume of a passive blood drop to be estimated from a bloodstain of known size, however, with no consideration given to the impact velocity of the drops, which will affect the stain spreading.

Knock and Davidson (2007), Hulse-Smith et al. (2005) and Hulse-Smith and Illes (2007) showed that under well-controlled conditions it is possible to calculate the volume and velocity of a falling drop from the diameter of the stain and the number of spines on the stain margin.

These approaches, however, have important limitations: their results are applicable only to certain types of target surfaces and the sometimes poor reproducibility of the stain morphology interpretation, for example due to impact surface irregularities or porosity. The studies, however, were limited to stains formed as a result of blood dripping from a wound or bloodied object (weapon). Further research is needed for other types of bloodstains and target surfaces.

It has also been shown that stain shape can also be correlated to the drop impact angle with a surface (Figure 2.1), the acute angle (α_{imp}), relative to the plane of a target surface, at which a drop strikes the surface (SWGSTAIN terminology, 2009), according to the so-called ‘Sine law’ (Balthazard et al., 1939; McDonell and Bialousz, 1971; 1979, McDonell, 1982 and DeForest et al., 1983) for impact angles less than 60° (Willis et al., 2001). The ‘sine law’ is routinely used in the analysis of crime scene bloodstain patterns.

So-called directional and glancing angles are also useful in the blood origin determination. The directional angle represents the angle between the long axis of the spatter and a reference line on a target surface. Whereas, the glancing angle is the angle between the drop flight directionality prior to impact and vertical (SWGSTAIN terminology, 2009).

The velocity a drop has upon impact with a target surface is termed ‘impact velocity’, v_{imp}.

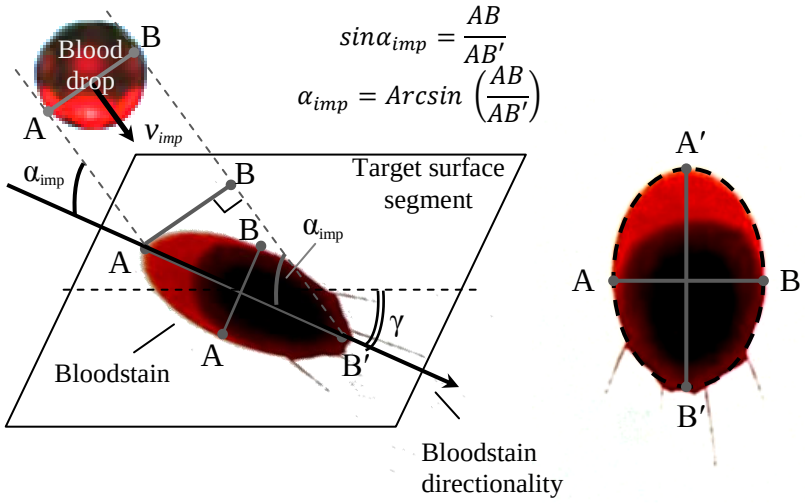

Figure 2.1. The ’Sine law’ (Balthazard et al., 1939) diagram and physical meaning of impact (α_{imp}) and glancing (γ) angles. AB and AB′ represent bloodstain width and length correspondingly, spherical blood drop shape assumed upon impact.

The drop trajectory may be reconstructed back from the stain location to the origin of the drop if size and impact velocity of the drop that produced a stain can be estimated at least within a certain range. This is only possible if there is only one combination of drop size and velocity which can result in a particular stain, i.e. when the drop flight path does not have multiple solutions (degeneracy). Indeed, at certain conditions a bigger but slower drop may leave similar stain to a smaller drop travelling with higher velocity (Hulse-Smith et al., 2005).

The problem, thus, is to limit the number of drop size and velocity combinations responsible for the formation of a particular stain to only one the most probable.

2.2 Blood drop flight and blood origin determination

If two or more backward drop trajectories can be accurately determined, the point at which they cross indicates the blood origin position and is the probable location of the victim at the time the wound was inflicted (Figure 2.2). The ‘area of convergence’ in BPA represents the 2D area containing intersections of the lines representing directionality of the stains within a pattern (SWGSTAIN terminology, 2009). The volume of blood origin or

simply ‘origin’ is the 3D region from which the blood pattern originated. This is sometimes called ‘area of origin’.

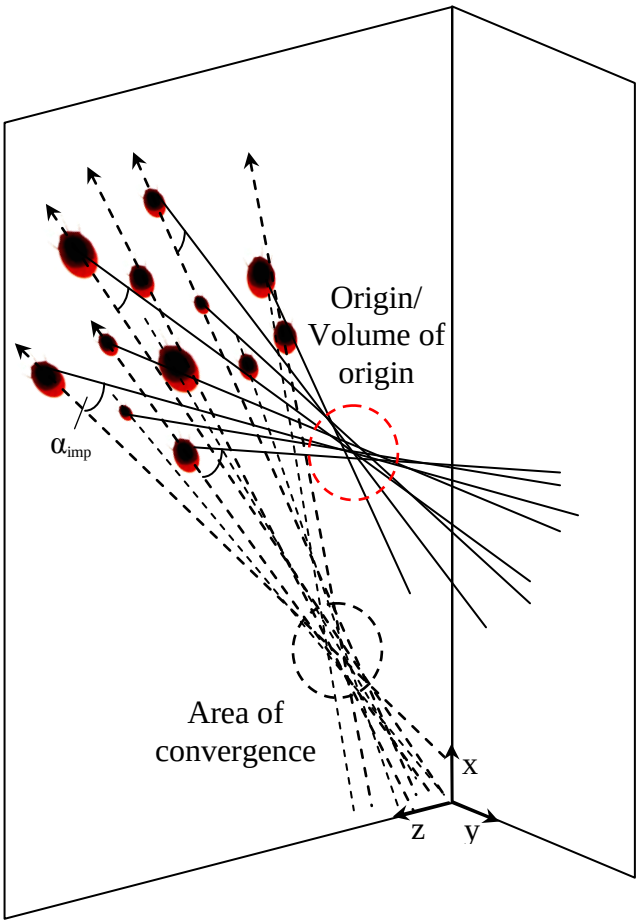

Figure 2.2. Area of convergence and blood origin (or volume of origin) determination from the directionality and impact angle estimation of the stains within a pattern.

To determine the trajectory of an individual drop, from measurements of the stain it leaves, requires some assumptions to be made.

The stringing method (Akin, 2005) assumes the drop trajectory is a straight line, gravitational and drag forces having a negligible effect on the direction of flight while the droplet is airborne. The Backtrak® (http://people.physics.carleton.ca/~carter/) and Haemospat® (http://hemospat.com/research.php) software programs are used for drop trajectory approximation.

The straight line blood drop trajectory approximation also underlies the tangent method (Bevel and Gardner, 2008).

This approach, however, was shown to produce considerable errors in point (and area) of origin determination, unless the trajectories are very short and the velocities relatively high (Behrooz, 2009, de Bruin, 2011 and Wells, 2006).

Another method of blood source determination proposed by (Podworny and Carter, 1989) assumes parabolic spherical drop trajectories and is argued by Buck et al. (2010) and Buck and Kneubuehl (2012) to be adequate for reconstructive purposes. Details of the assumptions used were not provided.

It was recognized that at formation and further in flight blood drops may undergo shape oscillations, deform from being spherical and at critical conditions may disintegrate into smaller fragments (see, for example, Bevel and Gardner, 2008 and Raymond et al., 1995).

The effects of these factors on blood drop trajectory, as well as drop spreading upon impact, impact velocity and impact angle, and as a result on the blood origin determination, need further investigation.

The air currents possibly present at a scene at the moment of drop generation may alter drop trajectory compared to the case of still air (Attinger et al., 2013).

The degree of evaporation of blood drops in-flight under typical crime scene conditions has not yet been evaluated.

3 Blood drop characteristics in BPA

Bloodstain patterns at scenes of violent crime are often analyzed in order to receive information about the events that led to the resulting bloodstains. The position and characteristics of the blood source is often of relevance.

Critical to any inference about the blood source is an estimation of the volume and velocity of the blood drop resulted in a particular bloodstain within a pattern, as well as accurate drop trajectory prediction from the stain position to its origin.

Bloodstain pattern classification by their appearance, mechanism of formation and/or the momentum or energy of the pattern generation event (see Chapter 2 for more details) is useful in providing the information on the ranges of blood drop sizes and velocities typical (or feasible) for a particular pattern type. This, in turn, may support/facilitate the inference of blood drop size and velocity upon impact with a surface from direct bloodstain measurements.

Based on the information of blood drop sizes and velocities ranges typical blood flight characteristics may be determined and incorporated in the accurate blood drop flight and origin prediction.

This chapter aimed to provide characteristics of typical blood drops in the fluid dynamics framework to describe important aspects of blood drop formation and behavior during flight. To author's knowledge this has not been done in this context in the BPA literature before.

Passive, cast-off, impact and gunshot drops were characterised in Table 3.1 according to dimensionless numbers relevant to drop formation and flight: Reynolds number ($Re = \frac{Vd_0}{\nu_{air}}$, which is the ratio of inertial to viscous forces acting on a drop), Weber number ($We = \frac{\rho_{air} V^2 d_0}{\sigma}$, the ratio of inertial and interfacial tension forces), Bond number ($Bo = \frac{\rho g d_0^2}{\sigma}$, the ratio of drop weight to interfacial tension forces), and Ohnesorge number ($Oh = \frac{\mu}{\sqrt{\rho d_0 \sigma}}$, the ratio of viscous to interfacial tension forces). The Weber number is as an indicator of the degree of drop deformation (Hsiang and Faeth, 1995). The drop can be considered effectively spherical for We < 1, whereas more pronounced deformation is associated with We > 1-3 and

at We higher than ~13 the drop breaks up (Wierzba, 1990). Average Weber number, We_{avg}, was based on the average blood drop diameter and velocity.

Mechanism	d, mm	V, m/s	Re	We	We_{avg}	Bo	Oh
Passive dripping (Laber, 1985a,b; Kabaliuk et al., 2013)	3÷7	< 7	< 3,200	< 7	~ 1	< 9	~ 0.01
Cast-off (Bevel and Gardner, 2008; Halse and Smith, 2005, 2007)	0.5÷4	1.5÷20	50÷5,300	0.02÷34	~ 6	0.05÷3	0.01÷0.02
Impact (Halse and Smith, 2005, 2007; Sweet, 1993)	0.2÷2	1.5÷30	20÷4,000	0.01÷39	~ 6	0.01÷0.7	0.01÷0.04
Gunshot (MacDonnell and Bialousz, 1971; Laber, 1985)	0.05÷1	15÷45	50÷2,000	0.24÷43	~ 10	< 0.2	0.02÷0.07

Table 3.1. Blood drop characteristics in BPA, where $\boldsymbol{\rho_{air} = 1.2\, kg/m^3}$, $\boldsymbol{\nu_{air} = 1.51 \times 10^{-5}\, m^2/s}$ are air density and kinematic viscosity at 20°C; $\boldsymbol{\rho = 1056\, kg/m^3}$, $\boldsymbol{\mu = 4\, mNs/m^2}$, $\boldsymbol{\sigma = 56\, mN/m}$ are blood density, high-shear-rate viscosity and surface tension, respectively, at 37°C.

The size and velocity of the gunshot drops were estimated from reported bloodstain sizes due to the lack of direct experimental data on drops. The gunshot drop volume (and hence diameter) calculations were based on the reported gunshot blood stain sizes (areas) and speculated stain thickness (calculated as a constant, ~10^2-10^3, times erythrocyte dimensions). The drop velocities were not clearly reported, thus, an approximate/intuitive range of velocities around the value of 30.5 m/s specified for the "high" velocity spatter (Laber, 1985) was used.

In Figure 3.1 blood drop sizes and velocities were plotted together with the experimental data on terminal velocities, the maximum velocity a falling drop can reach when the drag force prevents further acceleration, of water drops (having similar physical properties to blood) from Gunn and Kinzer (1949), which was expected to be a good approximation for blood drops at terminal velocity conditions.

The ranges of average Weber and Reynolds numbers for typical blood drops were presented in Figure 3.2. The error bars represented ranges of possible We and Re numbers for a certain blood drop type. The diagonal patterns indicated ranges of We and Re where either the drag (blue) or deformation (red) effects on blood drop trajectory are dominant, or where those two factors may compete (green).

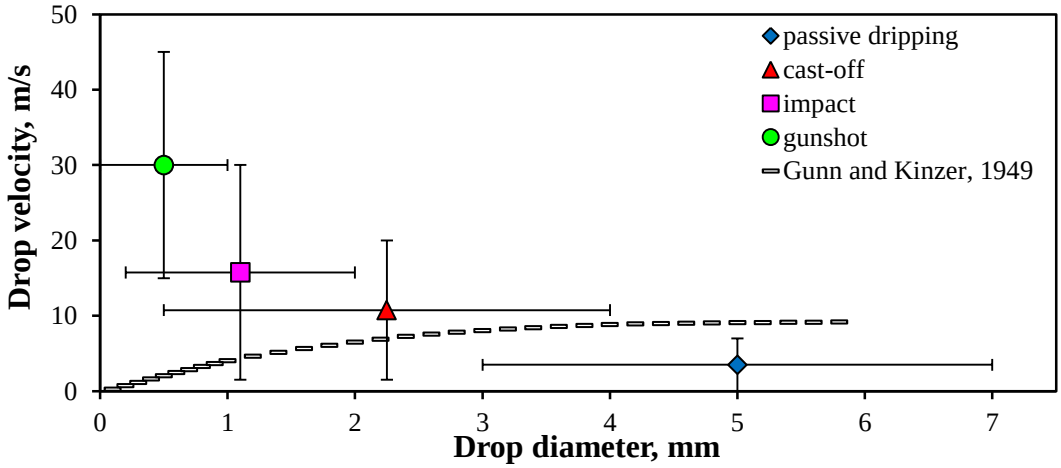

Figure 3.1. Blood drop velocities versus sizes relative to the terminal velocity data for water drops (Gunn and Kinzer, 1949).

Thus, different blood drops would be affected by the deformation differently.

Highly deformed drops (with high We numbers) travelling at low Re numbers (Re < 500-1000), such as smaller and faster cast-off, impact and gunshot blood drops, would be less affected by drop deformation itself compared to the effects of air resistance correlated to Re numbers of drop's flight than those travelling with higher Re numbers (effectively larger blood drops).

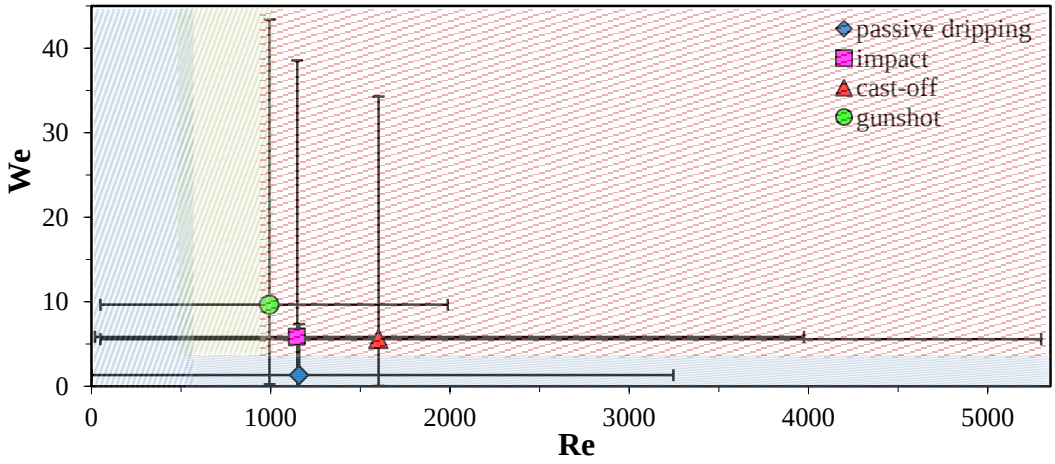

Figure 3.2. Weber and Reynolds number for blood drops in BPA context.

It is seen that **passive drops**, the largest of the types considered, hardly ever reach their terminal velocities in typical crime scene conditions (such as a living room, for example) and, consequently, possess lower levels of deformation during flight. It should be noted that from terminal velocity experiments drops as big as 10 mm in diameter survive their terminal

velocity conditions without disintegration (Gunn and Kinzer, 1949). In addition, for water drops van Boxel (1997) showed that only small drops (d < 1 mm) would reach 95% of their terminal velocities falling from rest (from the point of formation) less than 2 m. Larger drops need larger distances to reach terminal conditions. For example, for a 2 mm drop to attain 95% of its terminal velocity of 6.49 m/s it needs to fall 5.8 m.

Cast-off and **impact drops** may begin their flight with velocities much greater than their terminal velocities, and possess high levels of deformation (as indicated by We > 3).

In this light, in order to accurately predict deformation effects on drop trajectory it is not sufficient to assume the drag force (and drag coefficient, in particularly) is the same as that of a drop at terminal velocity. An accurate approach should infer the level of drop distortion depending on the degree of the distorting aerodynamic force expressed in terms of, for example, We number. This would change as the droplet moves.

In addition, the high Weber numbers of cast-off and impact drops (We > 13) suggest the possibility of drop breakup during flight.

The high levels of cast-off and impact drop deformation in flight may potentially affect drop trajectory, and thus blood origin, estimation.

Gunshot drops, the smallest of those considered, show signs of possible significant deformation during flight based on high We_{avg}. Breakup is predicted for bigger drops (d > 0.1-0.5 mm) in case they possess higher velocities (higher than ~30 m/s). Smaller gunshot drops (d < 0.1 mm) are expected to experience negligible deformation (We < 3) despite their relatively large velocities and may be approximated as rigid spheres when predicting their trajectories.

In addition, the small Ohnesorge numbers for spatter drops suggest possible existence of so-called oscillatory drop motion (mentioned in (Gardner, 1998) and described in (Hsiang and Faeth, 1995)) in the specific range of We numbers that may also affect drop flight.

In summary, based on dimensionless numbers relevant to typical blood drop formation flight the following drops' characteristics were revealed.

Passive blood drops were found to travel at velocities lower than terminal in typical crime scene conditions and possess low deformation levels, < 5-10% (Hsiang and Faeth, 1995), having $We_{avg} < 1$. These, however, are prone to high-amplitude initial oscillations (Raymond et al., 1995). The effect of passive blood drop initial oscillation and deformation on its flight and spreading upon impact needs further investigation.

Cast-off, impact and bigger gunshot (d > 0.5 mm) blood drops were characterized to undergo significant levels of in-flight deformation with a possibility of disintegration. These

may affect drop trajectory and origin prediction considerably and are worth of investigation. Smaller gunshot drops (d < 0.1-0.5 mm) may be treated as spherical during flight. It is however, unknown whether these drops could process velocities higher than 30 m/s to lead to significant drop deformation and breakup due to lack of reported gunshot drop velocity data.

In addition, the degree to which cast-off, impact and gunshot blood drops are affected by the initial (associated with drop formation) oscillations has not been reported in the BPA literature and needs to be evaluated.

Consequently, in order to make an accurate prediction of passive, cast-off, impact and bigger gunshot blood drop trajectories prior to impact on a surface, and estimate blood origin one needs to take into account the mechanism of drop formation, phenomena of initial drop oscillations, deformation and possible breakup during flight and drop drag Re number effects.

4 Methodology

Due to the complexity of the fluid dynamics of bloodstain pattern generation, from the characteristics of a blood source and blood rheology to the specifics of spatter formation mechanisms and impact dynamics, the experimentation is expected to be the most informative and accurate investigative method. This approach was employed in this thesis to study the formation and flight dynamics of passive, cast-off and impact blood drops.

4.1 High-speed digital imaging and image processing

The empirical investigation of the features of drop formation is complicated by the small time and spatial scales involved in an individual blood drop pinch-off dynamics (and subsequent oscillations with frequencies > 300 Hz for smaller blood drops), as well as in the high-kinetic energy disintegration of larger liquid masses at spatter formation.

Drop flight observation is also challenging due to relatively small sizes (< 1 mm) and high velocities (up to about 30 m/s and possibly higher) of typical blood drops. These are able to travel far over a short period of time compromising simultaneous observations of long flight paths and detailed drop shape features.

4.1.1 High-speed digital imaging

High-speed digital imaging capable of capturing events with short time frames has proved to be useful in experimental fluid mechanics (Thoroddsen et al., 2008) and in BPA related studies (Laber et al., 2008). From the images of a fast event (or object) sampled at sufficient frequency the speed and geometric features of the event may be quantified.

Backlighting (or shadowgraphy) is a simple frequently used imaging technique capable of providing images of an object with high contrast, which is particularly important if the imaged objects' shape and/or size are of interest. An object of interest, when back-lit by a light source, blocks light coming towards the photo sensitive element used for image capturing and creates a dark region on the acquired image (Figure 4.1).

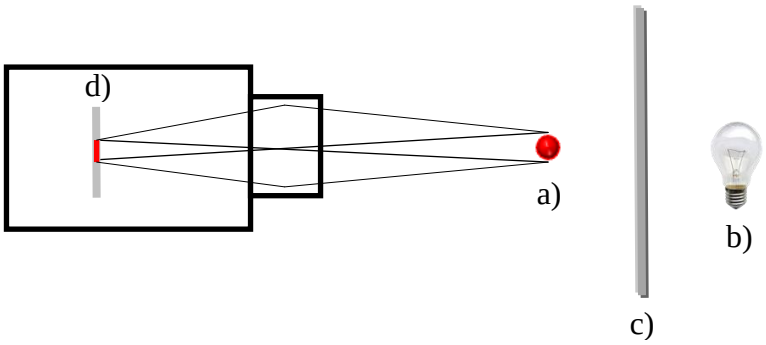

Figure 4.1. Backlighting imaging optical principle: object of interest (a) being back-lit by homogeneous light (light source (b) behind a diffuser screen (c) and captured on am image sensor (d).

The backlighting technique in conjunction with the high-speed imaging was used for this study of blood drop formation and flight.

Redlake MotionPro X3 and Photron SA1.1 high speed digital (CMOS) cameras (Figure 4.2) were used to capture blood drop formation and flight. These were capable to capture high resolution (with fine details) images at high frame rates, the number or frequency of images or frames taken per second (fps) (Table 4.1). The cameras had electronic shutter with shatter speed (or exposure time), the time during which an image sensor is exposed to light, variable from 1 μs.

Figure 4.2. Redlake MotionPro (left) X3 and Photron SA1.1 (right) high-speed digital cameras.

Camera	Sensor	Resolution, pixels	Frame rate, fps	Shutter speed
Redlake MotionPro X3	CMOS, monochrome	up to 1,280x1,024	1,040-64,000	from 1 μs
Photron SA1.1	CMOS, colour	up to 1,024x1,024	5,400-675,000	from 1 μs

Table 4.1. High-speed video cameras' performance specifications.

A Nikon 55mm f/2.8 AIS Micro-NIKKOR macro lens was used (Figure 4.3).

Figure 4.3. Nikon 55mm f/2.8 AIS Micro-NIKKOR macro lens.

The blood drop size, velocity and shape characteristics are one of the major parameters of interest for blood spatter investigation. For accurate qualitative analysis of the spatter by means of high-speed imaging a high quality photographic images are essential.

To capture sharp, detailed and proper illuminated images of an object or event (blood drop movement, for example) frame rate, exposure time and resolution need to be set correctly.

Higher image resolution is desired when object (blood drop) size and shape are of interest. It is believed that the finest image detail to be captured should not be less than 2 pixels in the camera's horizontal field of view (Adermann, 2004). A compromise between image resolution and field of view, however, sometimes needs to be made. This is particularly important for the movement tracking of a relatively small blood drop over a long flight path to determine its trajectory and impact characteristics when some information about its size and shape may be lost.

Inappropriate frame rate setting may result in object image jerkiness and loss of information about its possible movement (Ray, 1997). To eliminate this imaged object speed and imaged region size (or field of view) must be considered. Indeed, knowing how far in the field of view an object can move in one second and the level of details required an appropriate image sampling rate may be determined.

The shutter speed controls the amount of light reaching an image sensor. Thus, adequate illumination is desirable to produce quality images. Insufficient light or inadequate exposure time may lead too dark (under-exposed), too bright (overexposed), blurred (due to object movement during the time a shatter is open) or poorly coloured images (Adermann, 2004). The shutter speed required to capture blur-free image depends on the magnification, object velocity, frame rate and resolution, and should exceed the object velocity by at least a factor of ten.

F-number, the ratio of the lens's focal length to the diameter of the entrance pupil (effective aperture), also governs the amount of light detected by an image sensor. The larger the f-number, the smaller the aperture and the less incident light being detected by the image sensor. Depth of field, the distance between the nearest and farthest regions in a photographic image that are in focus (appear sharp), increases with f-number. The typical lens f-number used for blood drop imaging was f/8.

Consequently, to provide sufficient shutter speed and depth of field, adequate, homogeneous and intense, illumination is required.

For this study of blood spatter formation and flight 0.5 to 2 kW Courtenay Studio Flash incandescent lamps and a number of LED lights placed behind a diffusing screen of sandblasted PMMA were used (Figure 4.4).

The incandescent lamps produced luminous flux of ~8,000-54,000 lm (lumens) with warm color temperatures of ~3,200 K (Roy, 2006).

Eight Bridgelux BXRA-C8000 series LEDs with Britney Medium parabolic reflectors were powered by a Meanwell HLG series constant current power supply. These produced high flux density light, delivering 7,900 lm in cool white color temperatures (~5,665 K).

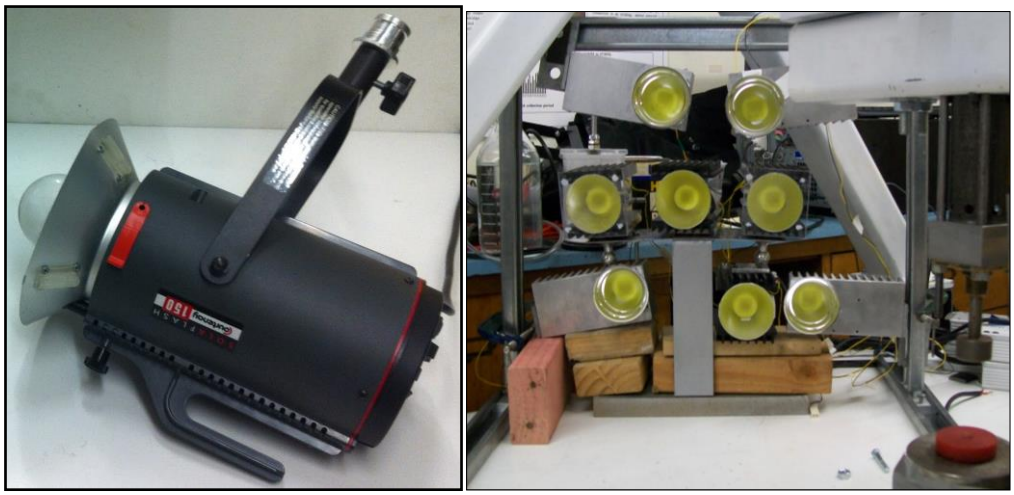

Figure 4.4. A 2 kW incandescent lamp (left) and an array of LED lights (right) used for backlighting.

Maximum camera resolution and corresponding frame rates (Table X above) were used for the experiments. Shutter speed ranged from 1/74000 to 1/183000 s for the Photron SA1.1 camera and 0.6-1 ms for Redlake MotionPro X3. The recording was manually synchronized to the imaged event.

A distance calibration (pixels/mm) was performed using an image of a ruler with the smallest division of 0.5-1 mm. Number of pixels per unit length was manually calculated. Magnification used for the experiments varied from 2 to 15 pixels/mm with the uncertainty of ±1 pixel. The larger values (9-15 pixel/mm) were used for "close-up" drop imaging to investigate individual drop size and shape details over relatively short trajectories, whereas the lower values (2-9 pixels/mm) were used to track drops over longer trajectories. These provided satisfactory image quality for the investigated drop formation and flight conditions.

Two examples of images captured with different magnification levels were depicted on Figure 4.5.

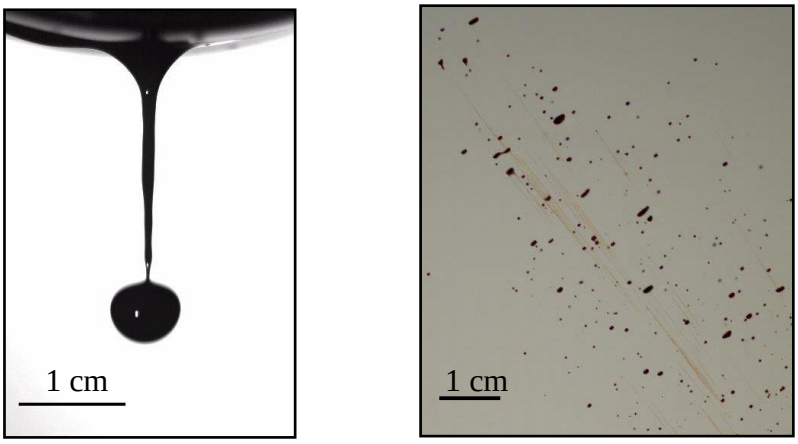

Figure 4.5. Examples of raw images captured with different magnification: passive dripping of blood imaged with 14 pixels/mm (1,040 fps, 0.8 ms shutter, incandescent-lamp lighting) (left) and impact spatter image with 8 pixels/mm (5,400 fps, 1/75000 s shutter, LED lighting) (right).

4.1.2 **Image processing and analysis**

To analyse the imaged object and its movement the object needs to be differentiated from the background. The process is called segmentation (Gonzalez, 2004). A thresholding segmentation technique was used to detect blood spatter in the images acquired at typical imaging settings and magnification (see above).

Recorded 'RGB' or 'truecolor' images (Figure 4.6a), images with each pixel is specified by three values for the red, blue, and green components of its color, needed to be converted to 'grayscale' (Figure 4.6b and c) when each pixel is represented by its intensity, or gray value, within a certain range. Pixel intensity '0' in a grayscale image, for example, corresponds to black and '1' or '255' to white.

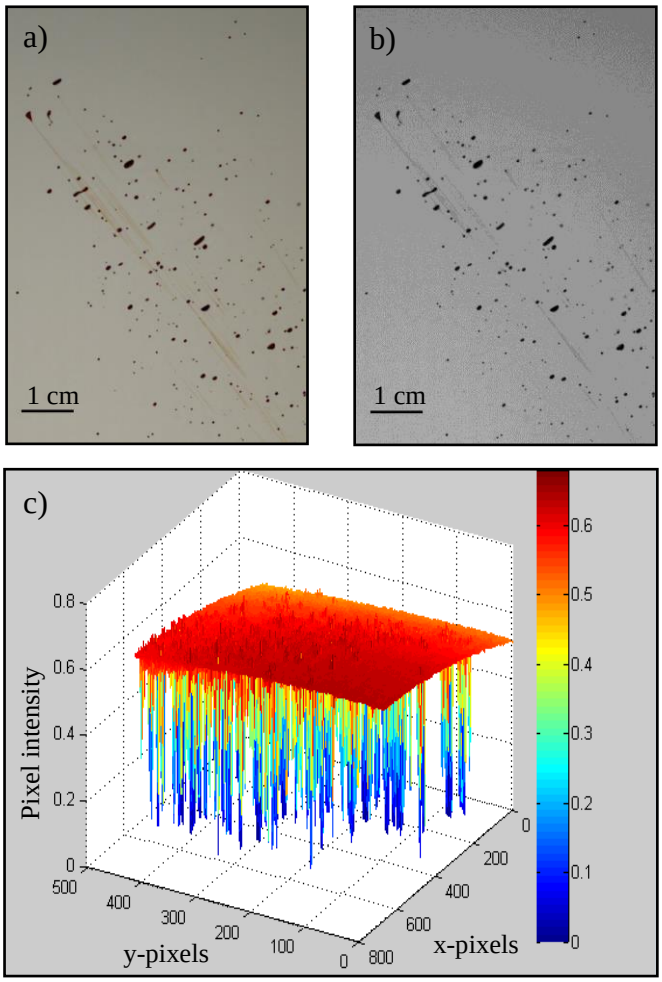

Figure 4.6. Axample of an RGB image of blood spatter (a) and a grayscale image with corresponding pixel intensities of $\in[0,1]$ (c) plotted using MATLAB®.

Thus, objects in an image could be distinguished from the background by their intensity relative to the surroundings (background). For this the grayscale images were converted into black or white (binary) images by thresholding.

To threshold the images either MATLAB® environment or a public-domain Java image processing and analysis program ImageJ were used, ImageJ allowed interactive image analysis which was beneficial for the densely-distributed drop images and large imaged region size, such as for the case of impact spatter (refer to Chapters 4.3.4 and 7.5). For the passive blood dripping study (refer to Chapter 4.2.3 below for more details) image analysis was performed manually.

The areas in an image with extreme changes in pixel intensity were than identified. The 'imextendedmin' MATLAB® function was used to identify the areas of the lowest intensity (blood drops, for example), called 'regional minima', where the difference in intensity of the regional minimum and the surrounding pixels (background) is less than a specified intensity

value (or threshold). This represented a so-called local thresholding method when the threshold is applied to each of the regional/local intensity minimum within an image.

The 'Default' thresholding algorithm was used in ImageJ. This is a global thresholding method performed by setting all pixels with intensity equal or greater than a certain threshold value to those that belong to an object (a drop) with other pixels recognized as background.

The Image/Adjust/Threshold tool was used to interactively adjust lower and upper threshold values when the automatic thresholding had not generated satisfactory results. As it was difficult to provide even (homogeneous) illumination of the bigger imaged regions (~40x40 cm for the impact spatter experiments discussed below) necessary for the global thresholding to perform best, the images were sometimes divided into a number of segments with relatively homogeneous background to be processed separately.

Typical threshold values used for blood spatter experiments were 60-115 gray levels.

The thresholded images were processed using MATLAB® based particle identification and tracking software to infer the geometric and movement characteristics of spatter drops. The function 'regionprops' was used to measure drop image properties such as x and y coordinates, area (or the total number of pixels in the drop image), equivalent diameter ($d_{eq} = [4 \cdot area/\pi]^{1/2}$) and aspect ratio (AR). The drop aspect ratio was determined from the ratio of minor to major drop axes lengths of the ellipse fitted onto the drop image by 'ComputeEllipseParams' subfunction.

The droplets were then tracked over time using Blair and Dufresne (2012) implementation of the IDL particle tracking algorithms developed by Crocker, Grier and Weeks (2012). The expected drop velocity range was specified before the video processing to enable the tracker to search for drops within the maximum distance for a drop to move between frames. A drop had to be tracked for at least 5 sequential frames to be accepted as a trajectory. Drop diameter (d_{eq}) was measured on each frame of the videos and then averaged and reported with standard deviation values. Drop velocity was calculated from a drop displacement (Δ) during two subsequent frames and video frame rate (FR) as $\Delta \cdot FR$.

In ImageJ drop position and geometric characteristics were analyzed using the Analyze/Analyze Particles panel.

A number of tracking plugins in ImageJ (such as MTrackJ and MTrack2) and particle tracking algorithms used for passive and cast-off drops failed for the videos of closely packed and fast moving blood drops (impact spatter). Instead, the drops flight paths were manually recreated with ROI Manager in ImageJ. The drops were labeled on a current time frame and

traced to the next frame. Drop velocity was manually calculated from a drop displacement during two subsequent frames and video frame rate.

4.1.3 **Image thresholding verification**

Image thresholding may directly affect the accuracy of qualitative blood spatter image analysis. It performs best for high-contrast images where the drops (or other objects) are very dark and background is even and very light. These are however ideal condition, and in practice an imaged object may reflect some light and illumination may be non-uniform along the imaged region and in time, Image magnification and resolution (how many pixels in devoted to an object) is also of importance. All these factors may affect image thresholding and result into loss of information about the imaged objects. Applicable to the blood spatter investigation, thresholding may lead to errors in individual blood drop size and shape measurements and through it to velocity and trajectory estimation errors.

To what degree thresholding can affect image analysis quality is unknown. To estimate the level of uncertainties in blood drop characteristics measurements induced by spatter images thresholding a number of verification experiments were performed. The main attention was dedicated to the effect of threshold value used for image segmentation on drop size and shape measurements. Threshold values varied from 10 to 100 gray levels.

Firstly, artificial high-contrast images of spherical and oblate drops (i.e. black-filled circles and ellipses) with set areas (in pixels) and aspect ratios of 0.5 were created using ImageJ. Images were processed using MATLAB® and ImageJ. Calculated and set artificial drop diameters and aspect ratios were identical.

Additionally, real spherical non-reflecting moving objects were imaged by a Photron SA1.1at typical camera settings, magnification and illumination. The objects were steel ball bearings of 0.97-4.76 ± 0.02 mm in diameter corresponding to typical blood drop sizes. The ball bearings were allowed to fall in the field of view of the camera. The imaging was repeated three times for each ball bearing.

Maximum camera frame rate and resolution; lower (used for blood spatter imaging) shutter speed of 1/74000 s; low-to-average magnifications of 6-8 pixels/mm and typical LED backlighting were used.

The ball bearing images were expected to be of similar nature and quality to those with blood drops imaged at similar high-speed camera settings, magnification and illumination.

The images were thresholded with MATLAB® and ImageJ with threshold values varied from 10 to 100 gray levels. It can be seen from the pixel intensities of the images of the

smallest and the largest ball bearings (Figure 4.7) that about ±2.5 pixels (for a 0.94 mm ball bearing) or ±5-7 pixels (for a 4.76 mm ball bearing) on the ball bearing image rim (or edge) had intensity between '0' (an object) and 100-125 (background). These might have been differentiated as those that belong to the ball bearing image or to the background depending on the threshold value used for image binarization.

This suggested that the uncertainty of an object (a ball bearing or a blood drop) size determination may significantly exceed that associated with the image magnification (or pixels/mm value) which is typically ±1 pixel length. This was most likely due to imperfect focus and/or light scattering from the edges, or due to residual motion blur.

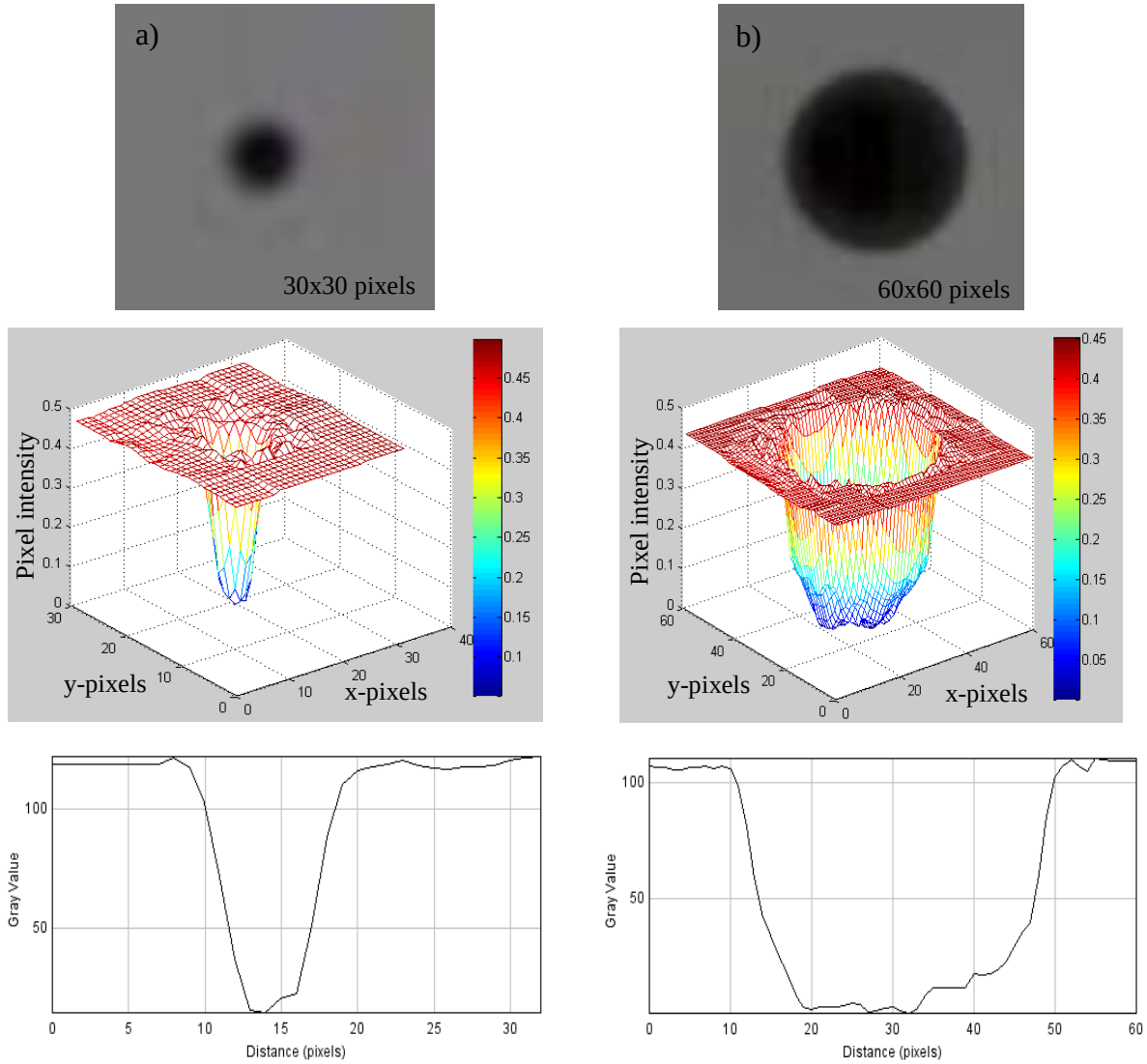

Figure 4.7. Grayscale images of a 0.94 mm (a) and 4.76 mm (b) ball bearings with 3D pixel intensity profiles generated with MATLAB® (c,d) and 2D intensities along a horizontal line drown through the middle of the ball bearing images using ImageJ. Image magnification was 8 pixels/mm.

After conversion to grayscale and thresholding ball bearing images were processed as was discussed above (Chapter 4.1.2) using MATLAB® and ImageJ. Ball bearing diameters calculated using ImageJ for one of the trial image sequence were plotted on Figure 4.8 over 100 imaged frames.

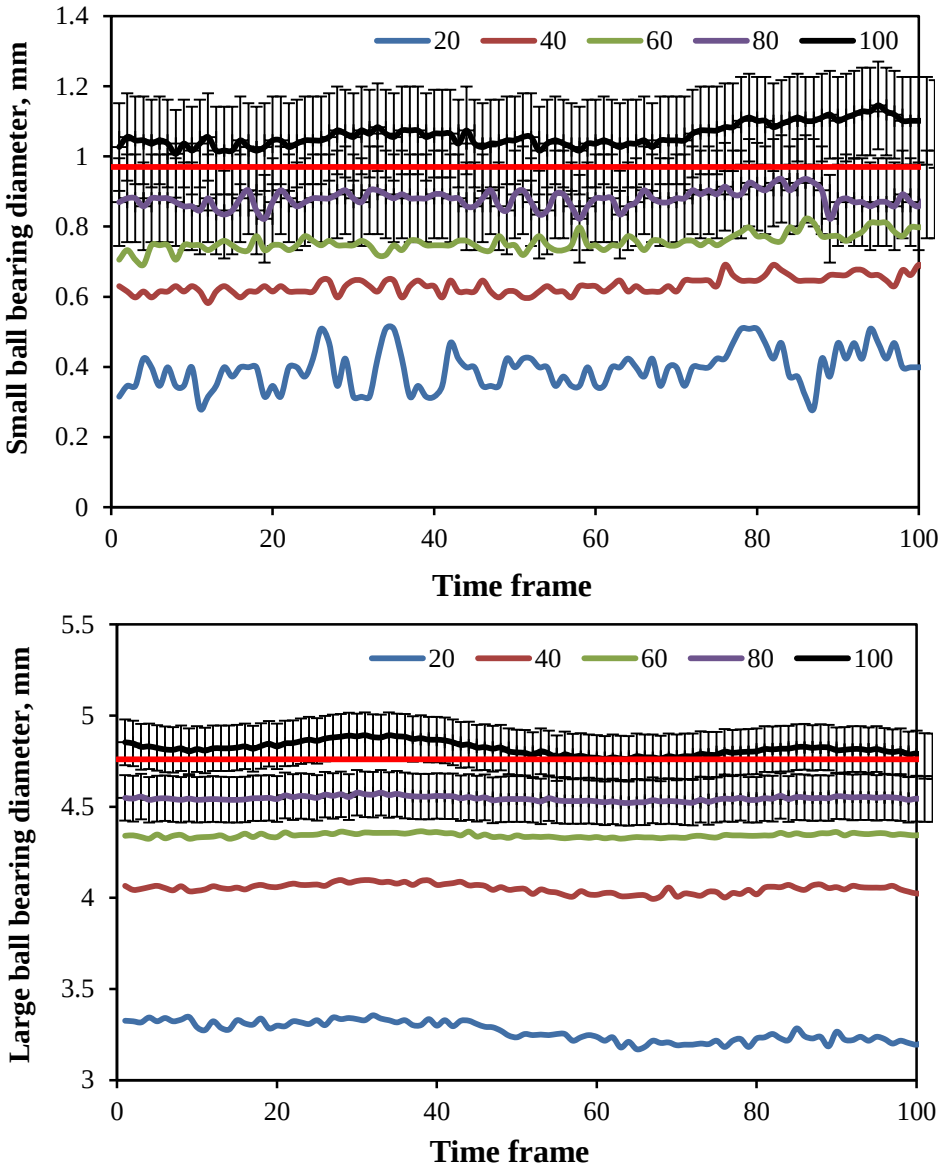

Figure 4.8. 0.94 and 4.76 mm ball bearing diameters obtained using ImageJ. Solid red line represented measured to within 0.02 mm ball bearing diameter. Threshold values ranged from 20 to 100 gray levels. Error bars represented two image magnification uncertainties of ±1 pixel length (0.125 mm in the considered case).

The level of data noise of about 0.1-0.2 mm was present which could be associated with the backlighting inhomogeneity and intensity pulsations. Noise levels decreased at higher threshold values. Threshold values of 20-70 gray levels were inappropriate for accurate

calculations. These resulted in calculated ball bearings diameter underestimation by as much as 31% for the largest ball tested and 57% for the smallest. Threshold values between 80 and 100 gray levels provided the most accurate (within the uncertainty associated with the image magnification, ±1 pixel/mm or 0.125 mm in the considered case) data for ball bearings of all sizes tested.

Similar correlations with optimal threshold values of 80-100 gray levels were observed after image processing with MATLAB®. Ball bearings' diameters estimated using MATLAB®, however, were by on average 5% higher than those determined with ImageJ independent of the threshold value. The latter may be associated with the local thresholding method used compared to the global thresholding in imageJ.

Ball bearing aspect ratios were also inferred from the processed images. Both MATLAB® and ImageJ recognized solid circular in cross-section (AR=1) ball bearing images as somewhat prolate ellipses (AR>1). This may be associated with the uneven lighting as well as some motion blur due to finite ball bearings' velocity. The ball bearings may not be manufactured perfectly spherical as well.

The degree of false oblateness (a ratio of the calculated to true ball bearing aspect ratio of ~1) detected increased at lower threshold values of 20-60 to about 50% and 6% for the smaller and larger ball bearings tested respectively. Aspect ratios were as high as 1.5 (smaller ball bearing) and 1.06 (larger) at changes from frame to frame. Some degree of false oblateness, 10% and 2% for 0.94 and 4.76 mm ball bearings correspondingly, remained even at optimal threshold values used for object detection.

In summary, the observed uncertainties in imaged ball bearing size measurement were 31% for the largest ball tested and 57% for the smallest at threshold values of 20-70 gray levels with false oblateness of 6% and 50% respectively. At optimal threshold values of 80-100 gray levels the size measurement uncertainty reduced to that associated with image magnification, some degree of false oblateness (10% for the smaller and 2% for the larger ball bearing) remained, however.

It should be noted that the threshold values used for segmentation of blood drop formation and flight images corresponded well with the optimal threshold values determined from the verification experiments. Thus the levels of measurement uncertainties (such as in drop size) due to image thresholding may be correlated to those observed for verification trials. Additionally, the levels of noise in aspect ratio observed for verification experiment suggested that the shape characteristics of blood drops, aspect ratios in particularly, may be

resolved with finite accuracy which decreases for smaller (d<1 mm) drops unless sufficient magnification is provided.

4.2 Passive dripping study methodology

To investigate the relationship between the volume of a blood drop formed by passive dripping and the nature of the dripping surface a number of dripping experiments with non-absorbent surface representatives of weapons frequently used in criminal assaults were performed. The methodology for this study follows. The results and discussion can be found in Chapter 5.

4.2.1 Test objects characteristics

Liquid drops were allowed to form from the surface of a number of objects representing common weapons (Figure 4.9, Table 4.2). Among them were five sets of AISI 304 stainless steel cylinders of diameter between 10 and 100 mm and two flat plates with different surface roughness.

Figure 4.9. Objects tested.

Different surface textures were produced by turning the cylindrical samples on a lathe and by vertical milling the flat samples. As a result the machining marks of the cylinders followed the circumferential direction (perpendicular to their axis of symmetry) whereas the flat plates had cross-hatched patterns.

It should be noted that each machining process removed a small amount of material from the specimen's surface to produce a higher degree of surface finish. Rougher surface finishes required more machining, so the actual diameter for the cylindrical objects tended to decrease slightly as the roughness increased.

A Taylor-Hobson TALYSURF 10 profilometer was used to measure average roughness values, $R_a = \overline{R_i}$ (Figure 4.10). R_i is half the average vertical difference between a peak and the adjacent valley. The profilometer tip was run in a direction perpendicular to the surface texture direction. Eight tests were performed with each object. The waviness (long wavelength undulation) of the machined surface profile was considered to be small and was not investigated.

Surface roughness values of the 'medium' cylindrical samples (10.01 mm and 39.5 mm in diameter) and all 'rough' samples were visually and tactile assessed using surface roughness standards, comparator Flexbar composite set No. 16008.

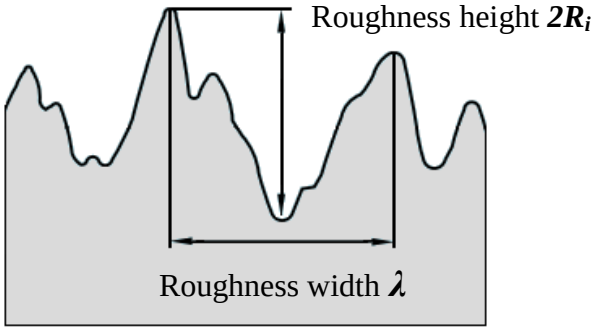

Figure 4.10. Basic surface texture characteristics.

The samples were then grouped in three categories: smooth with 0.1 μm < Ra < 0.7 μm, medium with 2.4 μm < Ra < 6.3 μm and rough objects with Ra ~12.5 μm.

Experimental data was assessed in terms of the mean curvature H of the test object surface as a measure of its convolution or deviation from flatness:

$$H = \frac{1}{2}\left(\frac{1}{R_1} + \frac{1}{R_2}\right),$$

where R_1 and R_2 are the principal radii of curvature, or maximum and minimum perpendicular radii of the surface curvature of the object from which the drops are formed. These are measured at a point on the surface in perpendicular (or principal) directions.

Flat surface objects had radii of curvature which tend to infinity and hence had close to zero mean surface curvatures. Each cylindrical test object had one radius of curvature equivalent to its geometrical radius and an infinite radius of curvature corresponding to its axial length. Mean surface curvature for these samples ranged from about 0.1 to 0.01 mm^{-1}.

A stainless steel kitchen knife and a chrome vanadium metric wrench were also tested. The knife blade had a body with flat parallel surfaces and an edge with a radius of curvature of about 20 cm. The tip of the knife had a radius of curvature of a few millimetres in the plane of the blade and a fraction of a millimetre in the other direction (see Figure 4.11) which gave *H* of about 5.25 mm^{-1}.

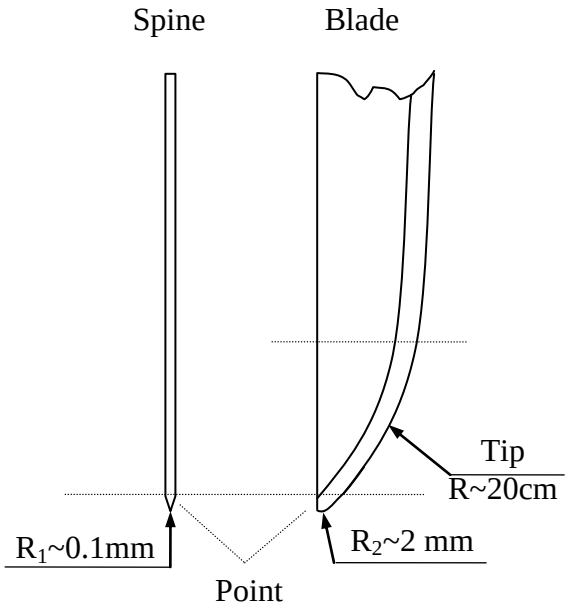

Figure 4.11. Knife diagram.

The wrench open end (opposite to the ring end) had a radius of curvature of a few centimeters in one direction, and a few millimetres in the other corresponding to *H* of about 0.2 mm^{-1}.

Surface characteristic / Object	**H**, mm^{-1}	**R_a**, μm		
		'smooth'	'medium'	'rough'
Cylinders	0.010	0.19 ± 0.02	3.59 ± 0.16	~12.5
	0.013	0.13 ± 0.09	2.4 ± 0.1	~12.5
	0.025	0.17 ± 0.02	~6.3	~12.5
	0.050	0.55 ± 0.19	3.7 ± 0.17	~12.5
	0.10	0.66 ± 0.07	~6.3	~12.5
Flat plates	~0	0.37 ± 0.05	~6.3	-
Wrench	~0.20	-	-	-
Knife	~5.25	-	-	-

Table 4.2. Dimensional and surface characteristics of the objects tested.

Smooth and rough cylinders were 50 mm long. The length of the medium-roughness samples was 100 mm. The flat plates were 100 x100 x 5 mm in size. The uncertainty in the dimensional measurements was ± 0.02 mm. The absolute errors in the measured roughness values in Table 1 include both the profilometer instrumental uncertainty and the standard deviations of the mean values for a 95% confidence interval.

Before each test all objects were carefully cleaned with 1% Virkon solution, rinsed with distilled water, acetone and ethanol and then dried in hot air to remove any deposits on their surfaces.

4.2.2 **Test liquids**

Both distilled water and 1-day-old abattoir porcine blood, used as a human blood substitute, were tested. Porcine and human blood have been shown to have similar physical properties and produce droplets similar in size (Raymond, 1996). To prevent the blood from clotting, EDTA was added at a concentration of 7 mg/ml of blood. The blood was stored at 4 °C for 24 hours before experimentation.

Density, surface tension and viscosity of porcine blood were controlled to match human values before and after the experiments. Measured mean values of blood density, surface tension and high-shear rate viscosity (at the shear rate of 1000 s^{-1}) together with the additional measurements of blood Packed Cell Volume (PCV) and plasma viscosity are listed in Table 4.3. Before each physical property measurement, calibrations with distilled water were conducted. The table includes data from distilled water calibrations with calculated absolute errors and corresponding reference values (Haynes, 2012). Density and surface tension tests were performed with the blood warmed to 37 ± 0.5 °C in a water bath.

Reference human blood properties values were taken from the published literature: PCV range (Dacie and Lewis, 1995); density (Trudnowski and Rico, 1974; Hinghofer-Szalkay and Greenleaf, 1987; Kenner, 1989); surface tension (Hrncir and Rosina, 1997; Rosina et al., 2007); whole blood and plasma viscosity (Lowe and Barbenel, 1988; Wells et al., 1961; Casson and Kurland, 1965; Chien, 1981; Ernst at al., 1985).

Temperature measurements for this study were obtained using Yokogawa TX10 digital thermometer.

The density of porcine blood was measured by a weighing syringe method using a Sartorius analytical balance ED224S. Six independent measurements were taken and

averaged. Corrections of the order of 1% were applied, based on the calibration with distilled water.

Porcine blood	Before the experiment	After the experiment	# of measure-ments	Published reference values
Age since collection from a pig	1-day-old	2-days-old	-	
PCV	0.39 ± 0.01	0.388 ± 0.006	6	0.40 - 0.45
Density, $\times 10^3$ kg/m^3	1.069 ± 0.022	1.069 ± 0.021	5	1.052 - 1.063
Surface tension, mN/m	62.47 ± 0.71	62.96 ± 0.49	15	55.5 - 63.1
Whole blood viscosity, mN·s/m^2	4.001 ± 0.008	4.133 ± 0.008	2	3.2 - 4.4
Plasma viscosity, mN·s/m^2	1.482 ± 0.003	-	2	1.025 - 1.029
Distilled water				
Density at 22 °C, $\times 10^3$ kg/m^3	1.007 ± 0.028	0.993 ± 0.030	5	0.998
Surface tension at 22 °C, mN/m	71.87 ± 0.35	72.06 ± 0.37	15	72.75
Viscosity at 22 °C, mN·s/m^2	-	-	-	1.002

Table 4.3. Measured physical properties of porcine blood and distilled water. Errors listed are either sample standard deviations or absolute errors for a 95% confidence interval.

Surface tension measurements were performed on a KSV Contact Angle and Surface Tension Meter with a CAM 200 CCD camera and CAM 2008 software. A 1.25 mm diameter hypodermic needle and a syringe were used to produce fifteen pendant blood drops with fully developed (elongated) neck. Before each test the needle was cleaned with 1% Virkon solution, rinsed with distilled water and acetone, then carefully dried with a hot air gun. Droplet images were captured and analyzed by fitting a curve to the image profile. The mean surface tension and standard deviation of the mean were calculated.

Packed cell volume (PCV) of pig blood was measured after 4 minutes centrifugation at 12,000 rpm in a Hettich EBA 21 Centrifuge (Andreas Hettich CmbH & Co.KG). An average value was taken from six capillary tube readings. Only slight, if any, haemolysis was visually observed in blood which had been used in the dripping experiment.

Porcine whole blood and plasma viscosity were measured at a shear rate of 1000 s^{-1} with a rotational rheometer HAAKE Rotovisco RV 20 with NV coaxial cylinders sensor system. The rheometer heating bath thermocontroller HAAKE F3 maintained blood at 37 ± 0.01 °C. Two verification runs were made for each sample. Shear stress correction factors of

the order of 3% and instrumental error based on the device calibration with a general purpose viscosity reference standard type N10 (Paragon Scientific Ltd.) were applied to the obtained data.

4.2.3 **Drop formation and flight imaging**

Liquid was introduced at the top of the object and allowed to flow over the surface to the lowest point, where the drops formed. A peristaltic pump (Gilson Minipuls 3 M312, Gilson LTD) with a speed controller and 4 mm diameter silicone tubing was used to draw the liquid from a reservoir flask to the experiment (see Figure 4.12 for the schematic representation of the experimental setup). A constant flow rate of 0.1 ± 0.02 ml/s (measured by weighing) was maintained. Distilled water was tested at ambient temperature 22 ± 0.5 °C. The blood was heated to 37.5 ± 0.5 °C in a reservoir flask placed in the water bath, both agitated by magnetic stirrers. The temperature of the blood leaving the supply tube was 36.8 ± 0.5 ^{o}C, but the objects were at ambient temperature 22 ± 0.5 °C.

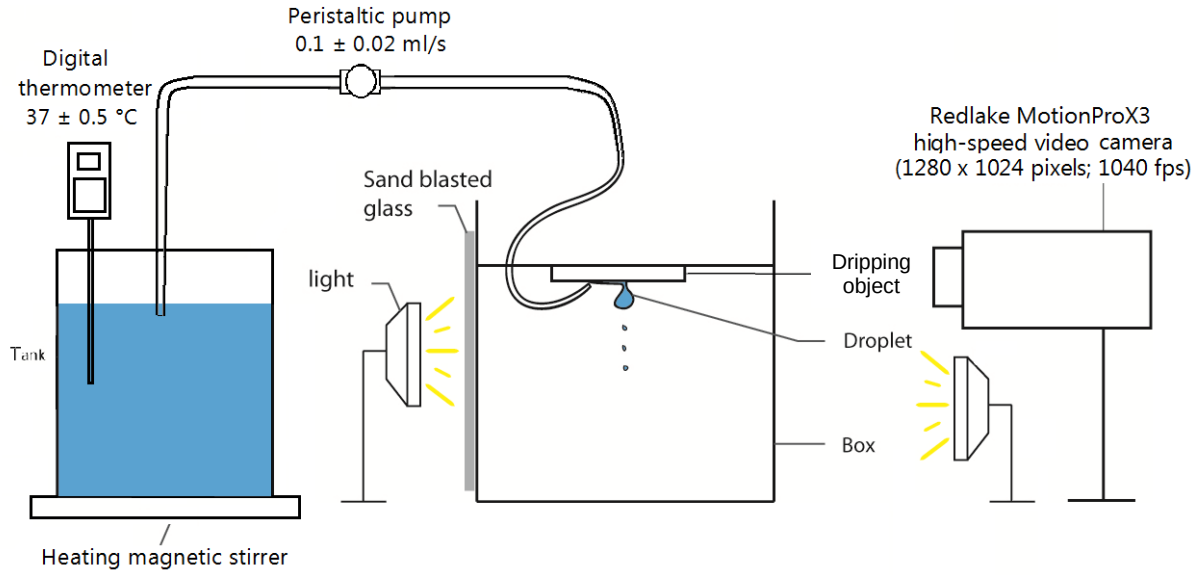

Figure 4.12. Schematic representation of the passive dripping experimental setup.

For each object studied and for each liquid tested, the formation process of twelve drops was captured on a Redlake MotionPro v3 (CCD or CMOS, resolution 1,280x1,024 pixels) at 1,040 frames per second. Motion Studio Ver. 2.09.00 (Integrated Design Tools (IDT), Inc.) software was used to operate the camera. The experimental set up was side- and back-lit by 0.5 to 2 kW incandescent lamps placed behind diffusing screens of sandblasted PMMA. The images were processed with Photron FASTCAM Viewer Ver.3.0 (Photron Ltd.) software.

Horizontal and vertical diameters of the primary drop were measured as it passed through the approximately spherical phase of its oscillation and then averaged. A distance calibration (pixels/mm) was made using an image of a steel ruler. Typical magnifications of 14 pixels/mm were used. The ruler was mounted vertically as close as possible to the object plane of the camera and within ± 2 mm of the perimeter of drop formation on the object surface. The second parameter of interest was the number of accompanying (satellite) droplets produced from the ligament breakup. Accompanying droplets were allowed to fall 6 cm from the object surface to ensure the cessation of inter-droplet interactions (collision and coalescence (Qian and Law, 1997)) and were then counted. Absolute uncertainties based on the standard deviation of the mean and instrumental uncertainties for each set of the experiments were calculated for a 95% confidence interval.

4.3 Blood spatter experimental methodology

This chapter describes the verification experiments for the developed numerical scheme for accurate blood drop in-flight behaviour prediction (see Chapter 6 and 7). These included the study of passive blood drop oscillations and terminal velocities, cast-off drop formation features and impact drop generation, flight and breakup.

4.3.1 Passive blood drops at terminal velocity

The data was provided by Dr. M.C. Taylor, B.P. Epstein and T.L. Laber. For this study donor human blood with EDTA was used. Blood density was determined by weighting and measuring the volume for 10 blood drops to be 1028 ± 25 kg/m^3. Blood viscosity and surface tension were not measured.

Before the experimentation the blood was agitated and heated to 36 ± 1 °C. Blood drops in the range of 3-5 mm in diameter were produced using Pasteur pipettes with different tip sizes. The drops were then released from a number of heights indoors to limit the effects of air currents and winds on drop flight. Ambient temperature was 21 ± 1 °C.

Each meter of drop flight (starting at 2 m of fall) was imaged using a Photron FASTCAM SA1 (Photron Ltd.) high speed video camera at 5,000 frames per second, with the shutter speed of 1/6000 s and resolution of 256x1024 pixel. Fall distance of a drop was measured with a tape measure within ± 5 cm.

A set of close-up videos of drops were also captured to measure drop diameters. Each test was repeated three times. Photron FASTCAM Viewer Ver.3.0 (Photron Ltd.) software

was used to operate the camera. The experimental set up was side-lit from both sides by 0.5 to 2 kW incandescent lamps.

A distance calibration (pixels/mm) was made using an image of a 1 m long ruler. The ruler was mounted vertically in the field of view of the camera. The drops were released to fall within ± 1 cm to the plane of the ruler location. Both the ruler and falling drops were expected to be within the camera depth of field. Typical magnifications for drop close-up and drop flight images were 0.9 ± 0.1 and 15 ± 1 pixels/mm correspondingly (the errors are due to image pixelation).

The images were processed using MATLAB® based particle identification and tracking software (refer to Chapter 4.1.2 for more details).

4.3.2 **Passive blood drop oscillations**

4.3.2.1 Blood physical properties measurement

Porcine blood, sourced from a slaughterhouse, with ACD at a concentration of 7 mg/ml to prevent coagulation, was used as a human blood substitute. The blood was stored at 4 °C and used within 4 days.

Porcine blood batches whose density, surface tension and viscosity fell within the normal range of human values were selected. The blood was warmed to 37.0 ± 0.5 °C. Before each physical property measurement, calibrations with distilled water were conducted. Measured blood density and surface tension were 1033 ± 20 kg/m^3 and 61.7 ± 0.8 mN/m correspondingly. Blood viscosity was measured to 4.6 ± 0.1 mN·s/m^2 at high shear rate (1000 s^{-1}) and to 21.3 ± 0.6 mN·s/m^2 at low shear rate (10 s^{-1}).

Blood density was measured by a weighing syringe method using a Sartorius analytical balance ED224S. Six independent measurements were taken and averaged. Corrections based on the calibration with distilled water of the order of 1% were applied. Surface tension measurements were performed on a KSV Contact Angle and Surface Tension Meter with a CAM 200 CCD camera and CAM 2008 software. A 1.25 mm diameter hypodermic needle and a syringe were used to produce fifteen pendant blood drops with fully developed (elongated) neck. Before each test the needle was carefully cleaned and dried. The mean surface tension and standard deviation were calculated.

Blood viscosities were measured at a shear rate of 1000 s^{-1} with a rotational rheometer HAAKE Rotovisco RV 20 with NV coaxial cylinders. Two runs were made for each test sample. Shear stress correction factors of the order of 3% and instrumental error based on the

device calibration with a general purpose viscosity reference standard type N10 (Paragon Scientific Ltd.) were applied to the data.

4.3.2.2 Drop formation and imaging

The blood was warmed to 37.5 ± 0.5 °C and agitated in a reservoir flask by a magnetic heater-stirrer. A Gilson Minipuls 3 M312 (Gilson Ltd.) peristaltic pump and 4 mm diameter silicone tubing were used to draw the liquid from a reservoir flask to the experiment. A constant flow rate of 0.10 ± 0.02 ml/s (measured by weighing) was maintained. Ambient temperature was 19.0 ± 0.5 °C.

Blood drops were formed from a number of stainless steel objects to produce a range of drop sizes. Those included a 21G ø0.8 mm blunt hypodermic needle, SWAGELOCK® hose connector with a 6.3 mm outer tube diameter, kitchen knife and ø100 mm cylinder (Figure 4.13). The objects were at ambient temperature.

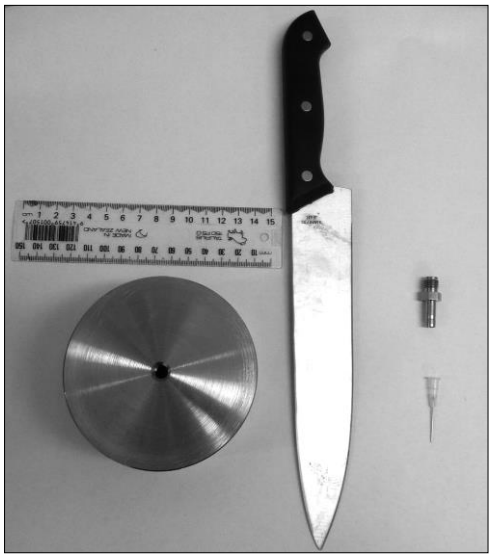

Figure 4.13. Dripping objects used.

The drops were allowed to fall 1.5 m in total. Owning to the image magnification necessary to accurately determine drop size and shape 10 cm of drop flight were imaged at a time. Drop fall distance was measured to ± 5 cm. Drop images upon its formation, after 20, 50, 100 and 150 cm of fall were taken with 10-15 repeats. A Photron FASTCAM SA1 (Photron Ltd.) high speed video camera at 5,400 frames per second, with the shutter speed of 1/75000 s and resolution of 1024x1024 pixels was used. The set up was back-lit with 8 LED lights.

A distance calibration (pixels/mm) was made using an image of a ruler. Typical magnification of 9 ± 1 pixels/mm (the error is due to image pixilation). The drops falling within ± 5 mm to the plane of the ruler location were recorded.

Drop images were processed in the same way as described above in Chapter 4.1.

4.3.3 **Cast-off drop formation and flight**

The drops were generated from a 60 cm diameter flat rotating stainless steel disk. The disc rotated clockwise about its symmetry axis, with the plane of the disc vertical. The speed of rotation was regulated by a single phase AC motor with a variable speed drive, with tangential velocity in the range of 1-20 m/s within 0.5 m/s (see Williams and Taylor (2013) for more details of the experimental rig).

Abattoir porcine blood with 7 mg/ml of ACD was used. The blood was stored at 4 °C and used within 2 days.

A KNF Flodos diaphragm pump NF 60 with 4 mm inside diameter insulated tubing was used to eject 2 ml of blood on the rotating disk surface for each experimental trial. The blood was fed onto the disc surface, at the lower part of the disc ~ 1 cm from the edge.

Density, surface tension and viscosity of porcine blood were measured using the same methodology described above for the initial passive drop oscillation investigation. The blood density and surface tension were 1054 ± 25 kg/m^3 and 63.8 ± 1.6 mN/m respectively. Blood viscosity was measured to 5.0 ± 0.7 mN·s/m^2 at high shear rate of 1000 s^{-1}. The blood was warmed to 35.0 ± 0.5 °C for all physical properties measurements and testing.

The drops were imaged in flight with a Photron FASTCAM SA1.1 (Photron Ltd.) high speed video camera at 5,400 frames per second, with the shutter speed of 1/75000 s and resolution of 1024x1024 pixels. The set up was back-lit with up to eleven LED lights.

The drops were observed to move along the plane of the disk with maximum deviation of about ± 1-1.5 cm. The camera was focused on the plane of the disk. Distance calibration (pixels/mm) was made using an image of a ruler. Only the drops that stayed in focus until they left the field of view were analyzed.

A set of experiments with close-up imaging were performed to study the initial phase of cast-off drop flight including shape oscillations. The drop formation from the rotating disk was imaged with typical magnification of 9 to 15 pixels/mm to allow quality drop shape recognition and processing. The recorded trajectory during close-up imaging was limited to less than 4 cm. It was experimentally difficult to determine drop sizes and track any shape changes over a meaningful length of trajectory and number of oscillation periods of the

smaller cast-off drops generated at the higher tangential velocities (> 6-7 m/s). Thus the study was limited to the lower tangential velocities.

Additional experiments were dedicated to capturing longer drop trajectories to allow a comparison with the numerical perditions. The typical field of view for these experiments was about 55x55 cm which corresponded to 60-70 cm length of imaged drop trajectory. However, owning to the image magnification necessary to accurately determine blood drop size at disc tangential velocities higher than 15 m/s (when the cast-off drops become significantly smaller), the resolution was decreased to about 30x30 cm (or ~ 40 cm of drop trajectory). The magnification was typically 2 pixels/mm.

The same image processing methodology as described above for passive blood drops were used for cast-off drop analysis.

4.3.4 **Impact spatter experiments**

The generation of blood drops as a result of a blunt force impact was studied by means of the "Impact machine" (Figure 4.14). A pneumatic cylinder (actuator) drove a piston and the attached rod to vertically impact a target surface. The driving air at gauge pressure of 2 to 6 bar (or 200 to 600 kPa) was supplied by a pressurized air tank.

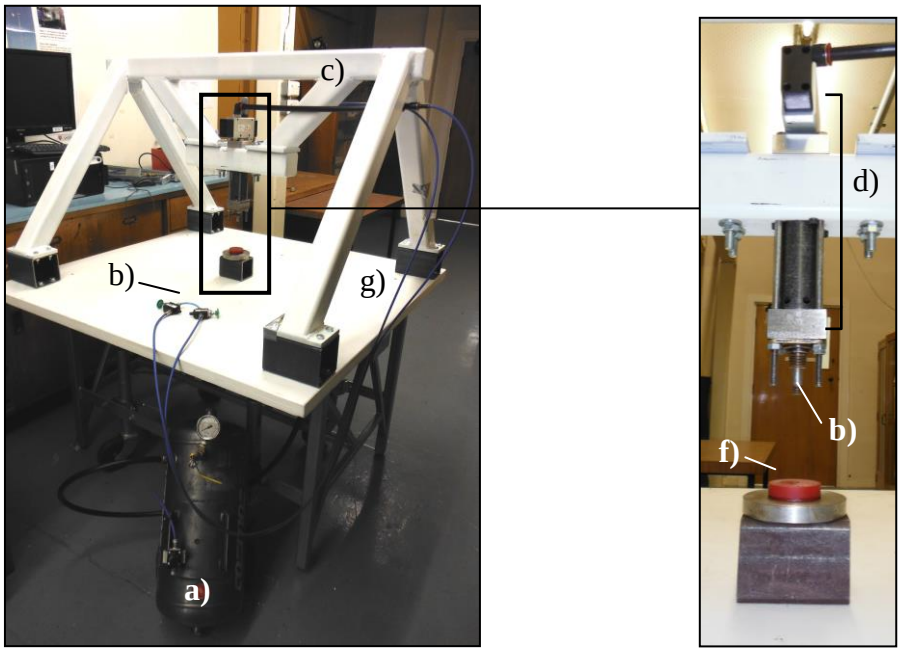

Figure 4.14. "Impact machine": pressurized air tank (a), safety valves (b), steel frame (c), actuator (d), rod (e) and polyurethane target (f) on a wooden bench (g).

The target was a 5 cm polyurethane block with a flat impact surface. The actuator and target were firmly mounted on a durable 6 cm thick wooden bench. The stroke length was

about 9.5±0.5 cm. The rod tip was fitted with a 3 cm diameter steel tip with radiused edges with a radius of curvature of ~ 1 mm, similar to a 16oz claw hammer head (Figure 4.15).

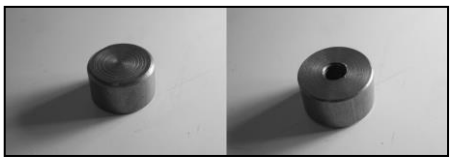

Figure 4.15. Top and bottom views of the claw hammer head stimulant.

4.3.4.1 Impact velocity

The impact speed of the rod with the hammer head simulant was measured at different driving air pressures by means of high-speed imaging. A Photron SA1.1 camera at 5400 fps, 1024x1024 pixel resolution and shutter speed of 1/75000 s was used with magnification of 6.8 pixels/mm. The impact event was back-lit with 5 LED lights. Five impacts at the same (±10 kPa) driving pressure were recorded for comparison.

The velocity was calculated from the vertical distance the tip of the rod with hammer head attached travelled in a certain time frame. The instrumental uncertainty of velocity measurements, one pixel length over the time frame duration, was of about 0.77 m/s. The standard deviation between velocity measurements at the same driving pressure (and stroke time/length) was about 3.5%.

The rod with hammer head velocity evolution with the stroke time and distance from one experimental trial was plotted on Figure 4.16a and b for visualisation. The maximum velocity deviation at any value of the stroke time or distance between trials of nominally the same driving pressure did not exceeded ±0.5 m/s.

The impact velocity, averaged over the experimental trials, prior to the contact with the target (within 1 cm of the target) was plotted on Figure 4.17 over the range of driving pressure values studied.

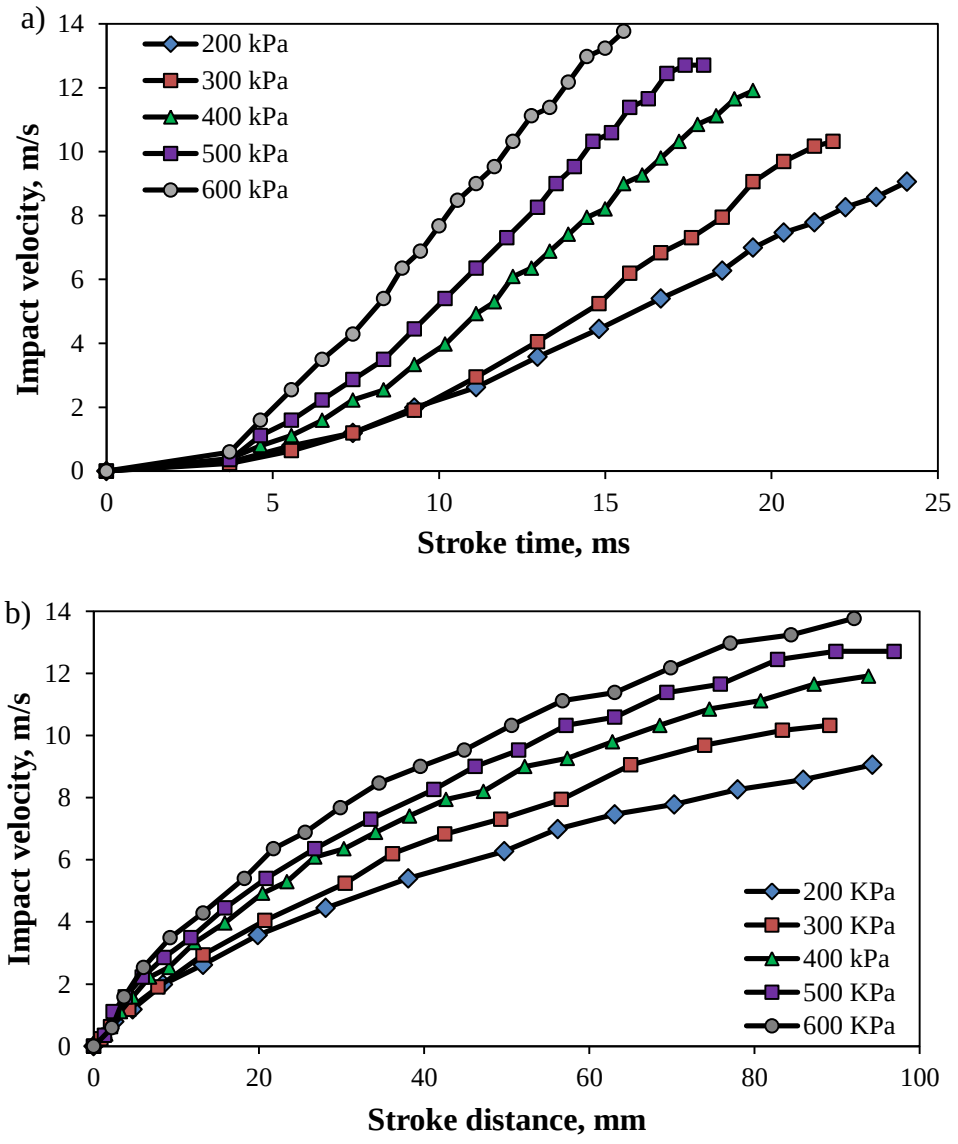

Figure 4.16. Impact velocity vs. stroke time (a) and stroke distance (b) at different values of driving air pressure.

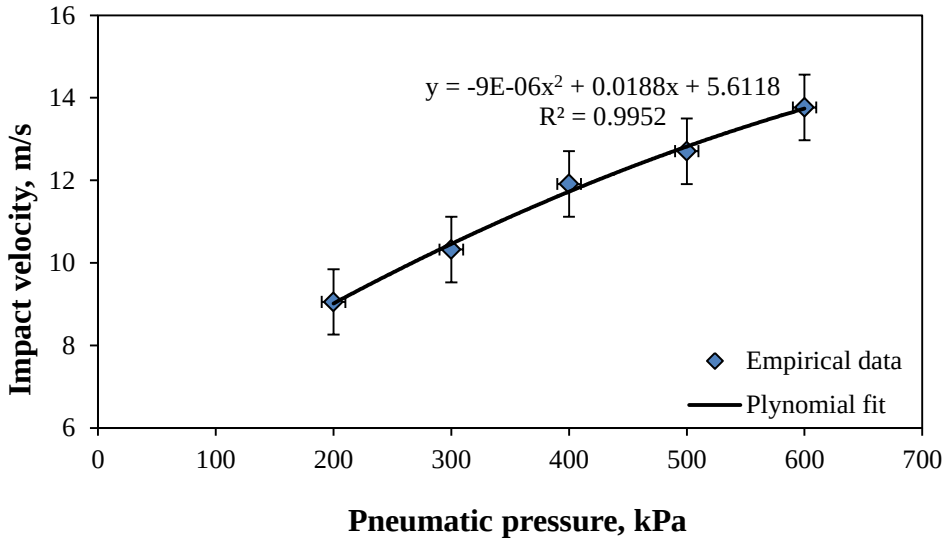

Figure 4.17. Impact velocity vs. driving air pressure. Vertical and horizontal error bars corresponded to two instrumental uncertainties of the velocity and pressure measurements correspondingly.

These showed impactor (the rod with the hammer head attached) acceleration during the stroke and an increase in the impact velocity with the driving pressure.

The impactor velocity prior to the impact increased from 9.1±0.3 m/s to 13.8±0.5 m/s with the increase in driving pressure from 200 to 600 kPa.

4.3.4.2 Impact spatter generation and imaging

2.0 ± 0.2 ml of abattoir porcine blood from the same sample used for the initial drop oscillation at passive dripping study was applied to the urethane target surface for each impact experiment. The blood was warmed to 37 ± 0.5 °C and ambient temperature of 18 ± 1 °C.

A 32x 32 cm region close to the point of impact (Figure 4.18) was imaged with a Photron SA1.1 camera at 5400 fps, 1024x1024 pixel resolution and shutter speed of 1/75000 s. The typical magnification for the videos was 5-9 pixels/mm. The drops were back-lit with 8 LED lights (Figure 4.4).

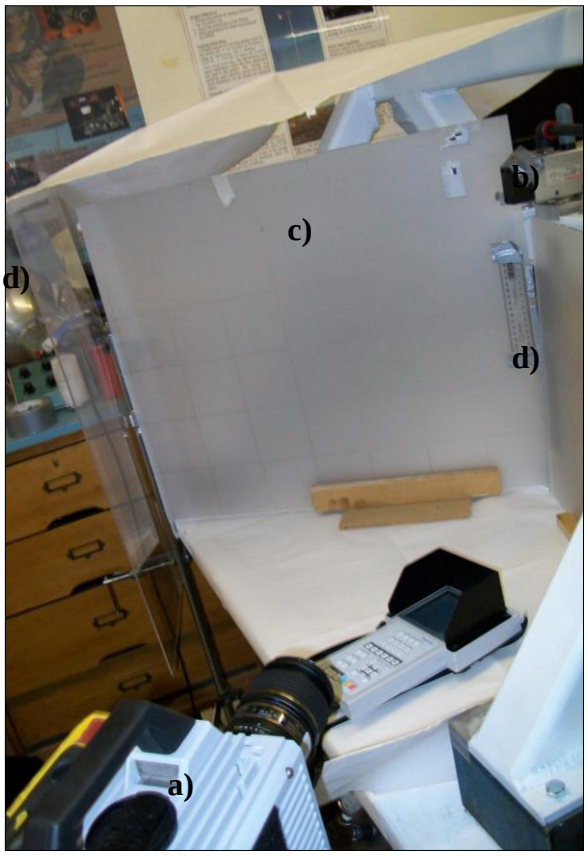

Figure 4.18. Imaging setup for impact spatter experiments: high-speed camera (a), pneumatic actuator (b), diffusing screen (c) and spatter capturing barriers (d).

The impact of the tip onto the pool of blood caused the blood to disintegrate into a dense mist of drops, moving radially outward from the impact centre (Figure 4.19).

In order to ease the image processing the number of drops captured needed to be reduced, and the movement perpendicular to the object plane eliminated. To this end, only those drops which passed through a 5 mm wide vertical slit between the point of impact and imaged region were recorded.

The images were processed using ImageJ, a public-domain Java image processing and analysis program. The digital videos of the impact drops were converted to grayscale using the Image/Type/8-bit function. The images were than thresholded using the Image/Adjust/Threshold menu with typical threshold values used of 80-115 gray levels. Drop position and geometric characteristics were analyzed using the Analyze/Analyze Particles panel. Drop velocity was manually calculated from a drop displacement during two subsequent frames and video frame rate. The drop movement perpendicular to the plane of view was considered negligible.

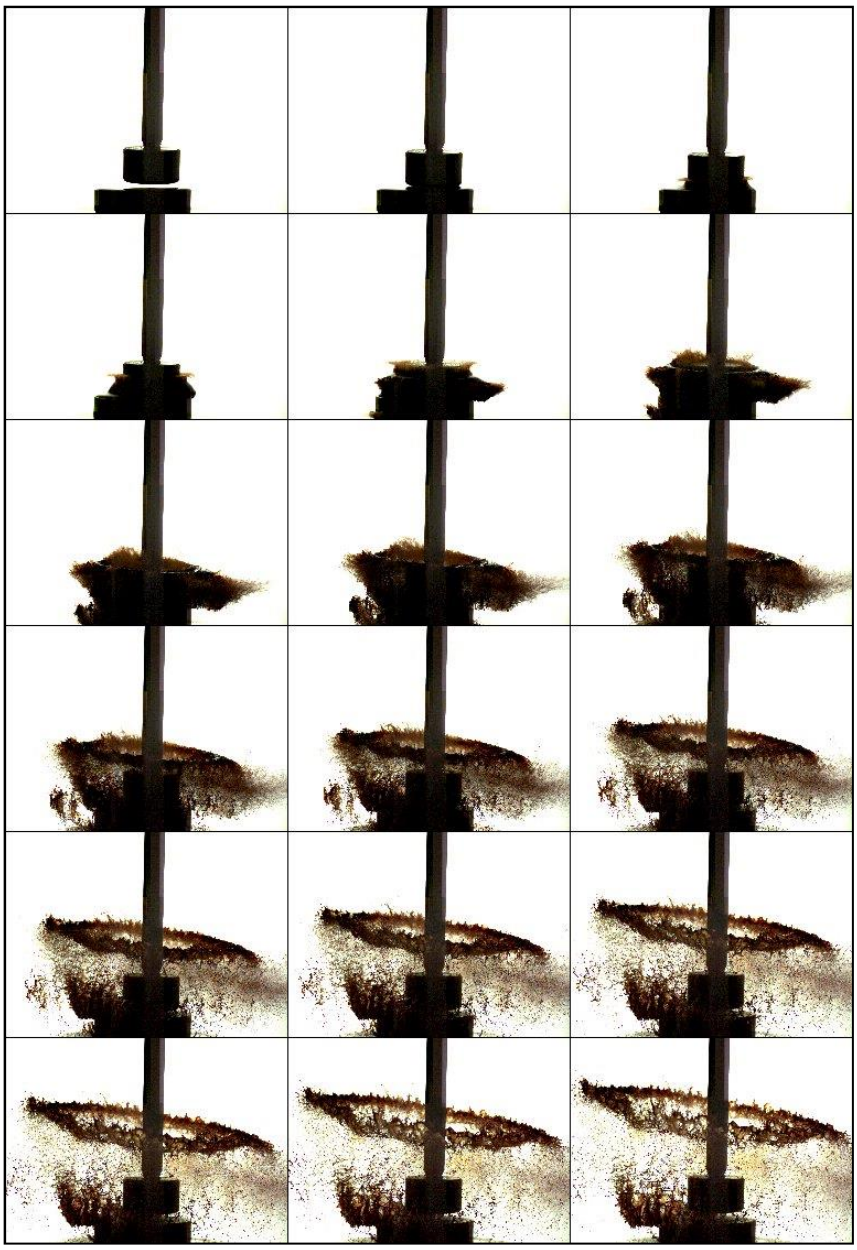

Figure 4.19. Rod with hammer head simulant impact onto a 2 ml pool of blood on a polyurethane target. The time interval between each image frame was 0.19 ms. The hummer head diameter was 3 cm. The images were about 15x15 cm.

5 Blood drop size in passive dripping

Passive dripping, the slow dripping of blood under gravity, is responsible for some bloodstains found at crime scenes, particularly drip trails left by a person moving through the scene. Previous work by other authors (MacDonnell and de Lige, 1989; Knock and Davidson, 2007 and Hulse-Smith et al. 2005, 2007) has established relationships, under ideal conditions, between the size of the stain, the number of spines and satellite stains, the roughness of the surface, the size of the blood droplet and the height from which it falls. To apply these relationships to infer the height of fall requires independent knowledge of the size of the droplet. This work aimed to measure the size of droplets falling from objects representative of hand-held weapons.

Balthazard et al. (1939) recognized that the volume of a drop was a crucial parameter in determining the size of a drip stain but did not attempt to quantify this relationship. The authors focused their study on the relationship between the stain size and drop velocity.

MacDonell and Bialousz (1971) and MacDonell (1982) originally proposed the concept of a "normal" or "typical" drop with a volume of 50 µL, based on the volume of a drop from a laboratory pipette or burette. In contrast, Pizzola et al (1986) suggested that drop size (and hence volume) is a function of the geometry of the surface from which the drop falls and its wettability.

Gardner (2006) claimed that there is an upper limit to the size of a drop based on the maximum size of a "stable free flight droplet" which he states is 5.5 mm in diameter. Laber (1985) asserted that there is no standard volume that can be assigned to a free falling drop of blood. He produced data that indicated that the volume of the falling drop is dependent on the nature of the object from which it has dripped, varying from less than 13 µL (human hair) to 160 µL (terry cloth). In contrast to Laber's findings, Wonder (2001) claimed that drops falling from absorbent surfaces will be smaller than those from non-absorbent ones but does not present any data to support this.

In a systematic but unpublished study, Parker et al. (1982) also showed that the volume of a blood drop was dependent on the nature of the surface from which the blood dripped. They produced blood drops ranging in volume from 42 µL (eye dropper) to 87 µL (pre-wetted palm of the hand). They showed that the use of anti-coagulant CPDA-1 reduced the

volume of a drop by about 10%, whereas lowering the temperature of the blood from 37 ˚C to a room temperature of 22 ˚C increased drop volume by about 5%, the latter being potentially relevant to blood dripping from an object. Furthermore they found that drop volume was also affected by flow rate, with larger drops forming under higher flow rates. However the authors pointed out that for drop volumes of 70 µL or greater there was a tendency to form what they termed "satellite" drops. This meant that drop volumes determined by the volumetric method they used tended to be overestimated. Ross (2006) looked at a range of objects that could be used as weapons and showed that drop volumes varied from 30 µL (small kitchen knife) to 210 µL (hammer). She also used a volumetric method and noted the presence of what she termed "follow-on" drops, especially for objects with a larger surface area in the dripping region. The results, in addition, were influenced by the varying flow rate of dripping from weapons dipped into blood.

MacDonnell and de Lige (1989) sought to develop a relationship that would enable the volume of a blood drop to be estimated from a bloodstain of known size. For this they produced spattered blood drops in the approximate range 0.6 µL to 55 µL and correlated these to stain sizes in the range 0.7 mm to 14.6 mm. However there was no consideration given to the impact velocity of the drops, which will affect the stain spreading. The authors defended the MacDonell and Bialousz's concept of a normal or typical drop but conceded that "pointed instruments" such as knives can produce a smaller volume drop, which they attributed to the lower (wetted) surface area of these objects.

Rogers (2009) produced evidence that suggests that blood drop volumes depend on blood hematocrit. She found that drip stain widths and lengths decreased by about 16% as the hematocrit was increased from 34 to 50, a relevant range for healthy humans.

Knock and Davidson (2007) and Hulse-Smith et al. (2005, 2007) showed that under well-controlled conditions it is possible to calculate the volume and velocity of a drop from the diameter of the stain and the number of spines on the stain margin. The limitations of this include the reproducibility in the counting of spines and the limited number, or even absence, of spines for low velocity impact on some surfaces. An alternative method to determine drop volume would complement this work.

A number of approaches exist to estimate the volume of a drop produced as a result of dripping from a surface. Dripping from the interior of a capillary tube, for example a pipette held vertically, is the basis of the pendant drop method (Harkins and Brown, 1919) in which the surface tension of a liquid is measured by inference from the shape of the hanging drop.

The theory describing the equilibrium shape of a hanging volume of liquid is described by Batchelor (1967). Pozrikidis (2012) studied the stability of pendant drops still attached to an object and determined the limits within which a pendant or sessile drop is stable. Tanasawa and Toyoda (1957) analyzed the dripping of a liquid film on the underside of a flat plate. They calculated the slow development of the pendant drop up to the first break, but their method was not capable of modeling the capillary waves which result and so could not calculate the length of the ligament or the size of the accompanying droplets.

As was mentioned in Chapter 1 Lefebvre (1989) reports an equation (Equation 1.1)

$$d_{drop} = 3.3\sqrt{\frac{\sigma}{\rho g}}$$

for the size of a drop falling from the underside of a flat plate, and references Lapple et al. (1957), who in turn reference Tamada and Shibaoka (1961). However this equation does not appear in Tamada and Shibaoka's paper (1961) or Hida and Nakanishi's paper (1970) and may be a correlation to their data. d_{drop} is the diameter of the drop, σ is the surface tension of the liquid, ρ the density of the liquid and g the acceleration due to gravity.

The purpose of this work was therefore to reconsider the relationship between the volume of a drop formed by passive dripping and the nature of the dripping surface. For this, dripping experiments with non-absorbent surfaces representative of weapons frequently used in criminal assaults were conducted in an attempt to quantify the size of drop formed by passive dripping under controlled temperature, flow rate and blood composition conditions.

High speed imaging was used to directly measure the size of the primary drop and to count accompanying droplets. The results were interpreted in terms of the roughness and curvature of the surface. The results of this study were published in Forensic Science International (Kabaliuk et al., 2013), an international peer-reviewed journal dedicated to the applications of medicine and science in the administration of justice.

5.1 Passive blood drop size and formation features

The primary drop size and number of accompanying droplets formed from objects of different surface curvature and roughness are shown in Figures 5.1a and b. The plots include data from dripping experiments with distilled water and with porcine blood, and error bars are equal to two times the square root of the sum of squares of the instrument error Δ_{in} (one

pixel) and standard deviation of the mean $\bar{S}_n$ multiplied by Student's coefficient $t = 2.2$ for 12 measurements and a 95% confidence interval: $\Delta = \sqrt{(\Delta_{in})^2 + (t\bar{S}_n)^2}$.

The measured drop size correlated to the size of the object from which it dripped. The mean primary drop size, for both distilled water and blood, decreased with the object surface mean curvature over the range 0.1 – 5.25 mm^{-1} (sharper objects), but was relatively constant for the blunt objects tested.

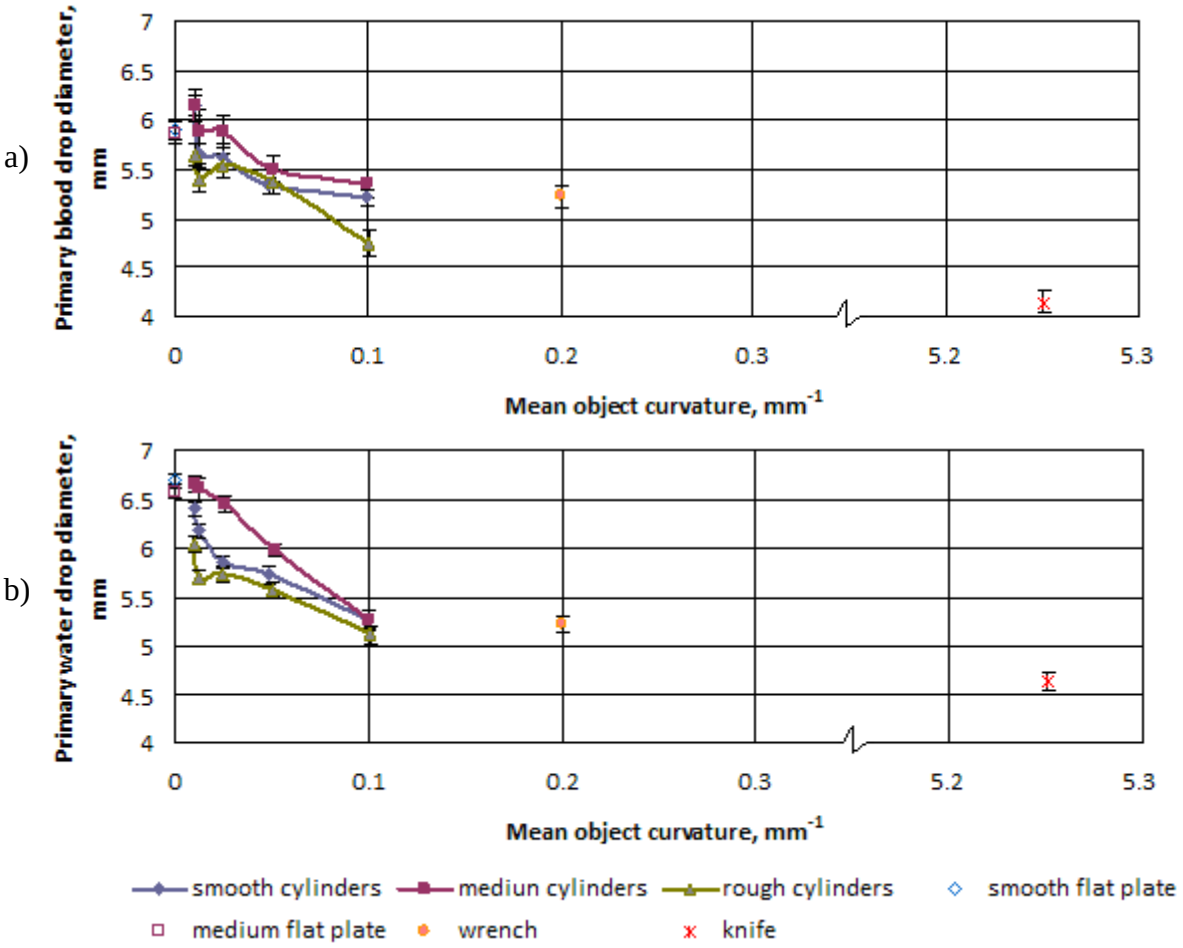

Figure 5.1. Primary drop diameter for (a) porcine blood and (b) distilled water.

The primary water drops tended to be slightly larger than blood drops. The observed range of blood drop diameters was 4.15 ± 0.10 mm (knife) to 6.15 ± 0.17 mm (cylinder with H = 0.01 mm^{-1} and 3.59 µm roughness). This corresponds to drop volumes of between 37.4 µL and 121.8 µL. Water drops varied in diameter from 4.63 ± 0.10 mm (knife) to 6.68 ± 0.05 mm (flat plate, 0.37 µm rough). This corresponds to drop volumes of between 52.0 µL and 156.1 µL. Blood drops tended to be more variable in size than water drops for a given object.

Primary drop size correlated weakly with object roughness over the roughness range studied, both for water and for blood. In particular, the maximum observed deviation in mean drop diameter due to difference in roughness of a particular sample was 0.9 mm for blood and 0.6 mm for water.

However, the obtained data showed a slight increase in the mean primary drop size as the object's roughness increased from 0.4 μm (smooth samples) to 6.3 μm (medium samples). A further increase in roughness to about 12 μm led to a decrease in drop size. This was seen in both water and blood data. The influence of surface roughness on the drop size tended to be more pronounced for water.

The number of accompanying water and blood droplets decreased with the object surface curvature (from blunt to sharp weapons), but the trends were not clear because of the high variability in the data (Figures 5.2a and b). No statistically significant correlation with the surface roughness was observed.

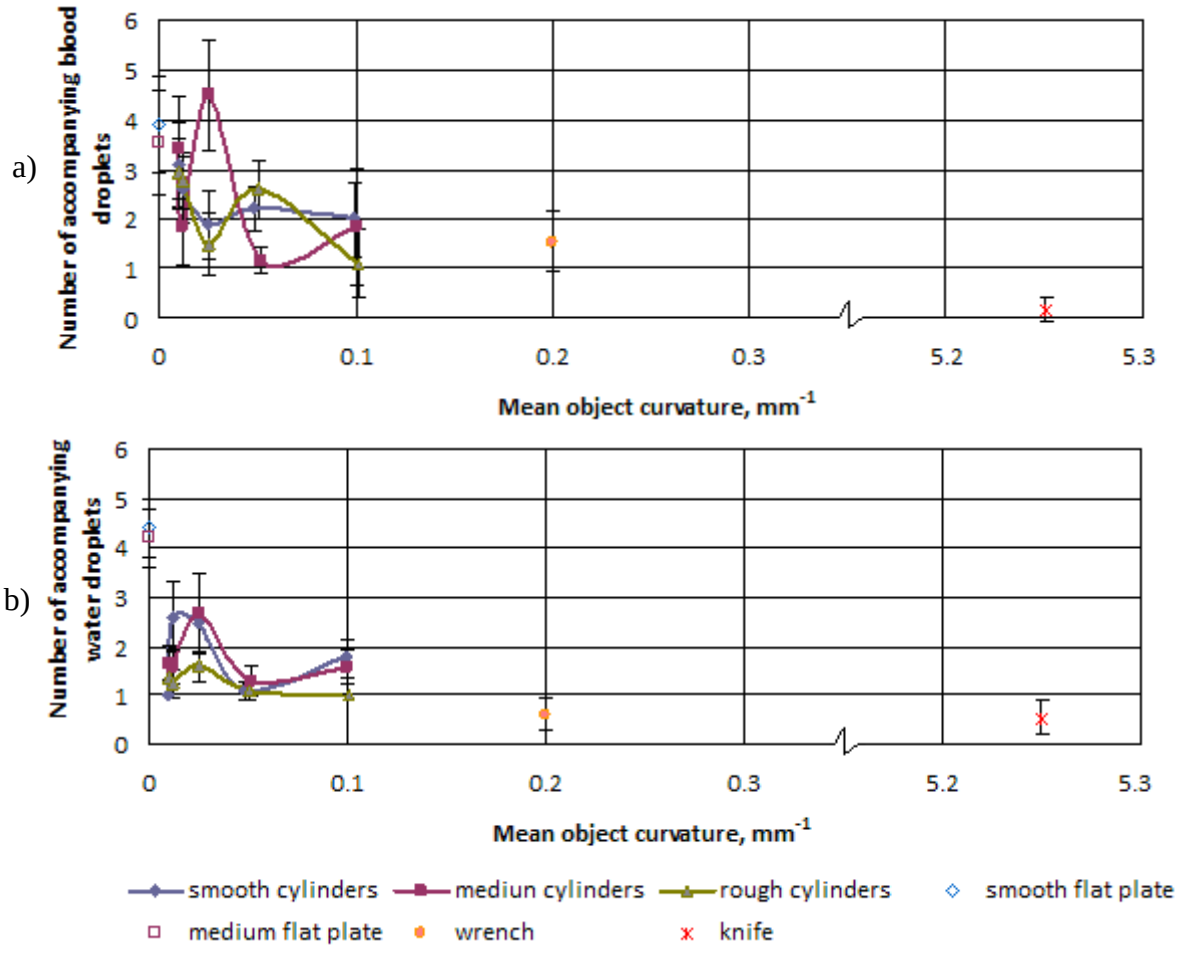

Figure 5.2. Number of accompanying (a) porcine blood and (b) distilled water droplets formed from the studied objects.

Blood was observed to produce a slightly higher number of accompanying droplets compared to water.

The process of passive blood drop formation differed from the formation of water drops and seemed to be more complex and variable. For both liquids, the process began with the slow formation and growth of a pendant drop at the lowest point of the object under the action of gravity. A drop with the critical weight then started to fall, but remained connected to the volume of liquid adhering to the object surface (residual liquid) by a liquid neck. The neck then elongated forming a thin ligament.

With water, uniform axisymmetric cylindrical ligaments were observed in all test cases. The water ligament when narrow enough broke up first at the bottom near the primary drop (Figure 5.3a). The surface tension force at the drop's ligament highly curved lower end pulled it upward (Figure 5.3b). Surface instabilities (waves) occurred, grew and propagated upward and eventually reached the upper end of the ligament. The ligament then broke off from the residual liquid at the top and contracted vertically into one or more accompanying (or satellite) droplets (Figures 5.3c and d). These oscillated in shape and occasionally collided or bounced from each other and moved with different velocities and trajectories.

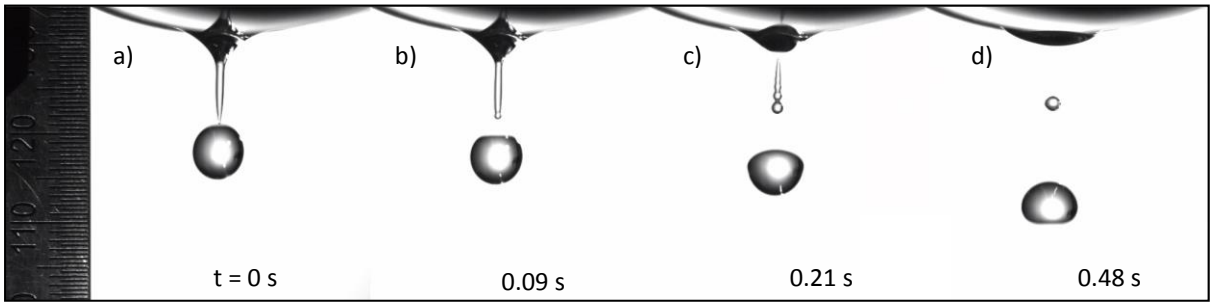

Figure 5.3. Dripping of water from the cylindrical object with H = 0.013 mm^{-1} and 2.4 μm surface roughness. Smallest scale division is 0.5 mm.

For the case of the dripping of blood, ligaments generally had non-uniform (stepped) shapes (though they are axis-symmetric). A number of liquid bulges (satellite beads) could be distinguished in the ligament body (Figure 5.4a).

The blood ligament narrowed with time and underwent several fragmentation phases. It occasionally ruptured firstly either at its lower end just near a primary drop or, more frequently, anywhere in the lower part of its body leaving a fragment attached to a primary drop (Figures 5.4b, f and g). It should be noted, however, that in several cases the initial blood ligament was observed to break first at the upper end or in the middle. The detached primary drop tended to merge with the adjacent ligament fragment while moving downward.

The ligament could subsequently break in one or more places along its length.

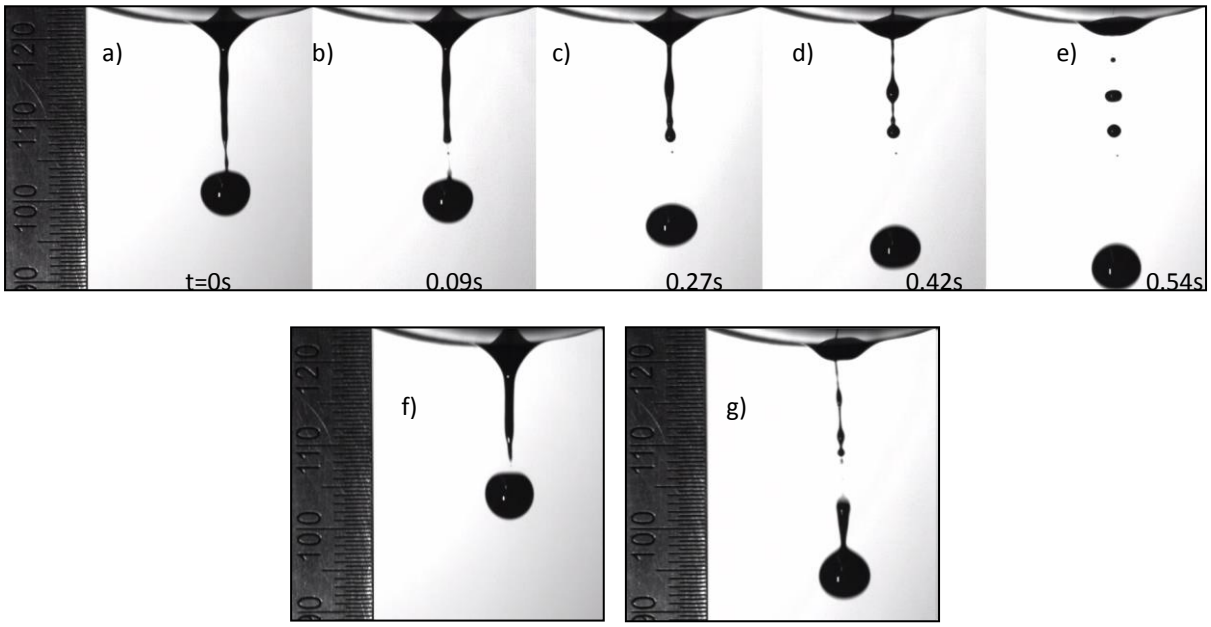

Figure 5.4. Dripping of porcine blood from the cylindrical object with H = 0.013 mm^{-1} and 2.4 μm surface roughness. (b), (f) and (g) are observed variants of the primary drop detachment. The smallest scale division is 0.5 mm.

Finally, the ligament ruptured close the residual liquid (the liquid which remained attached to the object). The size of the ligament fragment remaining connected to the residual liquid after the detachment varied from case to case. It was generally drawn back into the residual liquid.

Just prior to ligament breakup, thin threads were formed at the point of rupture which then produced one or more small droplets. Following this, the fragments of the ligament contracted into accompanying droplets (Figure 5.4c - e). Occasionally, one drop was seen to bounce off another. This is a recognized phenomenon which occurs over a certain range of Weber numbers and impact parameter (Qian and Law, 1997).

The fragmentation process seemed to differ for ligaments of different lengths. In particular, shorter ligaments, as seen during dripping from a knife, tended to rupture in only one or two places and subsequently produced fewer accompanying droplets (Figure 5.5).

It was observed that longer ligaments were formed on larger objects, both for water and blood. However, blood ligaments tended to be longer than those of water.

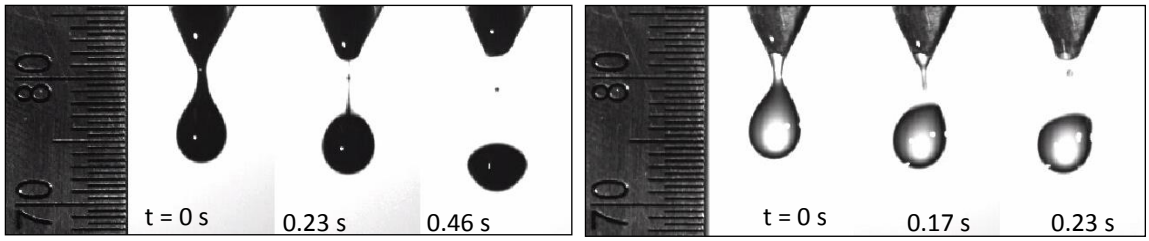

Figure 5.5. Porcine blood and distilled water dripping from a knife tip. Smallest scale division is 0.5 mm

Once separated from the ligament, primary blood and water drops continued to fall and experienced shape oscillations which damped with time. The amplitude of the oscillation seemed to depend on the way the drop was formed. The frequency of oscillation is known to depend on drop volume and surface tension and the rate of damping on viscosity (Raymond et al., 1996). In the present work blood drop oscillations were observed to damp more quickly than water drops.

5.2 Effects of object size, surface texture and dripping liquid physical properties

5.2.1 Effect of object size

The formation of larger primary drops from the less curved objects can be understood in terms of the increase in an available wetting area (Figure 5.6). On an object of greater radius of curvature, the edges of the suspended mass lie at an angle closer to the horizontal (and the vertical component of the surface tension force is smaller), unless the suspended mass extends further around the object.

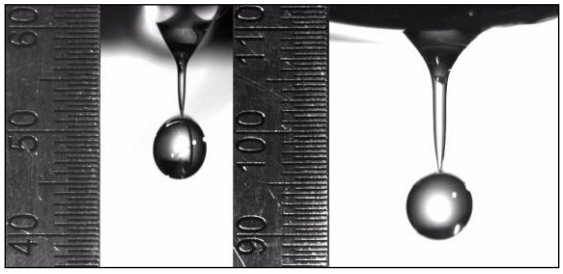

Figure 5.6. Dripping of water from (a) the cylinder with H = 0.1 mm^{-1} and 0.66 μm surface roughness and (b) form the cylinder with H = 0.01 mm^{-1} and 0.19 μm surface roughness. The smallest scale division is 0.5 mm.

The greater wetted area leads to an increase in total interfacial tension forces between the liquid and object surface which in turn can support a greater mass of liquid before it detaches. In addition, more liquid is available to flow into the ligament body as it extends, producing a large number of accompanying droplets. This effect, however, is not pronounced, possibly due to the low rate of liquid inflow.

5.2.2 **Effect of liquid properties**

The higher surface tension of water is believed to be responsible for the larger primary water drops in comparison to blood (see for example Zhang and Basaran (1995)). The higher surface tension of water supports a greater mass of liquid before the droplet separates.

The variability in the number of accompanying drops may be explained by the viscosity of the liquid. In particular, the higher viscosity of blood, especially at the low shear rates which occur in the dripping process, slows the liquid as it flows axially along the ligament. In addition, viscous forces damp capillary waves, stabilizing the ligament. Because of this blood ligaments tend to be longer and more uniform in diameter at the time of breakup, compared to water ligaments which have lower viscosity. This consequently leads to the formation of a slightly greater number of accompanying droplets as a result of the breakup of the longer blood ligaments.

It may be hypothesized that, due to the high elongational stresses generated during the evolution of the ligament, the viscoelastic nature of blood properties becomes apparent. The observed shape of the blood ligament with a number of liquid bulges on it may be associated with this viscoelasticity (Thurston, 1972). Similar structures were observed during the detachment of drops of dilute aqueous solutions of high molecular weight polymers exhibiting viscoelastic (with elevated elongational viscosity) behavior by Wagner et al. (2005). Alternatively, these bulges may simply be capillary waves on the surface of the ligament.

The main drop size does not seem to be influenced by the fluid viscosity since the velocity gradients during the drip formation process are low. However, the variability in the observed main blood drop sizes may be related to the variability of the ligament fragmentation process. Notably, whether the ligament first breaks up near the end where it joins the primary drop, or closer to the object. The latter case implies an increase in the drop volume due to merging with the attached ligament fragment.

A study of the motion and breakup of ligaments of liquids with different viscosities by Handerson et al. (2000) proposed a criterion for a ligament breakup/pinch off location based

on the growth rate of disturbances with various wave numbers. In short, a ligament breaks up in one or more interior points if the wavelength of the most unstable wave mode is shorter than the ligament length. The breakup occurs at the ends when the wavelength is approximately equal to the ligament length.

The complexity of the blood ligament formation, elongation and fragmentation invites further investigation.

EDTA used to prevent blood coagulation in this study was observed previously to increase blood density, viscosity and surface tension of blood by about 2% (Williams, 2014). This might have caused a slight increase in the sizes of primary blood drops and formation of longer blood ligaments and, consequently, more satellite droplets.

The detailed study of the influence of different anticoagulants of physical properties of blood will be addressed in future publications of this research group.

5.2.3 **Effect of surface roughness**

The role of the unidirectional texturing of the machined objects, meaning a complex periodic surface structure of parallel peaks and valleys, in the drop formation process can be elucidated considering the wetting phenomenon. A static or equilibrium angle between the solid-liquid interface and the liquid-air interface at the point of contact, called the contact angle θ (Figure 5.7), is used to quantitatively describe wetting and is defined by the Young-Dupre equation (Young, 1805 and 1855; Dupré, 1869 and Adamson, 1936).

The static contact angle on a rough surface generically differs from the contact angle θ_0 on an ideal (flat, rigid, smooth and chemically homogeneous) surface. In addition there is contact-angle hysteresis on non-ideal surfaces, defined as the difference between the advancing θ_a and receding θ_r contact angles during the dynamic wetting (Figure 5.7).

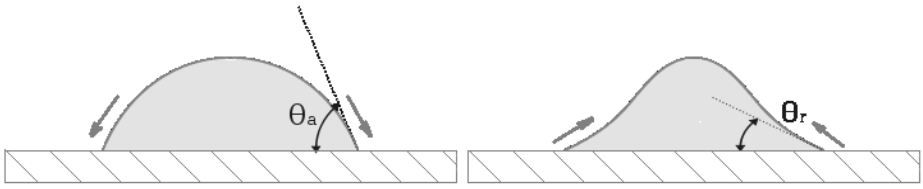

Figure 5.7. Diagram of advancing θ_a and receding θ_r contact angles.

Liquid can wet a rough surface by filling in the troughs between the surface asperities (Wenzel, 1936).

Assuming that the surface roughness scale is insignificantly small compared to the dimensions of the liquid-solid contact area, the apparent contact angle is believed to depend

on the ratio of actual to projected wetted area, called the roughness ratio, and increases with roughness if $\theta_0 > 90º$. Whereas, for $\theta_0 < 90º$ it decreases with roughness compared to the contact angle on the smooth surface (Good, 1952 and 1992).

This implies that hydrophobic surfaces become more hydrophobic, while hydrophilic surfaces become more hydrophilic when microtextructured. Consequently the liquid tends to spread more easily and cover larger areas on a rough hydrophilic surface.

The stainless steel used for the test objects has a high surface energy and exhibits hydrophilic properties where $\theta_0 < 90°$, which indicates its high degree of wettability by water (Thongyai, 2005 and Kim et al., 2010). The observed contact angles on the flat plate samples tested were $\theta_0 < 90°$.

From the present data, it is suggested that an increase in the area (and perimeter) covered by the liquid (caused by the decrease in contact angle) on roughening leads to an increase in the interfacial forces which in turn support larger liquid drops on rougher objects than on smoother objects.

In some cases (if the contact angle is large and the surface sufficiently rough), however, a thin layer of gas can be left between the liquid and solid surface (Cassie and Baxter, 1944 and Cassie, 1948). Such a system must be largely hydrophobic with relatively high contact angles, and is unlikely in the present system.

Asperities on rough surfaces could pose significant barriers for a liquid flow especially if the roughness scale is relatively high (Shuttleworth and Bailey, 1948; Johnson and Dettre, 1969; Huh and Mason, 1977; Eick et al., 1975 and Hitchcock et al., 1981). This results in the pinning of a contact line and an increase in an advancing contact angle depending on the slope of the surface asperities/roughness at the liquid perimeter (α) for both roughened wetted and non-wetted surfaces (Figure 5.8).

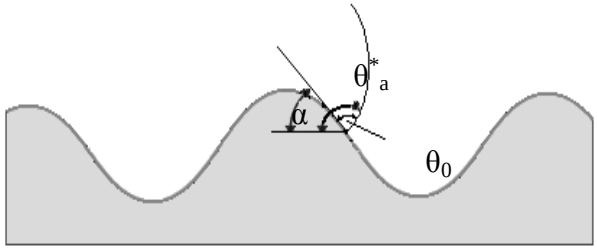

Figure 5.8. The increase in advancing contact angle θ^*_a due to the surface asperity slope α.

This effect may explain the formation of the smallest passive drops from the rough objects tested as a result of the reduction in the interfacial forces proportional to a decrease in

the liquid-solid contact perimeter which accompanies a decrease in the contact angle on a sufficiently rough surface.

However, the size of the primary drops varies little with roughness value (R_a) suggesting only slight alteration of the available for wetting area (and perimeter) over the roughness range studied.

It should be noted that the influence of the surface texture on wetting is not limited to the effects of surface roughness (R_a) only, but the process may be influenced by other topological characteristics, for example, by the orientation and form of the roughness asperities (Neumann and Good, 1979).

The present results are for a flow rate of 0.1 ml/s only and the effect of varying flow rate would benefit from future study. Temperature and surface tension gradients, pressure fluctuations, air currents and evaporation may also affect drop formation mechanism, possibly inducing variability in resulting drop sizes, but this is expected to be small in the present study.

In summary, blood drops with volumes of between 37.4 µL (knife) and 121.8 µL (cylinder with H = 0.01 mm^{-1} and 3.59 µm roughness) were observed. Higher number of accompanying droplets was produced with dripping blood than water. The primary drop size was relatively insensitive to the size of the object if the mean curvature of its surface was smaller than 0.10 mm^{-1}. Surface roughness influenced drop size and number of accompanying droplets only weakly over the hydrophobicity and the range of roughnesses studied. The effects of such factors as dripping flow rate, temperature, dripping object movement and wettability and blood composition on blood drop formation should, however, also be considered.

6 Blood drop flight modeling

Bloodstain Pattern Analysis (BPA) is the analysis of the position, distribution, size and morphology of the stains present at the crime scene, which may provide information about the events that gave rise to the bloodshed such as the wounding mechanism, position of assailant and victim at the moment of wounding, characteristics of the weapon used, etc. (Bevel and Gardner, 2008).

If two or more trajectories of the drops produced the stains can be determined, the point at which they cross is the probable location of the victim at the time the wound was inflicted.

In order to accurately predict the trajectory (flight path) of a drop, and therefore its origin, the initial state of the drop (size, shape and velocity) must be known and the forces acting during flight should be considered.

Depending on its mode of formation, when a drop is formed, it may be nonspherical, and experience shape oscillations under the influence of surface tension. Drop oscillations are damped exponentially in time by the drop fluid viscosity (Rayleigh, 1878; Raymond, 1995 and Gardner, 1998).

As the droplet travels through air it experiences inertial, gravitational and aerodynamic drag forces. The latter is proportional to drop projected area (the area facing the incident flow), the drag coefficient and the dynamic pressure exerted by the external fluid (air) flow.

Although surface tension forces at the free surface tend to minimize the drop's surface energy and shape it into a sphere having the smallest possible surface area, when subject to external fluid flow a drop deforms to balance normal and shear stresses on its surface (Clift, Grace and Weber, 1978). The level of drop deformation depends on the intensity of the deforming aerodynamic force.

Alteration of drop shape changes its drag properties. Distortion toward an oblate shape increases the projected area and drag coefficient (relative to the case of a spherical drop of the same volume). This may lead to a significant drop trajectory alteration (Luxford, 2005), which is of importance to the point of origin determination.

At certain critical conditions a drop may reach an ultimate deformation, a so-called 'liquid disc', and further deform into a hollow sphere or bag, a hollow sphere with a jet or

exhibit more irregular deformation and finally disintegrates (or breakup) into smaller 'child' drops (Krzeczkowski, 1980 and Hsiang-Faeth, 1995).

Currently, area (or volume) of origin estimation is only done with drops which are thought to have followed a straight trajectory, but 1) it has not been satisfactory determined which drops have followed sufficiently straight trajectory and 2) there is an interest in using other drops which have followed curved trajectories to extract more information. A tool is needed to predict trajectories so that knowledge about which drops can be used in area (or volume) estimation, and which cannot, may be extracted.

This raises two questions: 1) Under typical crime scene conditions, do the deformation and oscillation of blood drops appreciably affect their trajectory including, of importance to Bloodstain Pattern Analysis, the maximum distance a drop may have travelled and the impact angle? 2) Is mid-air breakup into smaller drops possible in typical crime scene conditions?

These issues was addressed by developing and validating a numerical code for accurate and detailed blood drop flight modeling with special attention to blood drops produced as a result of passive dripping, cast-off and impact. Numerical simulation, as a reliable and non-laborious method for understanding and predicting the flight characteristics of spatter drops, was used.

This chapter describes the development of a numerical scheme to accurately predict blood drop behaviour during flight. The proposed scheme incorporated the effects of inertial, gravitational and aerodynamic drag forces on drop flight as well as the variation in drag force as a result of shape oscillations and deformation due to aerodynamic forces. The most likely mechanisms of drop breakup during flight were also included in the scheme.

The proposed scheme could predict drop flight characteristics and paths in both 'forward' (from the drop origin till its impact on a surface) and 'backward' (from the drop position on the target surface to its origin) modes, and in both 2D and 3D cases. Among the output parameters are drop 3D coordinates and velocity along the flight trajectory, impact angle and velocity, range and height of drop flight and levels of drop deformation.

To compute the trajectory of a drop, time was divided into steps (typically 10^{-3}-10^{-5} s), the forces on the drop (including gravity, air resistance and buoyancy) were estimated at each timestep, the distance moved and velocity change during the timestep calculated, droplet position and speed updated before the next time-step.

6.1 Equation of drop motion and numerical solution

Blood drops were modelled using a Lagrangian approach, by applying Newton's Second Law to an individual drop travelling through air with density ρ_{air}:

$$m\vec{a} = \vec{F}_g + \vec{F}_b + \vec{F}_D . \tag{6.1}$$

Here $m = \frac{\pi}{6} d_0^3 \rho$ is a mass of a blood drop with density ρ and equilibrium (undistorted) diameter d_0. $\vec{F}_g = m\vec{g}$, $\vec{F}_b = \frac{\pi}{6} d_0^3 \rho_{air} \vec{g}$ and $F_D = -\frac{1}{2} C_d A \rho_{air} \vec{V}_{rel}^2$ are gravitational, buoyancy and air resistance forces respectively.

The buoyancy force is negligible, for blood drop in air, but was nevertheless included. $A = \frac{\pi}{4} d_0^2$ is the drops projected area that faces the flow, and $C_d = f(\mathrm{Re})$ is its drag coefficient as a function of Reynolds number ($\mathrm{Re} = \frac{V_{rel} d_0}{\nu_{air}}$).

$\vec{V}_{rel} = \vec{v} - \vec{u}$ is the relative drop velocity (relative to the air), where $\vec{u}$ is the incident (free) stream velocity and $\vec{v} = (v_x, v_y, v_z)$ is the drop intrinsic velocity with the angle to *x*-, y- and z-axes α ($\alpha = arctg \frac{v_y}{v_x}$ in a 2D case), β and γ respectively so that $\cos\alpha = \frac{v_x}{|\vec{v}|}$, $\cos\beta = \frac{v_y}{|\vec{v}|}$ and $\cos\gamma = \frac{v_z}{|\vec{v}|}$. $\vec{v}_0 = (v_{0x}; v_{0y}; v_{0z})$ is the initial particle velocity with initial velocity inclination angles α_0, β_0 and γ_0 (see Figure 6.1).

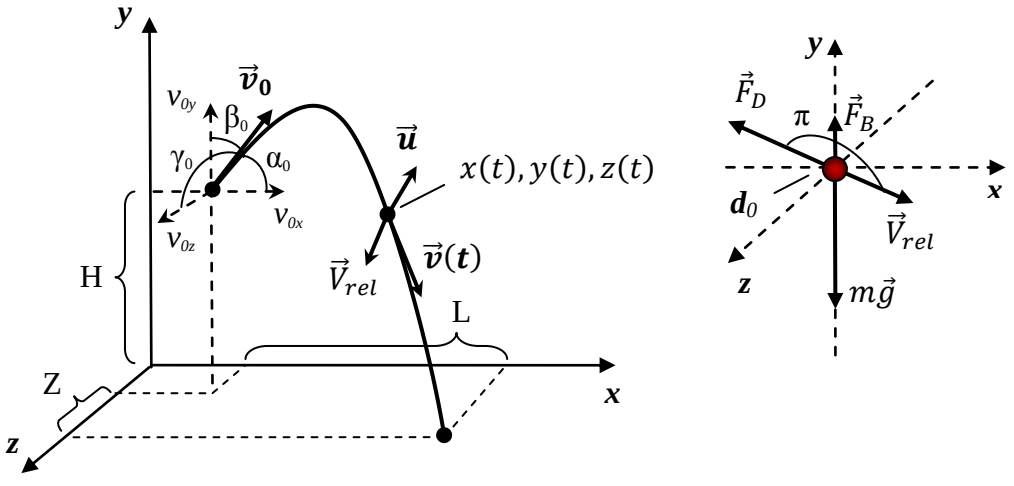

Figure 6.1. Drop trajectory segment (left) and force balance diagram (right). L, H and Z are the lengths of drop trajectory along *x*-, y- and z-axes.

For the 3D components of drop acceleration Equation 6.1 gives the following:

$$a_x = \frac{dv_x}{dt} = -\frac{1}{2m} C_d A \rho_{air} \frac{V_{relx}}{\left|\vec{V}_{rel}\right|}, \tag{6.2}$$

$$a_y = \frac{dv_y}{dt} = -\frac{g\left(\rho - \rho_{air}\right)}{\rho} - \frac{1}{2m} C_d A \rho_{air} \frac{V_{rely}}{\left|\vec{V}_{rel}\right|} \tag{6.3}$$

$$\text{and } a_z = \frac{dv_z}{dt} = -\frac{1}{2m} C_d A \rho_{air} \frac{V_{relz}}{\left|\vec{V}_{rel}\right|}. \tag{6.4}$$

In general, for a particle during its accelerating (transient) motion, the additional virtual mass force and Bassett history force should also be considered (Michaelides, 2006). However, due to the relatively high density ratio of blood (or water) to that of air ($831 < \rho/\rho_{air} < 880$) the virtual mass term was neglected. The Basset history term, however, is not generally negligible due to its complexity, difficulty in implementation and more pronounced effects for the movement at high acceleration it was not considered. Evaluation of the magnitude of Basset force in different multiphase flow applications can be found in (Liang and Michaelides, 1992). Liang and Michaelides (1992) found that the Basset force may be neglected in the particle equation of motion only when the fluid to particle density ratio is very high (gas bubbles in liquids) and the particle diameter is greater than 1 μm. Due to its complicated form and the difficulty of its implementation it is often neglected. However, for movement with high acceleration the Basset term can exceed the Stokes' term as much as a factor of two. The Basset term was neglected for this study of blood drop flight due to relatively low-to-moderate drop accelerations associated with blood spatter generation.

For a 2D case of drop motion the set of the first-order ordinary differential equations (ODEs) for drop velocity components (Equation 6.2, 6.3 and 6.4) in a form

$$\frac{dv_x}{dt} = f\left(t, v_x(t), v_y(t)\right),$$

$$\frac{dv_y}{dt} = g\left(t, v_x(t), v_y(t)\right), \text{ where } v_x(0) = v_{0x},\ v_y(0) = v_{0y},$$

were solved numerically at each time step using fourth-order Runge-Kutta algorithm implemented in the C++ programming language.

The numerical solution was found in a form:

$v_x^{n+1} = v_x^n + k$, $v_y^{n+1} = v_y^n + l$, with $k = \frac{1}{6}(k_1 + 2k_2 + 2k_3 + k_4)$, $l = \frac{1}{6}(l_1 + 2l_2 + 2l_3 + l_4)$, where

$k_1 = \Delta t \cdot f(t^n, v_x^n, v_y^n)$, $l_1 = \Delta t \cdot g(t^n, v_x^n, v_y^n)$,

$k_2 = \Delta t \cdot f\left(t^n + \frac{\Delta t}{2}, v_x^n + \frac{k_1}{2}, v_y^n + \frac{l_1}{2}\right)$, $l_2 = \Delta t \cdot g\left(t^n + \frac{\Delta t}{2}, v_x^n + \frac{k_1}{2}, v_y^n + \frac{l_1}{2}\right)$,

$k_3 = \Delta t \cdot f\left(t^n + \frac{\Delta t}{2}, v_x^n + \frac{k_2}{2}, v_y^n + \frac{l_2}{2}\right)$, $l_3 = \Delta t \cdot g\left(t^n + \frac{\Delta t}{2}, v_x^n + \frac{k_2}{2}, v_y^n + \frac{l_2}{2}\right)$,

$k_4 = \Delta t \cdot f(t^n + \Delta t, v_x^n + k_3, v_y^n + l_3)$, $l_4 = \Delta t \cdot g(t^n + \Delta t, v_x^n + k_3, v_y^n + l_3)$

with time discretization $t^{n+1} = t^n + \Delta t$, $n \in (0, N)$ and timestep $\Delta t = \frac{T}{N}$, here T was total time of simulation and N represented a total number of computational timesteps n.

The same routine was employed to find the solution of the equations for the drops Cartesian coordinates $\frac{dx}{dt} = v_x$, $\frac{dy}{dt} = v_y$ in a form $x^{n+1} = x^n + k$, $y^{n+1} = y^n + l$, where

$k = \frac{1}{6}(k_1 + 2k_2 + 2k_3 + k_4)$ and $l = \frac{1}{6}(l_1 + 2l_2 + 2l_3 + l_4)$ with $k_1 = \Delta t \cdot v_x^n$, $l_1 = \Delta t \cdot v_y^n$;

$k_2 = \Delta t \cdot \left(v_x^n + \frac{k_1}{2}\right)$, $l_2 = \Delta t \cdot \left(v_y^n + \frac{l_1}{2}\right)$;

$k_3 = \Delta t \cdot \left(v_x^n + \frac{k_2}{2}\right)$, $l_3 = \Delta t \cdot \left(v_y^n + \frac{l_2}{2}\right)$; $k_4 = \Delta t \cdot (v_y^n + k_3)$, $l_4 = \Delta t \cdot (v_y^n + l_3)$.

The computing time required for each simulation was typically 10 s with the time step $\Delta t = 10^{-3}$-10^{-5} s (with solution convergence up to the 5th or 6th decimal digit). For drop oscillations modelling each period of oscillations (T) was represented by at least 100 time steps according to Δt = T/100.

Same numerical method was used to find z-component of drop velocity in a 3D drop motion case.

6.2 Drop in-flight deformation models

The blood drop was considered to deform into an oblate or prolate spheroid (ellipsoid of revolution about its minor or major axes) (Clift, Grace and Weber 1979) when subjected to a deforming aerodynamic force (Figure 6.2).

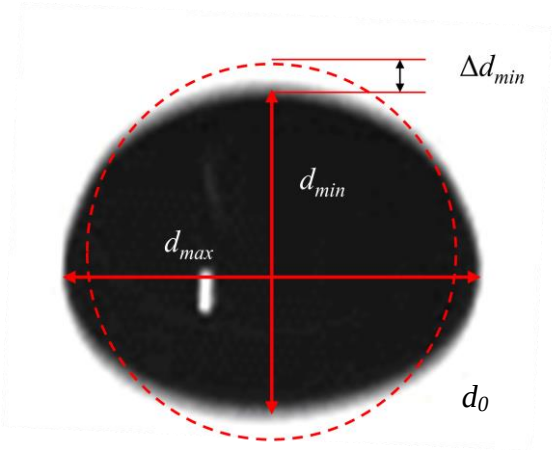

Figure 6.2. Diagram of a deformed drop and its shape at equilibrium.

For a deformed drop with the diameters of major and minor axes of the deformed drop $d_{\max}$ and $d_{\min}$ its volume is $V = \frac{\pi}{6} d_{\max}^2 d_{\min}$. $V_0 = \frac{\pi}{6} d_0^3$ is the volume of an undisturbed drop. From volume conservation considerations (assuming no significant evaporation occurs): $d_0^3 = d_{\max}^2 d_{\min}$.

The aspect ratio of a deformed drop $AR = \frac{d_{\min}}{d_{\max}} = \frac{d_0^3}{d_{\max}^3}$ was used as a measure of its distortion. The cross-sectional (projected) area of a drop, essential for drag force calculations, was also expressed in terms of drop aspect ratio: $A = \frac{\pi}{4} d_{\max}^2 = \frac{\pi}{4} \frac{d_0^2}{AR^{2/3}}$.

The level of drop deformation (and consequently *AR* values) during flight is believed to be influenced by both the intensity and the rate of change of the applied aerodynamic forces. A drop responds differently in the case of slow, gradual loading (as in free fall), compared to sudden or impulsive loading (e.g. shock wave disturbance).

In practice, the aerodynamic loading of the drop varies as its relative velocity changes during accelerated motion. It is, however, unknown what kind of an aerodynamic load a drop experiences as a result of a certain drop formation mechanism and during its decelerated motion.

In this light three alternative subroutines for the modelling of drop distortion during flight were incorporated in the present scheme.

Two of these included correlations for the aspect ratio of a deformed drop at **steady** terminal conditions, when drag force on a drop is balanced by its weight, with either

$$AR = \left[\frac{4}{17} \left(\frac{17Bo}{4} + 1 \right)^{1/2} + \frac{13}{17} \right]^{-3/2} \quad \text{(Green, 1975),}$$

where $Bo = \frac{\rho g d_0^2}{4\sigma}$ is the Bond number based on drop equilibrium number radius $d_0/2$ and drop liquid surface tension σ, or

$$AR = \frac{d_{\min}}{d_{\max}} = \left(1 + 0.07We^{0.5}\right)^{-3} \quad \text{(Hsiang and Faeth, 1995)}$$

with $We = \frac{\rho_a V_{rel}^2 d_0}{\sigma}$.

The models were assumed to be suitable for relatively large drops moving with velocities lower than their terminal velocities (e.g. passive drops) as an extreme case of maximum possible deformation.

It should be noted, however, that the latter correlation was reported to overestimate the deformation during steady disturbance for liquid drops in gases for We < 10 by (Hsiang and Faeth, 1995).

The third model for drop deformation was based on the Taylor Analogy Breakup (TAB) model for low-Weber number sprays (O'Rourke and Amsden, 1987).

The TAB model is based on an analogy between an oscillating and distorting drop and a string-mass system. The droplet distortion is represented as a one-dimensional harmonic oscillation under the deforming aerodynamic force, restoring surface tension force and damping viscous force. The droplet deformation in the direction of flow is expressed in terms of the dimensionless distortion $y = \frac{2\Delta d_{\min}}{d_0/2}$, where $\Delta d_{\min}$ describes the deviation of the minor drop diameter (or the one parallel to the direction of the flow or drop relative velocity) from its undisturbed value d_0 (see Figure 6.2).

The equation of motion of the deformation is

$$\frac{d^2 y}{dt^2} + \frac{4C_d \hat{\mu}}{\hat{\rho} d^2} \frac{dy}{dt} + \frac{8C_k \sigma}{\hat{\rho} d^3} y = \frac{4C_f \rho_a v_{rel}^2}{C_b \hat{\rho} d^2},$$

with the solution in the form

$$y(t) = We_C + e^{-t/t_D} \left\{ (y_0 - We_C) \cos \omega t + \frac{1}{\omega} \left(\frac{dy_0}{dt} + \frac{y_0 - We_C}{t_D} \right) \sin \omega t \right\},$$

where $We_C = We\dfrac{C_f}{C_k C_b}$ based on Weber number $We = \dfrac{\rho_a v_{rel}^2 d}{2\sigma}$, $\omega = \sqrt{\dfrac{8C_k\sigma}{\hat{\rho}d^3} - \left(\dfrac{1}{t_D}\right)^2}$ is a natural frequency of drop oscillations and $t_D = \dfrac{\hat{\rho}d^2}{2C_d\hat{\mu}}$ is the damping time.

C_b, C_d, C_f, C_k are model parameters. $C_b = 1/2$ is the scaling coefficient for deforming force non-dimensionalization, $C_d = 10$ is the dynamic coefficient, $C_k = 8$ is the restoring force coefficient and C_f is the aerodynamic force coefficient.

At shock tube conditions the critical drop deformation ($y \approx 1$) was associated at the critical We number of ~6. For a steady-state solution of $y(t)$ at $t \to \infty$ in a form $y(t \to \infty) = \dfrac{C_f}{C_k C_b} We$ this gives $y \approx 1 = \dfrac{C_f}{C_k C_b} 6$ and, thus, $C_f = 2/3$. Alternatively, at t <<1 drop dimensionless distortion may be expressed as $y(t) = \dfrac{C_f}{C_k C_b} We(1 - \cos \omega t)$, which for critical conditions gives $\dfrac{2C_f}{C_k C_b} 6 \approx 1$ and $C_f = 1/3$ (Schmidt et al., 1999).

The initial values of distortion $y_0 = y(t = 0)$ and distortion rate of change $\left.\dfrac{dy}{dt}\right|_{t=0} = \dfrac{dy_0}{dt} = \dot{y}_0$ are usually taken to be equal zero (Liu et al., 1993).

The drop aspect ratio and projected area were thus expressed as $AR = (1 - 0.5y)^{3/2}$ and $A = \dfrac{\pi d_0^2}{4(1 - 0.5y)}$ respectively.

The important limitation of the TAB model is that only the longest-lived fundamental (spheroidal or prolate-oblate) mode of drop oscillations is accounted for. Other modes may be present and contribute to drop deformation. Despite this, a good agreement between the TAB model prediction and experimental findings for atomization applications has been reported. Several non-linear TAB model extensions have been recently developed by (Schmehl, 2002) and claimed to be more accurate in large drop distortion prediction. These may be used for blood drop applications if higher level of accuracy was required.

6.3 Drag coefficient of a deformed drop

There are a number of possibilities of how to express the drag coefficient as a function of drop shape and Re number (Haider and Levenspiel, 1989; Liu et al., 1993; Schmehl, 2002; Luxford, 2005).

An initially spherical drop in the external flow at critical conditions reaches a maximum deformation when it takes the form of a disk (so-called 'liquid disk'). The drag coefficient of a deformed drop, thus, can be estimated by interpolating between that of a sphere C_D^{Sph} and of a disk C_D^{Disk} (Schmehl, 2002; Luxford, 2005): $C_D = AR \cdot C_D^{Sph} + (1 - AR) C_D^{Disk}$. For a sphere $AR = 1$, whereas, for a thin disk $AR \approx 0$.

The empirical expressions for the drag coefficient of a solid sphere and disk for a wide range of Reynolds numbers from (Clift, Grace and Weber, 1978 and Massey et al., 1989) were used in this study.

Drag coefficient of a rigid spherical particle:

$$C_d^{sph} = \frac{3}{16} + \frac{24}{\mathrm{Re}}, \text{ for } \mathrm{Re} \le 0.01;$$

$$C_d^{sph} = \frac{24}{\mathrm{Re}}\left(1 + 0.3115\,\mathrm{Re}^{(0.82 - 0.05x)}\right), \text{ for } \mathrm{Re} \le 20;$$

$$C_d^{sph} = \frac{24}{\mathrm{Re}}\left(1 + 0.1935\,\mathrm{Re}^{0.6305}\right), \text{ for } \mathrm{Re} \le 260;$$

$$C_d^{sph} = 10^{\left(1.6435 - 1.1242x + 0.1558x^2\right)}, \text{ for } \mathrm{Re} \le 1500;$$

$$C_d^{sph} = 10^{\left(-2.4571 + 2.5558x - 0.9295x^2 + 0.1049x^3\right)}, \text{ for } \mathrm{Re} \le 12000;$$

$$C_d^{sph} = 10^{\left(-1.9181 + 0.637x - 0.0636x^2\right)}, \text{ for } \mathrm{Re} \le 44000;$$

$$C_d^{sph} = 10^{\left(-4.339 + 1.5809x - 0.1546x^2\right)}, \text{ for } \mathrm{Re} \le 338000;$$

$$C_d^{sph} = 29.78 - 53x, \text{ for } \mathrm{Re} \le 400000;$$

$$C_d^{sph} = 0.1x - 0.49, \text{ for } \mathrm{Re} \le 10^6;$$

$$C_d^{sph} = 0.19 - \frac{80000}{\mathrm{Re}}, \ \mathrm{Re} > 10^6 \text{ where } x = \log_{10}\mathrm{Re}.$$

Drag coefficient of a rigid disk perpendicular to the flow:

$$C_d^{disk} = \frac{24}{\mathrm{Re}}, \text{ for } \mathrm{Re} < 1;$$

$C_d^{disk} = 10^{\left(0.00507 - 0.05161x^4 + 0.16082x^2 + 0.01987x^2 - 0.9735x + 1.39573\right)}$ with $x = \log_{10} \mathrm{Re}$ for $\mathrm{Re} \le 2000$ and $x = \log_{10} 2000$ for $\mathrm{Re} > 2000$.

Experimentally obtained drag coefficients of water drops at terminal velocity from Pruppacher and Pitter (1970) and interpolated values are plotted on Figure 6.3 together with the sphere and disk drag coefficients from Clift, Grace and Weber (1978) and Massey et al. (1989). The graph shows good accuracy of the interpolation formula used to predict deformed drop drag coefficient.

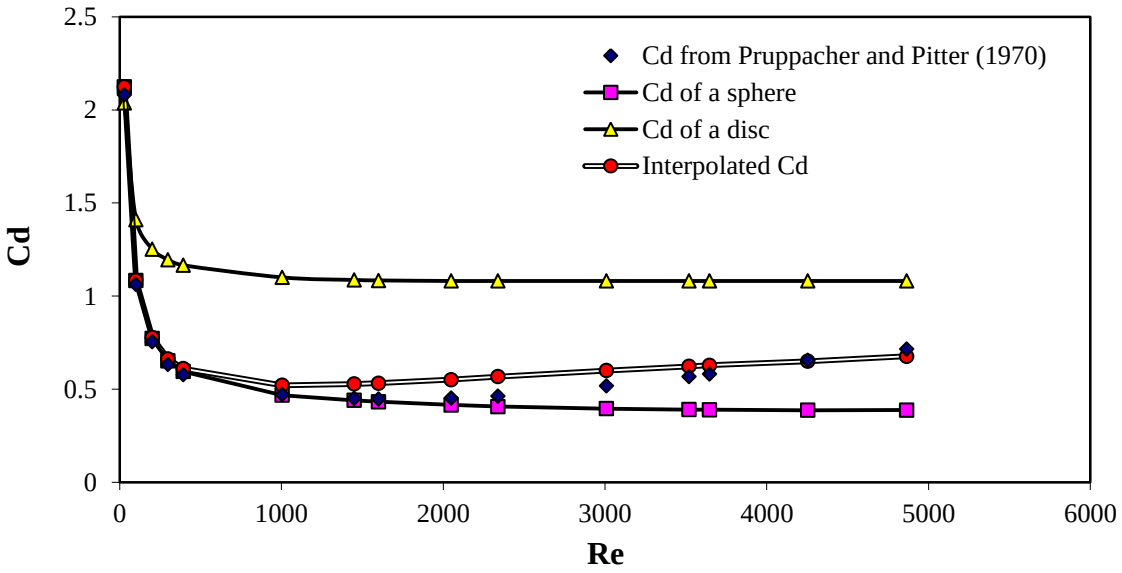

Figure 6.3. Interpolated and experimentally obtained (Pruppacher and Pitter, 1970) drag coefficients for drops at terminal velocities.

6.4 Drop breakup models

As soon as the maximum deformation is reached and the droplet is disk-like a drop may further deform and finally disintegrate into smaller or child drops. Two breakup mechanisms, namely bag and vibrational breakup, are characteristic for typical blood drops with We numbers of < 50 (Figure 6.4).

Bag breakup occurs at critical Weber numbers of $12 \le \mathrm{We} \le 50$. A drop undergoing bag breakup deforms into a hollow bag with a thick rim. The bag breakups into smaller drops first, the rim disintegrates subsequently.

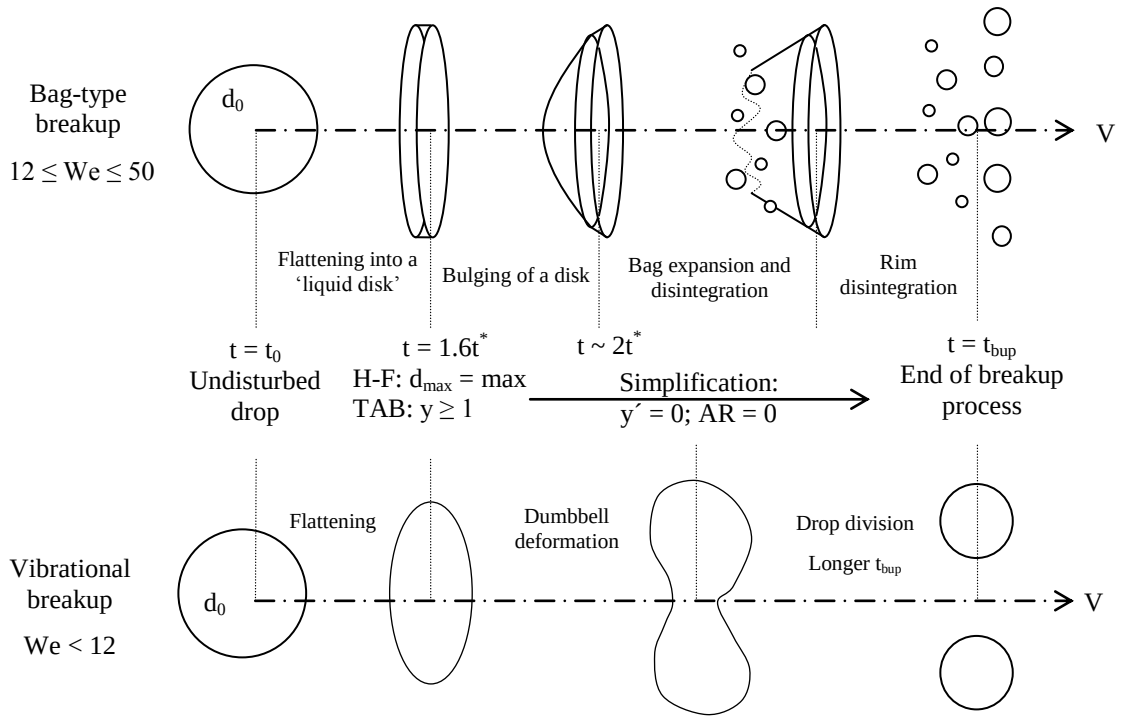

Figure 6.4. Schematic numerical representation of a vibrational and bag breakup of an initially undisturbed drop with diameter d_0.

In some instances at Weber numbers < 12, drop oscillations may trigger breakup. This referred as vibrational breakup. The latter has longer time frames for drop disintegration than other breakup types and does not always occur. Vibrational drop breakup is characterised by a dumbbell-like drop shape and its division into a few relatively large fragments which may subsequently undergo breakup. For this reason vibrational breakup type is generally ignored when secondary drop atomisation is considered (Ashgriz, 2011).

Two alternative models for bag drop breakup modelling were built into the developed numerical scheme to estimate the level of blood drop deformation prior to the breakup.

6.4.1 **Drop breakup model based on (Hsiang and Faeth, 1992 and 1995)**

The first model was based on the experimental findings of Hsiang and Faeth (1992 and 1995) for drops disintegrating after a shock wave disturbance.

In the proposed model a drop was considered to undergo breakup when the droplet Weber number is larger than a critical Weber number $We_{cr} = 12\left(1+1.077Oh^{1.6}\right)$ (Schmehl et al., 2002; Hsiang and Faeth, 1992 and Pilch and Erdman, 1987).

Hsiang and Faeth (1995) suggested that the maximum cross-sectional drop deformation may be approximated as $\frac{d_{\max}}{d_0} = \left(1+0.19We^{0.5}\right)$ (see Figure 6.4). The instantaneous cross

stream drop diameter d_c was estimated as a function of time *t* of drop deformation from the liquid disk distortion up to a drop breakup in a form $d_c = (d_{\max} - d_0) \cdot 0.625 \frac{t}{t^*} + d_0$, where $t^* = \frac{d_0}{V_{rel}} \sqrt{\frac{\rho}{\rho_a}}$ is the characteristic time of drop breakup for *Oh* < 0.1. It was assumed that the maximum drop deformation is reached at $t_i = 1.6t^*$. After that, a drop could undergo further irregular deformation (into a liquid bag, for example) and finally disintegrate. The time of drop breakup t_{bup} from the beginning of the deformation to drop's final disintegration was represented as $t_{bup} = t^* \cdot 6(We - 12)^{-0.25}$ for $12 \le We < 18$ and $t_{bup} = t^* \cdot 2.45(We - 12)^{0.25}$ for $18 \le We < 45$ at $Oh \le 1$ (Pilch and Erdman, 1987).

The deformed drop aspect ratio and projected area were $AR = \frac{d_0^3}{d_c^3}$ and $A = \frac{\pi}{4} d_c^2$ respectively. Thus the model allowed to estimate the instantaneous drop deformation after the critical for drop breakup condition had been met, hence allowing a prediction of when final breakup occurs.

For bag-type breakup, at 12 ≤ We ≤ 50, actual drop disintegration was expected to occur anytime in the second half of the interval from t_i to t_{bup} (Pilch and Erdman, 1987). In the numerical implementation of the model, a random time of breakup in a characteristic time frame was calculated using random number generator rand() in C++.

The final drop cross-sectional diameter was calculated subsequently. Using this distortion value a final drop velocity and coordinates were calculated.

6.4.2 **Taylor Analogy Breakup model**

Another drop breakup model employed was based on the breakup model which is part of the TAB model. For this the amplitude of an undamped drop oscillation was first calculated with

$$A = \sqrt{\left(y^n - We_c\right)^2 + \left(\frac{1}{\omega}\left(\frac{dy}{dt}\right)^n\right)^2},$$

where y^n is the dimensionless drop deformation in the direction of flow at nth time step. Drop breakup was considered to be possible only if $We_c + A > 1$ and y ≥ 1.

The drop was assumed to maintain its level of deformation (aspect ratio) as soon as it reached its critical deformation, up until the completion of the breakup.

When the condition for drop disintegration have been met, the lifetime of an unstable drop was calculated alternatively as $t_{bup} = 0.82\sqrt{\frac{3\rho d_0^3}{8\sigma}}$ (O'Rourke and Amsden, 1987) and $t_{bup} = \pi\sqrt{\frac{\rho d_0^3}{16\sigma}}$ (Reitz and Diwakar, 1987) or according to Pilch and Erdman (1987) discussed earlier.

For $t^n < t_{bup} \le t^{n+1}$ the breakup was considered to occur on the current time step.

However, for $t_{bup} > t^{n+1}$ the breakup would cease to occur on the current time step and the drop distortion and distortion rate were recalculated in the next time step t^{n+1} as

$$y^{n+1} = We_C + e^{-\Delta t/t_D}\left\{\left(y^n - We_C\right)\cos\omega\Delta t + \frac{1}{\omega}\left(\left(\frac{dy}{dt}\right)^n + \frac{y^n - We_C}{t_D}\right)\sin\omega\Delta t\right\} \text{ and}$$

$$\left(\frac{dy}{dt}\right)^{n+1} = \frac{We_C - y^{n+1}}{t_D} + \omega e^{-\Delta t/t_D}\left\{\frac{1}{\omega}\left(\left(\frac{dy}{dt}\right)^n + \frac{y^n - We_C}{t_D}\right)\cos\omega\Delta t - \left(y^n - We_C\right)\sin\omega\Delta t\right\}$$

respectively. The drop aspect ratio and projected area were then updated using

$$AR^{n+1} = \left(1 - 0.5y^{n+1}\right)^{1.5} \text{and } A^{n+1} = \frac{\pi d_0^2}{4\left(1 - 0.5y^{n+1}\right)}.$$

In conclusion, a numerical code for blood drop flight modeling was developed. Gravitational and aerodynamic drag forces as well as in-flight drop deformation, oscillations and possible secondary break-up were considered. Several drop in-flight deformation and breakup models with the deformable drop drag coefficient were incorporated. Thus, blood drop 2D or 3D coordinates, velocity along the flight trajectory, impact angle and velocity, distance travelled and drop aspect ratio in both 'forward' (from the drop origin till its impact on a surface) and 'backward' (from the drop position on the target surface to its origin) directions ccan be predicted. The effects of air currents and winds on drop travel distance and impact angle can be modelled using the developed code. The accuracy of the drop deformation and breakup models employed needed to be validated for typical blood drops. The validation process is described in the following chapter.

7 Numerical scheme validation and verification

The developed numerical code was verified and validated against a number of analytical and experimental cases of spherical and deformable drop flight. This ascertained code accuracy and ability to predict flight characteristics of typical blood drops. Particular attention was dedicated to sizes and velocities relevant to blood drops produced as a result of passive dripping, cast-off and impact. The characteristics of these drops were revealed in the process.

7.1 Analytical test cases

In order to verify the accuracy of drop velocity components and coordinates calculation subroutines of the program it was tested against simplified cases of **undeformed** (spherical) **drop flight with and without air resistance**. The numerical results were found to match exactly analytical solutions of the kinematic equations of drop motion without air resistance for:

i. projectile launched horizontally from height H with initial velocity components $v_{0x} = v_0,\ v_{0y} = 0$: $v_x = v_0, v_y = gt;\ x = v_0 t,\ y = gt^2/2$ with final flight time $T = \sqrt{2H/g}$ and range $L = v_0 T$;

ii. projectile launched under the initial angle to horizon α_0 and velocity v_0: $v_x = v_0 \cos\alpha_0\,, v_y = v_0 \sin\alpha_0 - gt;\ x = v_0 t \cos\alpha_0 + x_0,\ y = v_0 \sin\alpha_0 - gt^2/2,$

iii. as well as for the case of spherical drop flight at terminal conditions (when drag force is balanced by the drop weight) in ambient air with terminal velocity $v_t = \sqrt{\frac{4d_0 g}{3C_d}\left(\frac{\rho-\rho_a}{\rho_a}\right)}$, $C_d = 0.5$.

7.2 Passive drops at terminal velocity

7.2.1 Water drops

To test the performance of drop **deformation** models **at terminal velocity** numerically calculated terminal velocities for deformed water drops were compared to the experimental

data from Gunn and Kinzer (1949) and Best (1950). Three models of drop deformation (based on Green (1975), Hsiang and Faeth (HF) (1995), and the TAB model with different aerodynamic force coefficient (C_f) values) were tested.

Figure 7.1 shows good agreement between terminal velocities obtained from all the tested models with the reported experimental data for drops up to 5 mm in diameter with maximum relative deviation of 10 %. The most accurate fit (less than 4% error) to the experimental data from Pruppacher and Pitter (1987) and Grossard et al. (1992) was provided by the TAB model with $C_f = 1/4$ over the entire range of drop diameters studied. The models based on Green (1975) and Hsiang and Faeth (1995) empirical correlations for water drops predicted terminal velocities higher than reported experimentally for water drops with diameters > 6 mm.

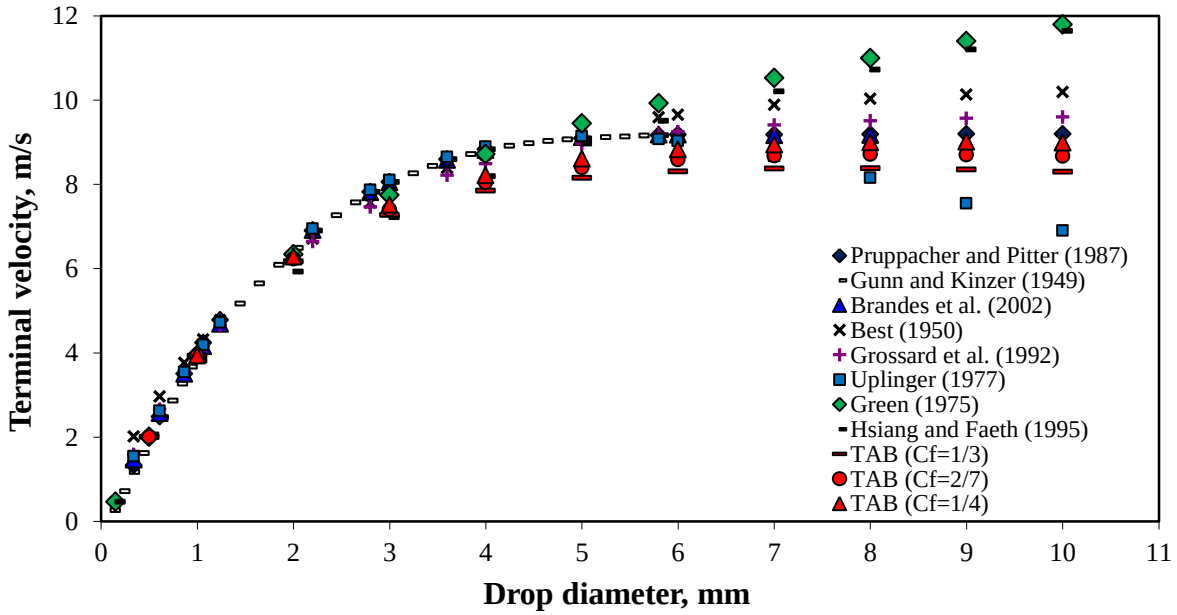

Figure 7.1. Comparison of numerical and empirical terminal velocities of water drops.

The TAB model and that based on Green (1975) provided good approximation of drop deformation levels at terminal conditions for a wide range of drop sizes as can be seen on Figure 7.2. HF model, however, predicted higher drop deformation for drops less than 8 mm in diameter.

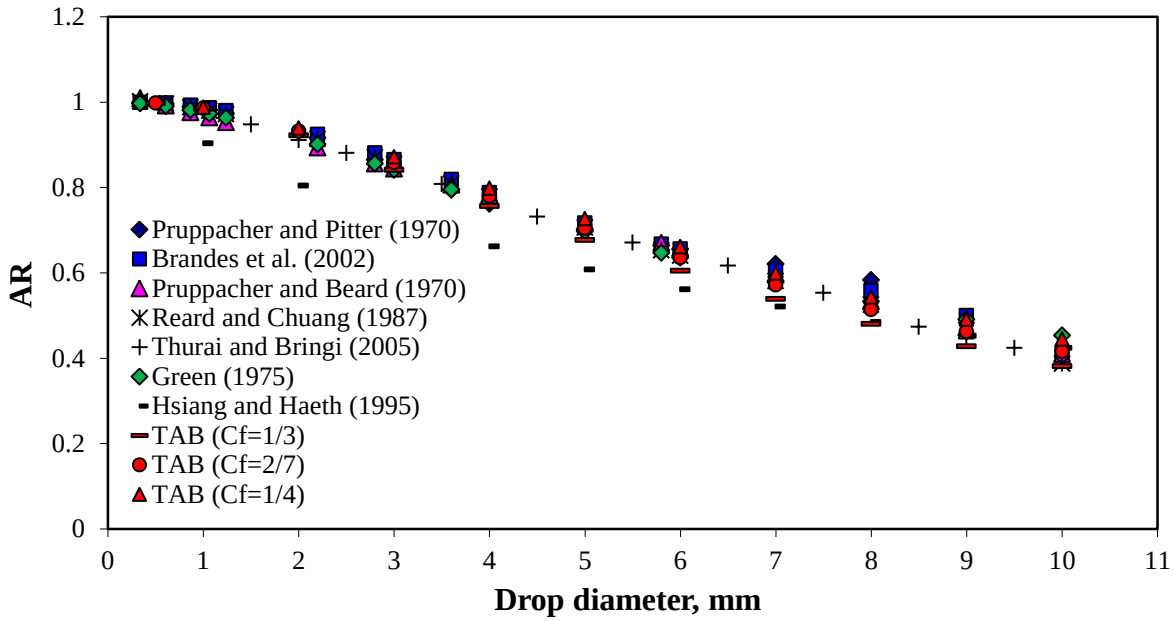

Figure 7.2. Comparison of numerical and empirical deformation levels of water drops at terminal velocities.

7.2.2 **Passive blood drops**

The validity of the code when predicting blood drops flight at conditions close to terminal was tested against experimental data on drops falling from up to 8 m. Experimental methodology can be found in Chapter 4.3.1.

7.2.2.1 Experimental results and analysis

From close-up drop images falling drop diameters with standard deviations were 3.31 ± 0.01 mm ('small'), 4.44 ± 0.05 mm ('medium') and 4.94 ±0 .04 mm ('large'). Drop diameters from drop flight images were within 0.5 mm of the close-up values. The error in drop diameter measurement associated with image pixelation and thresholding was estimated (from the number of pixels which belong to the edge of drop image) to be of around ± 3 pixels (or ± 0.2 mm) for close-up images. The accuracy of drop diameter determination for drop flight videos was limited by image resolution, which amounted to 1 pixel size (or ± 1 mm).

The velocity of the falling drops was observed to increase from about 5 - 6 m/s at 2 m of fall to 8 - 9 m/s at 9 m. The time-dependent evolution of falling drop velocity for the larger drops studied is plotted on Figure 7.3. Scatter of ± 3 – 4 m/s was observed in the data. This may be associated with an uncertainty in drop location (center of mass) determination from

pixilated and thresholded images (less than ± 1 pixel or ± 1 mm) that gives an uncertainty in velocity less than ± 5 m/s.

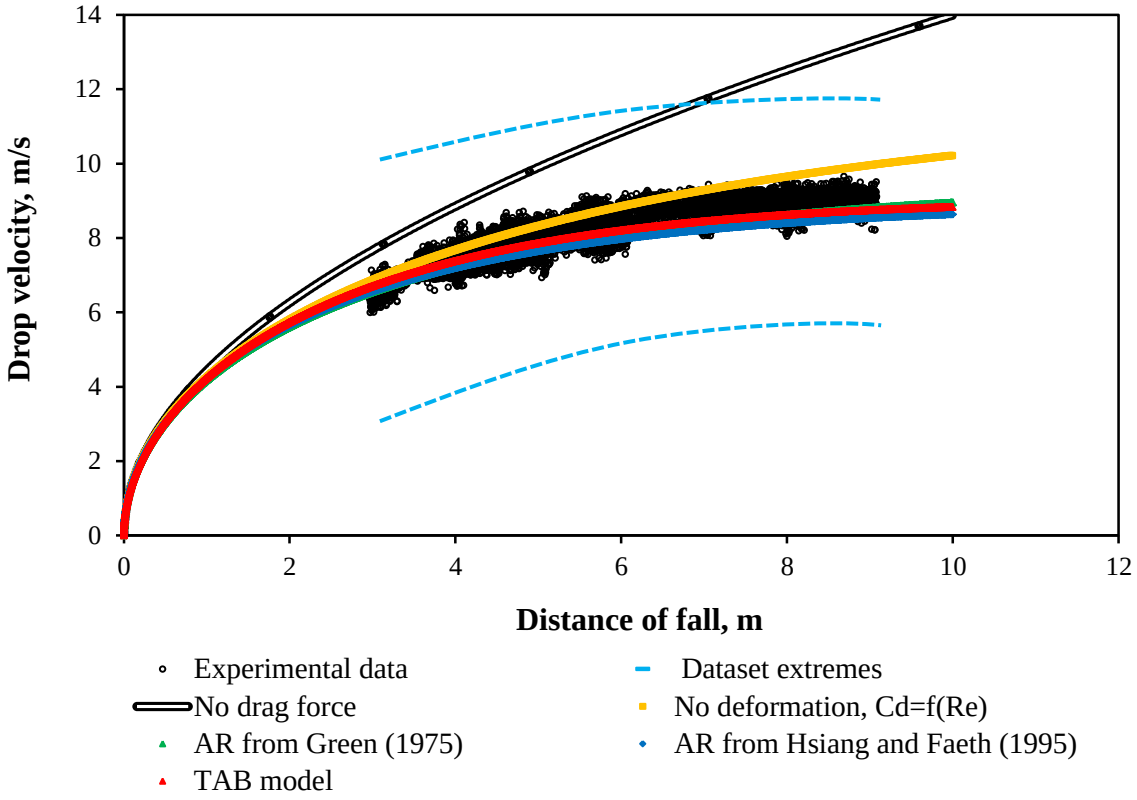

Figure 7.3. Empirical and numerical fall velocity of a ø4.94 mm passive blood drop. The dataset extreme line was fitted through the measured velocity data extreme (maximum or minimum) points.

7.2.2.2 Numerical blood drop fall simulation

Drop fall analogous to that studied experimentally was modeled using the developed code. The experimentally measured blood drop size and density were used. As the viscosity and surface tension of the blood were not measured, published values for human blood were employed for the numerical simulation. The high shear rate value of human blood viscosity of 4 mN·s/m^2 and surface tension of 62 mN/m were chosen (Casson and Kurland, 1965; Rosina et al., 2005).

It should be pointed that a change in a simulated blood drop viscosity value over the range of its natural variability caused no detectable difference in blood drop fall velocity (less than 1/10000%). A decrease in drop surface tension from 62 to 55 mN/m led to a less than 2% decrease in drop fall velocity. Measured blood density was slightly lower than published values. However, from the simulation a 3% increase in drop density from measured 1028 to 1063 kg/m^3 (upper level for human blood) increased drop velocity only by about 1%.

All the models for drop deformation during flight (based on Green (1975), Hsiang and Faeth (1995) and TAB) performed well when predicting drop fall velocity and consequently drop deformation levels which affect drag force and drop trajectory (or velocity in the case of drop fall). Numerical velocity predictions lie close (within 5%) to the mean of the experimental data as can be observed for the largest drop studied in Figure 7.3.

Numerical simulation with a drag coefficient dependent on Reynolds number, but assuming no drop deformation, predicted higher drop velocities compared to those with drop deformation, and higher than the experimental mean, although within the scatter of experimental data. The discrepancy, however, was observed only for fall distances higher than about 4 m.

If the drag force is entirely neglected, the predicted velocities deviate substantially from those of a droplet with drag by the time it has fallen 1.5 m. It is rare that a passive blood drop would fall (vertically) much more than 1.5 m at a crime scene. Such a short travel distance (and time of flight) would not allow a passive drop to experience any significant drag force effects or deformation to alter its flight velocities (in particularly, impact velocity) at typical crime scene conditions.

7.3 Initial oscillations of passive blood drops

The early stage of passive blood drop flight was also experimentally and numerically studied. Initial oscillation amplitude and damping rate for drops falling up to 1.5 m were investigated. Experimental methodology may be found in Chapter 4.3.2.

7.3.1 Experimental results and analysis

The drops formed from the objects tested ranged from 1-6 mm in diameter (see Table 7.1). Blood dripping from the hypodermic needle and kitchen knife generally produced uniform-size drops (main or primary drops). For the case of a dripping hose connector and cylinder, the primary drop was followed by one or rarely two (or more) smaller droplets (termed ‘accompanying drops’ or ‘satellite drops’). Initial oscillations of the needle, knife, hose connector and cylinder primary drops as well as uniform-sized hose connector satellite drops were investigated.

The error in drop diameter measurement due to image pixilation and thresholding was ± 1 pixel (or ± 0.11 mm).

Dripping object	Drop diameter, mm		Standard deviation, mm
Needle	2.83		0.01
Knife	3.96		0.11
Hose connector	Primary	5.34	0.06
	Satellite	1.25	0.08
Cylinder	5.83		0.15

Table 7.1. Passive blood drop diameters for initial blood drop oscillation study.

The primary drops were tracked as soon as the breakup from the ligament was commenced and the body of a drop could be differentiated from the residual liquid adhering to the dripping surface. Upon formation the drops experienced shape oscillations with axisymmetric mode predominating.

The satellite drops studied were formed from as a result of the break-off a highly elongated liquid ligament (length to width ratio of about 10) from the residual liquid and its subsequent strong contraction. The presence of a horizontal oscillation mode (see Testik et al., 2006) was noticed for the first ten to fifteen frames (mode-coupling phenomena (Basaran, 1992)).

Most of the passive blood drops possessed a prolate shape upon detachment, whereas the drops formed from the cylinder were oblate (at the time of recognition).

Aspect ratios of the representative oscillating drops are plotted on Figure 7.4 for the initial stages of flight where drop deformation by aerodynamic forces is less prominent due to low Weber numbers ($We << 1$). The drops oscillated around the spherical shape ($AR \approx 1$) with viscous damping reducing the amplitude and the shape tending to spherical over time.

The mean error in drop aspect ratio determination from ellipse-fitting was less than 1%. It should be noted that the fitting error for the first ten frames of the strongly deformed satellite droplet reached 3 %, but reduced for the following images. The uncertainty in drop location determination from the high-speed images was ± 1 mm.

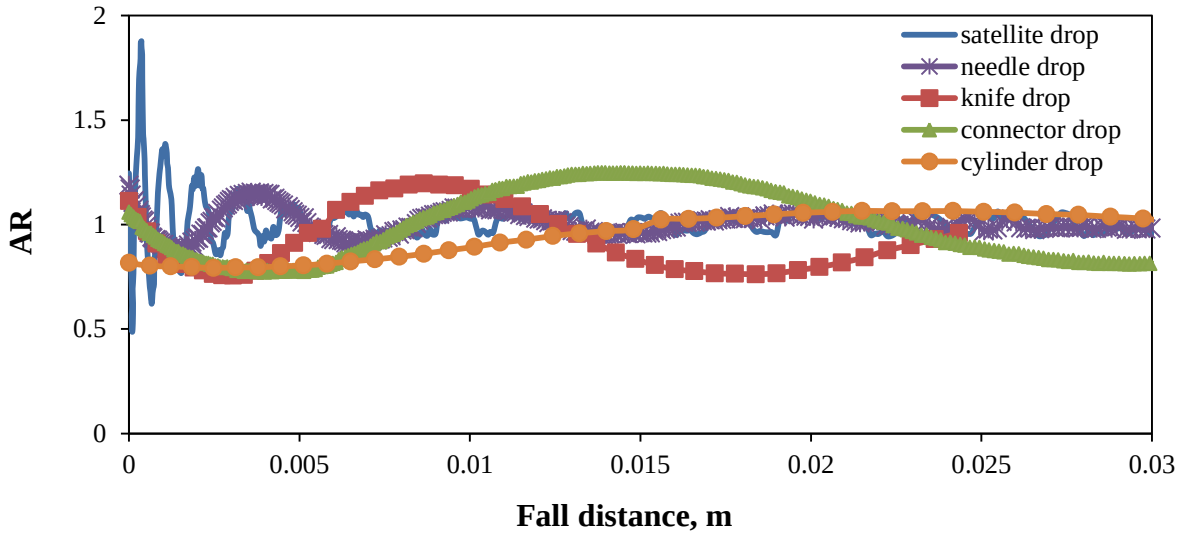

Figure 7.4. Initial oscillations of passive blood drops.

The primary drops experienced moderate- to small-amplitude oscillations with the dimensionless drop distortion y < 0.4 and |1-AR| ≤ 0.3. The satellite drops oscillated with higher amplitudes (y ≤ 0.8 and |1-AR| ≤ 0.9). Drop oscillations with the distortion of the drop diameter, Δd, less than 10% of its undisturbed value d_0 ($\Delta d/d_0 \sim 0.1$) are considered to be of small-amplitude.

The range of initial levels of drop distortion from sphericity $|1\text{-AR}|_0$ (or |1-AR| at t = 0) was also investigated. Drop distortion upon formation is determined by a number of factors such as, for example, dripping object characteristics (geometry, surface texture etc.), physical properties of the dripping liquid and liquid flow rate. Mean values of $|1\text{-AR}|_0$ with the ranges of the maximum and minimum values of the primary drop distortion are plotted on Figure 7.5 for a number of dripping objects tested.

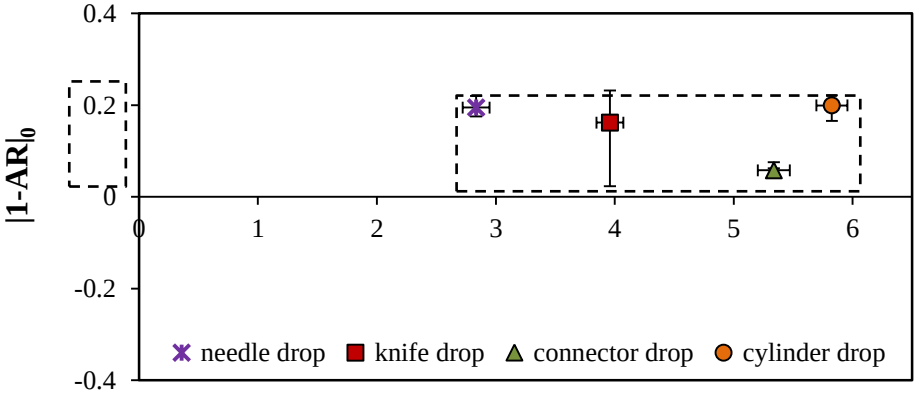

Figure 7.5. Passive blood drop distortion upon formation.

Initial values of |1-AR| ranged between zero for an undisturbed spherical drop and about 0.2-0.25. The measured values, however, are sensitive to the approach in drop detachment/formation recognition and the interactions between a contracting ligament and primary drop.

These establish the range of the initial dimensionless drop distortion y(t = 0) = y_0 of around 0-0.4 for the initial primary blood drop oscillations modeling using TAB model.

When during the drop formation process the thickness of the elongated liquid ligament reaches zero the liquid surface becomes highly concave at this region resulting in high Laplace pressure and rapid liquid displacement from the point of pinching (Eggers, 1995). As a result a part of the ligament retracts back into the primary drop provoking drop deformation and oscillations. In order to accommodate the effect of drop pinching (or breakup) on its further deformation and oscillations the rate of the initial drop distortion change, or initial distortion rate $\dot{y}_0$, was estimated from the first couple of detached primary drop images. It is believed to be a function of a number of parameters such as the dripping object geometry, drop size and physical properties and dripping rate.

The parameter ranged between 18 ± 8 s^{-1} (cylinder drops) and 128 ± 30 s^{-1} (needle drops) for the primary blood drops studied. The measured values are believed to be sensitive to the approach used in drop detachment/formation recognition and drop shape approximation.

The initial value of the distortion rate predicted by the equation for free drop oscillations in a form $\dot{y}_0 = -y_0/t_D$ predicted much lower (as much as by two orders of magnitude) values compared to those observed experimentally.

Comparison of the measured period and frequency of drop oscillations with theoretical predictions by Chandrasekhar (1959; cf. Lamb, 1932) for small-amplitude oscillations of a low-viscosity liquid drop in air is provided on Figure 7.6. The latter predicts dumping of the l^{th} oscillation harmonic (with *m = n + 1* unique oscillation modes) of an inviscid liquid drop having angular frequency $\omega = \left\{\frac{\sigma l(l-1)(l+2)}{\rho d_0^3/8}\right\}^{1/2}$ (Rayleigh, 1879) decay with time t as e^{-t/τ_D} where $\tau_D = \frac{\rho d_0^2/4}{\mu(l-1)(2l+1)}$ is the decay time. The oscillation frequency and period for a low-viscosity liquid drop are given by $\omega^* = \omega\{1-(\omega\tau_D)^{-2}\}^{1/2}$and $T = \frac{2\pi}{\omega^*}$. For the fundamental harmonic (*l = 2*) this gives oscillation frequency and decay time of as $\omega^* = \left\{\frac{64\sigma}{\rho d_0^3} -\right.$

$\left(\frac{20\mu}{\rho d_0^2}\right)^2\Big\}^{1/2}$ and $\tau_D = \frac{\rho d_0^2}{20\mu}$. The time for the oscillation amplitude to reach 1% of its initial value is $\tau_D = \frac{\rho d_0^2}{20\mu} ln(10^2)$.

The drop viscosity μ decreases the natural oscillation frequency. This effect is, however, of second order so the oscillation frequency reduction for low-viscosity liquids is small. The drop oscillations are generally limited to the first few harmonics due to rapid damping of higher harmonics.

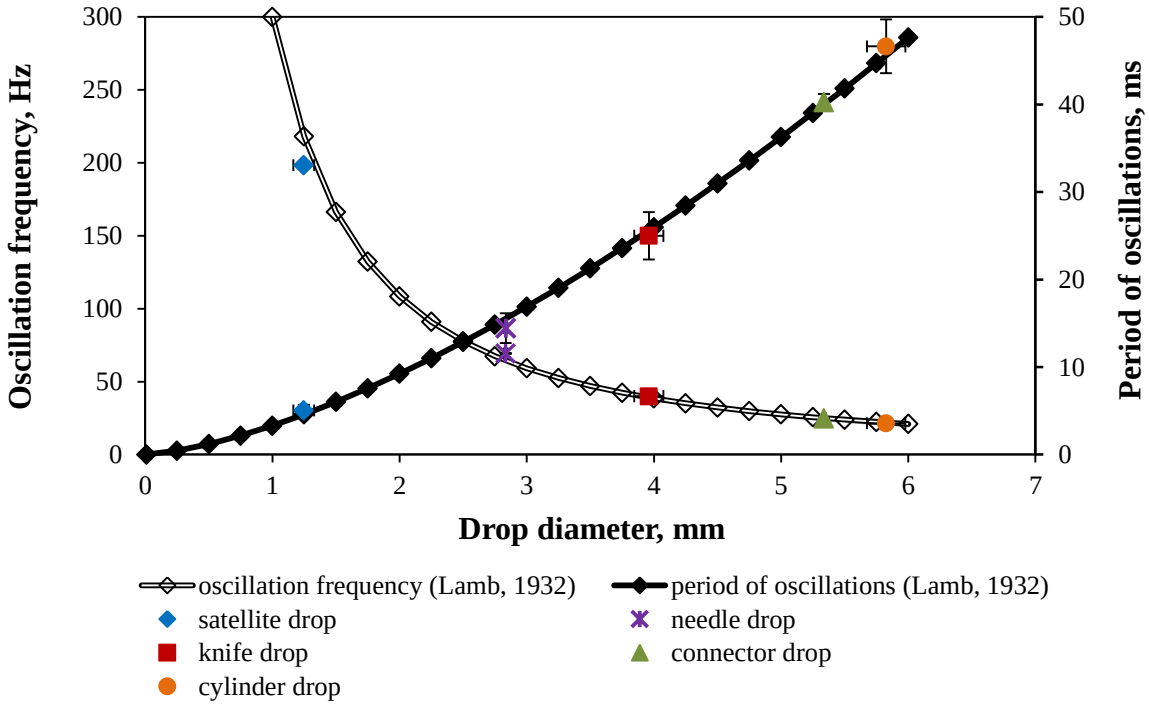

Figure 7.6. Frequency and period of passive blood drop oscillations.

Larger drops were observed to oscillate with lower frequencies and thus had longer periods. The frequency and period of oscillation of the largest drop studied (5.83 mm in diameter, from the cylinder) was about 21.4 ± 0.1 Hz and 47 ± 3 ms respectively. Whereas the needle drops (half as large) had an oscillation frequency three times higher of 69.2 ± 0.1 Hz and a shorter oscillation period of 14 ± 2 ms. Empirical and theoretical oscillation frequencies (and periods) are in good agreement. This is in concordance with the findings of Becker et al. (1991) that the asymptotic behavior of small and moderate low-viscosity drop oscillations can be well predicted by the linear theory (Lamb, 1932).

The shift in oscillation frequency of the satellite drop oscillations may be associated with the decrease in oscillation frequency of the fundamental mode with increasing amplitude (Tsamopoulos and Brown, 1983; Basaran, 1992). Indeed energy transfer between the

fundamental and higher modes (mode coupling) during high-amplitude oscillations changes the energy balance of the fundamental mode. Another possible explanation is the error in drop size estimation, which are critical during rapid oscillations.

As a passive drop velocity increases (We ≥ 1) with the distance of fall aerodynamic effects on drop deformation become more pronounced. The equilibrium drop aspect ratio shifts from that for a spherical drop (AR = 1) towards the values for an oblate spheroid (AR < 1). This was observed experimentally for the passive blood drops. The deformations naturally were more pronounced for the larger drops which also showed a non-elliptical profile with flattening at the bottom surface facing the flow. The images of the satellite, needle and hose connector drops after 1.5 m of fall are presented on Figure 7.7. It should be noted that the hose drops still showed some oscillations after 1.5 m of fall.

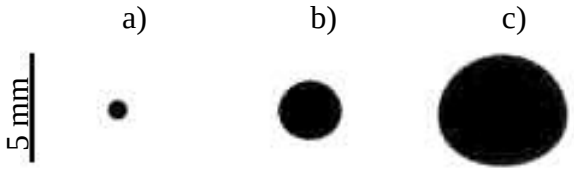

AR:	0.96	0.93	0.86

Figure 7.7. Passive blood drop shapes and aspect ratios after 1.5 m of fall: (a) satellite, (b) needle and (c) hose connector drops. Standard deviation of the aspect ratio measurements was ± 0.3.

7.3.2 **Initial oscillation modeling**

The TAB model considers the oscillations of a viscous liquid drop under the aerodynamic driving force. It requires knowledge of the initial drop distortion and distortion rate possessed by a drop at the early stages of flight. For the case of low Weber numbers TAB reduces to the modeling of free drop oscillation with damping due to the drop viscosity. When aerodynamic effects are small, however, drop distortion and oscillation originating from other sources such as primary or secondary drop breakup, drops collisions etc. may affect drop flight.

Due to the ligament breakup during drop formation and unbalanced surface tension forces drop distortion and oscillation towards a spherical shape is initiated and damped in time by drop viscosity along its accelerated flight. It is, however, difficult to incorporate/describe the effects of drop breakup or pinching (Eggers, 1995) on its further

deformation behavior, in particular, on the degree of initial drop deformation and rate of its evolution.

Drop oscillation is sensitive to a number of factors among which are the initial conditions of drop distortion, drop size, drop liquid and surrounding media physical properties and Weber numbers of flight. In order to predict passive drop distortion and oscillations induced by the drop formation process using TAB model initial drop distortion and distortion rate are needed to be specified. These could be calculated from the experimental data discussed above. Alternatively the value of initial distortion rate was numerically varied to provide the best fit to the experimental data and compared to the corresponding measured values from the experiment.

Measured blood drop density and surface tension values were incorporated into the model and performed well when modeling drop oscillations. Variations in the blood surface tension and density in the range of the instrumental errors had negligible effect on the numerical results. The effect of an increase in drop density is mainly to increase the oscillation decay time and to decrease oscillation frequency proportionally to about $\rho^{-1/2}$. Surface tension increases drop oscillation frequency as $\omega^{1/2}$. The main effect of drop viscosity is to damp the oscillations. As blood is a non-Newtonian fluid its viscosity depends on the shear rate of the flow. To define the apparent viscosity of an oscillating blood drop in an air flow the flow pattern and shear rates within the drop must be determined. The latter is a complex problem.

The value of apparent drop viscosity required to model drop oscillations was selected from the measured and published (Lowe and Barbenel, 1988 and Casson and Kurland) values of blood viscosity for shear rates of 1-2,700 s^{-1}. The selection was performed by matching the observed experimental and numerical data on the oscillation decay times. The viscosity value of 10 mNs/m^2 (for the shear rate of 10 s^{-1}) provided the most satisfactory data fit and was used for the simulations.

A comparison between the experimental and numerical data on drop oscillation from the moment of its formation is presented on Figure 7.8 for the hose connector drops.

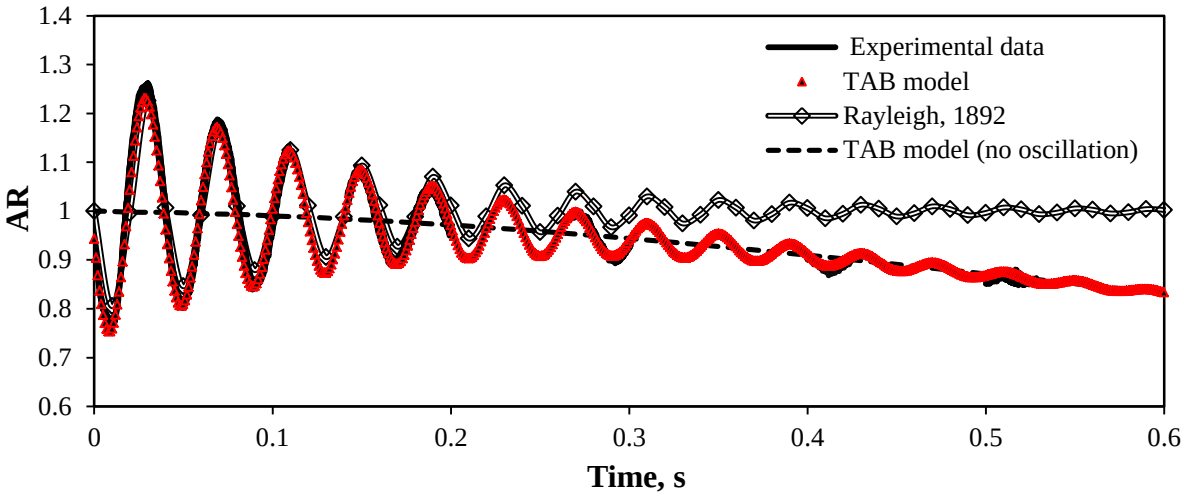

Figure 7.8. Experimental and numerical results for the initial oscillation of a 5.34 mm diameter passive blood drop. Initial distortion $\boldsymbol{y_0}$ and distortion rate $\boldsymbol{\dot{y}_0}$ used for the simulation were 0.076 and 55 s^{-1} correspondingly).

The analytical solution for the free drop oscillation around a spherical shape (Rayleigh, 1892) $AR = \left[1 + A_0 e^{-t/\tau_D} sin(\omega t)\right]^{-3}$ is shown on Figure 7.8. It models passive blood drop oscillation accurately up to the third period. The parameter $A_0 = 0.08$ was used to match experimentally observed drop oscillation data.

As the Weber number of drop flight exceeded about 0.4 at 0.15 s of fall, drop behaviour deviated from that predicted by the free oscillation theory. As the drop velocity increased due to the action of gravity the drop started to deform under the increased aerodynamic loading and oscillated around an equilibrium deformed shape. With further gradual rise in the aerodynamic loading the drop further deformed. The amplitude of oscillation was damped with time by viscous forces.

The simulation of the initial drop oscillation based on the TAB model and empirical data on drop sizes, properties, initial distortion levels and rates provided accurate prediction of the passive drop behavior during flight beginning from the moment of its formation.

The maximum relative error in drop aspect ratio values predicted numerically to that observed experimentally was about 1.6 % for the first period of drop oscillation which may be associated with the errors in the assumed shape of the newly formed drop.

The empirical levels of drop deformation after about 0.5 s (or 1.5 m) of fall were slightly lower (~ 5 %) than those calculated numerically with the TAB model based on the critical Weber number We_{cr} = 12 for secondary drop disintegration during shock loading (Wierzba, 1990). The latter gives the aerodynamic force coefficient C_f = 1/3. To improve the

agreement between the numerical and experimental data on passive blood drop deformation the value of C_f = 2/7, corresponding to slightly higher We_{cr} = 14, reasonable for a gradual increase in the aerodynamic loading to a constant value as at the terminal conditions, was employed in the computation. The TAB model based on the corrected aerodynamic force coefficient performed well for all the primary drops studied experimentally.

The value of the initial distortion rate (initiated by the retracting ligament) used for the simulations ranged from 20 to 94 s^{-1}. The values were higher at least by a factor of ten to those predicted from the free drop oscillation theory, but within the range estimated from the experiments.

The relative errors in drop fall velocity and distance between the numerical approximation and experimental data was generally smaller than 0.5%.

The steady state solution (without drop shape oscillation and initial distortion) for falling passive blood drops was also investigated. It should be noted that the deviation between the numerical solutions for an initially deformed, oscillating drop and the one for initially spherical, non-oscillating drop was negligibly small (<1/1000 %) when predicting the evolution of drop fall velocity, distance and time. This may suggest that the effect of drop initial oscillation and distortion from sphericity on its flight characteristics is negligibly small. Thus for all problems, other than the initial drop shape oscillation prediction, a passive blood drop can be modeled by an initially undisturbed non-oscillating drop undergoing deformation during flight under the aerodynamic forces.

7.4 Cast-off drops

The blood drops cast-off from a rotating disc served as a complementary validation case. Drop oscillations and deformation levels were examined. Experimental methodology may be found in Chapter 4.3.3.

The cast-off drops studied ranged in size from 0.4 to 4 mm in diameter and possessed velocities of 1-15 m/s. The uncertainty in drop diameter measurement due to image pixilation and thresholding was less than or equal to ± 0.11 mm for close-up images or ± 0.5 mm for longer drop trajectory videos. The uncertainty in drop velocity measurements was ± 0.4 m/s and less than ± 2 m/s respectively.

A liquid mass adheres to the surface of the disc by interfacial tension forces. If these forces are weaker than the centripetal force required to keep it rotating at the disc speed, the mass will break up into drops which fly off tangentially. Gravity also acts.

The blood deposited on to the lower disk surface was observed to move to and accumulate on the disk edge. As blood accumulated at the edge, and the weight of the adhering mass and the centripetal force required to keep it rotating with the disc increased. When the interfacial force was no longer competent, a hanging drop started to elongate and formed a liquid neck. The orientation of the liquid neck axis of symmetry changed during disk rotation and as the liquid mass increased. During the early stages of drop formation the axis was oriented perpendicularly to the tangent to the disk circumference at the point of drop contact. Later it further elongated and tilted from being perpendicular to the disk tangent. When the liquid neck narrowed enough it broke up in one or several places generally producing a primary drop and one or more accompanying or satellite drops. After the drop detached, some quantity of liquid was left adhering to the disk surface. As long as the liquid flow rate was sufficient the latter would undergo subsequent similar stages of drop formation (see Figure 7.9).

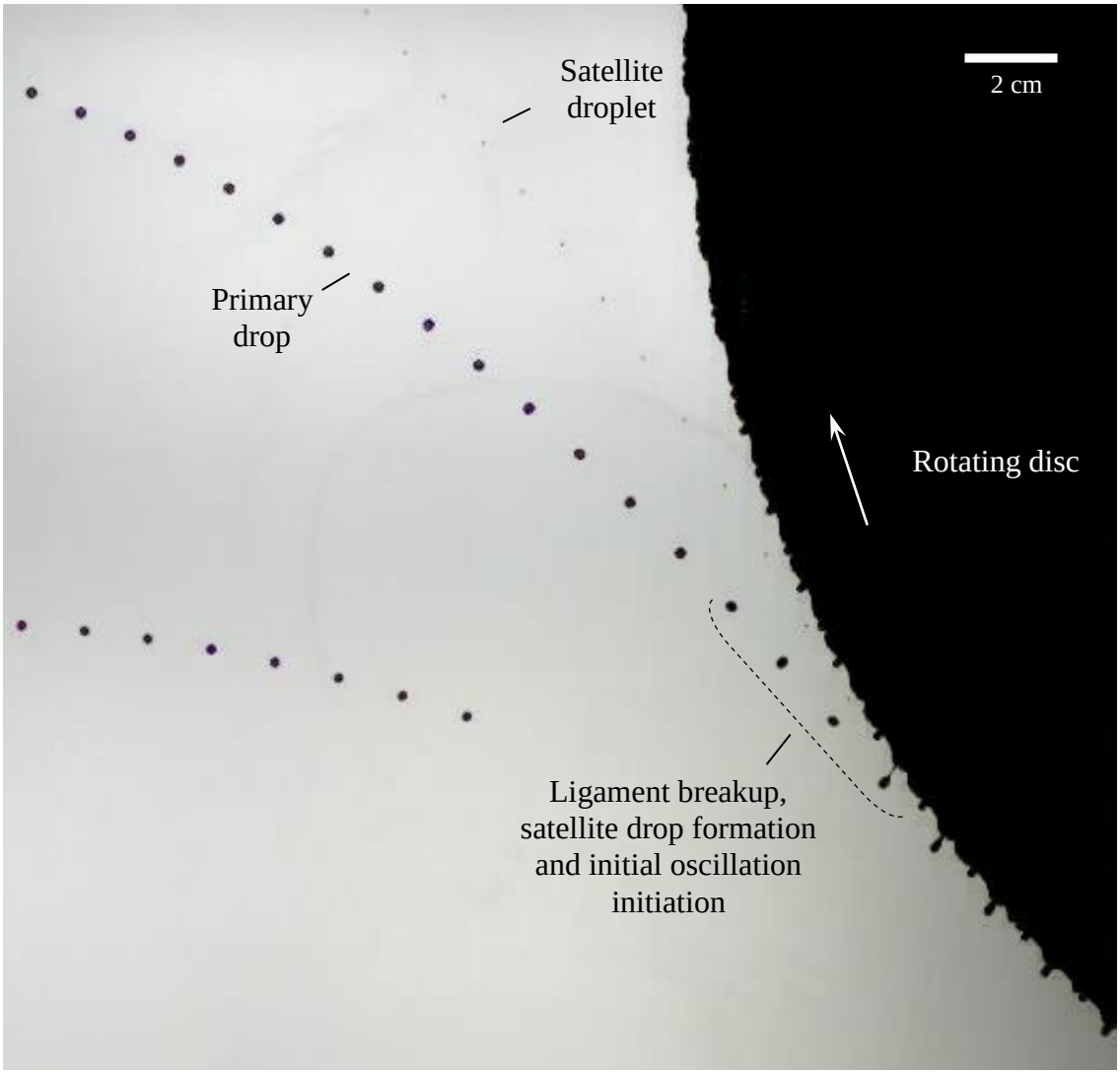

Figure 7.9. Superimposition of cast-off drop images. The disc rotates clockwise.

At lower disk velocities (up to about 6 m/s) the drops tended to detach from the lower part of the rotating disk whereas at higher rotational speeds (and thus higher centripetal forces required for adhesion) the detachment region extended to the whole disk perimeter.

Once released, the primary and accompanying cast-off drops continued to move away from the disk with velocities similar to the tangential velocity of the disc.

While in flight the drops experienced shape oscillations due to the unbalanced surface tension forces at the time of release. Most of the primary cast-off drops detached with a prolate spheroidal shape (with $|1\text{-}AR|_0 < 0.2$). They oscillated with moderate- to small-amplitudes with the dimensionless drop distortion ($y < 0.4$ and $|1\text{-}AR| \leq 0.3$) and damping rates within the range seen in passive dripping. This suggests that the initial oscillations of this type of drops may be successfully modeled with the numerical scheme that performed well for the passive blood drops oscillation simulation.

The size of the primary drops cast off from the disc decreased as the rotational velocity increased. The ligament length, on the contrary, increased with the speed of rotation. The longer ligaments, consequently, produced higher numbers of smaller diameter satellite drops.

The observed initial velocities for the primary cast-off drops are plotted in Figure 7.10a.

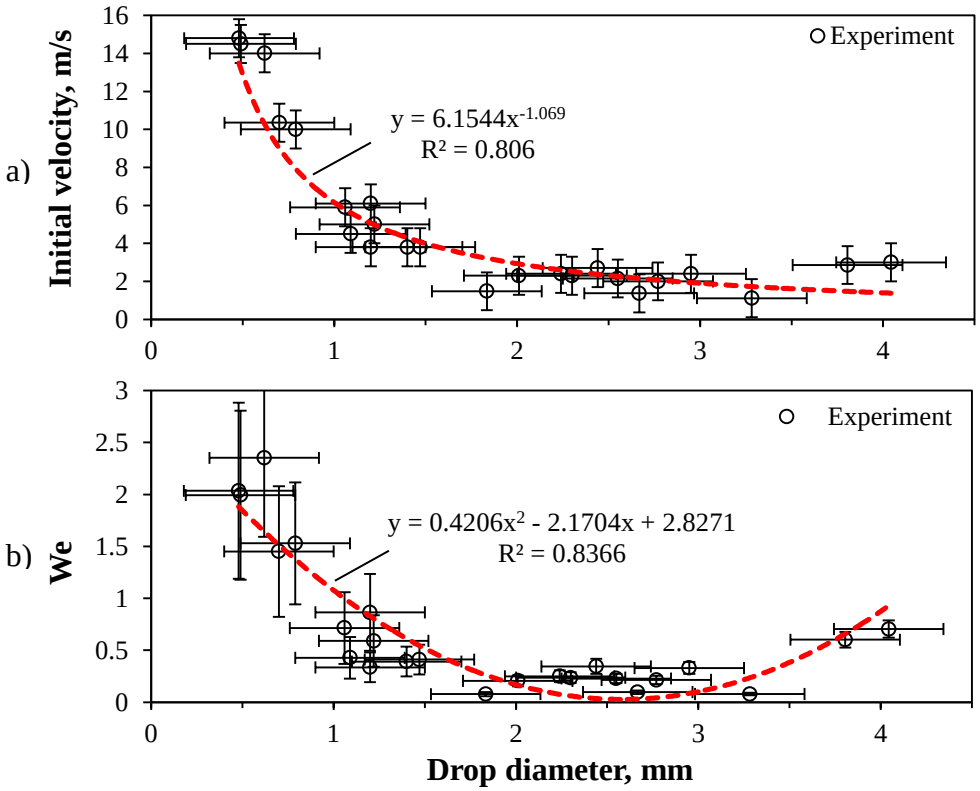

Figure 7.10. Initial drop velocity (a) and Weber number (b) for the 0.4 - 4 mm cast-off drops studied.

As the relatively larger cast-off drops was formed at lower velocities, whereas drops that possessed higher velocities were significantly decreased in size, the initial Weber numbers of the drops flight did not exceed 3. Moreover, as each drop was formed it would decelerate (and thus the We number of its flight would decrease) due to the combined action of air resistance and gravitational force. Such low Weber numbers for cast-off drops (see Figure 7.10b) indicate low deformation levels during flight which are unlikely to alter the drop's flight path and/or velocity at the moment of impact on a surface. Breakup in flight is highly unlikely.

Experimental and numerical cast-off blood drop trajectories for representative We numbers of 0.4 and 2 were compared. The Weber number of 0.4 (black dashed line on Figure 7.11) corresponded to a 1.46 mm drop with an initial velocity of 3.8 m/s detached from the disk rotating at 4 m/s. We = 2 (black solid line) was the highest We for which adequately long trajectories were captured experimentally, and occurred for a 0.48 mm blood drop cast off from the disk rotating at 15 m/s with the velocity upon detachment of 14.8 m/s.

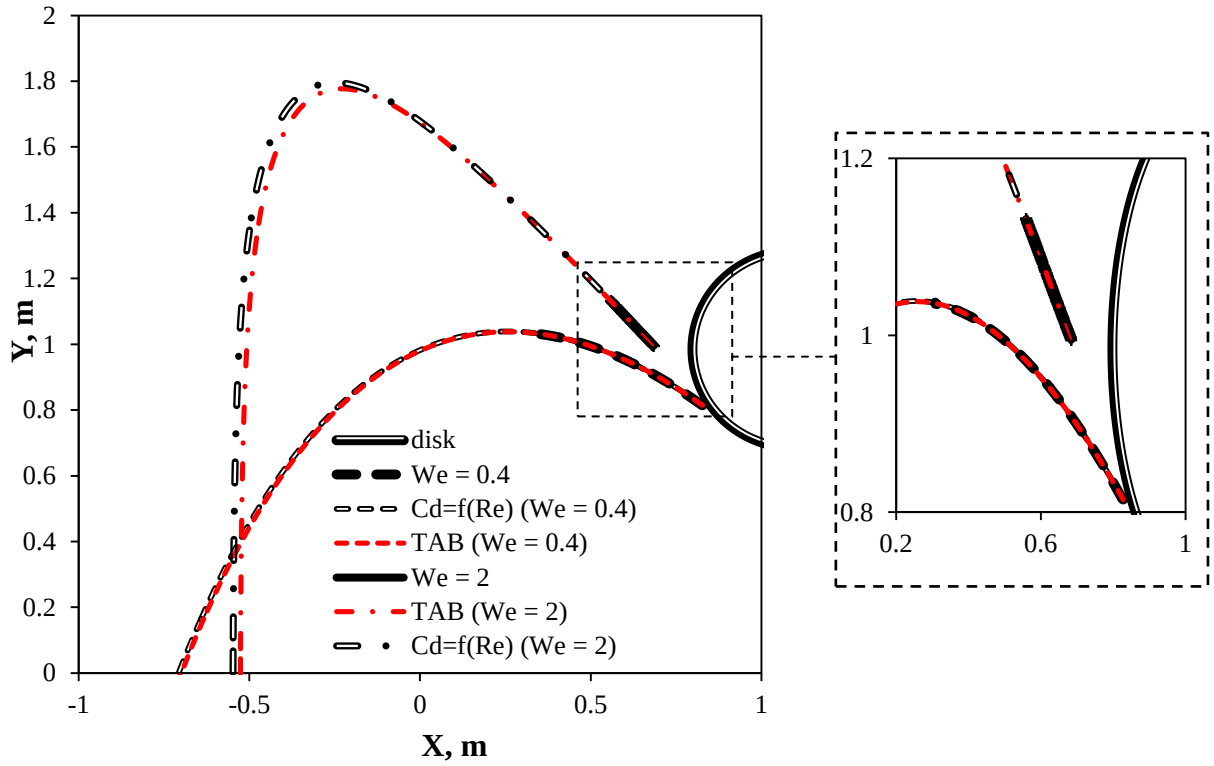

Figure 7.11. Empirical and numerical cast-off blood drop trajectories at We = 0.4 and 2..

Numerical solutions were computed with the spherical (C_d = f(Re) model) and deformable (TAB model) blood drop trajectories. Both models provided an accurate

prediction of the observed drop flight giving evidence of their validity, at least over the length of trajectories studied, for cast-off drop flight modeling.

The simulation was sensitive to the initial input data such as drop size, velocity and angle to the horizontal line which were measured with finite uncertainties. In order to corroborate the accuracy of the model, both drop trajectory and velocity evolution over the duration of imaging were compared to the experimental results. The maximum relative errors in drop position and velocity were less than 2%, which is within the experimental uncertainties.

When the trajectory predictions from the TAB model and the $C_d = f(Re)$ model for a spherical (undeformed) drop were continued till the moment of drop impact onto a horizontal surface ($y = 0$) for the low We number flight, the predicted drop height and range (vertical and horizontal distances traversed since separation, ~0.8 and 1.5 m respectively) were within 1 cm and the impact velocity was within less than 0.6%.

For higher We the numerical solution for a deformable drop predicts a shift in drop trajectory from that of a spherical drop and predicts faster drop deceleration and thus a smaller flight range and lower impact velocity. The deviation, however, was less than 4% (2.2 cm) for the flight range studied (~ 1.53 m) and 0.1% for the velocity at impact.

It is, however, an item for future work to investigate the possibility of the formation of larger cast-off drops from real sharp- and blunt-tip weapons at higher swing velocities which would possess higher We numbers and deformation levels.

7.5 Impact spatter

7.5.1 Level of impact drop deformation

Impact drops studied (Figure 7.12) ranged from 0.1 (limited by the image resolution and magnification) up to 2 mm in diameter (see Chapter 4.3.4 for details of spatter generation, imaging and analysis). Measured initial drop velocities were 14-25 ± 0.5 m/s.

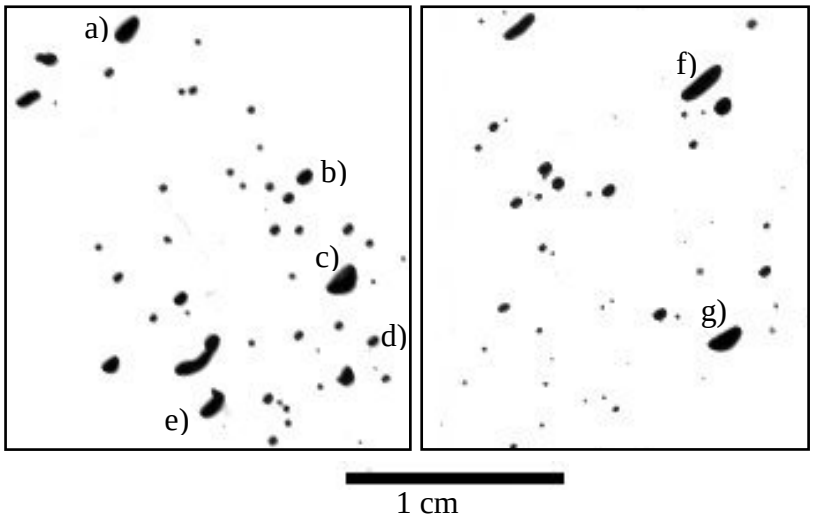

Figure 7.12. Highly deformed impact drops observed: a – d = 1.4 mm, AR = 0.67, We = 9.7; b – 0.9 mm, 0.86, 5.6; c – 'liquid bag' 1.54 mm, 0.75, 10.4; d – 0.68 mm, 0.92, 4.6; e – 0.9 mm, 0.86, 5.8; f – 1.6 mm, 0.37, 9; g – 'liquid bag' 1.5 mm, 0.6, 8.4.

The aspect ratios of the drops were plotted against flight Weber numbers (Figure 7.13). The aspect ratio (AR) and We numbers plotted are the average values over the first 3-5 frames of drop flight. Error bars for the aspect ratio values are equal to two standard deviations. The uncertainties in We were calculated from the uncertainties of drop size and velocity.

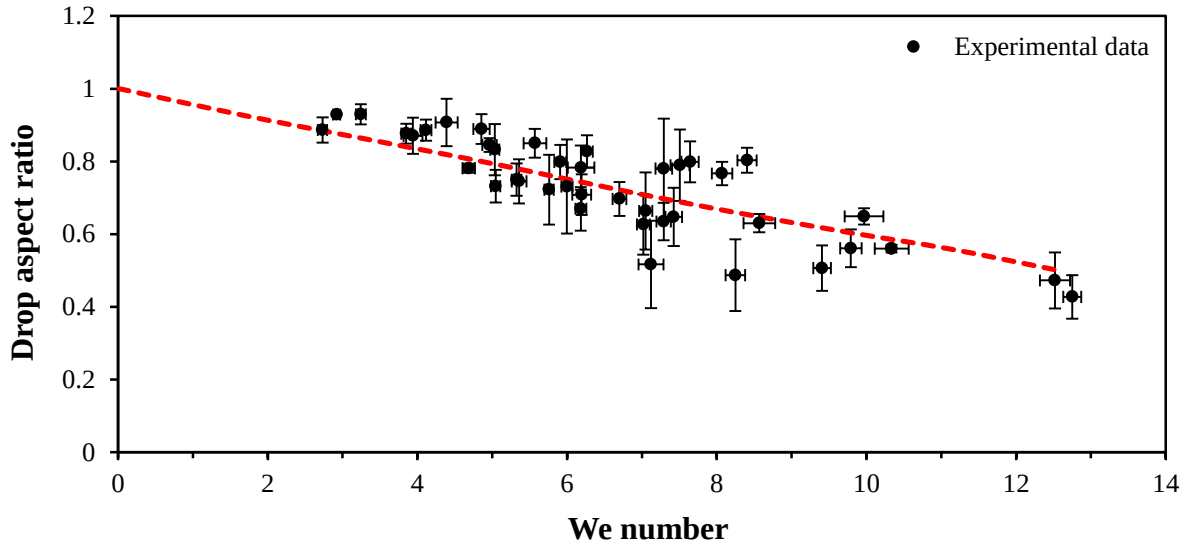

Figure 7.13. Aspect ratios versus Weber numbers for impact drops studied.

The correlation for the aspect ratios of drops at terminal velocities $AR = 0.9951 + 2.51 \times 10^{-2} d_0 - 3.644 \times 10^{-2} d_0^2 + 5.303 \times 10^{-3} d_0^3 - 2.492 \times 10^{-4} d_0^4$ (Brandes et al., 2002 based on Gunn and Kinzer, 1979) is plotted over the experimental data points and provides a good representation of the deformation levels of drops formed as a result of a blunt

force impact. In other words, the deformational response of an impact drop was concordant with that of a falling drop under steady aerodynamic loading at terminal deformation. The behaviour of drops at terminal conditions were shown earlier to be accurately predicted by all three deformation models employed, with the best fit provided by the TAB model.

7.5.2 **Drop breakup**

About seven vibrational, and eight bag-type secondary drop breakup cases were observed for the impact spatter (see, for example, Figure 7.14). The breakup was possible due to the presence of relatively big spatter blood drops (~ 1 – 1.5 mm) which upon formation possessed high velocities and thus Weber numbers (~ 11-15) larger than the critical Weber number (~ 8-12) for drop breakup commencement (Wierzba et al., 2005; Hsiang and Faeth, 1992; Pilch and Erdman, 1987). Most of the breakup cases occurred close to the impact point (within the first 10-20 cm of the spatter flight).

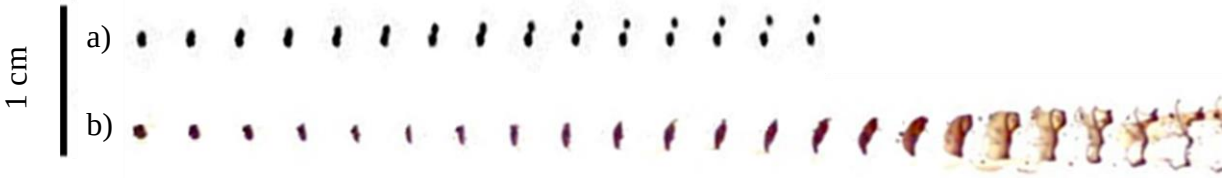

Figure 7.14. Examples of vibrational (a) and bag (b) impact blood drop breakup (drop movement is from left to right).

The drops were initially observed to deform into a ‘liquid disks’ with aspect ratios of 0.3-0.4.

The latter was in good agreement with the critical deformation level for drop breakup of y ~ 1 (or AR ~ 0.35) postulated in the TAB model.

The maximum cross-sectional drop diameter (d_{max}) predicted by the Hsiang and Faeth (1992) model was mostly within 5% of that measured experimentally (see Table X). Drops no.2 and 8, however, possessed slightly asymmetrical distortion which affected size and aspect ratio measurements and resulted in the discrepancy between experimental and numerical d_{max} (by about 13%) and discussed latter breakup time t_{bup}.

After the maximum drop deformation was reached, drops further deformed into a bag- or dumbbell-like shaped figure depending on the mode of breakup. The drops then disintegrated into smaller or child droplets. The vibrational drop breakup ordinarily resulted

in the parent drop dividing into two approximately equally sized child drops, whereas bag disintegration produced a number of different sized droplets.

#	d, mm	V, m/s	We	Breakup type	Empirical $d_{max,\ mm}$	d_{max} (Hsiang and Faeth, 1992), mm	Empirical t_{bup}, ms	t_{bup} (Pilch and Erdman, 1987), ms	t_{bup} (O'Rurke and Amsden, 1987), ms	t_{bup} (Reitz and Diwakar, 1987), ms
1	1.16	25.44	14.4	bag	1.99	1.98	6.4	6.4	3.6	5.1
2	1.02	27.58	15.1	bag	1.57	1.78	4.8	4.9	3	4.2
3	1.10	30.28	19.6	bag	2.13	2.02	3.9	3.9	3.1	4.4
4	1.15	29.66	19.6	bag	2.12	2.12	4.2	4.1	3.4	4.8
5*	1.75	24.08	19.6	bag	3.49	3.38	7.3	7.7	6.3	9.0
6	1.59	27.27	21.6	bag	3.02	3.01	6.1	6.2	5.4	7.7
7	1.45	28.38	22.6	bag	2.81	2.75	4.4	4.9	4.6	6.6
8*	2.20	25.85	28.4	bag	3.87	4.41	10.2	12.4	8.4	12.2

Table X. Empirical and numerical blood drop bag breakup time t_{bup} and maximum cross-stream diameter d_{max} comparison.

Breakup times predicted by Pilch and Erdman (1987), O'Rurke and Amsden (1987), Reitz and Diwakar (1987) were compared to the empirical results. Pilch and Erdman's (1987) expression approximated the breakup time within about 10% of the experimental values, whereas other two expressions predicted either lower or higher breakup time by as much as about 25%.

It should be noted that the TAB model with Pilch and Erdman's (1987) breakup time, as well as the breakup model based on Hsiang and Faeth (1995) overestimated the length of the drop trajectory undergoing breakup by as much as 20%. This was likely due to the disregard of the bag expansion phase of drop breakup in the models when the cross-stream drop diameter (and thus projected area) increases with time up until final drop disintegration. An increase in the droplet area facing the flow brings an increase in drag force and as a result a decrease in drop velocity. Consequently the droplet can reach shorter distances until t_{bup} is reached. If more detailed representation of the drop breakup process was needed an approximation of drop deformation during bag expansion (see Bratz et al. (2010)) may be implemented into the TAB model.

In summary, it was shown that all of the models for drop deformation (based on Green (1975), Hsiang and Faeth (1995) and the TAB model) performed well when predicting passive drop deformation levels and, consequently, fall velocity. The TAB model with the aerodynamic force coefficient $C_f = 2/7$, corresponding to critical Weber number for steady deformation We_{cr} of 14 provided accurate prediction of the initial passive drop oscillations. It

was concluded that a passive blood drop can be modeled using the developed model as an initially undisturbed non-oscillating drop undergoing deformation during flight under the aerodynamic forces for all problems other than the initial drop shape oscillation prediction. Variations in the blood surface tension and density in the range of the instrumental errors had negligible effect on the initial oscillations simulation. A low shear rate blood viscosity of 10 mNs/m^2 was advised to be used for blood drop oscillations modeling.

The size of the primary cast-off drops formed from a rotating disk decreased as the rotational velocity increased from 2 mm < d < 4 mm at ~2 m/s to 1.5 mm and 0.5 mm at 5 m/s and 15 m/s respectively. The ligament length and number of accompanying droplets, on the contrary, increased with the speed of rotation. The cast-off drops studies possessed low deformation levels (We < 3) that are unlikely to alter their trajectory compared to the case of a spherical drop flight.

0.1-2 mm impact drops observed as a result of a blunt force impact possessed high levels of deformation (We > 3) with aspect ratios as low as 0.4. That impact drop deformation at the studied conditions was shown to be accurately described with the correlations for falling drops based on flight Weber number (such as one according to Brandes et al. (2002)). The TAB model performed well when predicting drop deformation based on the variable aerodynamic loading on a drop during its decelerated (or accelerated) motion. Impact drops were observed to break-up at $We_{crit} \approx$ 12-14 within first 10-20 cm from the impact point. Vibrational and bag-type breakups were observed. The TAB model with Pilch and Erdman's (1987) expression for the time of drop breakup was found to be the most accurate when predicting impact blood drop breakup characteristics.

Future work, however, is required to consider gunshot blood drop properties; to investigate the possibility of the formation of larger and/or more deformed cast-off drops from real sharp- and blunt-tip weapons; and to correlate impact drop sizes and velocities to the impact force, shape, nature and surface characteristics of the impactor, nature of the target (soft targets mimicking human body, in particularly), as well as on the physical properties and amount of the atomizing liquid.

8 Blood drop flight study

8.1 Preliminary computational results

Preliminary computational results with the developed code for blood drop trajectories included the examination of the effects of air resistance with and without drag coefficient dependence on Re number; comparison of the trajectories of drops with different initial We numbers and study of the effect of drop deformation during flight.

Water drop flight paths were chosen for the first stage of the investigation as those have similar physical properties to blood drops and expect to behave similarly in-flight.

8.1.1 Kinematics and drag coefficient effects

Figure 8.1a illustrates clear difference in flight paths of a drop deduced from kinematic equations of motion with neglected air resistance and numerical calculations with the developed code considering air resistance force. Kinematics describes motion in a vacuum with gravity being the only force acting on a particle. Even bigger discrepancies were observed when drag coefficient dependency on flow conditions (Re number) was taken into account compared to the case when drop drag coefficient was assigned to be constant and equal to 0.5 (spherical drop shape) along drop flight. When C_d varies with Re, as the drop slows, C_d rises and it rapidly loses forward velocity and drops to the ground. However, due to the small size for the drop chosen for the investigation the difference in the drop range between two extreme cases was only about 7 cm.

The same drop projected with the initial velocity of 30 m/s in air travelled further than the slower drop. It was predicted by the Cd=f(Re) and Cd=0.5 for a spherical drop models to hit the ground much closer to its launch position than predicted according to kinematics. Significant differences between the model with the spherical drop drag coefficient and the Cd=f(Re) model remained. Differences in the drop flight range and height when considering constant and variable drag coefficient were about 53 and 26 cm correspondingly (Figure 8.1b).

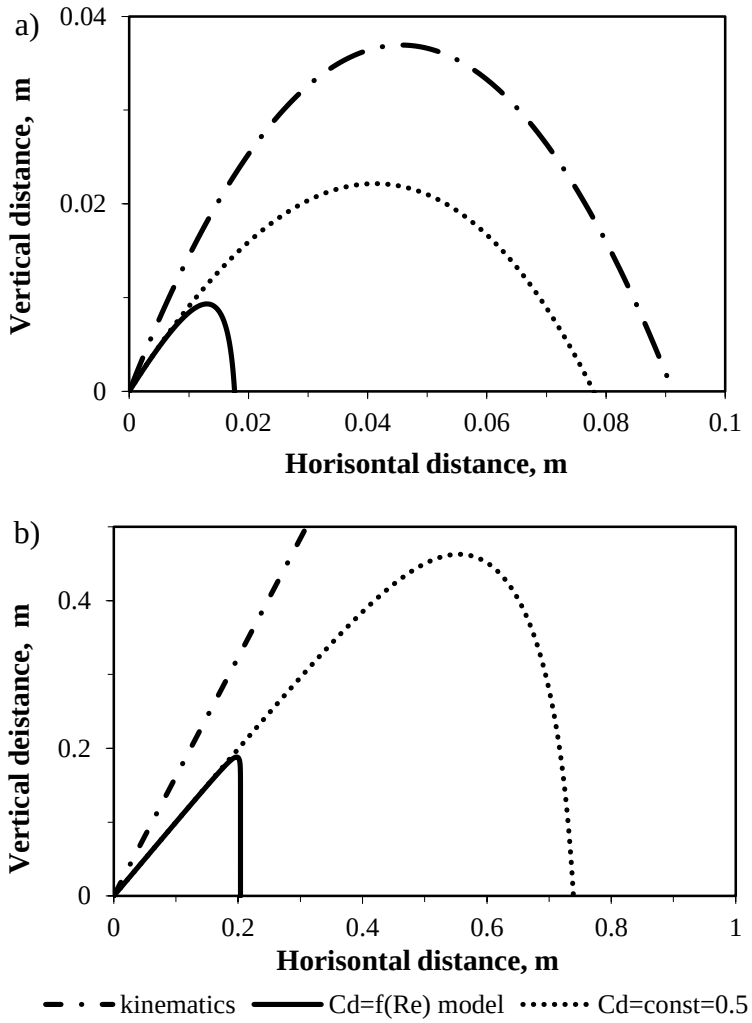

Figure 8.1. Trajectory of a 0.1 mm drop projected with initial velocity of 1 m/s (a) and 30 m/s (b) at 45º to horizontal.

Flight range and height of a 10 times bigger drop (d = 1 mm) were 4.8 and 2.8 m correspondingly which were about 15 and 25 times bigger than those for 0.1 mm drop.

This suggested that drop drag coefficient must be modelled as a function of the Reynolds number, or significant errors (> 100%) in drop flight range may result.

8.1.2 **Performance of the drop deformation models**

The effects of drop deformation models employed in the computational scheme are presented in Figure 8.2. The models based on the findings of Green (1975) for drop deformation at terminal velocity, Hsiang and Faeth (1995) for shock-tube loading on a drop and the TAB model for drop deformation and oscillations were examined.

Two sets of drop trajectories represented those for a 4 mm in diameter drop launched with 4 m/s at an angle to horizon of 45º and for a 2 mm drop with the initial velocity of 15

m/s. Weber numbers for these drops were 1 and 3 respectively showing the increased possibility of drop deformation during flight.

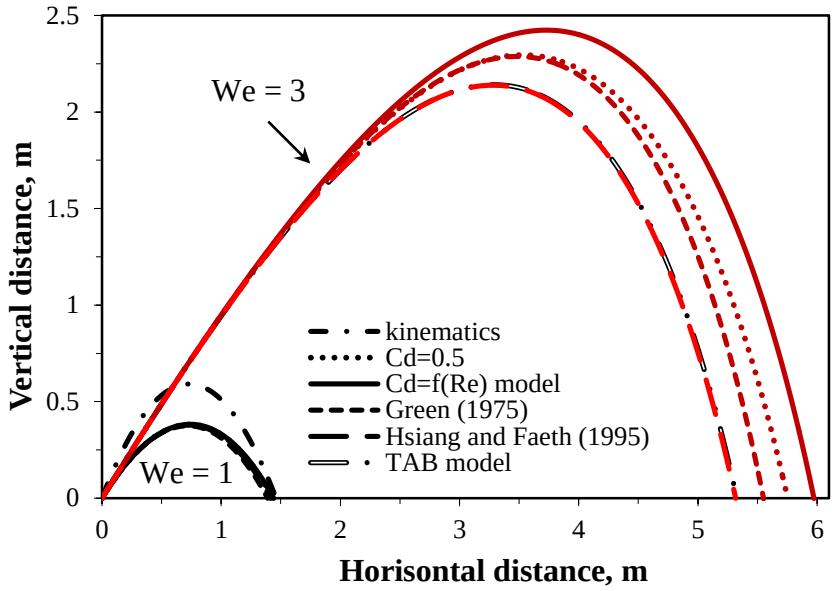

Figure 8.2. Effects of drop deformation during flight on drop flight path.

Indeed, for the drop with the initial We number of 1 the effects of drop distortion were negligible and trajectories predicted by the numerical scheme used lie close to each other and showed relatively small deviation from the kinematic solution. The biggest discrepancy was produced by considering drop deformation levels during flight as those at terminal velocity when drop aspect ratio was represented as a function of Bo number according to Green (1975). This is, however, not surprising due to the fact that the drop was assigned with the initial velocity lower than its terminal velocity. The model over-predicted drop deformation.

With the increase in We number to 3, however, the effect of deformation became more pronounced. The difference in the drop range neglecting and considering its distortion was about 70 cm. Aspect ratio approximation with Bo number for terminal conditions (Green, 1975) in this case predicted smaller levels of drop deformation (and longer drop flight distance as a result) than other models tested. Both Hsiang and Faeth (1995) model and the TAB model predictions were similar.

It should be noted that the importance of the deformation consideration is mostly due to the alteration of the drop drag coefficient with the change in drop shape (aspect ratio) with much smaller contribution due to the change in the drop projected area.

8.2 Forward blood drop trajectory study

Further research was dedicated to fully understand the influence of more pronounced drop deformation (at We > 3) and dynamic drag coefficient on a drop trajectory with special attention to the modelling of blood drops in BPA context. The conditions under which drop breakup occurs required special attention. The effects of likely cross-winds were also of major importance and were studied in the subsequent sections.

The developed numerical scheme for blood drop flight simulation (see Chapter 6 and 7) was used to study the effects of air currents, drop evaporation and in-flight deformation on drop flight characteristics. Blood drop oscillations and conditions for breakup were examined as well. The maximum feasible blood drop travel distance in typical indoor conditions was estimated. The validity of the straight-line blood drop trajectory approximation was tested.

Unless otherwise specified a blood density of 1056 kg/m^3, surface tension of 0.056 N/m and high-shear-rate viscosity of 0.01 N·s/m^2 were assumed for the calculations (see Chapter 4 for references). Drop in-flight deformation, possible oscillations and breakup were accounted in the numerical calculations. The time step used for time-discretisation was 10^{-3} s.

The maximum value of drop velocity considered for the calculations was 30 m/s, which is defined as a characteristic threshold value for "high-energy" spatter by Laber (1985). It should be noted that there is a lack of reported data on the measured blood drop velocities higher than 30 m/s with the stain measurements being the main focus of the studies of spatter patterns.

8.2.1 Straight-line trajectory assumption validity: forward approach

Blood spatter area-of-origin determination is one of the most widely used techniques in BPA. The approach is based on the stain morphology (and position) investigation and backward reconstruction of the trajectories of the drops producing stains upon impact with a surface.

Stringing and trigonometric methods (Bevel and Gardner, 2008) of blood drop trajectory reconstruction are based on the assumption that the trajectory is a straight line. Due to gravitational and air resistance forces, however, a drop's trajectory may be curved which may potentially result in errors in the area of origin determination, such as, for example, overestimation of the point/area of origin height (de Bruin et al., 2011).

Generally the values of drop impact angle, velocity and drop size are needed to be known to reconstruct a non-straight drop trajectory. Several attempts have been made to

correlate drop size and impact velocity with the stain size and appearance (MacDonell and de Lige, 1989, Knock and Davidson, 2007, Hulse-Smith et al., 2005 and Hulse-Smith and Illes, 2007). Universality of these approaches for different impact surfaces and spatter types, however, is still lacking.

The sine law is routinely used to infer the drop impact angle (Balthazard et al.,1939; McDonell and Bialousz et al.,1971, 1979 and McDonell, 1982). The typical uncertainty value of the impact angle determination is believed to be +/- 10% (Rowe, 2006; Connolly et al., 2012) with increased values at impact angles close to 90°.

The current study aimed to investigate the accuracy of the straight-line trajectory assumption by means of the analysis of the forward (i.e. blood size and initial velocity are known) numerical blood drop trajectories in simulated spatter formation conditions.

In particularly, the length of a straight-line segment of a typical, 0.1-2 mm in diameter, spatter drop trajectory was examined. The trajectory segment was assumed to be straight if its directionality (angle to the horizontal (α) or vertical (β) or axes in the considered 2D case) was within 10% of its value at the beginning of drop flight (α_0 or β_0). In this case the errors due to straight-line approximation associated with the trajectory curving would be within the above-mentioned typical uncertainties in the drop impact angle determination.

The developed numerical scheme for accurate blood drop trajectory prediction, with gravitational and air resistance as well as drop in-flight deformation and breakup possibility effects included, was used to plot the trajectories. Once, during the calculations, the trajectory 'straightness' criterion fails (when, for example, $\alpha > 0.1\alpha_0$) an approximate length of the straight trajectory was calculated as $\left(L^2+H^2\right)^{0.5}$, where L and H are the final trajectory height and range.

This corresponded to the maximum distance to which the drop trajectory can be backtracked from the stain in the direction determined by the measured impact angle without increasing the area (or volume) of origin determination error.

The spatter drops were assumed to originate and move in quiescent air with initial launch angles to horizontal, α, of 85, 45 and 0° (upward moving drops) and with representative velocities of 2-30 m/s. As the blood drops with d > 1 mm become unstable and disintegrate into smaller droplets at velocities > 24 m/s, the maximum possible velocities which do not result in drop disintegration were investigated. These included 24, 20 and 17 m/s for 1, 1.5 and 2 mm drops respectively. Smaller drops (0.1-0.5 mm) were tested at the

highest velocity of 30 m/s, characteristic for the high-energy spatter. Downward-moving spatter droplets (with α = -45°) were also investigated.

The straight blood drop trajectory length is plotted in Figure 8.3.

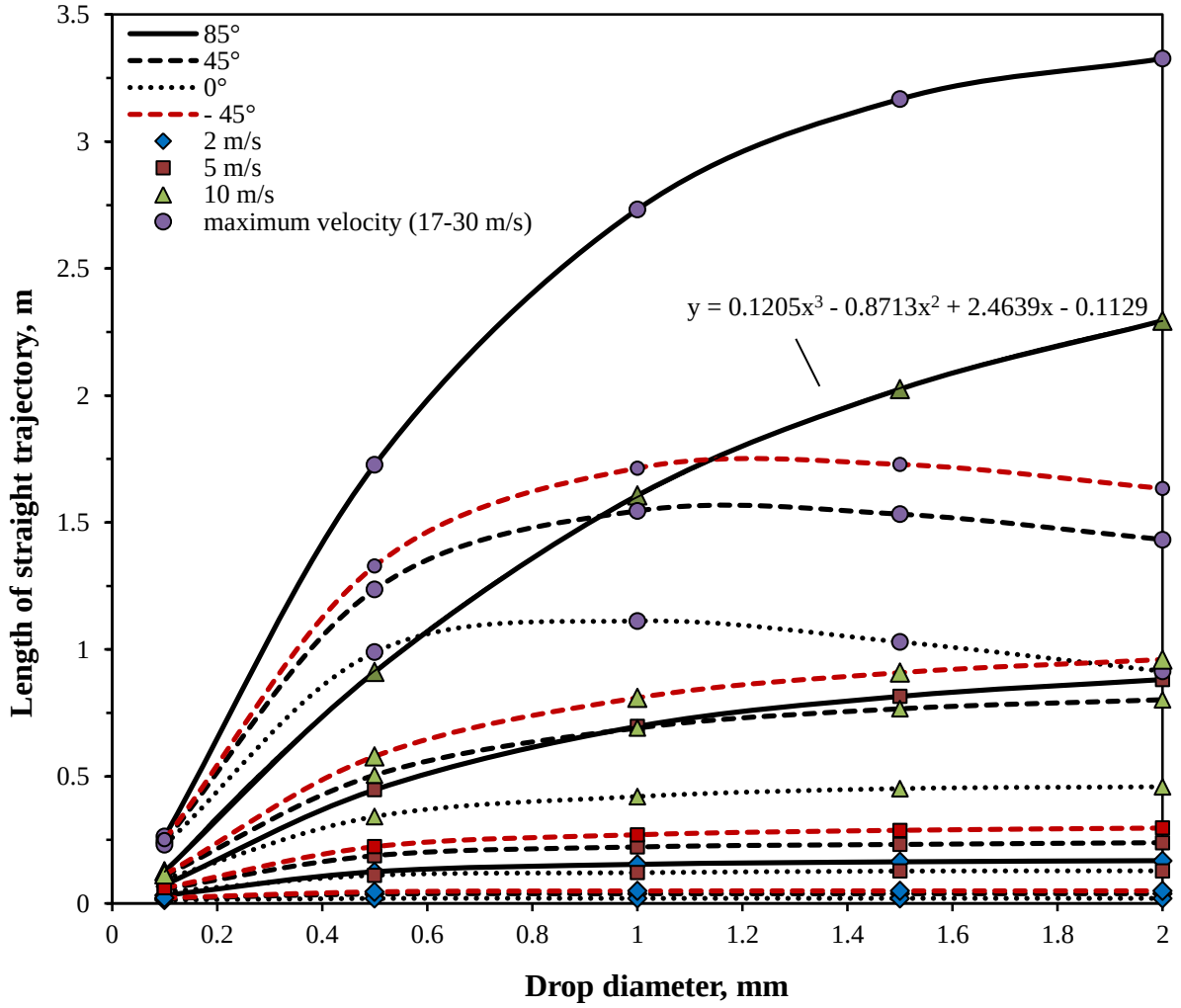

Figure 8.3. Straight trajectory length vs. blood drop size, launch velocity and angle to horizontal.

8.2.1.1 Trends observed

Naturally, the higher the drop velocity and drop size the longer the drop trajectory and its straight segment, in particular, is for **any drop directionality** (with some drop trajectory directionality dependence discussed below). Indeed, gravity acts along the drop trajectory and is expected to affect drop velocity significantly and, thus, curve its trajectory, if the work done by gravity along the trajectory (mgH) considerably exceeds drop initial kinetic energy ($mv^2/2$). The higher the initial kinetic energy, in particularly drop velocity, the less pronounced the effect of gravity on drop trajectory is. In addition, for spherical drops, the

drag coefficient of the bigger drops is lower (and, thus, the drag force) than for the smaller drops at the same velocity.

For **upward moving drops** the trajectories tended to be straighter over longer distances for less acute **angles** to horizontal or, in other words, for drops travelling upwards closer to the vertical. The effect of gravity tends to decrease the vertical velocity component of the drop. When a drop moves with a trajectory close to the vertical, gravity slows it down without significant deflection of its trajectory. On the contrary, the trajectory curvature increases for drops at initial launch angles close to 0º (moving horizontally) as can be seen from the decrease in the straight trajectory length as α approaches to 0º (or 360º). This effect is more pronounced for heavier drops as the force of gravity is proportional to mass.

Larger liquid drops at higher velocities, in addition, tend to deform during flight, which increases the drag force experienced by the drop, slows it down and facilitates the curving effect of gravity on drop trajectory. This can be illustrated by the flattening or even decline (decrease in the slope) of the straight-line trajectory length curves for drops bigger than about 1 mm in diameter in Figure 8.3.

For **downward-moving drops** the gravity acts against the air resistance force and tends to accelerate the drops, increasing the straight trajectory length.

8.2.1.2 Qualitative results

Blood drops with $d < 0.3$ mm having velocity ≤ 30 m/s (which may be associated with small, mist-like stains such as gunshot-related spatter) cannot travel in a straight line more than 25 cm, regardless of directionality. This is valid also for all drop sizes tested at initial velocities ≤ 5 m/s. The drops moving upward close to vertical, however, may reach a maximum of 1 m without significant trajectory curving.

It should be mentioned that the mist-like droplets ($d < 0.3$ mm), moreover, are highly susceptible to in-flight evaporation and drift along the surrounding air flow (refer to Chapter 8.2.6 and 8.2.7 below). The latter may additionally alter the area of origin calculations. They are initially moving along a relatively straight trajectory until they are completely slowed down and start to fall vertically.

At higher initial drop velocities (> 10 m/s), the upward-moving ($\alpha > \sim 70º$) drops larger than 0.3 mm in diameter could travel as much as 1-3.5 m in straight paths. The fast drops with $d > 0.8$ mm are expected to travel in a straight line for distances higher than the standard ceiling height of 2.4 m.

For more acute or reflex drop launch angles when drop flight directionality is close to horizontal the maximum straight-line trajectory is 1-1.5 m.

Drops with $\alpha = 0^{o}$ can travel horizontally for a maximum of 1 m even at the highest velocities (~30 m/s).

Practical analysis

The fast (with velocities higher than ~10 m/s) upward (at angles to vertical < 45°) moving drops (and resulting stains with impact angles > 45° if found on a ceiling or < 45° if found on a facing vertical wall) were found to be the most suitable for the stringing method to be accurate which is in agreement with the current practice in BPA (Connolly, Illes and Fraser, 2012).

8.2.1.3 Stains on a ceiling

The larger the stain (as is a drop) found on a ceiling the higher the possibility that the stain was produced by a drop travelling along a flat trajectory and, thus, the more reliable the straight-line approximation of blood drop trajectory is.

If mist-like stains are found on an object it may suggest that the object was in the vicinity of the blood origin (within 1 m) at the moment of spatter formation. The possibility of the droplet trajectory's alteration due to air currents, winds or muzzle gases present upon spatter generation should be examined in this case.

The smaller the impact angle of the stains with upward directionality located on a wall in the vicinity of a ceiling, the closer (in horizontal direction) the blood source was to the wall.

8.2.1.4 Stains on a wall

For stains with upward directionally and impact angles, α_{imp}, of $0° < \alpha_{imp} < 90°$ located on a wall, the maximum theoretical straight drop flight path length is 2 m (and less for smaller stains). For a stain on a wall at right angles, the maximum flight path length of a straight drop trajectory is ~1 m. It is however ambiguous whether the stains present on a wall were produced by straight-line moving drops, by drops with slightly curved trajectories or a combination of the two.

8.2.2 How far can a spatter drop travel under typical indoor conditions?

The presence of blood spatter stains on any object or surface may provide clues on what led to the bloodshed and who was or was not present at a crime scene.

If the stains are located on the clothing of a suspect it may be possible to determine whether the suspect was at the scene when the spatter was produced.

In light of this, the maximum distance that blood spatter drops can travel, or the maximum distance a crime scene participant may be from the blood source to still get blood stains on his or her clothing is worth investigating. If this distance is known, it may also be possible to conclude if the bloodstain patterns present in a scene might have been produced by the same or different blood-generating events (see Chapter 8.2.7 for more details).

This study aimed to determine the maximum distance typical blood spatter drops can travel in the horizontal direction (flight range, L) by means of numerical simulation of deformable blood drop flight. Idealized crime scene conditions were assumed, such as a room with no vertical walls, horizontal flat floor and still air. The drop in-flight evaporation, which when present leads to faster drop deceleration and travel distance reduction, was neglected to investigate the best case scenario for a drop to travel far.

In order for a drop to travel far it needs to be launched with appropriate initial conditions.

In particular, the greater the height of the blood source, the longer a drop can be in flight without reaching the ground (or floor). In light of this the standard ceiling height of 2.4 m was chosen as a maximum possible blood source position above the floor level.

The higher the drop velocity upon formation (launch velocity), the farther it can travel. The drag force, however, is proportional to the square of drop velocity, and the same drop at higher velocity experiences higher drag force and, as a result, more pronounced trajectory curving and flight range reduction. In addition, the larger drops at higher velocities may experience more pronounced deformation from sphericity during flight which additionally increases the net drag force.

The initial drop directionality (initial angle to horizon, α) is also of importance to the distance a drop can reach. From the kinematics of a projectile motion without air resistance at a fixed initial velocity, L is a function of α and is symmetrical (L is the same for 30 and 60°, for example) about $\alpha = 45°$. The latter is a so-called optimal angle which provides the maximum flight range. With air resistance taken into account the optimal angle is believed to be smaller than 45°. This is due to the fact that the lower trajectory ($\alpha < 45°$) reduces the time and distance over which the projectile experiences the decelerating drag force.

To determine the sizes (diameters) and velocities of the drops which are going to travel the longest distances, a number of numerical experiments with drops of 0.1-2 mm in diameter and initial velocities from 5 m/s (approximate lower limit for spatter drops) to 30 m/s were

performed. As the blood drops with d > 1 mm are expected to become unstable and disintegrate into smaller droplets at velocities > 24 m/s, these drops were tested at the maximum possible velocities which do not result in drop disintegration (see the chapter on drop breakup time and distance for more details).

Additional numerical tests were executed to estimate the optimal launch angles for which the maximum flight range may be achieved for the drops considered. The angles were found be relatively independent of the drop velocity and ranged from 0-5°, 0-10°, 10-20° and 25-35° for 0.1, 0.5, 1 and 2 mm blood drops respectively.

The drop maximum flight range (at optimal angles determined earlier) was observed to increase with the drop diameter and velocity from a maximum of 30 cm for a 0.1 mm drop at 30 m/s to as much as ~3 and 6 m for a 2mm drop at 5 and 17 m/s respectively. The data and the polynomial fits for the flight range vs. drop diameter are presented in Figure 8.4.

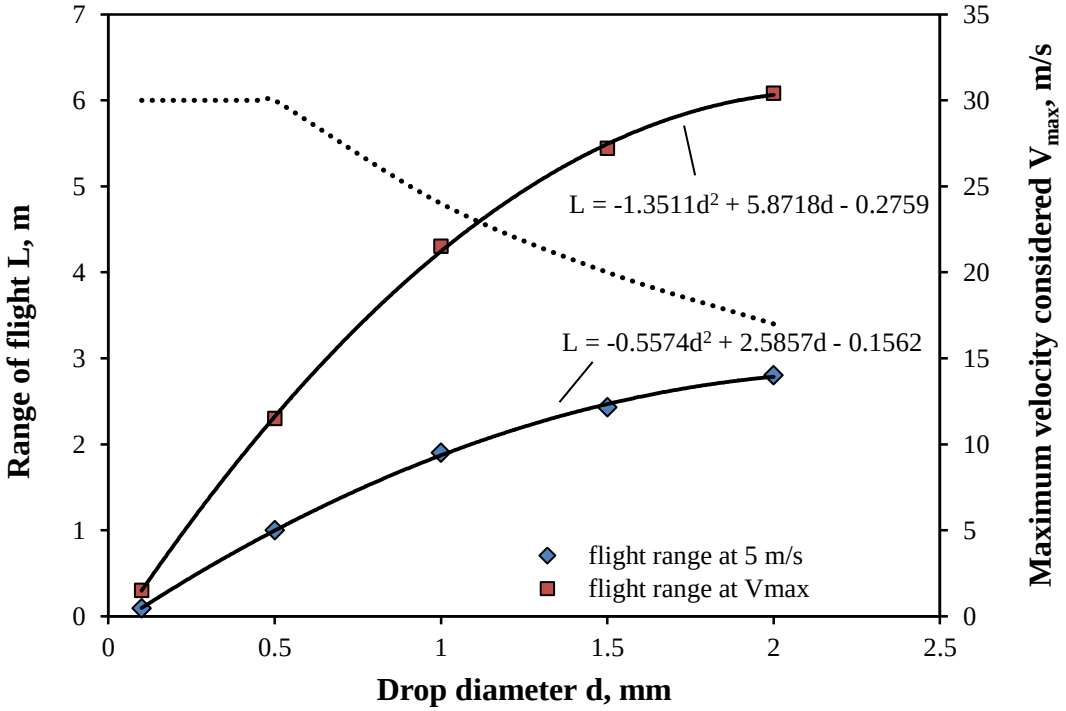

Figure 8.4. The maximum flight range of 0.1-2 mm drops at 5-30 m/s of initial velocity.

The drops of diameter 0.5-1 mm with velocities between 5-30 m/s which represent cast-off and impact spatter were found to travel on average a maximum of 2-3 m if not intercepted by a wall, or any other object, or subject. The flight range decreases to about 1 m for smaller drops d < 0.5 mm. The latter may produce the mist-like stains, which when present on an object or clothing may indicate its proximity (within <1 m radius) to the blood source at the moment of spatter generation.

8.2.2.1 Discussion with comparison to previous studies

The present results can be correlated to the reported data. There are only a few studies on blood spatter travel distances, (Skrebutenas, 2013) focusing on impact spatter and gunshot backspatter (Clayborn, 2012).

Impact spatter produced by a striking device onto a pool of sheep blood was found to travel up to 4.6 m horizontally, with highest concentration of the stains within 2 to 3 m from the spatter origin (Skrebutenas, 2013). This is in good agreement with the numerical results for typical impact spatter drops (0.5-1 mm in diameter at ~5-30 m/s with smaller drops forming at higher velocities), which are expected to travel on average up to 2-3 m with maximum distance from the origin of 4.5 m. In addition, the stains with the highest diameter were found farther from the origin, verifying the longest numerical travel distances of larger (1-2 mm) blood drops.

Back spatter which forms as a result of a different-caliber bullets penetrating through a simulated wound with a blood substitute was studied by (Clayborn, 2012). The maximum forward horizontal distance the spatter travelled from the target was around 5.5 m. The drop diameters and velocities were not measured for this study. For the speculated maximum gunshot spatter drop size of 1-2 mm, however, the numerical experiments predict 4.5-5.5 m maximum travel distance from the origin similarly to the above-mentioned experimental result.

8.2.3 Decay time and distance of blood drop oscillation

The drop impact angle (α_{imp}), the internal angle formed between the direction of a blood drop and the plane of the surface it strikes (James, Kish and Sutton, 2003; Bevel and Gardner, 2008), is one of the crucial parameters for the drop trajectory reconstruction and area of drop origin determination. The sine law is routinely used to calculate the drop impact angle from the bloodstain width and length measurements (Balthazard et al., 1939). The method is based on the assumption of the spherical drop shape on impact with a surface (James, Kish and Sutton, 2003).

A blood drop may be non-spherical and experience shape oscillations during flight and on impact with a surface. This may lead to the resultant stain shape alteration and, hence, to the errors in the angle of impact and drop origin determination.

A drop is expected to oscillate when it is exposed to an external distorting flow or force (Ashgriz, 2011).

In particular, a drop may oscillate due to unbalanced surface tension forces as a result of its detachment from a larger mass of liquid (a ligament, for example) upon formation. In this case a drop undergoes so-called initial oscillation. The drop oscillations, similar to the initial oscillations, may be induced by a disturbing external flow field due to an uneven pressure distribution over its surface. The latter provokes cross-flow drop shape deformation, whereas, the surface tension forces aim to bring the drop to the spherical shape with the lowest surface area.

An analogy between an oscillating and distorting drop and a spring mass system (Figure 8.5) forms the basis for the Taylor Analogy Breakup (TAB) model proposed by O'Rourke and Amsden (1987) for low-Weber number drops in spray modelling applications. The droplet distortion is viewed a one-dimensional (only prolate-oblate oscillations considered) driven damped harmonic oscillation of a spring-mass system. The driving F(t) represented by the aerodynamic force experienced by the drop during its flight, restoring force, $-\omega_0^2 x$, is due to the surface tension forces and the damping force $-2\beta\dot{x}$, is due to drop liquid viscosity μ. The governing equation for the displacement x of the droplet equator from its spherical (undisturbed) position x_{eq}, can be written in a form $\ddot{x} + 2\beta\dot{x} + \omega_0^2 x = \frac{F(t)}{m}$ for small-amplitude oscillations. The parameters β, ω_0 and m are the damping coefficient, undammed oscillation frequency and the drop mass correspondingly. The oblate and prolate drop shape deformations are represented by $x < 0$ and $x > 0$ respectivelly. The general solution of this equation consists of two parts. Namely, from the sum of the general solution for the free damped harmonic oscillations ($F(t) = 0$), so-called transient part, and the steady state solution ($t \to \infty$) when the transient solution approaches zero. The transient part is determined by the initial distortion level x_0 and its rate of change $\dot{x_0}$. The steady part is dependent on the driving force only.

The initial oscillations (Figure 8.5a) may be provoked either by the finite initial drop distortion ($x_0 \neq 0$) and/or by the finite initial drop distortion rate ($\dot{x_0} \neq 0$). The main effect of the driving aerodynamic force is to shift the equilibrium drop shape (x_{eq}^*) towards which the drop oscillates according to the transient solution.

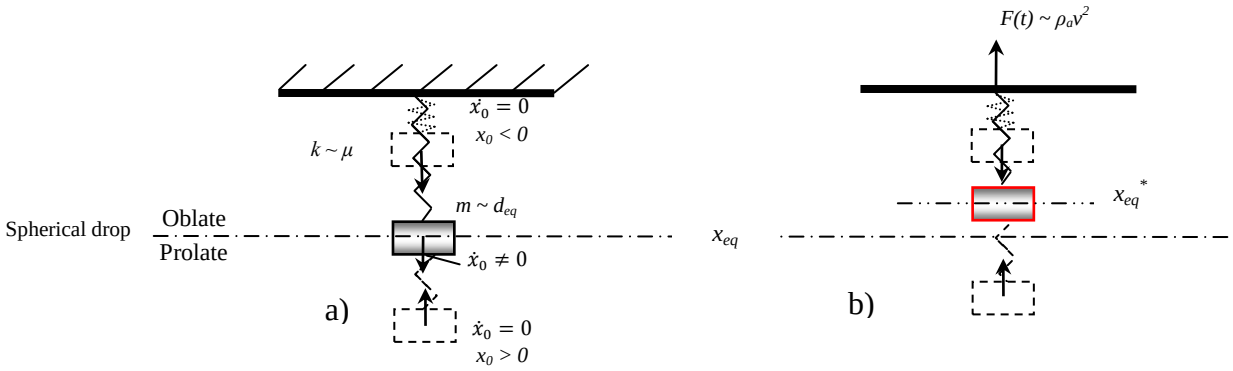

Figure 8.5. An oscillating and deforming drop and the spring-mass system analogy: (a) free damped harmonic oscillations analogous to the initial drop oscillations and (b) forced damped harmonic oscillations of a drop in a flow field. These two oscillations occur with the same damped oscillation frequency ω^*.

Passive blood drop initial oscillations were discussed above when numerical simulation and experimental data were compared (see Chapter 7). The experimentally observed passive blood drop behaviour soon after its formation was reasonably well predicted by the TAB model. An initially oscillating passive blood drop was observed to deform under the increasing with its fall velocity aerodynamic loading, while continuing to oscillate around an equilibrium deformed shape with the same frequency as predicted by the free oscillation theory (Rayleigh, 1892) (see Figure 6.2).

A superimposition of the initial and aerodynamically-induced oscillations may be expected, for example, in the case of the spatter drop formation and flight when the drop oscillations may be provoked by its separation from the bulk liquid as well as due to the aerodynamics effects associated with its motion. This is particularly applicable for the low to moderate Weber numbers of drop flight. This may either decrease or increase the drop oscillation amplitude.

For large-amplitude oscillations, or deformations (> 10% of the droplet radius), however, the forces governing the drop deformation are no longer independent of the degree of deformation. For large-amplitude oscillations the nonlinear mode coupling, or the dependence of the oscillation frequency on the amplitude, the asymmetry of the oscillation amplitude, and the interaction between modes occur (Becker et al., 1991; Tsamopoulos and Brown, 1983 and Basaran, 1992). The oscillation frequency of the fundamental mode decreases with the increasing amplitude. The signs of an increase in the large-amplitude oscillation decay rate have also been shown (Trinh and Wang, 1982).

This study aimed to analyze when the drop oscillations may be expected to affect the resultant bloodstain shape by investigating the oscillation lifetime and spatial dimensions (decay distance) for typical passive and spatter blood drops.

Due to the faster damping of the higher oscillation modes the fundamental mode of oscillations (with the highest oscillation frequency and lowest decay time) was considered for this study.

The oscillation frequency and decay time for the long-lasting fundamental harmonic (prolate-oblate oscillations) a drop with undisturbed diameter d are $\omega^* = \left\{\frac{64\sigma}{\rho d^3} - \left(\frac{20\mu}{\rho d^2}\right)^2\right\}^{1/2}$ and $\tau_D = \frac{\rho d^2}{20\mu}$ correspondingly (Chandrasekhar, 1959 cf. Lamb, 1932). The oscillation period is $T = \frac{2\pi}{\omega^*}$.

The time for the oscillation amplitude $A = A_0 e^{-t/\tau_D}$ to reach 1% of its initial value A_0, the oscillation lifetime, is $\tau_D^{1\%} = \frac{\rho d^2}{20\mu} ln(10^2)$. The number of oscillation periods during the oscillation lifetime can be expressed as $N = \tau_D / T$.

The time for the drop oscillation amplitude to reach 10 or 50 % of its initial value is $\tau_D^{10\%} = \frac{\rho d^2}{20\mu} ln(10)$ and $\tau_D^{50\%} = \frac{\rho d^2}{20\mu} ln(2)$ correspondingly.

In order to estimate the distance a blood drop needs to travel from its origin for the initial oscillations to decay, the drop flight was simulated with the developed code. The passive drops of 0.5-6 mm in diameter and 0.1-2 mm spatter drops were considered for this study. The passive drops were expected to form at zero initial velocity, and fall under the action of gravity and air resistance. The spatter drops with maximum possible initial velocities without drop disintegration under the most suitable for the longest drop flight conditions (see Chapter 8.2.2 and 8.2.5) were examined to estimate the maximum distance for the spatter drop oscillations to damp.

It was previously shown (Chapter 7) that the deviation between the numerical solutions for an initially deformed, oscillating drop and the one for initially spherical, non-oscillating drop was negligibly small when predicting the evolution of drop velocity, travel distance and time. Thus, for simplicity, the blood drops considered in this study were modelled as initially undisturbed, non-oscillating drops undergoing in-flight deformation due to the aerodynamic forces.

The oscillation decay time is strongly dependent on the drop viscosity, with main effect of drop viscosity to damp the oscillations. The higher the drop viscosity, the lower the

oscillation decay time. As was previously mentioned, for blood as a non-Newtonian fluid its viscosity depends on the shear rate of the flow. To define the apparent viscosity of an oscillating blood drop in an air flow the flow pattern and shear rates within the drop must be determined. The latter is a complex problem, the flow pattern and shear rate are often unknown.

So, there is an uncertainty over which values of blood viscosity to use for the calculations. This study aimed to study the effect of the viscosity on drop oscillations. The value of high-shear rate human blood viscosity of 4 mN·s/m^2 and the low-shear rate (~10 s^{-}1) viscosity of 10 mN·s/m^2 (Oguz, 2007) were used in the oscillation decay time calculations for comparison. The latter value was validated for the passive blood drop oscillation modelling (Chapter 7) and may serve as a better representation of the apparent viscosity of an oscillating blood drop.

The standard values of blood density of 1056 kg/m^3 and surface tension of 0.056 N/m at 37°C were assumed for the calculations.

The theoretical decay time and corresponding number of oscillation periods for 0.1-6 mm blood drops were plotted on Figure 8.6 for blood drop oscillation amplitude to reach 1, 10 and 50% of its initial value.

The decay time and number of oscillation periods are naturally lower for the smaller droplets and higher velocity values. A 6 mm drop needs 2.2 s or 0.9 s (for high- or low-shear rate viscosity values correspondingly) for the initial oscillations to die away. Whereas, a 0.1 mm blood drop has oscillation which decay over less than 0.5 ms. For drop oscillations to decay to 50% of the initial amplitude 0.1-6 mm drops need < 0.1-0.4 s.

The travel distance of the passive and spatter blood drops during the lifetime of the oscillations ($\tau_D^{1\%}$ and $\tau_D^{10\%}$) was plotted on Figure 8.7a and b for low- and high-shear rate blood viscosity values. The passive drops with d ≤ 2 mm were found to travel less than 30 cm before the initial oscillations die away to 1% and less than 10 cm to reach 10% of the initial oscillation amplitude. 6 mm drops needed as much as 14 m (μ = 4 mN·s/m^2) or 3.4 m (μ = 10 mN·s/m^2) of fall for the initial oscillations to decay completely. 5 m and 1 m required for oscillation amplitude to reach 10% of its initial value for the low- and high-shear rate viscosity respectively.

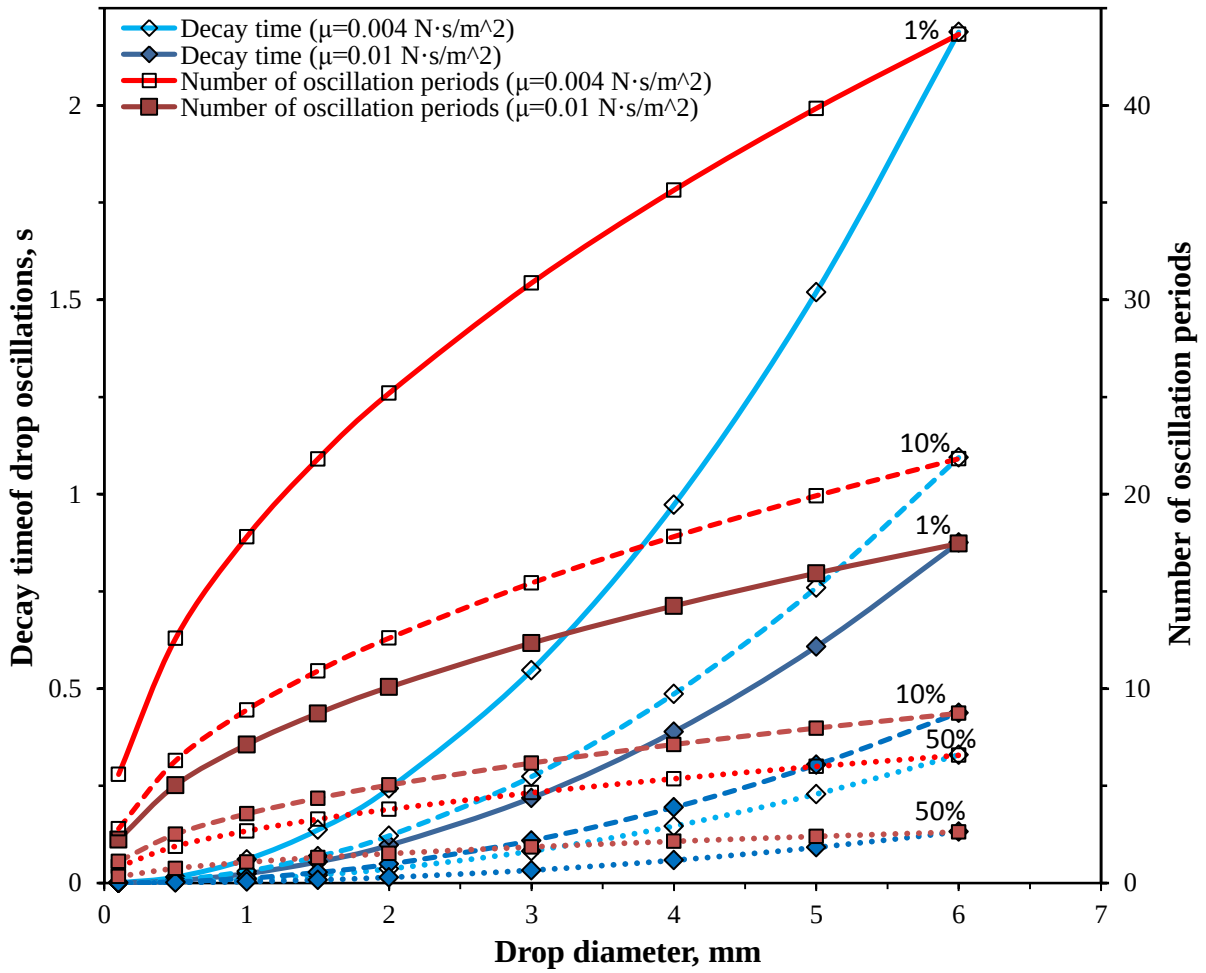

Figure 8.6. Decay time of blood drop oscillation amplitude to reach 1, 10 or 50% of its initial value and corresponding number of oscillation periods.

The spatter drops (d = 0.1-2 mm) were able to travel longer distances from the origin before the oscillations were damped due to higher velocities. These needed less than 2.5 (μ = 4 mN·s/m^2) and 1.2 m (μ = 10 mN·s/m^2) for the oscillation amplitude to reach 1% of its initial value and less than 1.4 m and 0.7 m to reach 10% of the initial amplitude respectively for the two viscosities studied.

The oscillation decay distance for the smaller spatter drops with d < 1 mm was < 0.5-1 m (for $\tau_D^{1\%}$) and < 0.3-0.6 m (for $\tau_D^{10\%}$) and well under 20-50 cm for mist-like drops with d < 0.5 mm.

The proposed polynomial correlations (see Figure 8.7a and b) may be used to predict the travel distance (y = (L^2+H^2)$^{1/2}$) of a drop with diameter d for its oscillations to decay.

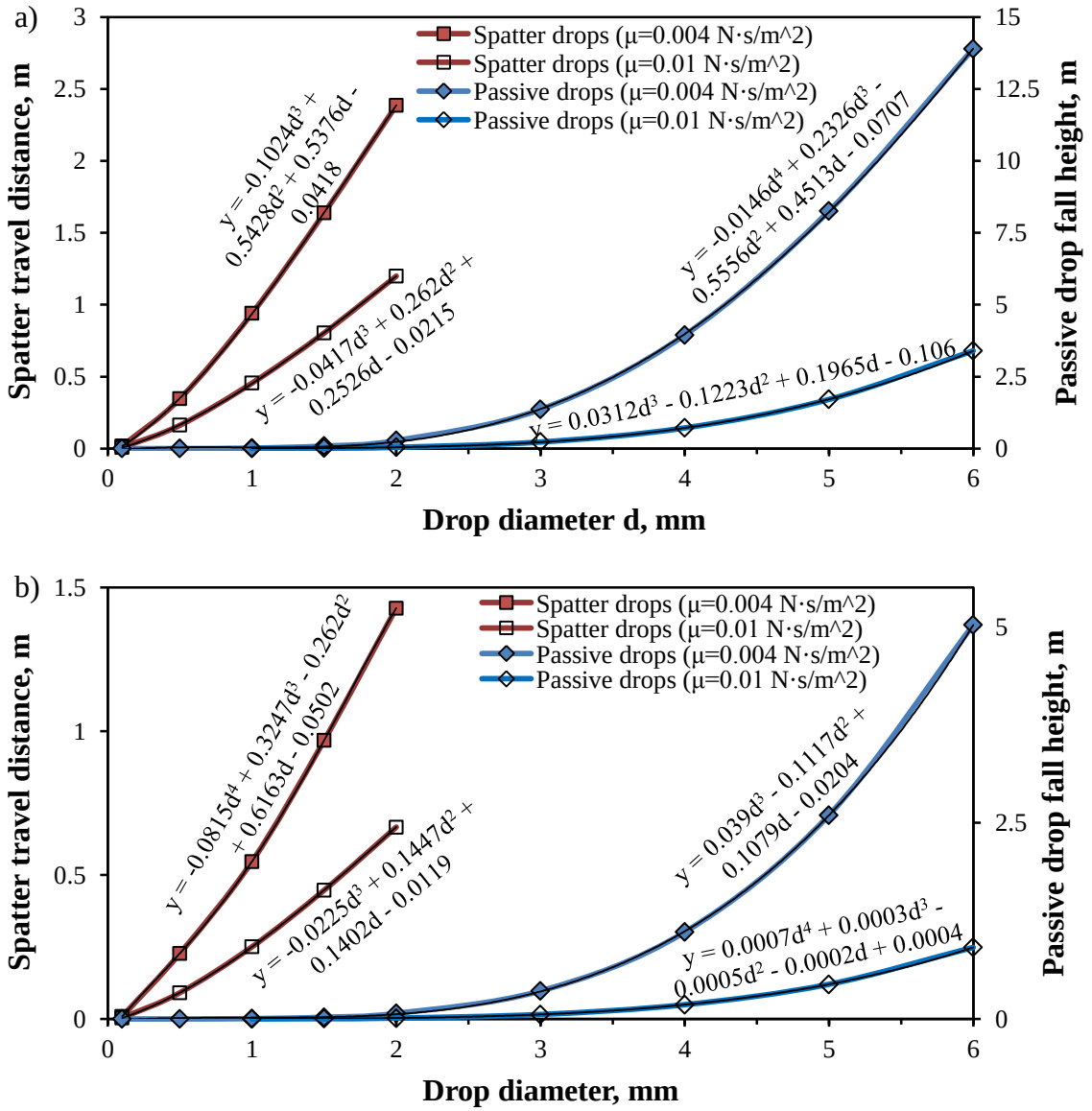

Figure 8.7. Spatter and passive drop oscillation decay distance for the oscillation amplitude to reach 1% (a) and 10% (b) of its initial value.

8.2.3.1 Comparison to previous findings

The findings of this study were in good agreement to the experimental finding for the initial oscillations of passive blood drops discussed earlier in Chapter 7. There the initial oscillations of 1.25 ± 0.05 mm blood drops were observed to decay over 0.5-1 cm and during 30-40 s. The corresponding numerical predictions of the oscillation decay time and distance were 35-40 ms and 0.6-0.8 cm. The signs of drop oscillation were experimentally observed for drops with d > 5 mm even after about 1.5 m of fall. Consistently, the predicted numerical decay distance for such drops was > 1.7 m.

Raymond et al. (1996) also investigated the initial oscillations of the passive blood drops. No detectable oscillations were found after the drops studied had fallen about 40 cm. 0.5 and 1 mm drops were argued to fall as much as 5 mm and 7 cm, correspondingly, before their oscillations damped. The numerically predicted fall distances for these drops were about five times smaller (even for the lower blood viscosity value considered) than those reported by Raymond et al.

The authors also reported shape alteration of the stains left by oscillating (distorted) drops, which they described as "unpredictable". No details of the stain shape changes were provided. Consequently, the stains located close to the presumable blood source were argued to be unreliable. Therefore, the stains further from the source were advised to be used for the drop impact angle and area of origin determination.

Gardner (1997) studied projected spatter blood drop oscillations. The drops ranged from 0.16 to 2 mm in diameter. For drop with $d < 1$ mm the oscillations were shown to damp to a negligible level within less than 0.1 s. The oscillation amplitude of drops with $d \geq 1$ mm was found to damp to about 10% of its initial value within 0.05 s from drop generation. These figures are in excellent agreement with the numerical findings discussed above with simulated low-shear rate blood viscosity of $mN \cdot s/m^2$ providing the best data fit. Smaller stains distant from the suspected blood source were recommended for the impact angle determination by Gardner.

Bond (2008) examined the necessity of the spherical drop shape assumptions for the impact angle calculations. By examining the width and length of the stains formed as a result of angled impact of oscillating passive blood drops, the author concluded that the calculated impact angles were not affected by the drop oscillations and, thus, the drop sphericity upon impact was not crucial for the sine method to be accurate. The oscillation amplitudes of the drops upon impact, as well as the experimental measurement uncertainties, however, were not reported.

8.2.3.2 Stain selection recommendations

Generally, the larger the drop (and, hence, the stain it leaves), the more long-lasting its initial oscillations. The larger blood drops, in addition, were shown to travel longer distances compared to the smaller drops at the same launch conditions (see Chapter 8.2.2).

As was mentioned earlier, drops which travelled short distances from the source may possess significant degrees of deformation (in terms of their oscillation amplitude). Based on the present findings, the blood stains (less than ~4-5 mm in diameter) formed by the spatter

blood drops with d < 1 mm may be considered reliable for the impact angle measurements if these are found more than 50 cm from the presumable blood source. Bigger stains, formed by the drops bigger than 1 mm, found 0.5-1 m away from the suspected blood source may also be suitable for the calculations. Typical passive blood drops (d > 3 mm), and corresponding stains, require more than 25 cm of the free fall for the initial oscillations to die away completely.

It should be noted that if blood drop density and/or viscosity were altered (as a result of blood dilution with other fluid, for example), the decay time and, hence, distance for the blood drop oscillations to damp would also change.

8.2.4 Effects of blood drop deformation on its trajectory and origin determination

Violent crimes involving bloodshed may result in the formation of a number of blood drops that move through air and eventually impact onto a surface producing a bloodstain pattern or blood spatter pattern. If two or more drop trajectories can be determined, from measurements of the stains it leaves, the point at which they cross is the probable location of the victim at the time the wound was inflicted. In order to accurately predict the trajectory of a drop, and therefore its origin, characteristics of drop formation mechanisms as well as all forces acting on a drop and its behaviour during flight should be considered. A drop may deform under aerodynamic loading during its flight (Clift, Grace and Weber, 1978). For high degrees of drop deformation, characteristic for the onset of liquid drop breakup, an increase in aerodynamic drag force experienced by a drop by a factor of four (steady loading) or thirteen (shock loading) was reported by Hsiang and Faeth (1995). This may lead to a significant drop trajectory alteration, which is of importance to the point of origin determination.

This study aimed to address these issues by, firstly, examining the possibility that blood drops experience pronounced deformation during flight. This has been done by analysis of the flight Weber number (We). Secondly, the flight of deformed droplets was studied numerically for typical drop sizes and velocities to reveal the effects of the drop deformation on its trajectory.

According to Hsiang and Faeth (1993, 1995) the liquid drops with flight We < 1 are effectively spherical during flight. The drop distortion from sphericity by more than 10-20% is associated with We > 3. If the flight Weber number of a drop is higher than ~10-13

(Wierzba et al., 2005; Hsiang and Faeth, 1992; Pilch and Erdman, 1987) the drop may become unstable and disintegrate into smaller fragments. The value of the critical Weber number depends on how rapidly the aerodynamic loading is applied. The deformation and breakup conditions were shown to be relatively constant for Ohnesorge numbers $Oh = \frac{\mu}{\sqrt{\rho d_0 \sigma}}$ < 0.1, which is representative for typical blood drops (see Figure 8.8).

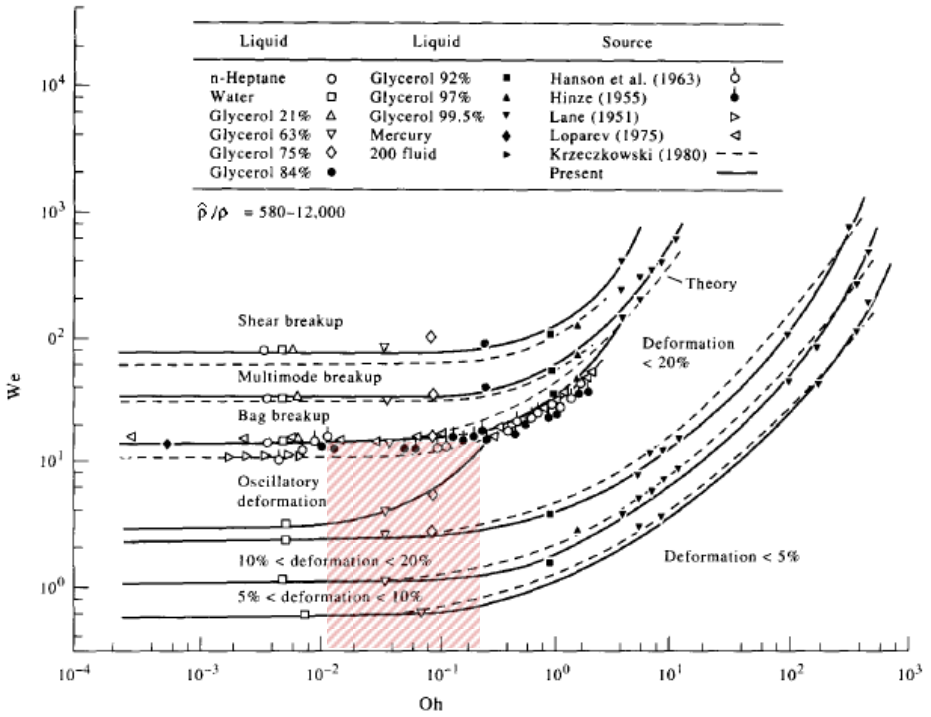

Figure 8.8. Deformation and breakup regimes for shock wave disturbance (from Hsiang and Faeth, 1995). Shaded regions correspond to We and Oh numbers of typical blood drops without drop disintegration.

The criterion for a blood drop to experience pronounced deformation during flight can thus be expressed as 3 > We > 13 or $\frac{3\sigma}{\rho} < v^2 d < \frac{13\sigma}{\rho}$. The critical Weber number of 13 was chosen to represent the extreme degree drop deformation while avoiding drop disintegration.

For the standard values of blood density of 1056 kg/m^3 and surface tension of 0.056 N/m at 37°C and the maximum critical Weber number of 13, the criterion gives $140 < v^2 d < 607$. This condition implies that the drops with d < 0.2 mm require velocities v > 30 m/s to deform significantly during flight. This may be correlated to the gunshot spatter formation conditions.

The drops with 0.2 < d < 1 mm travelling with velocities higher than about 10 to 20 m/s (impact or cast-off drops) are also expected to possess high deformation levels which may

affect their trajectory. For bigger blood drops (d > 1 mm) lower velocities (on average, less than ~15 m/s) are required for significant drop deformation to develop.

The velocity limits for pronounced blood drop deformation were plotted for blood drop with d ≤ 6 mm on Figure 8.9. The corresponding Reynolds numbers of the blood drops with initial Weber numbers of 3 and 13 were also given.

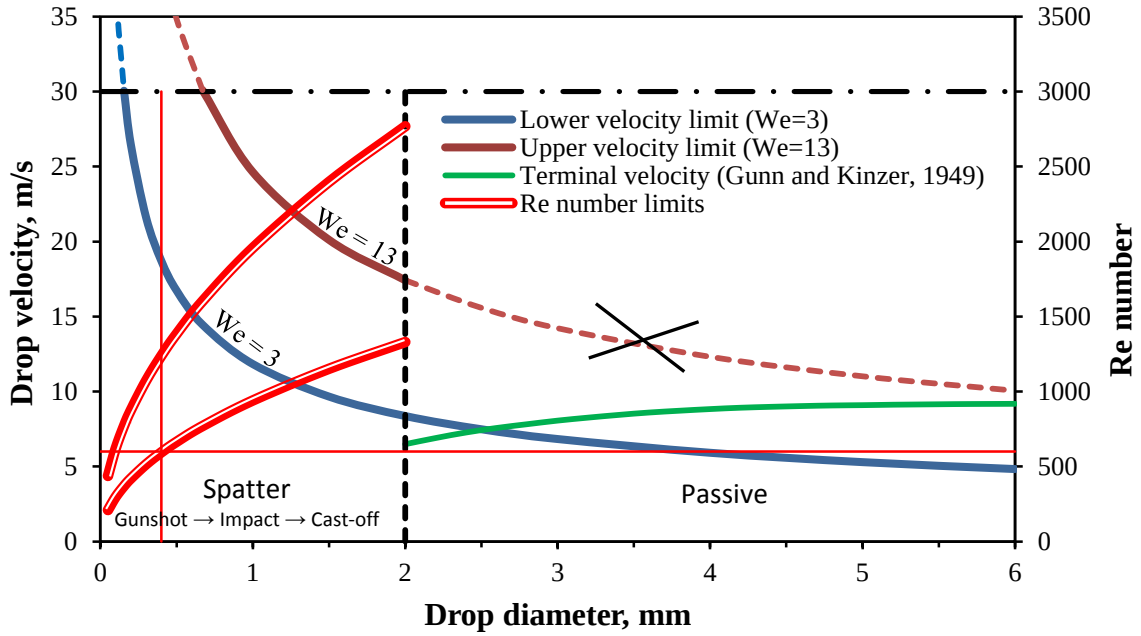

Figure 8.9. Deformable blood drop velocity and corresponding Reynolds number ranges.

The terminal velocity curve for water drops (the green curve) from Gunn and Kinzer (1949) was also plotted to show that the maximum possible velocities the passive drops may reach during flight. The dash-dotted spatter velocity curves represent the lack of experimental evidence for the feasibility of the drop velocities exceeding 30 m/s for smaller blood droplets.

The main effect of drop in-flight deformation on its trajectory is through the drag force. The latter is proportional to the square of drop velocity, projected area and drag coefficient as a function of the drop Reynolds number and shape.

Under the aerodynamic loading a drop tends to deform into an oblate spheroid. This brings an increase of the cross-flow (or projected) area of the drop; elevation of the drop drag coefficient towards that of an ultimately deformed disk-like drop. Consequently, the drag force experienced by a deformed drop rises and promotes more rapid drop deceleration and more pronounced drop trajectory curving earlier in the flight with possible impact angle and velocity alteration upon contact with a surface. The stain appearance and location may be affected as a result.

Different drops (and resulting bloodstains), however, would be affected by the deformation differently. The drop size, initial velocity and flight directionality should be considered when drawing conclusion regarding the possible effects of deformation on its trajectory.

The degree of drop deformation (or, in other words, drop aspect ratio) is correlated essentially to the drop Weber number. The drops travelling with similar We numbers would possess similar levels of deformation (namely, aspect ratios). The projected areas, however, would be different. In particular, the increase in the projected area of a drop due to its deformation is smaller for smaller drops having same levels of drop deformation as the bigger drops.

Additionally, the smaller drops have lower Reynolds number compared to the bigger drops travelling at similar velocities and Weber numbers (see Figure 8.9). The drop drag coefficient for both limiting drop shape configurations, a sphere and a disk, increases rapidly as Re reduces for low Re numbers ($Re < \sim 500\text{-}10^3$) (Clift, Grace and Weber, 1978). The latter leads to the drag force rise and rapid drop deceleration reducing the time and distance over which a drop may experience the effects of deformation.

This particularly applies to drops with $d < 0.5$ mm at lower We numbers and/or velocities. It is possible to say that these drops are more affected by the increase in drag due to the drag coefficient dependence on the Re number (with or without drop shape alteration) than due to the drop deformation.

The drag coefficient (both of a sphere and a disk) decreases with the increase in Re number and is relatively independent of Re number for $\sim 10^3 > Re > 3.5 \cdot 10^5$ (Figure 6.3). The deformation effects towards the drop drag increase are more important than the Reynolds number effects for the drops that travel with these Re numbers.

The drop launch conditions may also affect the way drop deformation affects its flight. Sufficient drop travel times, and distances, are needed for the effects of air resistance forces and, with it, drop deformation to influence its flight path. Thus those drops which originated, for example, at optimal angles for the furthest flight to have longer trajectories before impact with a surface and would be more susceptible to the effects of deformation.

The effects of drop deformation may result in significant drop trajectory curving and impact angle and velocity alteration. The downward-moving drops, however, are expected to target the floor at angles close to 90° and are rarely useful for the area of origin calculation. The effect of drag force (and deformation, in particular) on falling drops is to slow them down, not to deflect their trajectory.

To quantify the effects of drop deformation the numerical study of deformable and, for comparison, spherical drops flight was studied numerically. The limiting case of maximum drop deformation (We = 13) for typical blood drops of 0.2-2 mm in diameter was considered. Drops with upward directionality were studied.

The features of the drop deformation and drag coefficient effects above discussed were observed numerically. The trajectories of deformed drops became more curved earlier in flight compared to the undisturbed (spherical) drops.

The drops with d < 0.5 mm decelerated completely within less than 1 m of flight with slightly smaller (by less than 20 cm) flight height and range when the drop deformation was considered into calculations. The drop impact angle and velocity were not affected (<< 1%).

As the deformed drop size increased the trajectory deviation from that of a spherical drop became more pronounced.

Thus, for the biggest drop studied of 2 mm in diameter at We = 13 the maximum deviation between the flight height and range of a deformed and spherical drop were as much as about 1 and 2 m correspondingly (see Figure 8.10). About 25 % difference in the deformed and undisturbed drop impact angles on the wall, and less than 5 % on the ceiling, was observed with around ~ 30 % difference in the drop velocity at impact with the ceiling and wall.

The alteration of the impact angle observed was towards the way that may lead to overestimation of the blood source height. The blood drop origin height was overestimated (using the straight-line trajectory approximation) by about 1 m and 25 cm for the studied 2 mm blood drop impacted a vertical wall in 2 m of flight in horizontal direction and the ceiling 1 m above the drop origin respectively.

Drop deformation, however, was observed to affect drop trajectory considerably only after about 1-2 m of its flight.

Summarizing, the impact and larger gunshot spatter drops are expected to be affected by the drop deformation. Larger drops at higher velocities are more affected by the deformation.

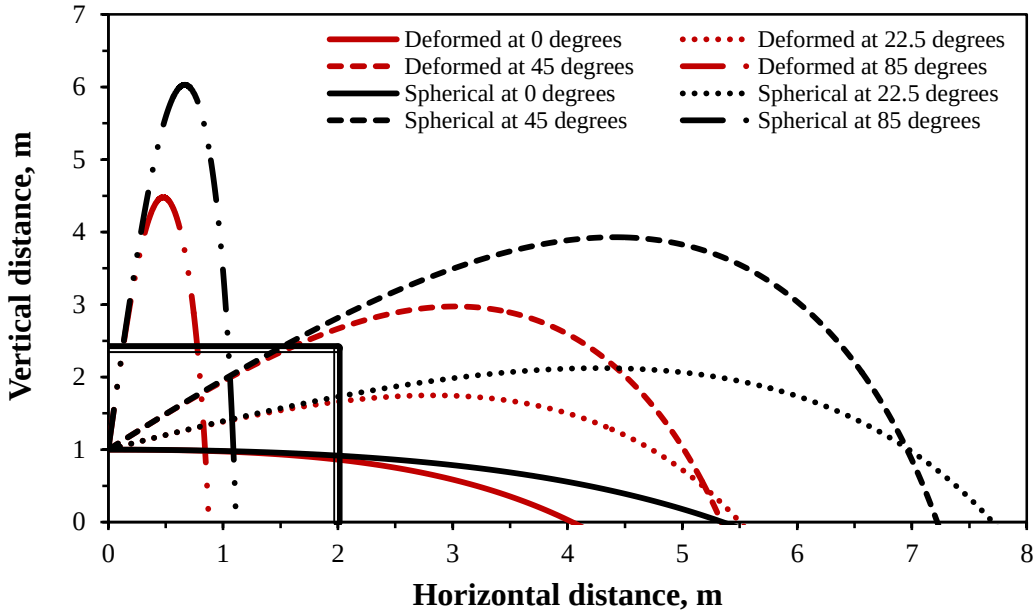

Figure 8.10. Drop trajectories of a deformable and spherical 2 mm blood drop launched from 1 m above the ground. The thick-thin lines represent ceiling (2.4 m-high) and a wall 2 m away from the blood source.

The effects of drop deformation generally should not be neglected as these may lead to the flight trajectory curving earlier, and changes in drop impact angle and velocity. This may result into the blood drop origin height overestimation for stains found on walls and ceiling. A sufficient flight distance (> 1.5-2 m) is needed for the effects of drop deformation to be noticeable, however.

8.2.5 **Blood drop breakup conditions, time and distance**

Spatter patterns are produced as a result of blood put into motion by an external force applied to a source of blood (SWGSTAIN terminology, 2009). Examples are the impact and gunshot spatter patterns produced by blunt force impact or bullet penetration.

Spatter formation can be viewed as the series of the liquid mass disintegration stages with smaller fragments forming on each stage. In particularly, blood masses, put into motion by an external force, may protrude in a form of ligaments, jets or sheets. The latter under the action of aerodynamic and surface tension forces become unstable and disintegrate into smaller liquid fragments (droplets and/or ligaments), which may subsequently breakup under appropriate conditions. Such process of successive liquid mass division (or disintegration) stages is called the cascade atomization (Tanner, 2003).

The spatial boundaries of this process may be associated with the spatter origin, a region in space where the process of the liquid mass disintegration was completed with the fragments (drops or ligaments) produced being stable. The latter may move further from the origin and eventually target a surface and produce a stain.

The duration and, hence, spatial dimensions (or origin) of the spatter formation is expected to depend on the magnitude and impulse of the external disturbing force applied to the source of blood, blood source characteristics and response behaviour and, subsequently, on the physical properties and Weber numbers of the liquid fragments (drops) formed.

In this light, the distinct drop (or ligament) disintegration can be viewed as a part of the spatter formation process. The duration and the dimensions of the spatter formation region (origin) are generally different from the breakup time and distance of a single fragment (drop for instance). However, the distance a single liquid mass can travel away from its origin before it completely disintegrates may be correlated to the typical dimensions of the spatter formation region (or the blood origin).

The drop breakup occurs when the flight Weber number of a drop is higher than some critical value (~8-13 according to (Wierzba et al., 2005; Hsiang and Faeth, 1992; Pilch and Erdman, 1987)). As was mentioned in Chapter 7, the blood drops from the impact experiments were observed to breakup at Weber numbers of ~13-20.

These two extreme values, i.e. 13 and 20, were used to determine the critical for drop breakup conditions in terms of drop size and corresponding velocity. The time for a drop to breakup was calculated according to the Pilch and Erdman's (1987) expression as $t_{bup} = t^* \cdot 6(We - 12)^{-0.25}$, where $t^* = \frac{d_0}{V_{rel}}\sqrt{\frac{\rho}{\rho_a}}$ is the characteristic time of drop breakup for Oh < 0.1 and 12 < We < 20, which has been validated for blood drops in Chapter 7.

To infer the distance an unstable blood drop can travel before the disintegration (during t_{bup}) the ideal scenario of the furthest drop flight (described in Chapter 8.2.2) was considered. The drop trajectory length (or its distance from the origin) was approximated as $\left(L^2+H^2\right)^{0.5}$, where L and H are the final trajectory range and height.

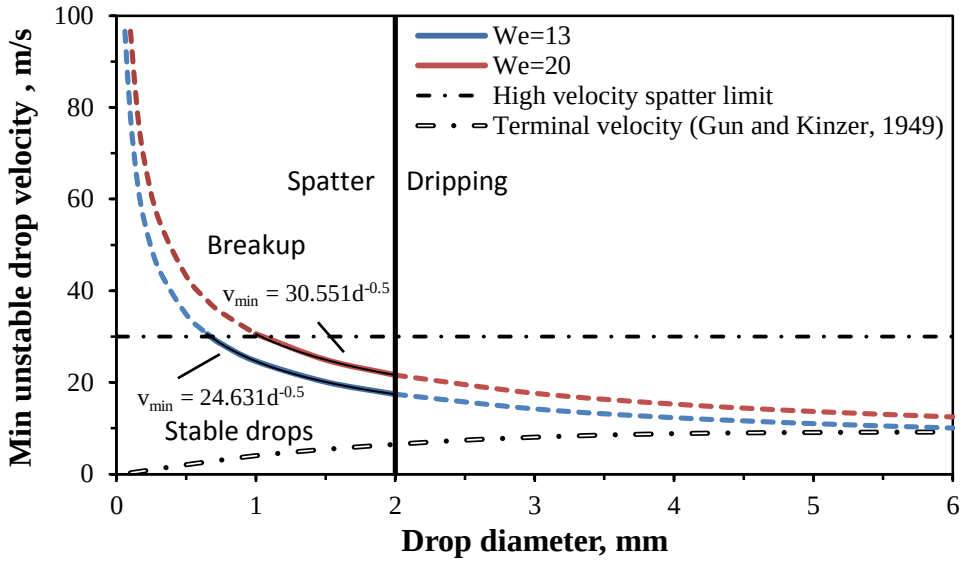

Figure 8.11. Minimum unstable blood drop velocity.

The minimum velocities necessary for drop disintegration to commence were plotted for We=13 and 20 on Figure 8.11. The minimum breakup velocity in m/s could be correlated to the negative square root of the blood drop diameter, $d^{-0.5}$, for $0 < d < 6$ mm and We = 13 and 20 (see Figure 8.11 for the expressions).

The blood drops with $d > 2$ mm (dashed curve segments) were considered to form as a result of passive dripping. The terminal velocity curve for water drops (the double dash-dotted curve) from Gunn and Kinzer (1949) was also plotted to show that the passive drops are unlikely to reach the predicted unstable velocities during their fall and disintegrate into smaller droplets. To break up, any drop of $d < 6$ mm will need to travel at more than its terminal velocity, so will be decelerating, whatever direction it travels in. It can only break up if it starts to travel at a velocity greater than terminal.

The spatter drops with $0.5 < d < 2$ mm for We=13 or $1 < d < 2$ mm for We=20 require velocities upon formation less than 30 m/s to breakup. The smaller droplets ($d < 0.5$ mm), typical for gunshot spatter, are expected to breakup at much higher velocities. More detailed investigation of the gunshot drop size and feasible (or realizable) velocity ranges is required, however. The single dash-dotted line represented the velocity of 30 m/s, characteristic for "high-velocity" spatter (Laber, 1985).

The breakup time and corresponding distance for typical blood drops were plotted for the Weber numbers considered on Figure 8.12. The dash-dotted breakup time curves represent the unlikelihood of the breakup for passive drops ($d > 2$ mm) or the lack of

experimental evidence for the feasibility of the drop velocities exceeding 30 m/s for smaller, mist-like, blood droplets.

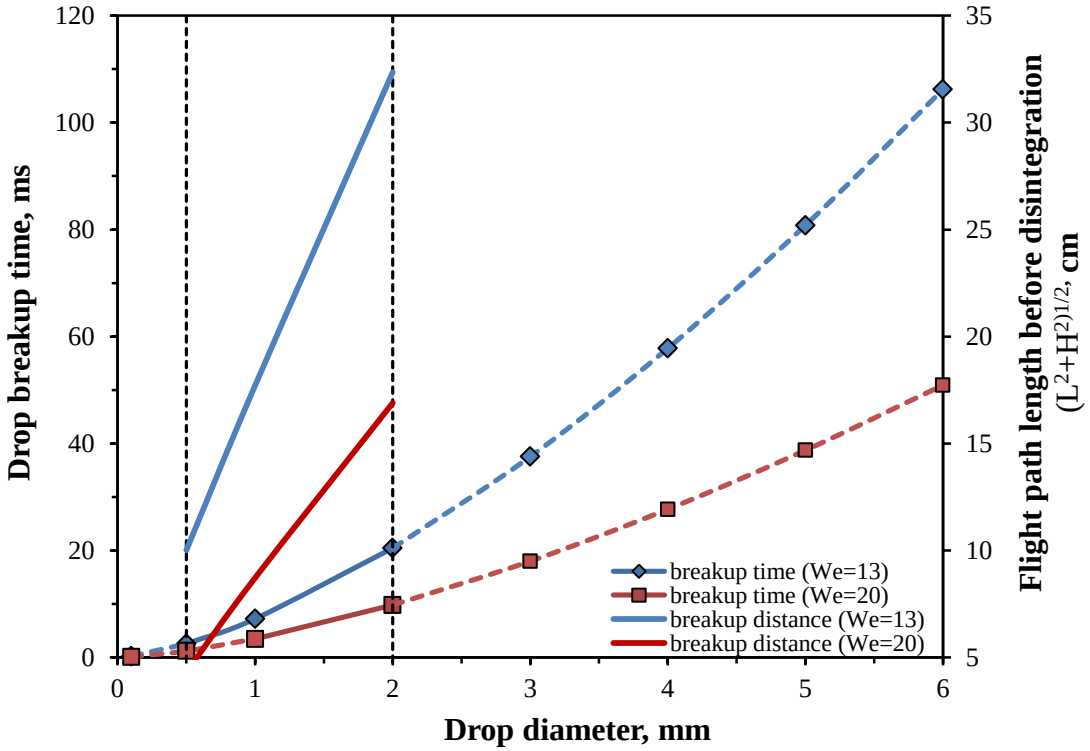

Figure 8.12. Blood drop breakup time and distance.

The breakup time was seen to increase as drop diameter and initial Weber number increase. For the spatter drops (d < 2 mm), the maximum breakup time was about 20 and 10 ms for d=2 mm at We=13 and 20 correspondingly. For the smaller droplets (0.5 < d < 1 mm) the breakup time decreased to 2.5-3.5 ms. The corresponding spatter drop breakup distance ranged from 32 cm (We=13) or 17 cm (We=20) for a 2 mm blood drop to 10 cm (We=13) or 4 cm (We=20) for a 0.5 mm drop.

Even smaller droplets (d < 0.5 mm), especially at higher velocities (>> 30 m/s), possibly characteristic to the condition of the gunshot spatter formation, would breakup much faster and over much shorter distance (a couple of centimetres or even millimetres).

These numerical results were in good agreement with the experimental findings for the impact spatter drop disintegration (see Chapter 7 for more details) when the most of the breakup cases observed occurred close to the impact point, within the first 10-25 cm of the spatter flight, for drops with d ≤ 1.5-2 mm.

This suggested that the special dimensions of the spatter formation process associated with an impact event (impact or gunshot spatter) may be of a couple of millimetres or

centimetres to around tens of centimetres in radius. The latter should be taken into account when drawing conclusions about the area (or volume) of blood origin determination.

Additionally, it can be argued that if bloodstains with estimated original drop diameters > 2 mm are found at a crime scene, they are most likely originated with velocities less than ~14 m/s. Blood drops with d = 0.5-2 mm (and resulting stains) had probably formed with velocities less than 30 m/s.

8.2.6 **Effects of air currents and winds on blood drop flight**

Drops are not necessary travelling in still air before impacting a surface. Indoor or outdoor air currents or winds add to the drop relative velocity, and, consequently, may alter the drag force experienced by a drop and its trajectory. The effects of air movement on drop flight depend on the air velocity magnitude and directionality as well as drop size (weight) and velocity. Naturally, the greater the velocity of a drop the less pronounced the effects of air movement on its flight. Larger drops experience more drag, but also have greater inertia. The validated model was used to study the effect of indoor air currents and outdoor winds on the trajectories of representative blood drops.

The trajectories of drops moving with a tailwind are generally longer and less curved, than for the same drop moving through still air. In turn, the trajectory of a drop moving into a head wind may curve more compared to the same drop moving through still air. In some cases a drop may even reverse its movement and be blown back towards its source. Downward air currents may reduce and flatten drop trajectory.

All these effects may lead to drop impact angle, impact velocity, stain morphology and stain position differing from those which would result from the same drop moving in still air. If, when a stain pattern at a crime scene is being analyzed, still air is assumed, the area of origin inferred may be in error.

In order to estimate possible drop trajectory alteration by the surrounding air movement numerical tests with the developed code for deformable blood drops were performed. The investigated blood drop size and velocity ranged from 0.1 to 5 mm and from 0 to 30 m/s correspondingly. These values represent typical spatter and passive drops. The blood source height was fixed at 1.4 m (typical of a kneeling victim); launching angles of spatter drops were 0º and 45º to the horizontal.

From standards and regulation on indoor air conditions (Brelih, 2011) the maximum permissible air velocity in dwellings is 0.15 – 0.3 m/s. To investigate the effects of these air currents on blood drop flight air velocity of 0.5 m/s was chosen as a worst case scenario.

To represent outdoor conditions wind velocity of 5 m/s was considered. According to the meteorological data on wind velocity in New Zealand, the average annual wind speed is ~ 8 m/s (www.metservise.co.nz).

In order to simplify the problem the air velocity was considered to be constant in magnitude and direction for the duration and range of the drop fight (generally less than 1 s and < 2.5 m). Drop flight under head, tail and cross wind conditions was studied (see Figure 8.13).

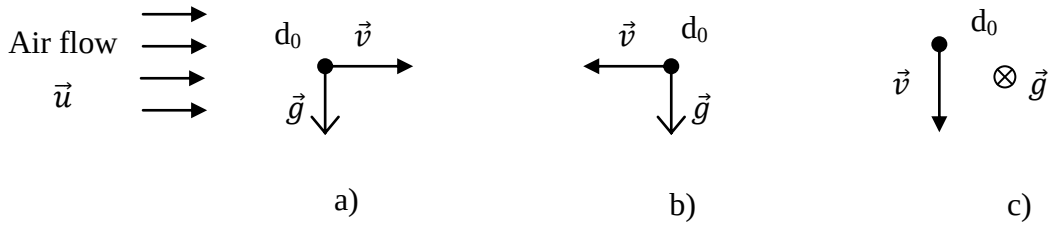

Figure 8.13. Air flow and blood drop directionality arrangements studied: (a) downwind/tail wind, (b) upwind/head wind and (c) cross wind.

The calculated trajectories for passive drops (falling perpendicular to the air flow) experiencing air currents of 0.5 m/s were displaced from their undisturbed (no wind) flight paths by less than 2 cm for a 5 mm diameter drop and by 20 cm for the case of a 1 mm diameter blood drop.

Under a 5 m/s wind, however, passive stain location (or passive drop position at impact with the floor) shifted by as much as 0.5 m for the 5 mm drop and 2.3 m for the 1 mm drop. The displacement will increase if the blood source is higher.

The spatter drops moving against the headwinds landed closer to the horizontal position of the blood source that they would in still air. The maximum reductions in drop flight range due to air current (horizontal distance travelled) were 1-1.5 m for smaller droplets studied. The spatter droplets (0.1-1 mm in diameter at velocity ≤ 30 m/s) moving into a headwind of 5 m/s reversed their flight direction and eventually landed within 1 m vertically from the blood source position.

As the air motion affects drop trajectory, the impact angle of the drop onto a ceiling or wall will also be affected. This depends on the drop and air flow directionality and velocity, as well as the blood source location relative to a wall or ceiling. This may lead to the blood source height overestimation from the blood stain measurements.

The minimum air velocity for a spatter blood drop to reverse its flight direction and reach its initial horizontal coordinate (or the horizontal position of its origin) was also

investigated (see Figure 8.14). Blood drops with diameters of 0.1, 0.5 and 1 mm launched at 0° to horizontal at velocities of 1, 10 and 30 m/s moving against the parallel air flow were considered.

Spatter drops of d < ~0.5 mm are highly susceptible to drift along the air flow, especially at lower velocities. These require headwinds of < 1 m/s to reverse their direction, over a wide range of their initial velocities. These, in addition, travel quite short distances and can land on the floor within 50-60 cm from the origin.

Drops larger than 0.5 mm may reverse their directionality at incident air velocities less than 2-5 m/s depending on their initial velocity. The higher the launching angle (i.e. closer to vertical), the lower the air velocity required to alter its flight path by a given amount, due to the decelerating action of the gravitational force.

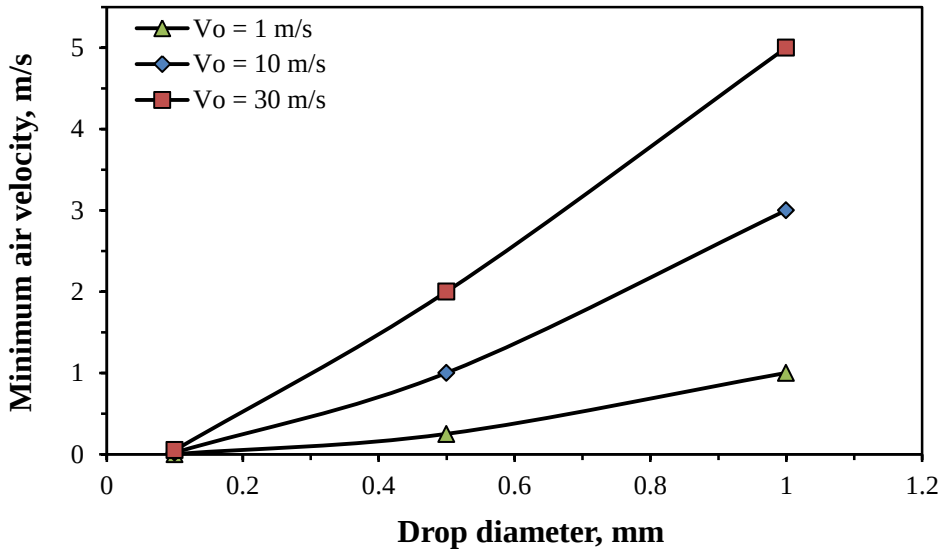

Figure 8.14. Minimum air velocity necessary to reverse spatter blood drop directionality. V_0 is the blood drop initial velocity. Note: 1 mm drop at 30 m/s is unstable and will break up soon after formation.

For the case of a downwind drop motion with a tailwind velocity of 5 m/s (in idealized outdoor conditions) a spatter drop may travel as much as 5-10 m.

In cross- wind conditions the drop trajectory tends to deflect in the direction of the air flow. In an enclosed space, such as a room, a drop may cease to target one surface (wall) and end up on the floor or adjacent wall or other surface depending on the surrounding air velocity. The smaller droplets may land on the surface facing the air flow. The drop may travel further horizontally from its source compared to a similar drop in still air.

The smaller the size and lower the velocity of a drop, the more pronounced the effects of cross-current and wind on the drop's flight path. Thus for a 1 mm blood drop originated at 1.4 m above the ground level with initial velocity of 1-30 m/s the maximum numerical trajectory deflection from its undisturbed path was 10-30 cm and 2-4 m for the case of cross-wind (0.5 m/s) and (5 m/s) correspondingly. For a 0.1 mm drop these values increased to 2-3 m (0.5 m/s) and ~10 m (5 m/s).

8.2.7 **In-flight blood drop evaporation considerations**

In-flight evaporation of water from a blood droplet may affect its size, surface tension and viscosity, and as a consequence, trajectory. To determine whether this is a significant effect, the evaporation of water from an airborne blood droplet was estimated for typical ambient conditions.

In the vicinity of a water droplet surface S_d water vapour is in equilibrium with the water in the drop. It is saturated and has a high density ρ_s (number of water molecules per unit volume) at the given (droplet) temperature. Far away from the droplet water vapour density ρ_{amb} is determined by the ambient temperature and humidity, and normally is lower than that close to the droplet. Water molecules are continuously transported to the environment (in the direction of lower density) by molecular and/or convective diffusion. In the case of a water droplet falling in air, forced convection is the prevailing transport mechanism.

There are a number of differences between the case of blood and water droplets. First, water vapour density at blood droplet surface is expected to be lower than for pure water at the same temperature. This is due to the lower concentration of water molecules in blood and their interactions with other constituents of blood (salts, proteins, etc.). Furthermore, evaporation from the surface decreases the water content of blood even more. So, another mass transfer process occurs – water diffusion within the blood droplet (from the inside towards its surface). It can only decrease the overall rate of the water transfer from the droplet.

By assuming in the evaporation calculations water vapour density at the blood droplet's surface to be the same as on a pure water surface, one overestimates the corresponding mass transfer rate. Nevertheless, this approach provides good estimation of the maximum possible evaporation rate of the blood droplets.

The rate of mass transfer process (kg of water evaporated from 1 m^2 per 1 s) is: $j = \beta(\rho_s - \rho_{amb})$, where β is the mass transfer coefficient determined by the intensity of the

active transport mechanisms. In the case of a water droplet with initial diameter d moving with velocity V in air forced convection is the prevailing transport mechanism and the following relationship for the mass transfer number applies $Nu' = \frac{\beta d}{K}$ (Kincaid and Longley, 1989): $Nu' = 2 + 0.6Sc^{1/3}Re^{1/2}$, where $Re = \frac{dV}{\nu}$ is the Reynolds number, $Sc = \frac{\nu}{K}$ is the Schmidt number, $K = (101.3/P_{amb})8.8 \times 10^{-10}T_{amb}^{1.81}$ is the diffusivity of water vapor in air in m2/s. The loss of mass from a spherical drop is then $\Delta m = \int j dS_d = \pi d^2 j$ in kg/s.

The percentage reduction in drop diameter, $\Delta d/d \times 100\%$, was estimated for 0.1-6 mm blood drop moving with constant velocities of 1-30 m/s in air with relative humidity RH = 50% and 0%, T_{amb} = 20 ºC and P_{amb} = 101.3 kPa (see Figure 8.15). The drop flight was considered to be 0.5 s long. The drops were at the constant temperature of 37 ºC during the flight.

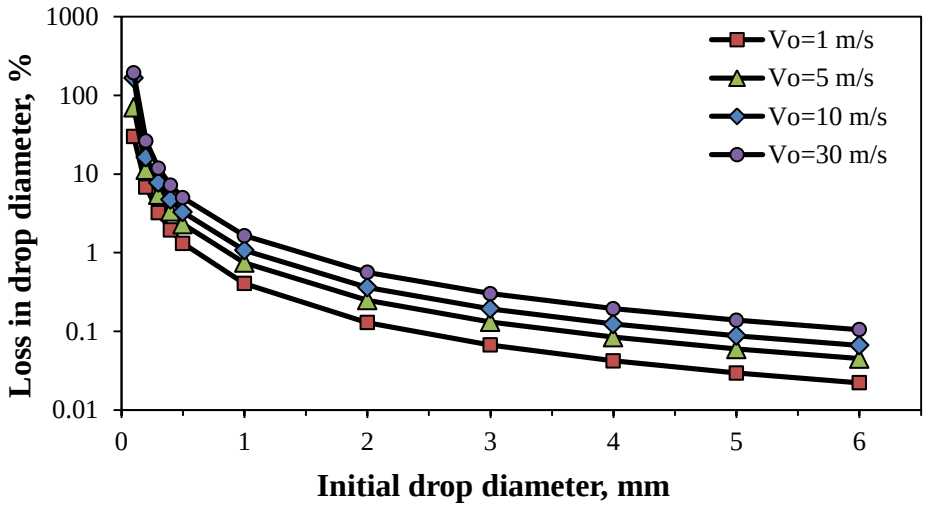

Figure 8.15. Drop diameter loss due to in-flight evaporation for RH = 50 %.

The increase of the relative humidity from 50% for 'normal' conditions to 0% corresponding to dry air conditions led to the increase in the evaporation rate and 60% increase in the drop diameter loss irrespective of drop velocity. A drop with $d \geq 1$ mm was predicted to lose less than 1% (RH = 50%) and 3% (RH = 0%) of its diameter regardless of its initial velocity. The drops with $0.2 < d < 1$ mm in diameter lost 1-30% (RH = 50%) and as much as 50% (RH = 0%) in their diameters. Drops of < 0.2 mm were expected to most likely to evaporate completely shortly after formation. As the majority of measureable stains result from droplets of >1 mm in diameter, the effect of water evaporation on the trajectory of the drop was negligible under the studied conditions.

The drop velocity may change rapidly during the droplet's flight which would reduce the mass transfer and drop diameter loss.

Along with the evaporation, heat transfer also takes place during the flight of blood droplets. It tends to bring temperature of the droplet from body temperature to the ambient temperature and in the end affects the evaporation rate through a decrease in saturation pressure at the droplet surface. The latter is due to the direct proportionality of the vapour saturation pressure to the drop surface temperature, which decreases in the considered scenario.

This, however, only decreases the mass transfer from the drop surface.

Therefore if the more detailed estimation of the effects of drop in-flight evaporation was required the study of the combined heat and mass transfer processes accompanying projection (flight) of warm blood droplets under various (ambient) conditions needs to be conducted (see for example Kincaid and Longley, 1989).

In addition, there are reports that the evaporation rates (per unit area) are greater for deformed (Jeng and Deng, 1996) and oscillating drops (Zhu et al., 2002; Guan et al., 2005). It has been shown that the mass flux varies along the surface of a deformed drop (Mashayek, 2001). The evaporation rate of an oscillating drop changes in time, equaling or exceeding or the evaporation rate of an equivalent spherical drop. It should be mentioned that these data was produced for the case of high surrounding air temperatures (fuel combustion).

8.3 Backward trajectory reconstruction considerations

BPA analysts deal with a complex problem to determine the origin and mechanism of formation of bloodstain evidence (inverse or 'backward' problem). Ideally, to reconstruct the sequence of events in inverse order from drop staining on a target surface, drop impact, drop flight and formation and, desirably, wound and wound-inflicting event characteristics, all relevant physics phenomena need to be considered and accounted for. Rarely can this be achieved in practice.

Here is where the study of the events preceding bloodstain formation in their actual order ('forward' approach) from the known blood origin to stain formation proves to be valuable in describing the character of the events in opposite order supporting the inverse problem solution. This applies to all of the phenomena involved in bloodstain formation: blood drop impact, flight and formation dynamics. The study of blood drop flight dynamics, for instance, may promote understanding and provide better means of investigation of the

behaviour of blood drops after generation. This helps to distinguish possible and dismiss unfeasible or improbable blood drop flight and, to some extent, formation scenarios.

The extent to which bloodstain patterns may be traced back to the origin and the mechanism of their formation be determined depends on the amount and accuracy of the information that can be extracted from the bloodstain evidence and on the accuracy of the methods used for blood origin determination.

The uncertainties associated with the stain-related measurement, such as in drop diameter, impact velocity, impact and glancing angles estimation from stain characteristics, remain high in BPA. Reliable correlations may be made only for certain types of stains and target surfaces (MacDonell and De Lige, 1989, Rowe, 2006 and Wells, 2006).

Another source of uncertainties in the blood origin is associated with the trajectory reconstruction methods. To reduce the errors in blood origin determination an accurate (full and validated) model for blood drop trajectory prediction should be used.

Even providing the accurate estimates of blood drop size, impact angle and velocity and trajectory reconstruction method blood origin determination remains a complex problem since some amount of the information about the event that led to bloodstain pattern formation tends to be lost in the process. This includes the initial conditions of spatter generation such as the energy of the blood drop generation, characteristics of wound and wounding mechanism. Initial characteristics of formed blood drops (initial oscillations and deformation levels, for example) may also be lost while the drop is in flight prior to the impact.

The final part of this thesis was dedicated to the implementation of an accurate technique for blood drop trajectory reconstruction back from the stain to blood origin (called ‘backward’ further in the text). The developed and validated model earlier (Chapter 6 and 7) of blood drop trajectory simulation from the blood origin to the stain (or ‘forward’) was used as a basis for ‘backward’ calculations.

This chapter describes the model aspects of backward trajectory reconstruction. The effects of uncertainties of drop size, impact angle and velocity on deformable blood trajectory and the area of origin determination are discussed. The estimated uncertainties in blood origin inference associated with the range of natural variability of human blood physical properties (density, surface tension and viscosity) are included for typical blood drop flight conditions. The discussion of the extent to which a blood drop trajectory can be traced back to the origin for passive, cast-off and impact blood drops is provided.

8.3.1 **Backward blood drop flight model implementation**

The backward blood drop trajectory was simulated on the basis of the developed forward model for deformable blood drop flight simulation (Chapter 6 and 7).

The symmetry of Newton's Second Law with respect to inversion of time (a substitution of time direction from *t* to -*t*) was used to rewrite the equations for drop acceleration for the reverse (backward) motion into a form with the sign of the drop relative velocity V_{rel} inverted:

$$a_{x,z} = \frac{dv_{x,z}}{dt} = \frac{1}{2m} C_d A \rho_a \frac{V_{rel\,x,z}}{|\vec{V}_{rel}|}$$

for x- and z-components and

$$a_y = \frac{dv_y}{dt} = -\frac{(\hat{\rho} - \rho_a)g}{\hat{\rho}} + \frac{1}{2m} C_d A \rho_a \frac{V_{rel\,y}}{|\vec{V}_{rel}|}$$

for y-components of drop acceleration. The force of gravity was directed downwards along y-axis.

From the backward point of view on the event preceding stain formation a blood drop tends to accelerate during its reversed movement. The aerodynamic loading on a drop increases with the relative drop velocity, thus it deforms and at some conditions develops oscillations.

The two models of droplet deformation based on the findings of Green (1975) and Hsiang and Faeth (1995) for steady drop deformation described in Chapter 6 provided straightforward approach for reverse drop deformation calculations based on either drop the Bond number or We number of accelerated reverse drop motion calculation.

The more detailed and accurate (refer to Chapter 7) TAB model for drop deformation, oscillation and breakup modelling needed to be amended in order to predict reverse in time drop distortion.

The equation of motion of the dimensionless drop distortion *y* (Figure 6.2) after time inversion was written in a form

$$\frac{d^2y}{dt^2} - \frac{40\hat{\mu}}{\hat{\rho}d^2}\frac{dy}{dt} + \frac{64\sigma}{\hat{\rho}d^3}(y - We_C) = 0.$$

After the substitution of variables $y(t)$ by a new variable $y'(t) = (y(t) - We_C)$ the roots (r) of the characteristic equation for the differential equation of drop distortion

$$r^2 - \frac{40\hat{\mu}}{\hat{\rho}d^2}r + \frac{64\sigma}{\hat{\rho}d^3} = 0$$

were found in a form

$$r = \frac{20\hat{\mu}}{\hat{\rho}d^2} \pm \sqrt{\left(\frac{20\hat{\mu}}{\hat{\rho}d^2}\right)^2 - \frac{64\sigma}{\hat{\rho}d^3}}.$$

For the case of blood drops $\left(\frac{20\hat{\mu}}{\hat{\rho}d^2}\right)^2 < \frac{64\sigma}{\hat{\rho}d^3}$, which gave two complex roots for the equation of motion of drop distortion in a form

$$y' = \frac{20\hat{\mu}}{\hat{\rho}d^2} \pm i\sqrt{\frac{64\sigma}{\hat{\rho}d^3} - \left(\frac{20\hat{\mu}}{\hat{\rho}d^2}\right)^2}.$$

The general solution of the equation of motion of drop distortion thus was

$$y'(t) = e^{t/\tau_D}\{C_1 \sin(\omega t) + C_2 cos(\omega t)\}$$

with $\omega = \sqrt{\frac{64\sigma}{\hat{\rho}d^3} - \left(\frac{1}{\tau_D}\right)^2}$ and $\tau_D = \left(\frac{20\hat{\mu}}{\hat{\rho}d^2}\right)^{-1}$.

The drop distortion rate

$$\frac{dy'}{dt} = \frac{1}{\tau_D} e^{t/\tau_D}\{C_1 \sin(\omega t) + C_2 cos(\omega t)\} + e^{t/\tau_D}\{C_1\, \omega\cos(\omega t) - C_2 \omega sin(\omega t)\}$$

was found subsequently.

The constants C_1 and C_2 were chosen from the initial conditions:

$$y'(t=0) = y_0 - We_C = C_2$$

and

$$\left.\frac{dy'}{dt}\right|_{t=0} = \dot{y_0} = \omega C_1 + \frac{1}{\tau_D} C_2 = \omega C_1 + (y_0 - We_C)\frac{1}{\tau_D}$$

from where

$$C_2 = \frac{1}{\omega}\left(\dot{y_0} - \frac{(y_0 - We_C)}{\tau_D}\right).$$

Consequently, the reversed (backward) dimensionless drop distortion y and corresponding rate of distortion change $\dot{y}$ were

$$y(t) = We_C + e^{t/\tau_D}\left\{\frac{1}{\omega}\left(\dot{y_0} - \frac{(y_0 - We_C)}{\tau_D}\right)\sin(\omega t) + (y_0 - We_C) cos(\omega t)\right\}$$

and

$$\dot{y}(t) = \frac{dy}{dt} = \frac{(y - We_C)}{\tau_D} + \omega e^{t/\tau_D}\left\{\frac{1}{\omega}\left(\dot{y_0} - \frac{(y_0 - We_C)}{\tau_D}\right)\cos(\omega t) - (y_0 - We_C) sin(\omega t)\right\}.$$

The inverse equations of blood drop motion and drop distortion and distortion rate of change were then solved numerically with time discretization $\mathrm{t}^{n+1} = \mathrm{t}^{n} + \Delta\mathrm{t}$ in the same way as the 'forward' set of equations (Chapter 6). The explicit finite-difference expressions for the drop distortion

$$y^{n+1} = We_C + e^{\Delta t/\tau_D}\left\{\frac{1}{\omega}\left(\dot{y}^n - \frac{(y^n - We_C)}{\tau_D}\right)\sin(\omega\Delta t) + (y^n - We_C)cos(\omega\Delta t)\right\}$$

and distortion rate of change for each time step

$$\dot{y}^{n+1} = \frac{(y^{n+1} - We_C)}{\tau_D} + \omega e^{\Delta t/\tau_D}\left\{\frac{1}{\omega}\left(\dot{y}^n - \frac{(y^n - We_C)}{\tau_D}\right)\cos(\omega\Delta t) - (y^n - We_C)sin(\omega\Delta t)\right\}$$

were solved.

The aspect ratio of a deformed blood drop and corresponding drag coefficient were subsequently found. The fourth-order Runge-Kutta algorithm was used to find deformed blood drop velocity and coordinates components on each time step.

Estimates of blood drop size (or diameter d^*), impact velocity $\vec{v}^*_{imp}$, position and orientation in space (such as impact angle α^*_{imp} and stain/drop coordinates x_0, y_0 and z_0) prior to impact with a target surface serve as the input (or initial) parameters for backward blood drop trajectory reconstruction (Figure 8.16). Blood drop physical properties (density, surface tension and viscosity) also need to be specified as those are used in drop distortion and flight path calculations.

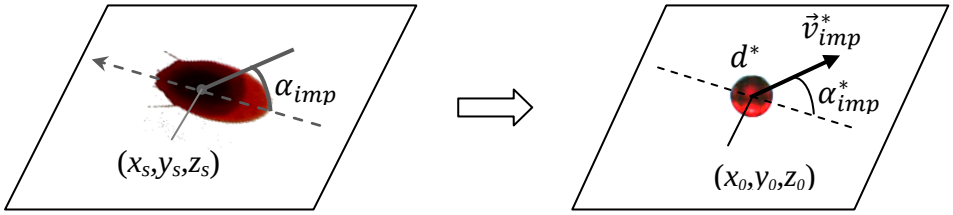

Figure 8.16. Input parameters for backward blood drop trajectory reconstruction from bloodstain analysis (left) to initial conditions for backward calculations (right).

In addition, some assumptions must be made towards the shape (distortion level/oscillation amplitude) prior to impact which may affect drop drag characteristics and thus trajectory. The importance of the drop shape history prior to impact for backward trajectory reconstruction of typical blood drops needs further investigation.

The accuracy of all of the input variables is required for accurate backward blood drop trajectory reconstruction and, as a result, blood origin determination.

8.3.2 Backward model performance and effects of uncertainties of stain estimates

Bloodstains found on a crime scene are analysed in several steps in order to estimate the origin of blood produced the stains. The morphology (i.e. shape, spines present) of the

stains is analysed to deduce their directionality, whereas from stain aspect ratio (width divided by length) impact angle may be found. Special attention is dedicated to proper stain selection to limit the errors in blood origin determination. Generally, a number of well-defined, elliptical (α_{imp} < 60°) stains with upward directionality are selected within a pattern. The uncertainties in the measured impact angle have been associated with the irregularities in stain shape (more severe on certain surfaces) and errors in manual (using protractor) or computer-aided (ellipse fitting procedure) stain length and width measurements (Templeton, 1990; Pace, 2005, Rowe, 2006, Wells, 2006 and Connolly et all, 2012). The uncertainties in impact angle determination was found to increase with impact angle from ~2° at α_{imp} <50°-60° to >>15% at α_{imp} close to 90°.

A number of attempts were made to correlate stain spreading features (and blood physical properties) to the diameter and impact velocity of the drop produced a particular stain (Hulse-Smith et al., 2005; Hulse-Smith and Illes, 2007; Knock and Davidson, 2007). The approach however is limited to ceratin types of surfaces as the effects of surface characteristics (roughness, permeability, wettability) on stain appearance remain poorly described (Attinger et al, 2013). Another approach in drop size determination involved 3D-measurements of stains and liquid to solid content of a blood drop (Laan and de Bruin, 2011). The errors associated with drop size and velocity estimation are believed to be within 10% (Hulse-Smith and Illes, 2007, MacDonell and de Lige, 1989).

The effect of the described above uncertainties in impact angle, velocity and drop size on blood drop trajectory reconstruction was considered in BPA literature previously for the case of different trajectory reconstruction techniques. Impact angle was shown to affect the blood origin height predicted by stringing and tangential methods (underestimation of blood source height with impact angle underestimation) (James et al., 2005). The uncertainties in impact angle and velocity were found to influence parabolic (with only gravitational and drag forces considered, **no drop deformation**) drop trajectories to a greater extent than errors associated with drop size estimation (Attinger et al., 2013 with c.ref. to H. MacDonell). Consequently, the blood origin estimated from the stain analysis is considered to be an approximate, "within a volume of a grapefruit or basketball" (MacDonell, 2005), position of blood source at the time bloodstains were formed and is useful in determination whether the victim was standing, sitting or lying at the moment bloodstains were formed. The effects of blood physical properties values used for drop trajectory reconstruction and blood origin determination require further investigation.

This study aimed to demonstrate the developed backward trajectory reconstruction model and to reconsider the effects of the uncertainties of stain- and blood physical properties related estimates on drop trajectory reconstruction for the case of a **deformable** blood drop, and elucidate associated with this additional errors (if any) in blood origin determination.

The effects of the above mentioned uncertainties on trajectory reconstruction were studied by comparison between forward and backward numerically calculated blood drop trajectories. To investigate the 'worst case scenario' with pronounced effects of the uncertainties long (in terms of time and distance) blood drop flights, the most affected by gravitational, drag and drop deformation effects, were considered. Blood drops of 0.5 and 5 mm in diameter (d) were assumed to originate 1.8 m above the ground (or horizontal flat floor) at initial (launch) angle to horizontal of 0°. Initial drop velocity ranged from 5 m/s to the maximum stable, without drop disintegration, drop velocity of around 11 m/s for the larger drop and 30 m/s for smaller drop (see Chapter 8.2.5 for more details). These drop size and velocity combinations were representative of typical passive and spatter blood drops. Drops of d<0.5 mm were not considered as those tend to quickly decelerate during flight and do not travel far, <0.5-1 m (Chapter 8.2.2).

To eliminate or limit the effects (if any) of drop oscillations of both forward and backward drop trajectories at the beginning of calculation drops were assumed to have the shape corresponding to the initial aerodynamic loading i.e. $y(t=0) = We_C(t=0)$ and $\dot{y}(t=0) = 0$ ('equilibrium' shape). The discussion towards the validity of this assumption for the accurate trajectory reconstruction was provided further in the text.

Once forward trajectories were calculated, from the simulated blood origin to the moment of drop hitting the floor, the drop characteristics at the final position (velocity, impact angle and directionality) were used to reconstruct the backward trajectory.

Firstly, different trajectory reconstruction approaches (considering gravity only or gravity and drag force with drag coefficient dependant on the Reynolds number with or without drop deformation based on TAB model) were used for comparison.

Additionally, the representative uncertainty values of 10% in impact angle, velocity and drop diameter were applied to the forward trajectory calculation output data (when drop hits the floor). The reported range of healthy human blood physical properties at human body temperature of 37°C (density ρ ranging from 1,052 and 1,063 kg/m^3, surface tension σ from 55 to 63 mN/m and low shear rate viscosity μ between 3.2 and 4.4 mNs/m^2) was used for calculations (see Chapter 4.2.2 for the list of references). The reference forward blood drop trajectories were built based on average healthy human blood density (1057 kg/m^3), surface

tension (60 mN/m) and viscosity (3.8 mNs/m^2) values. The trajectories were reconstructed using extreme values of ρ, σ and μ and for high-shear rate blood viscosity of 10 mNs/m^2 for comparison.

8.3.2.1 General trends

Based on the TAB model data 0.5 mm blood drops possessed low (|AR-1| < 0.02) to moderate (|AR-1| < 0.4) deformation levels at 5 m/s and 30 m/s respectively. Whereas, 5 mm drops had |AR-1| < 0.2 travelling initially at 5 m/s and the highest level of deformation of |AR-1| ~ 0.6 at 30 m/s.

According to the detailed blood drop flight model (including gravity, drag and drop deformation) 0.5 mm blood drop impacted the ground (floor) with impact angle of 80°±1° and impact velocity of ~2.1 m/s regardless of considered impact velocity. The higher initial velocity (by 6 times) resulted in increase of the horizontal distance travelled by a drop from 0.9 m to 2.3 m (by about 2.5 times). Whereas, a 5 mm drop had impact angle of ~60° and velocity of 6 m/s when was launched with initial velocity of 5 m/s, and impact angle of ~40° and velocity of 7 m/s at initial velocity of 30 m/s. It travelled around 3 m and 5 m horizontally corresponding to the lower and higher initial velocity.

When only gravity was considered for blood drop trajectory prediction from the origin to impact, the calculated impact position was overestimated (in horizontal direction). The error increases with drop initial velocity (Figure 8.17). Taking into account only gravity for backward trajectory reconstruction from the impact position to origin resulted, on the contrary, in significant underestimation of the origin in both horizontal and vertical direction. This is due to the fact that the drag force, when considered, leads to more rapid drop deceleration (or acceleration for the case of backward drop trajectory) and, thus, to decrease (increase) of the travelled distance. As was discussed in Chapter 8.1 smaller blood drops (d ≤ 0.5 mm) are affected by drag effects the most. This supports the finding that the underestimation of drop travel distance (horizontal) becomes less pronounced when the drop diameter increases (Figure 8.18). Thus, the drag effects must be considered if one attempts to reconstruct drop flight using curved trajectories.

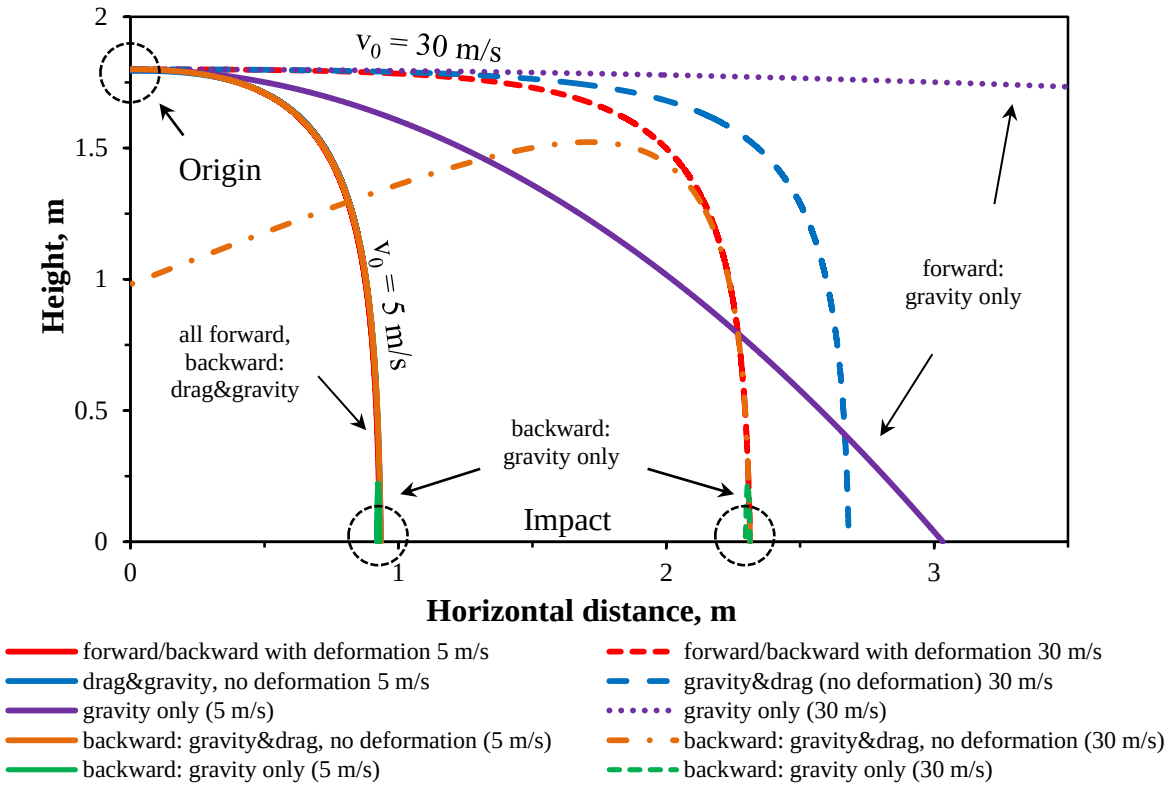

Figure 8.17. Different forward and backward blood drop trajectory reconstruction models performance and comparisonfor a 0.5 mm blood drop launched at 0° to horizontal from 1.8 m above the ground with initial velocity v_0 of 5 and 30 m/s.

As can be judged from the data for a 5 mm blood drop (Figure 8.18) the error associated with the neglect of drag increases with the initial drop velocity (and thus observed impact velocity) due to the drag increasing with the square of drop velocity.

The forward blood drop trajectory for v_0 = 5 m/s predicted with both gravity and drag (no deformation) considered and that predicted with the TAB model for drop deformation coincided within less than 1% for a 0.5 mm drop and 5% for a 5 mm drop. At higher velocities (due to increased drop deformation levels) the predictions differed for both 0.5 and 5 mm drops. The horizontal distance travelled by drops was overestimated by ~20% from 2.3 m to 2.7 m for the smaller drop and from 4.9 m to 5.8 m for the larger drop when in-flight drop deformation was neglected.

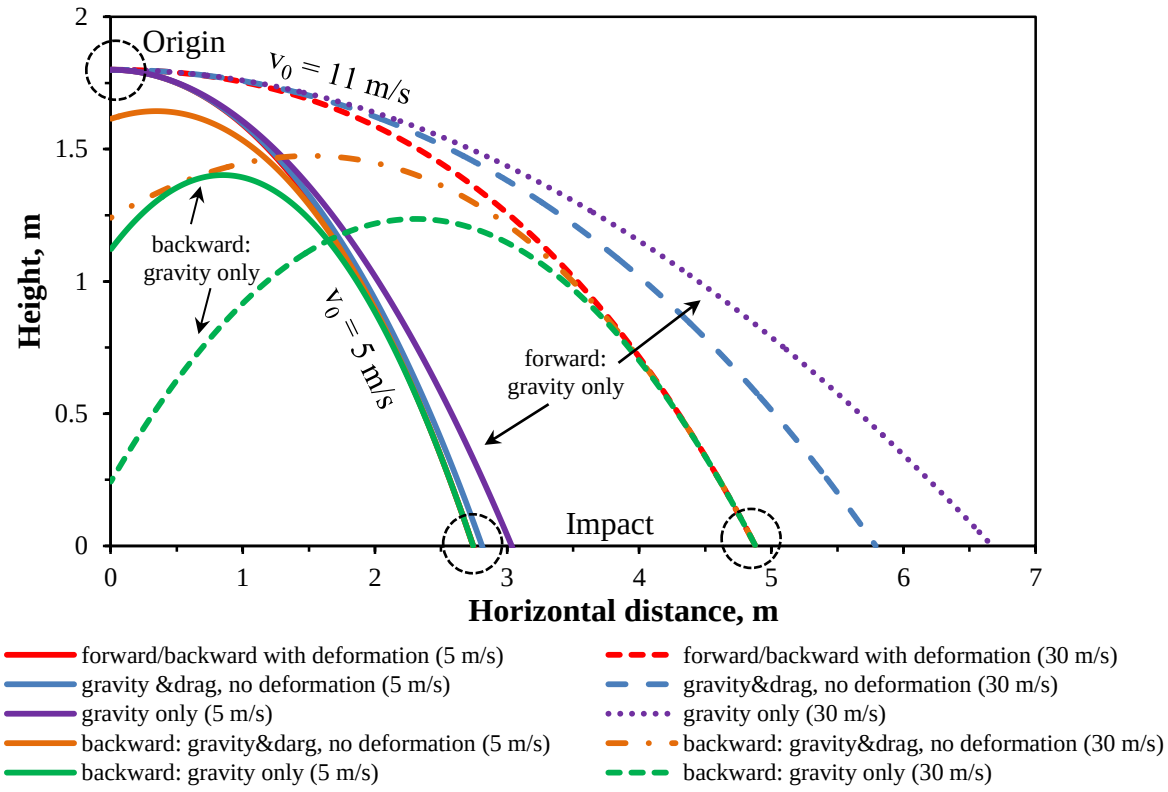

Figure 8.18. Different forward and backward blood drop trajectory reconstruction models performance and comparison for a 5 mm blood drop launched at 0° to horizontal from 1.8 m above the ground with initial velocity v_0 of 5 and 11 m/s.

The deformation of a blood drop towards the increase in drops projected area increases drag and more rapidly slows down (or accelerated in the backward case) the drop. This effect is more pronounced at higher drop sizes and velocities. This was observed for backward trajectories of the 0.5 mm and 5 mm drops at 30 m/s and 11 m/s correspondingly. The vertical position of the blood origin was calculated in error when drop deformation was not considered. The error increased with drop initial velocity from a negligible (<<1 mm) amount to 0.75 m for the 0.5 mm drop, and from ~0.25 m to 0.5 m for the 5 mm drop at 5 m/s and 30 m/s (or 11 m/s for the larger drop) respectively.

The performance of the backward model for drop in-flight deformation prediction and the validity of the equilibrium drop shape assumption for trajectory reconstruction were analysed. The predicted forward and backward drop dimensionless distortion y and distortion rate dy/dt based on the output drop distortion data from the forward model (blue line), which is not known for blood drops in practice, and on the model assumption that a drop shape corresponds to the instantaneous aerodynamic loading on the drop (green line) were plotted in Figure 8.19 for 5 mm drop launched initially at 30 m/s.

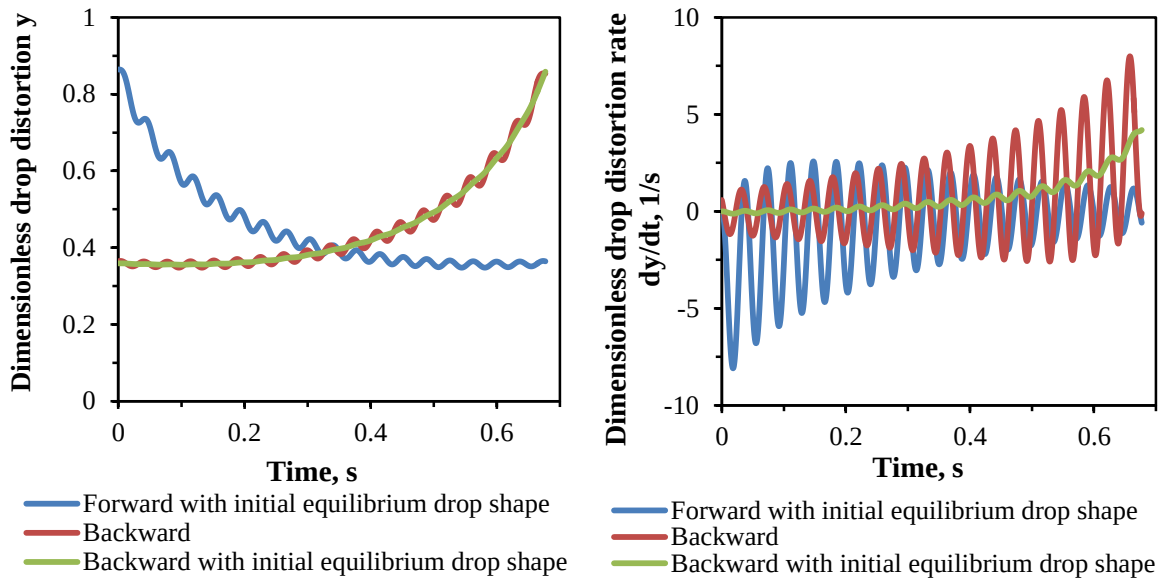

Figure 8.19. Dimensionless distortion and distortion rate of a 5 mm blood drop: forward and backward predictions.

Forward and backward predictions of drop distortion as well as deformable drop trajectories were in good agreement for both approaches in backward drop distortion reconstruction. As can be seen from Figure 8.19 backward drop distortion reconstructed from the output data of the forward trajectory was identical (or mirror reflection in terms of the direction of time) to that of the forward case. Backward drop distortion with the assumption of the initial equilibrium drop shape captured well the time-average drop distortion levels. Backward and forward drop coordinates and velocities in this case matched to the 5^{th} decimal digit suggesting the validity of the initial equilibrium drop shape assumption.

8.3.2.2 Effects of uncertainties on blood drop trajectory reconstruction

The effects of impact angle and velocity were found the most prominent among the other factors tested (such as the drop diameter, drop liquid surface tension and viscosity) (Figure 8.20a and b). As was mentioned earlier the impact angles of the 0.5 mm blood drop were close to 90° for the studied long trajectories. As a result when the uncertainty in α_{imp} was considered the trajectory was affected significantly, especially for the case of the overestimated impact angle (purple dashed line) for both initial drop velocities tested. The height of the blood drop source was underestimated by ~25 cm both using underestimated and overestimated impact angles. The overestimated impact angle, however, suggested horizontal blood drop source location in the opposite direction (see Figure 8.20a).

For the case of the 5 mm blood drop with more acute impact angles of 40-60° the effects of impact angle over- or underestimation was also significant, but less dramatic. The position of the blood source was underestimated in vertical (similar to the case of a 0.5 mm drop) and horizontal direction (due to the predicted drop breakup) by ~1 m and 0.5 m respectively due to 10% impact angle underestimation. Whereas, overestimation of the impact angle led to the origin height overestimation for the 5 mm drop by ~1 m.

Similar trends were observed for the case of the uncertainties in drop impact velocity with more pronounced effects on backward drop trajectory reconstruction with drop size and velocity decrease.

10% variation in the drop diameter affected backward 5 mm drop trajectory only slight. The height of the blood source varied less than a couple of millimetres for the smaller blood drop and ≤ 15 cm for the larger drop tested. On the contrary, the variations in the smaller 0.5 mm drop diameter caused rapid drop deceleration (for overestimated drop size) or acceleration (drop size underestimation) and as a consequence significant errors in blood origin determination (see Figure 8.20a).

These findings were in an agreement with the previous studies for spherical (undeformed) blood drops and visually demonstrated the importance of the accuracy in impact angle measurements and stain selection importance.

The effects of stain-related uncertainties on a deformable and spherical drop trajectory reconstruction differ primarily in the way described above in Chapter 8.8.2.1 for the different approaches in backward trajectory reconstruction. It should be noted that the drop trajectory reconstructed based on gravity only was relatively insensitive to the drop size variations compared to those reproduced with the drag and deformation considered. The latter suggested that the drop size effects on drop trajectory reconstruction manifest by affecting the amount of drag experienced by a drop through the increase in the projected area and drag coefficient with Re number.

Blood drop surface tension and viscosity variation had negligible effect on trajectory reconstruction. The extreme variation in blood viscosity resulted in the blood source position prediction errors less than a couple of millimetres for both smaller and larger blood drops. Whereas, the surface tension extremes affected the blood origin position by less than 10 cm. Higher blood surface tension values brought underestimation of the blood origin height and vice versa.

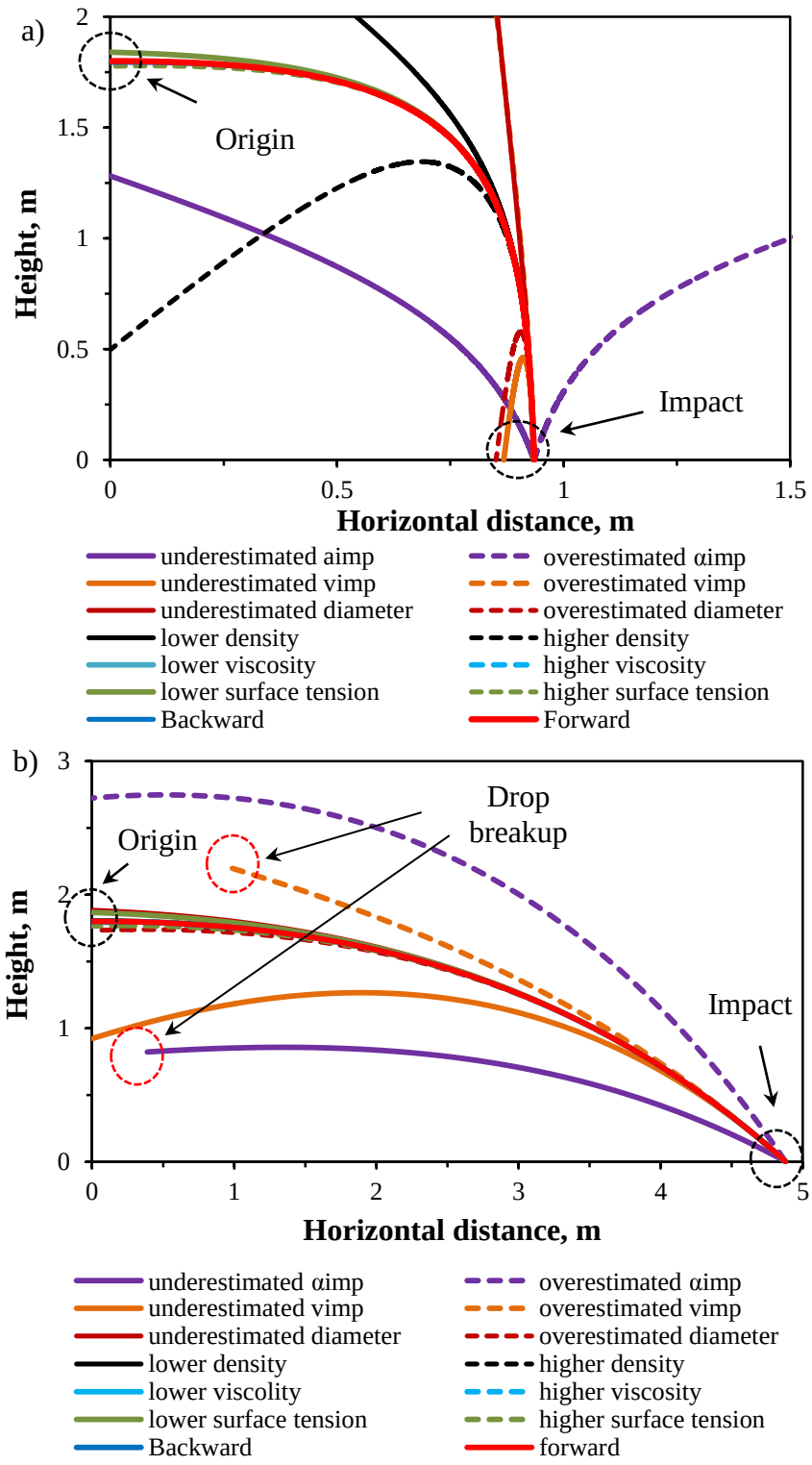

Figure 8.20. Effects of stain-related and blood physical properties uncertainties on deformable blood drop trajectory reconstruction: 0.5 mm drop at initial velocity of 5 m/s (a) and 5 mm drop at 11 m/s (b).

This suggested that deformation is important in backward trajectory reconstruction using curved trajectories, whereas, precise determination of blood surface tension and viscosity is not.

Similarly to the effects of drop diameter, the variation in blood drop density over the healthy human range affected trajectory reconstruction of the smaller blood drop the most resulting in considerable underestimation (~1.5 m regardless of drop velocity) of the blood origin height. The errors in blood drop origin height reduced to ±2 cm with the increase in blood drop size to 5 mm.

It should be noted that the amount of errors in trajectory reconstruction and blood origin determination associated with the studied uncertainties would vary with a number of factors such as drop size, velocity, angle of impact and tracked trajectory length. The presented data provided an indication of the character and magnitude of these effects.

Even in the case of the known (or estimated) size, velocity and directionality of the drop that produced a stain and its accurate trajectory reconstruction the blood origin determination remains a complex problem as there is an uncertainty in the initial condition of drop formation. Consideration of a number of stains within a pattern and the interception of their trajectories may facilitate the blood origin determination. This, however, is applicable to certain types of bloodstains originated from common position in space (impact spatter, for example). Supplementary methods, arguments or bounds are needed for other bloodstain types such as when drop cast-off a weapon along its trajectory at different points in space.

For this reason the studies of the drop formation mechanisms in BPA context, such as those described in Chapter 7 and 8, may provide information towards the typical conditions of blood drop formation which may be used as a reference for the blood origin prediction. Future studies, however, are required in this area.

Summarising, the maximum horizontal distance typical blood spatter drops can travel in idealized crime scene conditions was investigated. The maximum flight range was shown to be achieved by the spatter drops (0.1-2 mm) if upon formation it had directionality in the range of 0°-35° to the horizontal irrespective of drop's initial velocity. The maximum drop flight range increased with the drop diameter and velocity from a maximum of 30 cm for a 0.1 mm drop at 30 m/s to as much as ~3 and 6 m for a 2mm drop at 5 and 17 m/s respectively.

Cast-off and impact spatter drops representatives (d = 0.5-1 mm with velocities of 5-30 m/s) travelled a maximum of 2-3 m. Mist-like drops with d < 0.5 mm travelled less than 1 m.

Thus, the presence of the mist-like stains on an object or clothing may indicate its proximity (within <1 m radius) to the blood source at the moment the spatter was formed.

Moreover, the maximum straight-line trajectory length of typical blood drops was studied. Mist-like blood drops of $d < 0.3$ mm at ≤ 30 m/s as well as drops as large as 2 mm in diameter with velocity less than 5 m/s do not travel in a straight line more than 25 cm, regardless of directionality. At higher initial drop velocities (> 10 m/s), the upward-moving ($\alpha > \sim 70^{o}$) drops with $d > 0.3$ mm could travel as much as 1-3.5 m in straight paths and with $d > 0.8$ mm are expected to travel in a straight line for distances higher than the standard ceiling height of 2.4 m. Drops travelling at $0^{o} \pm 20°$ to horizontal had a straight-line trajectory length of no mere than 1-1.5 m.

For blood drops with Weber number between 3 and 13 or with $140 < v^2 d < 607$, v denotes drop velocity, drop in-flight deformation should be considered when predicting trajectory as those may significantly deform during flight. These included drops with $0.2 < d < 1$ mm travelling with velocities higher than about 10-20 m/s (impact or cast-off drops), blood drops with $d > 1$ mm at lower velocities (on average, less than ~14-15 m/s) and drops with $d < 0.2$ mm at velocities > 30 m/s (possibly gunshot spatter). The deformation effects were found to be more important for blood drops that travel Reynolds numbers of $\sim 103 > Re > 3.5 \cdot 105$. The effects of drop deformation may lead to the flight trajectory curving earlier in flight (< 1.5-2 m), and changes in drop impact angle and velocity especially for the case of larder $d > 0.5$ mm impact and gunshot spatter drops. The deformation effects may be ignored for drops smaller than 0.5 mm in diameter and for fast (with velocities close to the maximum without disintegration) blood drops with probable trajectories shorter than 1 m.

The maximum drop velocity in m/s at which a typical blood drop will not disintegrate into smaller droplets was correlated to the blood drop diameter for drops with $0 < d < 6$ mm in a form of $v_{max} = 24.631\ d^{-0.5}$ for a critical for drop breakup Weber number of 13.

The lifetime of initial blood drop oscillations were subsequently investigated. Passive drops with $d \leq 2$ mm needed less than 30 cm of flight before the initial oscillations die away. Whereas, 6 mm drops needed as much as 14 m (for a high-shear-rate blood viscosity of 4 $mN \cdot s/m^2$) or 3.4 m (for a low shear rate viscosity of 10 $mN \cdot s/m^2$) of fall for the initial oscillations to decay completely. Spatter drops (d = 0.1-2 mm) need less than 2.5 (4 $mN \cdot s/m^2$) and 1.2 m (10 $mN \cdot s/m^2$) for the oscillation amplitude to decay. The oscillations of drops < 1 mm decay over less than 1 m.

The effects of air movement (indoor air currents of 0.5 m/s and outdoor winds of 5 m/s) on the flight of typical spatter and passive drops were additionally investigated for the case of

downwind/tail winds, upwind/head winds and cross winds. These were highly depend on the air velocity magnitude and directionality as well as drop size and velocity. The smaller the size and lower the velocity of a drop, the more pronounced the effects of cross-current and wind on the drop's flight path. Due to the affected drop trajectory, the impact angle of the drop onto a ceiling or wall may also be affected. Consequently, the possibility of the air motion during spatter generation should be taken into account when the drop's trajectory is reconstructed. The drop and air flow directionality and velocity, as well as the blood source location relative to a wall or ceiling need to be considered to draw any conclusions on the effects of the air motion on drop trajectory, impact angle and blood source determination.

Evaporation rate of blood drops at typical flight conditions was considered. A drop with $d \geq 1$ mm was shown to lose less than 1% (at conditions with 50% relative humidity) and 3% (at extremely dry conditions) of its diameter regardless of its initial velocity. The drops with $0.2 < d < 1$mm in diameter may lose 1-30% (and up to 50% at the extremely dry conditions) in their diameters. Drops of < 0.2 mm are most likely to evaporate completely shortly after formation.

Backward trajectory reconstruction was possible with some adjustment to the TAB model. The latter predicted reverse blood drop deformation with the decrease in drop's aspect ratio well. By means of the backward drop trajectory model the effects of the drop size, impact angle and velocity estimates and uncertainties in the physical properties of human blood produced a stain on deformable blood trajectory and the area of origin determination were investigated.

Finally, the effects of uncertainties in impact angle, impact velocity, diameter and density were found the most prominent among the other factors affecting backward trajectory reconstruction and need to be considered when drawing conclusions regarding the origin of a blood drop and bloodstain spatter overall. On the contrary, blood surface tension and viscosity variation over the healthy human range were shown to have negligible effect on both forward drop trajectory and backward trajectory reconstruction.

9 Conclusions and Future work

9.1 Passive blood drop size estimation

The process of passive dripping from blunt and sharp objects with different surface curvatures and roughnesses has been studied with high speed video and the size of the primary drops and number of accompanying drops have been measured. These objects were chosen to represent weapons that might be used during the commission of a crime. Distilled water and porcine blood, controlled so that the surface tension and viscosity fell within the normal human range, were used.

Previous observations (Laber, 1985, Parker, 1982 and Ross, 2006) that the size of a primary passive blood drop decreases as the surface curvature of the object from which it drips increases, have been confirmed by our findings, and systematically quantified. Blood drop volumes of between 37.4 µL (knife) and 121.8 µL (cylinder with H = 0.01 mm^{-1} and 3.59 µm roughness) were recorded. The primary drop size was, however, relatively insensitive to the size of the object if the mean curvature of its surface was smaller than 0.10 mm^{-1} (primary blood drop size 87–125 µL, diameter 5.5–6.2 mm in this range). Surface roughness influenced drop size only weakly, so is not a complicating factor, over the hydrophobicity and the range of roughnesses studied.

Blood on average tended to produce a slightly greater number of accompanying droplets than water and there was some dependence on object size, but the number of accompanying droplets showed great variability even under nominally identical conditions. The surface roughness had a small effect on the drop formation mechanism, over the roughness range studied.

It is possible, under favorable conditions, to infer the impact velocity and hence fall height of a passive drop hitting a target surface, from the stain size, if the primary drop volume can be ascertained using a correlation such as that between stain spreading and the impact Weber number (Hulse-Smith et al., 2005). The findings of this study suggested that primary drop size could be estimated for smaller weapons if the dripping object is known. It may also be possible to distinguish dripping from blunt objects such as baseball bats and iron bars from that of sharp weapons such as knives and screwdrivers.

Further work, however, is required to determine the reliability of such methods when factors such as blood flow rate, temperature, movement or vibration of the object and blood composition are considered. Weapon representatives with both hydrophobic and hydrophilic surfaces may also be tested to infer the effects of the dripping object's surface wettability on passive blood drop formation characteristics, resultant primary drop size and number of satellite droplets.

9.2 Accurate blood drop flight modeling

A numerical code for accurate modeling of blood drop flight was developed. Gravitational and aerodynamic drag forces as well as in-flight drop deformation, oscillations and possible secondary break-up were incorporated. The latter were recognized as factors which may significantly affect blood drop trajectory and, ultimately, the area (or volume) of origin determination (Bevel and Gardner, 2008; Raymond et al., 1995 and Attinger et al., 2013), but were poorly investigated in BPA.

The code provides a reliable and non-laborious method for understanding and predicting the flight characteristics of typical blood drops including drop oscillations, deformation and breakup. The developed numerical scheme is able to predict drop 2D or 3D coordinates, velocity along the flight trajectory, impact angle and velocity, distance travelled and drop aspect ratio in both 'forward' (from the drop origin till its impact on a surface) and 'backward' (from the drop position on the target surface to its origin) directions. Moreover, the effects of air currents and winds on drop travel distance and impact angle can be modelled using the developed code.

The code was extensively validated against experimental and analytical data.

The analytical test cases included a number of cases of undeformed (spherical) drop flight with and without air resistance. Without air resistance the numerical results matched exactly analytical solutions of the kinematic equations of drop motion. Code predictions matched experimental data for the case of spherical drop flight at terminal velocity (when drag force is balanced by the drop weight) in ambient air, verifying the accuracy of drop velocity components and coordinates calculation subroutines of the program.

A number of validation experiments with blood drops commonly found at a crime scene were conducted. The main focus was dedicated to testing the performance of the drop deformation models (based on Green (1975) and Hsiang and Faeth (1995) for steady drop disturbances and the TAB model for low-Weber number atomisation) employed for passive,

cast-off and impact blood drops. Additionally, typical ranges for the characteristics of these drop types relevant to BPA were defined. To the author's knowledge this has not been done previously in the BPA community.

9.2.1 **Terminal velocity**

To test the performance of drop deformation models at terminal velocity numerically calculated terminal velocities for deformed water drops were compared to the experimental data from Gunn and Kinzer (1949) and Best (1950).

The TAB model was found to be the most accurate in predicting drop **deformation at terminal velocity** for water drops (with physical properties close to blood drops) up to 10 mm in diameter. The models based on Green (1975) and Hsiang and Faeth (1995) provided satisfactory estimation of terminal velocities of water drops with $d < 6$ mm, but overestimated terminal velocities of drops with $d > 6$ mm.

The validity of the code when predicting passive blood drops flight with velocity close to terminal was investigated by comparing numerical predictions and experimental data on blood drops falling from up to 8 m. All the models for drop deformation during flight (based on Green (1975), Hsiang and Faeth (1995) and the TAB model) performed well when predicting drop deformation levels and, consequently, drop fall velocity. Numerical velocities lie within 5% to the mean of the experimental data. The model based on a drag coefficient dependent on Reynolds number, but with drop deformation ignored, predicted higher drop velocities compared to those with drop deformation. The discrepancy, however, was observed only for fall distances higher than about 4 m. When the drag force was entirely neglected, the predicted velocities deviated substantially from those of a droplet with drag by the time it has fallen 1.5 m. It is rare that a passive blood drop would fall (vertically) much more than 1.5 m at a crime scene. Such a short travel distance (and time of flight) would not allow a passive drop to experience any significant drag force effects or deformation to alter its flight velocities (in particularly, impact velocity) at typical crime scene conditions.

Thus, terminal velocities of blood drops and distances and times required to reach them may be accurately predicted using the proposed numerical approach.

9.2.2 **Initial oscillations**

Typical passive blood drops with diameters of $1 \text{ mm} < d < 6$ mm on early stages of flight (falling up to 1.5 m) were also experimentally and numerically studied.

Upon formation the drops oscillated in, predominantly, axisymmetric (prolate-oblate) mode. Most of the passive blood drops detached from the ligament having a prolate shape, whereas some drops were oblate.

The primary drops experienced small- to moderate-amplitude oscillations with $|1\text{-}AR| \leq 0.3$, where AR is the drop's aspect ratio. The satellite drops, being formed as a result of strong ligament contraction, oscillated with higher amplitudes ($|1\text{-}AR| \leq 0.9$).

Smaller drops were observed to oscillate with higher frequencies and thus had shorter periods. The frequency and period of oscillation of the passive drops studied ranged from about 21.4 ± 0.07 Hz and 47 ± 3 ms (for a 5.8 mm drop) to 198.4 ± 0.1 Hz and 5 ± 0.6 ms (for a 1.25 mm drop) respectively. The latter were in good agreement with the linear theory of low-viscosity drop oscillations (Lamb, 1932) ascertaining its applicability for passive blood drop oscillations description.

To model initial oscillations of passive drops the TAB model which considers the oscillations of a viscous liquid drop under the aerodynamic driving force with damping due to the drop viscosity was used. The accuracy of the TAB model to predict passive blood drop oscillations was examined by comparison of the numerical and experimental data.

The simulation of the initial drop oscillation based on the TAB model provided accurate prediction of the passive drop behavior during flight beginning from the moment of its formation. The relative error in drop aspect ratio values predicted numerically to that observed experimentally was within 1.6 %.

The value of the aerodynamic force coefficient $C_f = 2/7$, corresponding to critical Weber number for steady deformation We_{cr} of 14, performed best when predicting empirical levels of passive blood drop deformation. This is recommended to be used in the TAB model when passive blood drop flight is considered.

It was recognized that the prediction of the passive drop distortion and oscillations induced by the drop formation process using TAB model requires initial drop distortion and distortion rate (initiated by the retracting ligament) to be known. The values of the initial distortion rate (dy/dt) used for the simulations ranged from 20 to 94 s^{-1} and were within the experimentally determined range for the primary blood drops studied of 18 ± 8 s^{-1} (5.8 mm drops) and 128 ± 30 s^{-1} (2.8 mm drops). The experimentally determined range of initial dimensionless passive blood drop distortion (y) of 0 to 0.4 was used for the initial primary blood drop oscillations modeling using TAB model.

Measured blood drop density and surface tension values were incorporated into the model and performed well when modeling drop oscillations. Variations in the blood surface

tension and density in the range of the instrumental errors had negligible effect on the numerical results. A blood viscosity of 10 mNs/m^2 (for the low shear rate of 10 s^{-1}) provided the most satisfactory data fit and was recommended for passive blood drop oscillations modeling.

The empirically measured passive drop fall velocity was predicted by the TAB model within 0.5%. Based on the TAB model prediction of the fall velocity, distance and time of an initially deformed, oscillating drop and initially spherical, non-oscillating drop it was suggested that the effects of drop initial oscillation and distortion from sphericity on its flight characteristics are negligibly small. Thus, a passive blood drop can be modeled using the developed code by an initially undisturbed non-oscillating drop undergoing deformation during flight under the aerodynamic forces for all problems other than the initial drop shape oscillation prediction.

9.2.3 **Drop deformation and breakup**

The deformation levels of cast-off and impact blood drops were studied.

The blood drops cast-off from a rotating disc with diameters from 0.4 to 4 mm and velocities of 1-15 m/s were studied. These experienced shape oscillations due to the unbalanced surface tension forces at the time of detachment from the disk. Most of the primary cast-off drops detached with a prolate spheroidal shape (with $|1\text{-}AR|_0 < 0.2$). Similar to the passive drops, they oscillated with small- to moderate-amplitudes with the dimensionless drop distortion ($y < 0.4$ and $|1\text{-}AR| \leq 0.3$) and damping rates within the range seen in passive dripping. This suggests that the initial oscillations of cast-off drops may be modeled with the TAB model that performed well for the passive blood drops oscillation prediction.

The size of the primary drops cast off from the disc decreased as the rotational velocity increased. Blood drops with $2\ mm < d < 4\ mm$ formed at disk rotational velocities close to ~2 m/s. Whereas, drops smaller than 1.5 mm and 0.5 mm were generated at rotational velocities higher than 5 m/s and 15 m/s respectively. The ligament length, on the contrary, increased with the speed of rotation which, consequently, disintegrated into higher numbers of smaller diameter satellite drops.

The Weber numbers of the cast-off drops studied did not exceed 3 indicating low deformation levels present. The latter are unlikely to alter the drop's flight path and/or velocity at the moment of impact on a surface and thus area (or volume) of blood origin determination. Breakup in flight is also highly unlikely.

Both the model with the spherical $C_d = f(Re)$ and the TAB model for drop deformation accurately predicted cast-off drop flight giving evidence of their validity, at least over the length of trajectories studied.

At low Weber number of cast-off drops drop deformation was found to alter drop flight range by less than 4% the maximum flight range of ~ 1.5 m studied and to have negligible effects on impact velocity.

Future work is, however, required to investigate the possibility of the formation of larger cast-off drops from real sharp- and blunt-tip weapons at higher swing velocities and, thus, higher Weber numbers and deformation levels.

Impact drops with d = 0.1-2 mm and velocities of 14-25 m/s formed as a result of a blunt force impact were also investigated. This possessed high levels of deformation with aspect ratios as low as 0.4. It was shown that impact drop deformation at the studied conditions can be accurately described with the correlations for falling drops (such as one according to Brandes et al. (2002)). The TAB model, however, provides a possibility to predict the change in the drop deformation according to the variable aerodynamic loading on a drop during its decelerated (or accelerated) motion.

Larger impact blood drops (~1-1.5 mm in diameter) was observed to breakup at $We_{crit} \approx$ 12-14. The majority of the breakup case occurred within 10-20 cm from the impact point.

The critical drop deformation measured experimentally (AR = 0.3-0.4) corresponded well to the critical deformation level for drop breakup of y ~ 1 (or AR ~ 0.35) employed in the TAB model. Vibrational and bag-type breakups were recognized.

The drop breakup model based on Hsiang and Faeth (1992) predicted the critical empirical impact drop deformation levels within 5%. Pilch and Erdman's (1987) expression for the time of drop breakup was found to be the most accurate when predicting impact blood drop breakup.

The trajectory length of the drop undergoing breakup was overestimated by the TAB model with Pilch and Erdman's (1987) breakup time, however. This was associated with the neglect of the bag expansion phase of drop breakup in the model when the cross-stream drop diameter (and thus projected area and drag) increases with time up until final drop disintegration. As a result, the drop decelerated more rapidly and travels shorter distances before complete disintegration.

Future work may be conducted on more accurate bag expansion modelling using the TAB model (see Bratz et al. (2010)). In addition, the expressions for the number and size of blood droplets (called 'child') that form as a result of the parent drop disintegration exist

(O'Rourke and Amsden, 1987) and can be incorporated into the TAB model. The validation for the case of blood drop disintegration is required, however.

The deformation levels and breakup possibility and modes of gunshot drops require additional investigation. The range of sizes and feasibility of the gunshot drops to possess high velocities (> 30 m/s specified by Laber (1985)) and, thus, high Weber numbers and deformation is of major interest.

Characteristics of the impact spatter are also of a great interest for the future work. It is particularly important to understand what are the sizes and velocity values for the drops produced by an impact event. The correlation of impact drop sizes and velocities on the impact force; shape, nature and surface characteristics of the impactor; nature of the target (soft targets mimicking human body, in particular), as well as on the physical properties and amount of the atomizing liquid is of interest.

In summary, the developed approach in forward blood drop trajectory reconstruction was shown to be accurate in predicting blood drop flight characteristics; and may help to distinguish possible and dismiss unfeasible or improbable blood drop trajectories and, to some extent, formation scenarios supporting the inverse (backward) problem; promote understanding and provide better means of investigation of the behaviour of blood drops after generation, as well as help in BPA research problem hypothesis formulation and effective experimental design development.

9.2.4 **Backward trajectory reconstruction**

The backward blood drop trajectory was simulated on the basis of the developed forward model for deformable blood drop flight simulation. Drop backward acceleration was found from Newton's Second Law after time inversion. The TAB model for drop deformation, oscillation and breakup modelling was amended in order to predict in reverse the drop distortion.

The TAB model performed well when predicting reverse blood drop deformation with the decrease in drop's aspect ratio and, in some instances, the excitation of drop shape oscillation during its accelerated inverse motion.

The importance of a known blood drop shape upon impact on trajectory reconstruction was examined. The actual blood drop shape upon impact is, however, unknown in practice. A model assumption of an 'equilibrium' drop shape upon impact with a surface, the shape corresponding to the aerodynamic loading prior to impact, was found to be adequate for backward blood trajectory reconstruction. This suggested that to improve the accuracy of the

deformable blood drop trajectory reconstruction the blood drop shape prior to impact needs to be inferred from the aerodynamic loading on a drop prior to impact. The loading may be estimated based on the drop impact velocity data.

The effect of a blood drop shape upon impact on the impact dynamics, however, remains not fully understood in BPA and requires further investigation. The possibilities of the developed code may be exploited to predict the conditions for the pronounced levels of blood drop deformation. The latter may be experimentally simulated to investigate the effects of drop deformation on the resultant stain shape by comparison to the data on effectively spherical blood drops impact at similar dynamic conditions.

It was found that drop deformation should be taken into account for backward drop trajectory reconstruction purposes, otherwise, errors in the vertical blood origin position would arise. The latter would depend on the blood drop size, velocity and directionality. The maximum errors in the predicted blood origin height observed for the 0.5 mm and 5 mm blood drops studies originated 1.8 m above the ground with 30 m/s and 11 m/s (associated with high levels of drop deformation) respectively were ~0.8 m for smaller drop and 0.5 m for larger drop. The drops' trajectories were reconstructed from the point of impact with the ground.

In addition, blood drops smaller than d < 0.5 mm (which correspond to 'mist-like' spatter) were shown to be strongly affected by drag which may bring significant errors in blood origin determination. Thus, the drag effects must be considered if one attempts to reconstruct drop flight using curved trajectories. The errors in drop travel distance (and origin determination) associated with the drag effects on drop trajectory are expected to decrease for larger drops (d > 0.5 mm). For those drops, as it was mentioned earlier, drop deformation needs to be considered in trajectory reconstruction.

The effects of errors of up to 10% of the drop size, impact angle and velocity on deformable blood trajectory and the area of origin determination were investigated with the aim to provide an indication of the character and magnitude of these effects. The uncertainties associated with the range of natural variability of human blood physical properties (density, surface tension and viscosity) were also examined.

The effects of impact angle and impact velocity were found the most prominent among the other factors affecting backward trajectory reconstruction (such as the drop diameter, drop liquid surface tension and viscosity) supporting the previous findings of James et al. (2005) and MacDonell (2005). Impact angle overestimation generally resulted in the blood source (or origin) height overestimation and vice versa.

For the case of a 5 mm blood drop released from 1.8 m above the ground horizontally and impacted the ground with an impact angle of 40°-60° (depending on its velocity upon formation) the vertical position of the blood source was underestimated by a maximum of ~1 m with the impact angle underestimated by 10%.

More severe effects on blood drop trajectory reconstruction (and blood origin estimation) were detected for the blood drops impacting the ground (or surface) at impact angles close to 90° supporting the belief of that the bloodstains impacted a surface at right angles are unsuitable for reconstruction purposes. The developed numerical code, however, can be used to investigate different scenarios that might have led to a blood drop impacting a surface at an angle within the range of the impact angles estimated from the bloodstain characteristics. The latter in conjunction with the analysis of other bloodstains within a pattern may provide useful supplementary data in the blood pattern origin determination.

Similarly, the underestimation of the drop impact velocity resulted in blood drop origin height underestimation with more pronounced effects for smaller and slower blood drops.

10% variation in drop diameter and drop density variation over the healthy human range were found to affected the trajectory reconstruction of smaller blood drops ($d < 1$ mm, especially 'mist-like') the most leading to significant (of an order of 1-2 m) errors in the blood drop origin height and horizontal position determination. It is suggested that these factors need to be considered when drawing conclusions regarding the origin of a blood drop and bloodstain spatter overall. On the contrary, blood surface tension and viscosity variation over the healthy human range were shown to have negligible effect on both forward drop trajectory and backward trajectory reconstruction even for the case of long drop flight.

The developed numerical approach in trajectory reconstruction may be used in future to investigate the severity of error in trajectory reconstruction and blood origin estimation for particular combinations of drop size, velocity, directionality and space characteristics surrounding a drop.

9.3 Factors affecting blood drop trajectory in typical crime scene conditions and bloodstain selection recommendations

9.3.1 Maximum blood drop travel distance and straight trajectory length

The maximum horizontal distance typical (0.1-2 mm in diameter travelling at 5-30 m/s) blood spatter drops can travel in idealized crime scene conditions (a room with no vertical

walls, horizontal flat floor, still air no drop evaporation) was investigated to provide some quantitative information towards the maximum distance a crime scene participant may be from the blood source to still get blood stains on his or her clothing or the distance different patterns may be separated.

Drop source height, drop size, initial velocity and directionality as well as gravitational and drag forces and drop deformation affect how far a drop would travel.

The optimal launch angles for which the maximum flight range may be achieved by the spatter drops studies were found to range from 0-5° to 25-35° for blood drops with diameters of 0.1-2 mm and were independent of the drop initial velocity.

The maximum drop flight range was observed to increase with the drop diameter and velocity from a maximum of 30 cm for a 0.1 mm drop at 30 m/s to as much as ~3 and 6 m for a 2 mm drop at 5 and 17 m/s respectively.

Cast-off and impact spatter drops representatives (d = 0.5-1 mm with velocities of 5-30 m/s) were found to travel on average a maximum of 2-3 m if not intercepted by a wall, or any other object, or subject. Drops with d < 0.5 mm (associated with mist-like stains) travelled less than 1 m. The latter suggested that the presence of the mist-like stains on an object or clothing may indicate its proximity (within <1 m radius) to the blood source at the moment of spatter generation.

The maximum distance to which the drop trajectory can be reconstructed as a straight-line from the stain in the direction determined by the measured impact angle without increasing the area (or volume) of origin determination error was also investigated.

The trajectory of a drop was assumed to be straight if its directionality was within typical uncertainties in the drop impact angle determination from the stain-related measurements (~10%).

Typical upward- and downward-moving spatter drops of 0.1-2 mm in diameter at velocities of 2-30 m/s in quiescent air were studied.

For any drop directionality the straight trajectory length was shown to increase with drop size and initial velocity. For upward moving drops the trajectories tended to be straighter over longer distances for drops travelling closer to vertical (90°). On the contrary, the trajectory curvature increases for drops moving horizontally (0°) with more pronounced effects for larger drops (d > 0.8 mm). Downward-moving drops were susceptible to trajectory curving the least. The deformational effects were found to decrease the straight trajectory length of drops with d > 1 mm travelling at initial velocities higher than ~5 m/s.

It was shown that blood drops of d < 0.3 mm with initial velocity ≤ 30 m/s (with small, mist-like stains such as gunshot-related spatter) as well as drops as large as 2 mm in diameter with velocity < 5 m/s cannot travel in a straight line more than 25 cm, regardless of directionality. This supports the view that mist-like stains are unreliable for backward trajectory reconstruction, but as was mentioned earlier may provide some information on the proximity of the surface these stains were deposited on to the blood source at the moment of spatter generation. The possibility of the droplet trajectory's alteration due to air currents, winds or muzzle gases present upon spatter generation should be examined in this case.

At higher initial drop velocities (> 10 m/s), the upward-moving ($\alpha > \sim 70^{o}$) drops with d > 0.3 mm could travel as much as 1-3.5 m in straight paths and with d > 0.8 mm are expected to travel in a straight line for distances higher than the standard ceiling height of 2.4 m. Drops travelling at $0^{o} \pm 20°$ to horizontal had straight-line trajectory lengths of no more than 1-1.5 m.

Thus the following stain selection recommendations for the straight-line trajectory reconstruction and blood source determination can be drawn:

- fast (with velocities higher than ~10 m/s) upward (at angles to vertical < 45°) moving drops (and resulting stains with impact angles > 45° if found on a ceiling or < 45° if found on a facing vertical wall) were found to be the most suitable for the stringing method to be accurate in agreement with the current practice in BPA (Connolly, Illes and Fraser, 2012);
- fast drops travelling at more acute angles to horizontal (< 45°) can also be used for the straight-line trajectory reconstruction if the proposed blood source is within less than 1 m radius from the stain location;
- the larger the stain (as is a drop with estimated d > ~0.8 mm) found on a ceiling the higher the possibility that the stain was produced by a drop travelling along a flat trajectory and, thus, the more reliable the straight-line approximation of blood drop trajectory is;
- the smaller the impact angle of the stains with upward directionality located on a wall in the vicinity of a ceiling, the closer (in horizontal direction) the blood source was to the wall;
- the maximum theoretical straight drop flight path length is 2 m for the stains with upward directionally and impact angles between 0° and 90° located on a wall (and less for smaller stains). For a stain on a wall at right angles, the maximum flight path length of a straight drop trajectory is ~1 m. It is however ambiguous whether the stains

present on a wall were produced by straight-line moving drops, by drops with slightly curved trajectories or a combination of the two.

9.3.2 **Drop deformation and oscillations**

The conditions for a blood drop to experience pronounced deformation during flight were examined. The criterion for a typical blood drop to experience pronounced deformation during flight was expressed in a form 3 > We > 13 or $140 < v^2 d < 607$. From which it was inferred that drops with 0.2 < d < 1 mm travelling with velocities higher than about 10-20 m/s (impact or cast-off drops) are expected to possess high deformation levels which may affect their trajectory. For bigger blood drops (d > 1 mm) lower velocities (on average, less than ~14-15 m/s) are required for significant drop deformation to develop. Drops with d < 0.2 mm require velocities v > 30 m/s, possibly gunshot spatter conditions, to deform significantly during flight.

Moreover, significantly deformed drop trajectories were studied numerically for typical drop sizes and velocities to reveal the effects character of the drop deformation effects.

The main effect of drop in-flight deformation on its trajectory is to increase the drag force by an increase of the projected area which, additionally, raises the drop drag coefficient towards that of an ultimately deformed disk-like drop. This leads to more rapid drop deceleration and more pronounced drop trajectory curving earlier in the flight with possible impact angle and velocity alteration upon contact with a surface.

The drop size, initial velocity and flight directionality should be considered when drawing conclusion regarding the possible effects of deformation on its trajectory.

The deformation effects were found to be more important for blood drops that travel Reynolds numbers of ~10^3 > Re > $3.5 \cdot 10^5$.

The trajectories, impact angles and velocities of drops with d < 0.5 mm would not affected be the deformation.

The flight height and range of an upward-moving 2 mm blood drop reduced by as much as about 1 and 2 m respectively due to their high levels of deformation. In addition, impact velocities of the deformed drop were lower (by ~ 30 %) than those of an effectively spherical drop. Drop deformation resulted in a 25% impact angle increase (upon impact with a vertical wall) and a less than 5 % decrease (upon impact with a ceiling) over the first 2 m and 1 m in the horizontal and vertical directions from the blood drop origin. Such alteration of the impact angle is expected to lead to blood source height overestimation (possibly > 100%,

depending of the distance traveled and drop trajectory curvature) when the straight-line trajectory reconstruction is used.

Thus, it is recommended that the effects of drop deformation not be neglected as these may lead to the flight trajectory curving earlier in flight (< 1.5-2 m), and changes in drop impact angle and velocity especially for the case of larger (d > 0.5 mm) impact and gunshot spatter drops. The deformation effects may be ignored, however, for drops smaller than 0.5 mm in diameter and for fast (with velocities close to the maximum without disintegration) blood drops with probable trajectories shorter than 1 m.

The distance a blood drop needs to travel from its origin for the initial oscillations to decay, i.e. the distance of a bloodstain location from the suspected blood drop source after which the initial oscillation effects (if any) on the stain appearance and 'Sine law' applicability may be safely ignored, was studied for typical passive and spatter blood drops. The long-lived fundamental mode of oscillations and farthest possible drop flight paths was considered.

Generally, the larger the drop (and, hence, the stain it leaves), the more long-lasting its initial oscillations and the higher the possibility that the resulting stains were affected by the oscillations.

The passive drops with $d \leq 2$ mm were found to travel less than 30 cm before the initial oscillations die away. 6 mm drops needed as much as 14 m (for a high-shear-rate blood viscosity of 4 $mN \cdot s/m^2$) or 3.4 m (for a low shear rate viscosity of 10 $mN \cdot s/m^2$) of fall for the initial oscillations to decay completely. Consequently, typical passive blood drops found at a crime scene are most likely oscillating upon impact with a surface.

The spatter drops (d = 0.1-2 mm) at the maximum stable velocities need less than 2.5 (4 $mN \cdot s/m^2$) and 1.2 m (10 $mN \cdot s/m^2$) for the oscillation amplitude to decay. The oscillation decay distance for the smaller spatter drops with $d < 1$ mm was < 0.5-1 m and well under 50 cm for 'mist-like' drops with $d < 0.5$ mm. Thus, drops < 1 mm (these are the most abundant within impact and possibly gunshot spatter) are expected to be in equilibrium with the aerodynamic loading shape upon impact with a surface. The corresponding stains may be treated as those that were not affected by the impacting drop initial oscillations.

Further investigation of the effects (if any) of drop deformation and oscillations upon impact with a surface on the stain appearance is required.

9.3.3 **Blood drop breakup**

The distance an unstable blood drop can travel before the disintegration in relation to the spatial dimensions (or origin) of the spatter (in particularly, impact or gunshot) formation was investigated.

The maximum drop velocity, v_{max}, in m/s at which a typical blood drop will not disintegrate into smaller droplets was correlated to the negative square root of the blood drop diameter for $0 < d < 6$ mm in a form of $v_{max} = Cd^{-0.5}$, where C is a constant equal to 24.631 and 30.551 for a critical for drop breakup Weber number of 13 and 20 respectively.

Passive drops were shown to unlikely reach the predicted unstable velocities during their fall and disintegrate into smaller droplets. To break up, any drop of $d < 6$ mm will need to travel at more than its terminal velocity, so will be decelerating, whatever direction it travels in. It can only break up if it starts to travel at a velocity greater than terminal. The spatter drops with $0.5 < d < 2$ mm for We=13 or $1 < d < 2$ mm for We=20 require velocities upon formation less than 30 m/s to breakup. The smaller droplets ($d < 0.5$ mm), typical for gunshot spatter, are expected to breakup at much higher velocities. As was mentioned earlier, more detailed investigation of the gunshot drop size and feasible velocity ranges is required, however.

The breakup time and distance were seen to increase as drop diameter and initial Weber number increase. For the spatter drops ($d < 2$ mm), the maximum breakup time was about 10-20 ms. For the smaller droplets ($0.5 < d < 1$ mm) the breakup time decreased to 2.5-3.5 ms. The corresponding spatter drop breakup distance ranged from 17-32 cm for a 2 mm blood drop to 4-10 cm for a 0.5 mm drop. Smaller droplets ($d < 0.5$ mm), especially at higher velocities (>> 30 m/s), possibly characteristic to the condition of the gunshot spatter formation, would breakup much faster and over much shorter distance (a couple of centimeters or even millimeters).

This suggested that the special dimensions of the spatter formation process associated with an impact event (blunt force or bullet impact, in particularly) may be of a couple of millimeters or centimeters to around tens of centimeters in radius. The latter should be taken into account when drawing conclusions about the area (or volume) of blood origin determination.

Additionally, it can be argued that if bloodstains with estimated original drop diameters > 2 mm are found at a crime scene, they are most likely originated with velocities less than

~14 m/s. Blood drops with d = 0.5-2 mm had probably formed with velocities less than 30 m/s.

9.3.4 **Air currents, winds and in-flight evaporation**

The effects of air movement (indoor air currents of 0.5 m/s and outdoor winds of 5 m/s) on the flight of 0.1-5 mm drops travelling at 0-30 m/s (typical spatter and passive drops) were additionally investigated. These depend on the air velocity magnitude and directionality as well as drop size and velocity. The drops were assumed to originate 1.4 m above the ground at 0º and 45º to the horizontal. For simplification, the air velocity was considered to be constant in magnitude and direction for the duration and range of the drop fight (generally less than 1 s and < 2.5 m). Drop flight under head, tail and cross wind conditions was studied.

Passive drops falling perpendicular to the air currents direction were displaced from their undisturbed (no wind) flight paths by less than 2 cm for a 5 mm diameter drop and by 20 cm for the case of a 1 mm diameter blood drop. Under a 5 m/s wind, however, passive stain location (or passive drop position at impact with the floor) shifted by as much as 0.5 m for the 5 mm drop and 2.3 m for the 1 mm drop. The displacement increases with the blood source height.

The spatter drops moving against the headwinds landed closer to the horizontal position of the blood source compared to their movement in still air. The maximum reductions in drop flight range due to air current (horizontal distance travelled) were 1-1.5 m for smaller droplets studied.

Spatter drops less than 0.5 mm in diameter were highly susceptible to drift along the air flow, especially at lower velocities. These required headwinds of < 1 m/s to reverse their direction, over a wide range of their initial velocities. Drops larger than 0.5 mm may reverse their directionality at incident air velocities less than 2-5 m/s depending on their initial velocity. The higher the launching angle (i.e. closer to vertical), the lower the air velocity required to alter its flight path by a given amount, due to the decelerating action of the gravitational force.

Downwind drop motion with a tailwind velocity of 5 m/s (in idealized outdoor conditions) a spatter drop may travel as much as 5-10 m.

In cross- winds the drop trajectory tends to deflect in the direction of the air flow. In an enclosed space, such as a room, a drop may cease to target a surface (wall) and end up on the floor or adjacent wall or other surface depending on the surrounding air velocity. The smaller

droplets (d < 0.5 mm) may land on the surface facing the air flow. The drop may travel further horizontally from its source compared to a similar drop in still air.

The smaller the size and lower the velocity of a drop, the more pronounced the effects of cross-current and wind on the drop's flight path. Due to the affected drop trajectory, the impact angle of the drop onto a ceiling or wall may also be affected. Consequently, the possibility of the air motion during spatter generation should be taken into account when the drop's trajectory is reconstructed. The drop and air flow directionality and velocity, as well as the blood source location relative to a wall or ceiling need to be considered to draw any conclusions on the effects of the air motion on drop trajectory, impact angle and blood source determination.

To determine whether this is a significant effect, the evaporation of water from an airborne blood droplet was estimated for typical ambient conditions.

The percentage reduction in drop diameter, $\Delta d/d \times 100\%$, due to drop in-flight evaporation of was estimated for 0.1-6 mm blood drop moving with constant velocities of 1-30 m/s in still air with a relative humidity of 50 % (normal conditions) and 0% (very dry condition) and normal ambient temperature and pressure of 20 ºC and 101.3 kPa respectively. A typical 0.5 s long flight of blood drops at body temperature was considered.

A drop with $d \geq 1$ mm is expected to lose less than 1% (at conditions with 50% relative humidity) and 3% (at extremely dry conditions) of its diameter regardless of its initial velocity. The drops with 0.2 < d < 1mm in diameter may lose 1-30% (and up to 50% at the extremely dry conditions) in their diameters. Drops of < 0.2 mm are most likely to evaporate completely shortly after formation. As the majority of measureable stains result from droplets larger than 0.5-1mm in diameter, the effect of water evaporation on the trajectory of the drop is expected to be negligible under the studied conditions.

The drop velocity may change rapidly (as what happens with typical blood drops) during the droplet's flight which would reduce the mass transfer and drop diameter loss.

Along with the evaporation, heat transfer also takes place during the flight of blood droplets which tends to bring temperature of the droplet from body temperature to the ambient temperature and affects the evaporation rate through a decrease in saturation pressure at the droplet surface. This would decrease the mass transfer from the drop surface.

As the drop cools during its motion in air its physical properties change which also may alter the evaporation rate and is worth investigating.

The future study of the combined heat and mass transfer processes accompanying projection (flight) of warm blood droplets under various (ambient) conditions may be

performed if more the detailed estimation of the effects of drop in-flight evaporation was required. This can be based on the model of Kincaid and Longley (1989) for drop evaporation due to forced convection. In addition, the effects of drop deformation and oscillations towards the increase of drop's surface-to volume ratio on the evaporation rate can be investigated.

References

Absolom, D.R., C.J. van Oss, W. Zingg, and A.W. Neumann. Biochemical Biophysics. Acta 670, 74, 1981.

Achenbach, E., The Effects of Surface Roughness and Tunnel Blockage on the Flow Past Spheres. Journal of Fluid Mechanics, 1974. 65(1): p. 113 - 125.

Adamson, A.W., Physical Chemistry of Surfaces, 5th ed. "A Willey-Interscience publication", 1990.

Adermann, D., High Speed Video 101: Measurement & Analysis Australia. Camera Systems Pty Ltd., 2004.

Akin, L.L., A Blood Spatter Primer: Dirrectional Analysis of blood spatter at Crime and Accident Scenes for the Responding Officer. Blu Line Magazine, 2005. p. 14-15.

Ambravaneswaran, B., S. D. Phillips and O. A. Basaran, Theoretical Analysis of a Dripping Faucet. Physical Review Letters, 2000. 85: p. 5332-5335.

Andsager, K.K, V. Beard, and N. L. Laird, Laboratory Measurements of Axis Ratios for Large Raindrops, Journal of the Atmospheric Sciences, 1999. 56: p. 2673-2683.

Arai, T., and H. Hashimoto, Disintegration of a Thin Liquid Sheet in a Concurrent Gas Stream. Proceedings of the Third International Conference on Liquid Atomization and Spray Systems, London, 1985, pp. V1B/1/1-7.

Arcoumanis, C., D.S. Whitelaw, J.H. Whitelaw, Breakup of Newtonian and Non-Newtonian Fluids. Atomization of Sprays, 1994. 6: p. 245-256.

Ashgriz, N., Handbook of Atomization and Sprays. Springer, 2010.

Auton, T. R., The Lift Force on a Spherical Body in a Rotational Flow. Journal of Fluid Mechanics, 1987. 183: p. 199-218.

Auton, T.R., J.C.R. Hunt, and M. Prud'Homme, The Force Exerted on a Body in Inviscid Unsteady Non-Uniform Rotational Flow. Journal of Fluid Mechanics, 1988. 197: p. 241-257.

Balthazard, V., R. Piedlievre, H. Desoille, and L. DeRobert, Etude des gouttes de sang projete (Study of projected drops of blood), in Annual Medecine Legale Criminol Police Science Toxicology. 1939, 22nd Congress of Forensic Medicine: Paris, France. p. 265-323.

Barbee, J.H., The Effect of Temperature on the Relative Viscosity of Human Blood, Biorheology, 1973. 10: p. 1.

Bartz, F.-O., R. Schmehl, R. Koch, and H.-J. Bauer, An Extension of Dynamic Droplet Deformation Models to Secondary Atomization. ILASS – Europe 2010, 23rd Annual Conference on Liquid Atomization and Spray Systems, Brno, Czech Republic, 2010, p. 1-14.

Basaran, O.A. Nonlinear Oscillations of Viscous Liquid Drops. Journal of Fluid Mechanics, 1992. 241: p. 169.

Baskurt, O. K. and H. J. Meiselman, , Handbook of Hemorheology and Hemodynamics, Baskurt, O. K., M. R. Hardeman, M. W. Rampling and H. J. Meiselman, eds, IOS Press, Amsterdam, The Netherlands, 2007.

Basset, A. B., Treatise on Hydrodynamics, 2. Cambridge: Deighton, Bell and Co., 1888.

Batchelor, G.K., An Introduction to Fluid Mechanics. Cambridge University Press, 1967.

Beard K.V., and C. Chuang, A New Model for the Equilibrium Shape of Raindrops. Journal of the Atmospheric Sciences, 1987. 44: p. 1509-1524.

Beard, K.V., and H.R. Pruppacher, A Determination of the Terminal Velocity and Drag of Small Water Drops by Means of a Wind Tunnel. Journal of Atmospheric Sciences, 1969. 26: p. 1066-1072.

Beard, K.V., and R. J. Kubesh, Laboratory Measurements of Small Raindrop Distortion. Part 2: Oscillation Frequencies and Modes. Journal of Atmospheric Sciences, 1991. 48: p. 2245-2264.

Beard, K.V., Terminal Velocity and Shape of Cloud Drops Aloft. Journal of the Atmospheric Science, 1976. 33: p. 851-864.

Becker, E., W.J. Hiller, and T.A. Kowalewski, Experimental and Theoretical Investigation of Large Amplitude Oscillations of Liquid Droplets. Journal of Fluid Mechanics, 1991. 231: p. 189-210.

Behrooz, N., Bloodstain Pattern Analysis of Determination of Point of Origin. BSc dissertation, Department of Mechanical and Industrial Engineering, University of Toronto, 2009.

Best, A.C., Empirical Formulae for the Terminal Velocity of Water drops Falling Through the Atmosphere. Quart. J. Meteor. Soc., 1950. 76: p. 302-311.

Bevel, T., and R.M Gardner, Bloodstain Pattern Analysis with an Introduction to Crime Scene Reconstruction, 3rd Ed. (Practical Aspects of Criminal & Forensic Investigations), Boca Raton: CRC Press, 2008.

Blair, D.and E. Dufresne, The Matlab Particle Tracking Code Repository, from http://physics.georgetown.edu/matlab/, accessed 2012.

Bond, N.I., Validation of Assumptions Underlying the Angle of Impact Calculation for a Bloodstain and the Development of a Synthetic Blood Substitute, MSc Thesis, University of Auckland, 2008.

Bond, W. N., and D. A. Newton, Bubbles, Drops, and Stokes' law (paper 2), Philosophical Magazine, 1928. 5(31): p. 794.

Bond, W. N., Bubbles and Drops and Stokes' law, Philosophical Magazine, 1927. 4(24): p. 889.

Boussinesq, J. 1913 Existence of a Superficial Viscosity in the Thin Transition Layer Separating One Liquid from Another Contiguous Fuid. C. R. Hehbd. Seanc. Acad. Sci., 1913. 156: p. 983-989.

Boussinesq, V., Sur la Résistance qu'oppose un Fluide Indéfini au Repos, Sans Pesanteur, au Mouvement Varié d'une Sphère Solide qu'il Mouille sur Toute sa Surface, Quand les Vitesses Restent bien Continues et Assez Faibles Pour que Leurs Carrés et Produits Soient Négligeables, Comptes Rendu de l'Academie des Sciences, 1885. 100: p. 935–937.

Brandes, E., G. Zhang, and J. Vivekanandan, Experiments in Rainfall Estimation with a Polarimetric Radar in a Subtropical Environment, Journal of Applied Meteorology, 2002. 41: p. 674-685.

Brelih, N and Seppanen, O., Ventilation Rates and IAQ in European Standards and National Regulations, AIVC Conference, Brussels, Belgium, 2011.

Brodkey, R.S., The Phenomena of Fluid Motions, Addison-Wesley Pub. Co., 1967.

Buck, U. and B. Kneubuehl, Response to "3D Bloodstain Pattern Analysis: Ballistic Reconstruction of the Trajectories of Blood Drops and Determination of the Centres of Origin of the Bloodstains", Forensic Science International, 2012. 220: p. e41.

Buck, U., B. Kneubuehl, S. Nather, N. Albertini, L. Shmidt, M. Thali, 3D Bloodstain Pattern Analysis: Ballistic Reconstruction of the Trajectories of Blood Drops and Determination of the Centres of Origin of the Bloodstains. Forensic Science International, 2010. 6114: p. 1-7.

Buzzard J.L., and R.M. Nedderman, The Coefficient of Liquid Droplets Acceleration Through Air. Chemical Engineering Science, 1967. 22(312): p.1577-1586.

Carter A.L., Forsythe-Erman J., Hawkes V., Illes M., Laturnus P., Lefebvre G., Stewart, C., and

Cassie, A.B.D. and S. Baxter, Wettability of Porous Surfaces. Transactions of the Faraday Society, 1944. 40: p. 546-551.

Cassie, A.B.D., Contact Angles. Discussions of the Faraday Society, 1948. 3: p. 11-16.

Casson, S. and G. Kurland, Viscometry of Human Blood for Shear Rates of 0 - 100,000s^{-1}. Nature, 1965. 206: p. 617-618.

Chandrasekhar, S., The Oscillations of a Viscous Liquid Globe, Proceedings of the London Mathematical Society, 1959. 9: p.141.

Chang, E. J., and M. R. Maxey, Accelerated Motion of Rigid Spheres in Unsteady Flow at Low to Moderate Reynolds Numbers, Journal of Fluid Mechanics, 1994. 277: p. 347-379.

Cheng, P., D. Li, L. Boruvka, Y. Rotenberg, and A. W. Neumann, Automation of Axisymmetric Drop Shape Analysis for Measurements of Interfacial Tensions and Contact Angles, Colloids and Surfaces, 1990: 43, p. 151-167.

Chester, W., and D. R. Breach, On the Flow Past a Sphere at Low Reynolds Numbers. Journal of Fluid Mechanics, 1969. 37: p. 751-760.

Chhabra, R.P., and J.F. Richardson, Non-Newtonian Flow in the Process Industries: Fundamentals and Engineering Applications, Butterworth-Heinemann, 1999.

Chhubra, R.P., Bubbles, Drops, and Particles in non-Newtonian fliud. Boca Raton, FL: CRC Taylor&Francis, 2nd Ed., 2007.

Chien, S., Determinants of Blood Viscosity and Red Cell Deformability. Journal of Clinical Laboratory Investigations, 1981. 156: p. 7-12.

Chien, S., Present State of Blood Rheology, in Hemodilution: Theoretical Basis and Clinical Application, Massmer, K. and Schmid-Schonbein, H, Eds, S. Karger, Basel, 1972, 1.

Chigier, N., The Physics of Atomization. In: Proceedings of the Fifth International Conference on Liquid Atomization and Spray Systems (Semerijan, H.G., ed.), ILASS-Americas and NIST, USA, 1991, p. 49-64.

Chisnell, R.F., The Unsteady Motion of a Drop Moving Vertically Under Gravity. Journal of Fluid Mechanics, 1987. 176: p. 443-464.

Clanet, C. and J.C. Lasheras, Transition from Dripping to Jetting. Journal of Fluid Mechanics, 1999. 383: p. 307-326.

Clasen, C., J. Eggers, M.A. Fontelos, J.Li and G.H. McKinley, The Beads-on-String Structure of Viscoelastic Threads. Journal of Fluid Mechanics, 2006. 556: p. 283-308.

Clift, R,J. R.Grace, and M. E. Weber, Bubbles, Drops and Particles, Academic Press, 1978.

Clyborn, J., Determining Distance Between Shooter and Victim Using Blood and Backspatter Patterns, Michigan-Ontario Identification Association Newsletter, 2010. 12.

Connolly, C., M. Illes, J. Frazer, Affect of Impact Angle Variation on Area of Origin Determination in Bloodstain Pattern Analysis. Forensic Science International, 2012. 223: p. 233-240.

Couper A., Surface Tension and Its Measurement, in Rossiter B. W. and R. C. Baetzold (eds.), Physical Methods of Chemistry, 9A, 2nd ed., New York: John Wiley & Sons, 1993.

Crocker J.C., D. Grier and E.R.Weeks, Particle Tracking Using IDL from http://www.physics.emory.edu/~weeks/idl/, accessed 2012.

Dacie, J.V. and S.M. Lewis, Practical Haemotology. Churchhill Livingstone, London, 1995, p. 12-17.

de Bruin, K.G., R.D. Stoel, J.C.M. Limborgh, Improving the Point of Origin Determination in Bloodstain Pattern Analysis. Journal of Forensic Science, 2011. 56: p. 1476-1782.

Decoslis, A., R.F. Giese and C.J. van Oss, Influence of the Water–Air Interface on the Apparent Surface Tension of Aqueous Solutions of Hydrophilic Solutes. Colloids and Surfaces B: Biointerfaces, 2000. 19(2): p. 147-162.

Dinnar U., Cardiovascular Fluid mechanics. CRC Press, Boca Raton, FL, 1981.

Dintenfass, L., Blood Viscosity. Springer, 1985, 496p.

Dombrowski, N. and W.R. Jones, The Aerodynamic Instability and Disintegration of Viscous Liquid Sheet, Chemical Engineering Society, 1963. 18: p. 203-214.

Dombrowski, N., and R.P. Fraser, A Photographic Investigation into the Disintegration of Liquid Sheets, Phil. Trans. R. Soc. London Ser. A, Math. Phys. Sci., 1954. 247(924): p. 101-130.

Dreyer K. and F.R. Hickey, The Route to Chaos in a Dripping Water Faucet. American Journal of Physics, 1991. 59(7): p. 619-627.

Dupré A., Theorie Mecanique de la Chaleur, Gauthier-Villars: Paris, 1869. p. 368.

Edgerton, H.E., E.A. Hauser and W.B. Tucker, Sudies In Drop Formation As Revealed by The High-Speed Motion Camera. Journal of Physical Chemistry, 1937. 41: p 1017-1028.

Eggers J., Theory of Drop Formation. Physics of Fluids, 1995. 7: p. 941.

Eggers, J. and T.F. Dupont, Drop Formation in a One-Dimensional Approximation of The Navier-Stokes Equation. Journal of Fluid Mechanics, 1994. 262: p. 205-221.

Eggers, J., Drop Formation - An Overview. ZAMM, 2005. 85: p. 400-410.

Eggers, J., Universal Pinching of 3D Axisymmetric Free-Surface Flow. Physical Review Letters, 1993. 71: p.3458.

Eick, J.D, R.J. Good and A.W. Neumann, Thermodynamics of Contact Angles. II. Rough Solid Surfaces. Journal of Colloid and Interface Science, 1975. 53: p. 235-238.

Ernst E, Ch. Monshausen and A.Matrai, Blood Viscosity - a Comparative Study On Three Rotational Instruments. Biorheology, 1985. 22: p. 471-475.

Faxén, H., Der Widerstand gegen die Bewegung einer starren Kugel in einer zähen Flüssigkeit, die zwischen zwei parallelen ebenen Wänden eingeschlossen ist, Annalen der Physik, 1922. 373(10): p. 89–119.

Fordham, S., On the Calculation of Surface Tension from Measurements of Pendant Drops. Proceedings of the Royal Society of London. Series A, 1948. 194 (1036): p. 1-16.

Forensic Ident., accepted for publication. (re good stringing methot+tangent method applicab to some drops)

Fuchikami, N., S. Ishioka and K. Kiyono, Simulation of a Dripping Faucet. Journal of the Physical Society of Japan, 1999. 68: p. 1185-1196.

Fung, Y.C., Biomechanics: Mechanical Properties of Living Tissues. Springer, New York, 1993.

Gabelnick H.L. and M. Litt, Rheology of Biological Systems, Conference in English, 1973.

Gardner, R.M., Defining the Diameter of the Smallest Parent-Stain Produced by a Drip. Journal of Forensic Identification, 2006. 56(2): p. 210-221.

Gaspar-Rosas, A., and G.B. Thurston, Erythrocyte Aggregate Rheology by Transmitted and Reflected Light. Biorheology, 1988. 25: p. 471.

Gillaspy, P. H., and T. E. Hoffer, Experimental Measurements of the Effect of Viscosity on Drag for Liquid Drops. AIChE Journal, 1983. 29: p. 229-236.

Goddard, J. W. F., J D. Eastment, and J. Tan, Self-Consistent Measurements of Differential Phase and Differential Reflectivity in Rain. Proc. 1994 Int. Geoscience and Remote Sensing Symp., Pasadena, CA, IEEE, 1994, p. 369-371.

Goldin, M., J. Yerushalmi, R. Pfeffer, and R. Shinnar, Breakup of a Laminar Capillary Jet of a Viscoelastic Fuid. Journal of Fluid Mechanics, 1968. 38: p. 689.

Goldstein, S., Forces on a Solid Body Moving Through Viscous Fluid. Proceeding of the Royal Society of London, 1929. A123: p. 216-235.

Gonzalez, R.C., R.E. Woods and S.L. Eddins, Digital Image Processing Using MATLAB. Upper Saddle River, NJ: Pearson/Prentice Hall, 2004.

Good, R. J., A Thermodynamic Derivation of Wenzel's Modification of Young's Equation for Contact Angles; Together with a Theory of Hysteresis. Journal of the American Chemical Society, 1952. 74: p. 5041. see also Good, R. J., Contact angle, wetting, and adhesion: a critical review. Journal of Adhesion Science & Technology, 1992. 6(12): p. 1269-1302.

Gossard, E.E., R.G. Stauch, D.C. Welsh, and S.Y. Matrosov, Cloud layer, Particle Identification, and Rain Rate Profiles from Z. RV Measurements by Doppler Radars. J. Atmos. Oceanic Technol., 1992. 9: p. 108-119.

Grace, J.R., T. Wairegi, and T.H. Nguygen, Shapes and Velocities of Single Drops and Bubbles Moving Freely Through Immiscible Liquids. Trans. Inst. Chem. Eng., 1976. 54: p. 167.

Green, A.W., An Approximation for the Shape of Large Raindrops. Journal of Applied Meteorology, 1975. 14: p. 1578-1583.

Guan G., Zhu J., Xia S., Feng Z., and Davis E.J., Simulation of mass transfer from an oscillating microdroplet, International journal of heat and mass transfer, 2005, 48(9), pp: 1705-1715.

Gun, R., and G.D. Kinzer, The Terminal Velocity of Fall for Water Droplet in Stagnant Air. Journal of Meterology, 1949. 54: p. 243-248.

Gurkan, T., Motion of a Circulating Power-Law Drop Translating Through Newtonian Fluids at Intermidiate Reynolds Numbers. Chemical Engineering communications, 1989. 80: p. 53-67.

Guyton, A.C., and J.E. Hall, Textbook of Medical Physiology, 9th edition. W.B. Sanders Company, Philadelphia, 1996.

Guyton, A.C., and J.E. Hall, Textbook of Medical Physiology. (10th ed.). Philadelphia: W.B. Saunders, 2000.

Hadamard, J. S., Mouvement Permanent lent d'une Sphere Liquide et Visqueuse dans un Liquide Visqueux. Comptes rendus de l'Académie des sciences, 1911. 152: p. 1735.

Hagerty, W.W., and J.F. Shea, A Study of the Stability of Plane Fluid Sheet, Br. J. Appl. Phys., 1953. 4: p. 167-169.

Haider, A., and O. Levenspiel, Drag Coefficient and Terminal Velocity of Spherical and Nonspherical Particles. Powder Technology, 1989. 58: p. 63-70.

Happel, J., and H. Brenner, Low Reynolds Numbers Hydrodynamics, 2nd ed., Noordhoff International Publishing: Leyden, 1973.

Harkins, H.N., and W.D. Harkins, The Surface Tension of Blood Serum, and the Determination of the Surface Tension of Biological Fluids. J. Clin. Invest., 1929. 7(2): p. 263-281.

Harkins, W.D. and Brown F.E., The Determination of Surface Tension (Free Surface Energy), and The Weight of Falling Drops: The Surface Tension of Water and Benzene by The Capillary Height Method. Journal of American Chemical Society, 1919. 41(4): p. 499–524.

Harper, J.F., and D.W. Moore, The Motion of a Spherical Drop at High Reynolds numbers. Journal of Fluid Mechsnics, 1968. 32(2): p. 367-391.

Haynes, W. M., ed., CRC Handbook of Chemistry and Physics, 92nd Edition, CRC Press/Taylor and Francis, Boca Raton, FL, 2012.

Heertjes, P.M., L.H. De Nie and H.J. DeVries, Drop Formation in Liquid-Liquid Systems – I Prediction of Drop Volume at Moderate Speed of Formation. Chemical Engineering Science, 1974. 29: p. 441-449.

Hida, K. and T. Nakanishi, The Shape of a Bubble or a Drop Attached to a Flate Plate. Journal of the Physical Society of Japan, 1970. 28(5): p. 1336 - 1339.

Hinghofer-Szalkay, H., and J.E. Greenleaf, Continuous Monitoring of Blood Volume Changes in Humans. Journal of Applied Physiology, 1987. 63(3): p. 1003-1007.

Hinze J.O., Forced Deformation of Viscous Liquid Globules. Applied Science Research. 1948. Al: p. 263.

Hinze, J.O., Fundamentals of the Hydrodynamic Mechanism of Splitting in Dispersion Processes. AlChE Journal, 1955. 1: p. 289-295.

Hiroyasu, H., M., Shimizu and M. Ari, The Breakup of High Speed Jet in a High Pressure Gosous Atmosphere. Proceedings of the Second International Conference on on Liquid Atomization and Spray Systems, Madison, Wis., 1982, p. 62-74.

Hitchcock, S.J., N.T. Carrol and M.G. Nicholas, Some Effects of Substrate Roughness on Wettability. Journal of Materials Science, 1981. 16: p. 714-732.

Hrncir, E., and J. Rosina, Surface Tension of Blood. Physiological Research, 1997. 46(4): p. 319-321.

Hsiang L-.P., and G.M. Faeth, Drop Properties After Secondary Breakup. International Journal of Multiphase Flow, 1993. 19(5): p. 721-735.

Hsiang, L-P., and G.M. Faeth, Drop Deformaion and Breakup due to Shock Wave and Steady Disturbances. International Journal of Multiphase Flow, 1995. 21: p. 545-560.

Hsiang, L-P., and G.M. Faeth, Near-limit Drop Deformation and Secondary Breakup, International Journal of Multiphase Flow, 1992. 18: p. 635-652.

Huang, C.R., M. Siskovic, R.W. Robertson, W. Fabisiak, E.J. Smitherberg, A.L. Copley, Quantitative Characterization of Thixotropy of Whole Human Blood. Biorheology, 1975. 12: p. 279.

Hughes, R. R., and E. R. Gilliand, The Mechanics of Drops. Chemical Engineering Progress, 1952. 48: p. 497-504.

Huh C. and S.G. Mason, Effects of Surface Roughness on Wetting (theoretical). Journal of Colloid Interface Science, 1977. 60: p. 11-38.

Hulse-Smith, L. and M. Illes, A Blind Trial Evaluation of a Crime Scene Methodology for Deducting Impact Velocity and Droplet Size from Circular Bloodstains. Journal of Forensic Sciences, 2007. 52(1): p. 65-69.

Hulse-Smith, L., N.Z. Mehdizadeh, and S. Chandra, Deducing Drop Size and Impact Velocity from Circular Bloodstains. Journal of Forensic Science, 2005. 50(1): p. 1-10.

Humphrey J.A.C., Note on Drop Formation at Low Velocity in Quiescent liquids, Chemical Engineering Science, 1980. 35: p. 1452-1554.

Hunderson, D., H. Segur, L. Smolka and M. Wadati, The Motion Of a Falling Liquid Filament. Physics of fluids, 2000. 12(3): p. 550-563.

James, S., P. Kish, and P. Sutton, Principles of Bloodstain Pattern Analysis: Theory and Practice, (Practical Aspects of Criminal & Forensic Investigations), CRC Press, 2005.

Jeng S.M., and Deng Z., Numerical simulation of deformed droplet dynamics and evaporation, Recent advances in spray combustion: Spray combustion measurements and model simulation., 1996, 2, pp: 305-328.

Johnson, R.E. and R.H. Dettre, Wetting and Contact Angle. Surface and Colloid Science, 1969. 2: p. 85-153.

Joseph, D.D., G.S. Beavers, T. Funada, Rayleigh-Taylor Instability of Viscoelastic Drops at High Weber Numbers. Journal of Fluid Mechanics, 2002. 453: p. 109-132.

Kabaliuk, N., M.C. Jermy, K. Morison, T. Stotesbury, M.C. Taylor and E. Williams, Blood Drop Size in Passive Dripping From Weapons, Forensic Science International, 2013. 228: P. 75-82.

Kenner, T., The Measurement of Blood Density and Its Meaning. Basic Research in Cardiology, 1989. 184: p. 111-124.

Kim I., S. Elghobashi and W.A. Sirignano, On the Equation for Spherical-Particle Motion: Effect of Reynolds and Acceleration Numbers. Journal of Fluid Mechanics, 1998. 367: p. 221-253.

Kim, H.S. , W.S. Kang, and S.H. Hong, Metal Surface Treatment for Enhancement of Hydrophilic Property Using Atmospheric-Pressure Dielectric Barrier Discharge. IEEE Translations on Plasma Science, 2010. 38: 1982.

Kincaid, D.C. and T.S. Longley, A Water Droplet Evaporation and Temperature Model, American Society of Agricultural Engineering, 1989. 32(2): p. 457-463.

Kiyono, K. and N. Fuchikami, Dripping Faucet Dynamics by an Improved Mass-Spring Model. Journal of the Physical Society of Japan, 1999. 68: p. 3259-3270.

Knock, C. and M. Davison, Predicting the Position of the Source of Blood Stains for Angled Impacts. Journal of Forensic Science, 2007. 52(5): p. 1044-1049.

Kratochvil A, and E. Hrncir, Correlation Between the Blood Surface Tension and the Activity of Some Enzymes. Physiol. Res., 2001. 50: p. 433-437.

Krishnan, A., A. Wilson, J. Sturgeon, C.A. Siedlecki, and E.A. Vogler, Liquid-Vapor Interfacial Tension of Blood Plasma, Serum and Purified Protein Constituents. Theory of Biomaterials, 2005. 26: p. 3445-3453.

Krzeczkowski, S.A., Measurement of Liquid Droplet Disintegration Mechanisms. International Journal of Multiphase Flow, 1980. 6: p. 227-239.

Kumar, R. and Kuloor, N.R., The Formation of Bubbles and Drops, Advances in Chemical Engineering, 1970. 8: p. 256-365.

Laber, T.L., B.P. Epstein and M.C. Taylor, High Speed Digital Video Analysis of Bloodstain Pattern Formation from Common Bloodletting Mechanisms, IABPA News, 2008, p. 4-12.

Laber, T.L., Bloodspatter Classification. IABPA News, 1985a. 2(4).

Laber, T.L., Diameter of a Bloodstain as a Function of Origin, Distance Fallen, and Volume of a Drop. International Association of Bloodstain Pattern Analysts News, 1985. 2(1): p. 12-16.

Lamb, H., Hydrodynamics. Cambridge University Press, 1932.

Landau, L.D., and E.M. Lifshitz Fluid, Fluid Mechanics, 2nd Ed., (Course of Theoretical Physics; Vol. 6), Pegamon Press, 1987.

Lando, J.L. and H.T. Oakley, Tabulated Correction Factors for The Drop-Weight-Volume Determination of Surface and Interfacial Tensions. Journal of Colloid and Interface Science, 1967. 25(4): p. 526-530.

Lane, W.R. and H.L. Green, Surveys in Mechanics. Cambridge University Press, 1956.

Lane, W.R., Shatter of Drops in Streams of Air. Inustrial and Engineering Chemistry, 43: p. 1312-1317.

Lapple, C.E., J.P. Henry, and D.E. Blake, Atomization - a Survey and Critique of The Literature, in Stanford Research Institute Technical Report 1957. 6.

Lautrup, B., Physics of Continuous Matter, 2nd ed., CRC Press, 2010.

LeClair, B.P., and A.E. Hamielec, Viscous How Through Particle Assemblages at Intermediate Reynolds Numbers - a Cell Model for Transport in Bubble Swarms. Canadian Journal of Chemical Engineering, 1971. 49: p. 713-720.

Lefebvre A.H., Atomization and Sprays. Hemisphere, 1989.

Levich, V. G., Physicochemical Hydrodynamics. Prentice-Hall, New York, 1962.

Lewis, J. A., and F. G. Carrier, Some Remarks on the Flat Plate Boundary Layer. Quarterly of Applied Mathematics, 1949. 7: p. 228-234.

Liang, L., and Michaelides, E. E., The Magnitude of Basset Forces in Unsteady Multiphase Flow Computations. Journal of Fluids Engineering, 1992. 114: p. 417-419.

Licht, W., and G.S.R. Narasimhamurty, Rate of Fall of Single Liquid Droplets. AIChE Journal, 1955. 1: p. 366-373.

Lindt, J. T., On the Periodic Nature of the Drag of a Rising Bubble, Chemical Engineering Science, 1972. 27: p. 1775-1781.

Liu, A.B., D. Mather, and R.D. Reitz, Modeling the Effects of Drop Drag and Breakup on Fuel Sprays. SAE Technical Paper 930072, SAE, 1993.

Liu, H., Science and Engineering of Droplets: Fundamentals and Applications. Nyes Publications/William Andrew Publish11ing, LLC, 1981.

Lovalenti, P.M., and J.F. Brady, The Hydrodynamic Force on a Rigid Particle Undergoing Arbitrary Time-Dependent Motion at Small Reynolds Numbers. Journal of Fluid Mechanics, 1993. 256: p. 561-605.

Lowe, G. D. O. and J. C. Barbenel, Plasma and Blood Viscosity. Clinical Blood Rheology, 1988. Vol.1, ed. by G. D. O. Lowe, CRC Press, Boca Raton Florida, p. 11-44.

Luxford, G., Experimental and Modelling Investigation of the. Deformation, Drag and Break-up of Drizzle Droplets Subjected to Strong Aerodynamic Forces in Relation to SLD Aircraft Icing, PhD Thesis, Cranfield University, 2005.

MacDonell, H.L. and K. DeLige, On Measuring the Volume of very small Drops of Blood and Correlation of this relationship to Bloodstain Diameter, in International Association of Bloodstain Pattern Analysts. 1989.

MacDonell, H.L. and L.F. Bialousz, Flight Characteristics and Stain Patterns of Human Blood. Law Enforcement Assistance Administration, National Institute of Law Enforcement and Criminal Justice, 1971.

MacDonell, H.L., Bloodstain Patterns. 1997, New York: Laboratory of Forensic Science. 1982.

Maromottant, P. and E. Willermaux, Fragmentation of Stretched Liquid Ligaments. Physics of Fluids, 2004. 16: p. 2732-2742.

Mashayek F., Dynamics of evaporating drops. Part I: formulation and evaporation model, International journal of heat and mass transfer, 2001, 44(8), pp: 1517-1526.

Masliyah, J. H., Ph.D Thesis, University of British Columbia, Vancouver, 1970.

Massey, B.S., Mechanics of Fluids, Chapman Hall, 6th Ed., 1989.

Maxey, M. R. and J. J. Riley, Equation of Motion for a Small Rigid Sphere in a Nonuniform Flow. Physics of Fluids, 1983. 26: p. 883-889.

McCarthy, M.J. and N.A. Molloy, Review of Stability of Liquid Jets and the Influence of Nozzle Design, Chemical Engineering Journal, 1974. p. 7-10.

McLaren, C.E., G.M. Brittenham, V. Hasselblad, Statistical and Graphical Evaluation of Erythrocyte Volume Distributions. American Journal of Physiology, 1987. 252(4 Pt 2): p. H857-66.

Merrill, E.W., Rheology of Blood. Physiological Reviews, 1969. 49(4): p. 863-888.

Michaelides, E. E., and Z.-G. Feng, The Equation of Motion of a Small Viscous Sphere in an Unsteady Flow with Interface Slip. International Journal of Multiphase Flow, 1995. 21: p. 315.

Michaelides, E. E., Particles, Bubbles and Drops - Their Motion, Heat and Mass Transfer, World Scientific Publishers, New Jersey, 2006.

Morgan, J.L.R., and H.E. Woodward, The Weight of a Falling Drop and the Laws of Tate. J. Am. Chem. Soc., 1913. 35: p. 1249-1262.

Motion Studio Cross-Platform User Manual (For Windows and MAC), Integrated Desidn Tools, Inc., v.2.06, 2008.

Narasinga Rao, E.V.L. and R. Kumar and N.R. Kuloor, Drop Formation Studies in Liquid-Liquid Systems. Chemical Engineering Science, 1966. 21: p. 867-880.

Neumann, A.W. and R.J. Good, Techniques of Measuring Contact Angles. Surface and Colloid Science, 1979. 11: p. 31-91.

Nguen, T.H.I., Technical Paper. .Department of Chemical Engineering, McGill University, Montreal, 1973.

Odar, F., and W.S. Hamilton, Force on a Sphere Accelerating in a Viscous Fluid. Journal of Fluid Mechanics, 1964. 18: p. 302-314.

Odar, F., Unsteady Motion of a Sphere Along a Circular Path in a Viscous Fluid. Journal of Applied Mechanics, 1968. 90: p. 652-654.

Oguz, K.B., Handbook of Hemorheology and Haemodynamics. IOS Press, 2007.

O'Rourke,P.J., and A.A. Amsden, The TAB Method for Numerical Calculation of Spray Droplet Breakup. SAE Technical Paper 872089, 1987.

Oseen, C. W., Über die Stokessche Formel und über eine verwandte Aufgabe in der Hydrodynamik. Ark. Mat., Astron. Fys., 1910. 6(29): p. 1-20.

Papageorgiou., D.T, On the Breakup of Viscous Liquid Threads. Physics of Fluids, 1995. 7: p. 1529-1544.

Parker, N.L., L.R. Bedore, K.K. Cooper, P. Fowler, T.A. Miller, and J. Showalter, Summary Report of Bloodstain Pattern Analysis Research Group. 1982. p. 1-91.

Peregrine, D.H., G. Shoker and A. Symon, The Bifurcation of Liquid Bridges. Journal of Fluid Mechanics, 1990. 212: p. 25-39.

Photron FASTCAM Viewer for High Speed Digital Imaging User Manual, 2007. Version 3.0 Revision 1.01E. Tokyo: Photron Limited.

Pilch, M., and C. Erdman, Use of Break-up Time Data and Velocity History Data to Predict the Maximum Size of Stable Fragments for Acceleration-Induced Break-up of a Liquid Drop. International Journal of Multiphase Flow, 1987. 13: p. 741-757.

Pizzola, P.A., S. Roth, and P.R. De Forest, Blood Droplet Dynamics-I. Journal of Forensic Sciences, 1986. 31(1): p. 36-49.

Plateau, J., Satique Experimental et Theorque des Liquids Soumle aux Seule Force Moleculaire. Gauthier Villare, 1873. Vol. 1, 2.

Podworny, E.J. and A.L. Carter, Computer Modelling of the Trajectories of Blood Droplets and Bloodstain Pattern Analysis with a PC computer. 2nd Training Conference in International Association of Bloodstain Battern Analysis, 1989.

Pozrikidis C., Stability of Sessile and Pendant Drops, Journal of Engineering Mathematics, 2012. 72: p. 1-20.

Proudman , I., and J. R. A. Pearson, Expansions at Small Reynolds Number for the Flow Past a Sphere and a Circular Cylinder. Journal of Fluid Mechanics, 1957. 2: p. 237-262.

Pruppacher, H. R., and R.L. Pitter: A Semi-empirical Determination of the Shape of Cloud and Rain Drops, Journal of Atmospheric Sciences, 1971. 28: p. 86-94.

Pruppacher, H.R., and K.V. Beard, A Wind Tunnel Investigation of the Internal Circulation and Shape of Water Drops Falling at Terminal Velocity in Air, Quart. J. Roy. Meteor. Soc., 1970. 96: p. 247-256.

Puig-de-Morales-Marinkovic, M., T.K. Turner, J.P. Butler, J.J. Fredberg, S. Suresh, Viscoelasticity of the Human Red Blood Cell. Am J Physiol Cell Physiol., 2007. 293(2): p. C597-605.

Qian J. and Law C.K., Regimes of coalescence and separation in drop collision. Journal of Fluid Mechanics, 1997. 33: p. 59-80.

Rampling, M. W., Red cell aggregation and yield stress. Clinical Blood Rheology, ed. by G. D. O. Lowe, CRC Press, Boca Raton Florida, 1988. 1: p. 65-86.

Ray, S., High Speed Photography and Photonics. Focal Press, Butterworth-Heinemann Oxford, UK, 1997.

Rayleigh, Lord, Investigations in Capillarity. Philosophical Magazine, 1899. 48: p. 321-337.

Rayleigh, Lord, On the Capillary Phenomena of Jets. Proceedings of the London Mathematical Society, 1879. 29: p.71-97.

Rayleigh, Lord, On the Instability of Cylindrical Fluid Surfaces. Philosophical Magazine, 1892. 34 (207): p. 177-180.

Rayleigh, Lord, On the Stability of Jets. Proceedings of the London Mathematical Society, 1878. 10: p. 4-13.

Rayleigh, Lord, Some Applications of Photography. Nature, 1891. 44 (1133): p. 249-254.

Rayleigh, Lord, The Principle of Similitude. Nature, 1915. 95: p. 66-68.

Raymond M.A., Smith E.R. and Liesegang J., Oscillating Blood Droplets--implications for crime scene reconstruction, Science and Justice, 1996. 36: p. 161-171.

Raymond, M.A., E.R. Smith, and J. Liesegang, The Physical Properties of Blood - Forensic Considerations. Science & Justice, 1996. 36(3): p. 153-160.

Reitz, R.D. and F.V. Bracco, Encyclopedia of Fluid Mechanics, vol. 3, chap. Mechanism of Breakup of Round Liquid Jets, Gulf Publishing, Houston, Texas, Houston, Texas, 1986. p. 233-249.

Reitz, R.D. and R. Diwakar, Structure of High-Pressure Fuel Sprays, Society of Automotive Engineers Technical Paper 870598, SAE Transactions, 1987. 96(5): p. 492-509.

Risk, N.K., and A.H. Lefebvre, Influence of Liquid Film Thickness on Airblast Atomization. Trans. ANME J. Eng. Power, 102: p. 706-710.

Rodrigue, D., The Effect of Surfactants on Deformation of Falling Non-Newtonian Drops in a Newtonian Fluid. The Canadian Journal of Chemical Engineering, 2008. 86: p. 105-109.

Rogers, N., Hematocrit - Implications for Bloodstain Pattern Analysis, in Centre for Forensic Science. 2009, University of Western Australia: Perth. p. 128.

Rosina, J., E. Kvašňák, D. Šuta, H. Kolářová, J. Málek, and L. Krajči, Temperature Dependence of Blood Surface Tension. Physiological Research, 2007. 56 (Suppl. 1): p. S93-S98.

Ross, E.S., The study of bloodstain patterns resulting from the release of blood drops from a weapon, in Chemistry. 2006, The University of Auckland: Auckland.

Rotenberg, Y., L. Boruvka and A. W. Neumann, Determination of Surface Tension And Contact Angle from the Shapes of Axisymmetric Ffluid Interfaces, Journal of Colloid Interface Science, 1983. 93: p. 169-183.

Rowe, W.F., Errors in the Determination of the Point of Origin of Bloodstains. Forensic Science International, 2006. 161: p. 47-51.

Roy, K., Illuminating Engineering, Firewall Media, 2006.

Rybczynski, W., Über die fortschreitende Bewegung einer flüssigen Kugel in einem zähen Medium. Bull. Acad. Sci. Cracovi, 1911. A: p. 40-46.

Saito, S., On the Shape of the Nearly Spherical Drop which Falls through Viscous Fluid. Sci. Rep. Thoku Imp. Univ., 1913. 1(2): p. 179-201.

Savart, F., Mémoire sur la Constitution des Veines Liquides Lancées par des Orifices Circulaires en Mince Paroi. Annalj Chimica, 1833. 53; p. 337-386.

Savic, P., Circulation and Distortion of Liquid Drops Falling Through a Viscous Medium. National Research Council of Canada, Division of Mechanical Engineering Report MT-22, 1953

Saylor, J.R., and B. K. Jones, The Existence of Vortices in The Wakes of Simulated Raindrops. Physics of Fluids, 2005. 17: p. 031706-1-4.

Scheele, G.F. and B.J. Meister, Drop Formation at Low Velocities in Liquid-Liquid Systems: Part I. Predicting drop volume. A.I.Ch.E Journal, 1968. 14: p. 9-19.

Schlichting, H., Boundary Layer Theory, 6th Ed. McGraw-Hill, New York (1968).

Schmehl, R., Advanced Modeling of Droplet Deformation and Breakup for CFD Analysis of Mixture Preparation. 1-10. In 18th Annual Conference on Liquid Atomization and Spray Systems, ILASS 2002, 2002.

Schmehl, R., Modeling Droplet Breakup in Complex Two-Phase Flows. 1-3. In 9th International Conference on Liquid Atomization and Spray Systems, ICLASS 2003, 2003.

Schmidt, D.P., I. Nouar, P.K. Senecal, C.J. Ruthland, J.K. Martin and R.D. Reitz, Pressure-Swirl Atomization in the Near Field. SAE Technical Paper Series 1999-01-0496, 1999.

Schroeder, R.R., and R.C. Kintner, Oscillations of Drops Falling in a Liquid Field. AIChE Journal, 1965. 11: p. 5-8.

Scriven, L.E., Dynamics of a Fluid Interface, Chemical Engineering Science, 1970. 12: p. 98-108.

Shaw, R. S., The Dripping Faucet as a Model Chaotic System. Aerial Press, 1984.

Shi, X.D, M.P. Branner and S.R. Nagel. A Cascade of Structure In a Drop Falling From a Faucet. Science, 1994. 265: p. 219-222.

Shore, H.J. and G.M. Harrison, The Effect of Added Polymers on the Formation of Drops Ejected from a Nozzle. Physics of Fluids, 2005. 17: p. 033104.

Shuttleworth, R., and G.L.J. Bailey, The Spreading of a Liquid Over a Rough Solid. Discussions of the Faraday Society, 1948. 3: p. 16-22.

Skelland, A. H. P., Non-Newtonian Flow and Heat Transfer. Wiley, 1967. 469p.

Skrebutenas, R., Variables Affecting the Flight of Blood Droplets and Maximum flight distance, BSc Thesis, Trent University, 2013.

Smagina, I., M. Pathak, O.M. Lavrenteva and A. Nir, Motion and Shape of an Axisymmetric Viscoplastic Drop Slowly Falling Through a Viscous Fluid. Rheologycal Acts, 2011. 50: p. 361-374.

Smagina, I., M. Pathak, O.M. Lavrenteva and A. Nir, Motion and Shape of an Axisymmetric Viscoplastic Drop Slowly Falling Through a Viscous Fluid. Rheologycal Acts, 2011. 50: p. 361-374.

Somer, T., and H.J. Meiselman, Disorders of blood viscosity. Annals of Medicine, 1993. 25(1): p. 31-9.

Sostarecz, M.C. and A. Belmonte, Motion and Shape of a Viscoelastic Drop falling Through a Viscous Fluid. Journal of Fluid Mechanics, 2003. 497: p. 235-252.

Spells, K.E., A Study of Circulation Patterns within Liquid Drops moving through a Liquid. Proceedings of the Physical Society B, 1952. 65: p. 541-546.

Stauffer, C.E., The Measurement of Surface Tension by the Pendant Drop Technique. The Journal of Physical Chemistry, 1965. 69(6): p. 1933-1938.

Stokes, G.G., On the Effect of the Internal Friction of Fluids on the Motion of Pendulums. Trans. Cambridge Philos. Soc, 1851. 9: p. 8-27.

Stoltz, J. F., M. Singh, and P. Riha, Hemorheology in Practice. IOS Press, 1999.

Stone, H. A. and L. G. Leal, Relaxation and Breakup of an Initially Extended Drop In an Otherwise Quiescent Fluid. Journal of Fluid Mechanics, 1989. 198: p. 399.

Strengthening Forensic Science in the United States: A Path Forward, Committee on Identifying the Need of the Forensic Sciences Community. National Research council, 2009.

Strutt, J.W., Lord Rayleigh, On the Instability of Jets. Proceedings of the London Mathematical Society, 1878. 10: p. 4-13.

Strutt, J.W., Lord Rayleigh, Some Applications of Photography. Nature, 1891. 44(1133): p. 249-254.

Sweet, M.J., Velocity Measurements of Projected Bloodstains from a Medium Velocity Impact Source. Journal of the Canadian Society of Forensic Science, 1993. 26(3): p. 103-110.

SWGSTAIN BPA Terminology, 2009. Scientific Working Group on Bloodstain Pattern Analysis (SWGSTAIN) website, accessed 7/25/2010.

Sy, F., and E. N. Lightfoot, Transient Creeping Flow Around Fluid Spheres, AIChE Journal, 1971. 17: p. 177.

Sy, F., J. W. Taunton, and E. N. Lightfoot, Transient Creeping Flow Around Spheres. AIChE Journal, 1970. 16: p.386.

Szakall, M., K. Diehl, S.K. Mitra and S. Borrmann, A Wind Tunnel Study on the Shape, Oscillation, and Internal Circulation of Large Raindrops with Sizes between 2.5 and 7.5 mm. American Meteorological Society, 2009. 66: p. 755-765.

Tamada, K. and Y. Shibaoka, On the Pendent Drop, International Journal of the Physical Society of Japan, 1961. 16(6): p. 1249 - 1252.

Tanasawa, Y. and S. Toyoda, Technical Report of Tohoku University, Japan, 1955. N19-2, p. 135.

Tanner, F., "A Cascade Atomization and Drop Breakup Model for the Simulation of High-Pressure Liquid Jets," SAE Technical Paper 2003-01-1044, 2003, doi:10.4271/2003-01-1044.

Tate, T., On the Magnitude of a Drop of Liquid Formed Under Different Circumstances. Philosophical Magazine, 1864. 27: p. 176-180.

Taylor, T.D., and A. Achrivos, The Deformation and Drag on Falling Viscous Drop at Low Reynolds Numbers. Journal of Fluid Mechanics, 1964. 18: p. 446-470.

Temkin, S., and H. K. Mehta, Droplet Drag in an Accelerating and Decelerating Flow, Journal of Fluid Mechanics, 1982. 116: p. 297-313.

Temkin, S., and S. S. Kim, Droplet Motion Induced by Weak Shock Waves, Journal of Fluid Mechanics, 1980. 96: p. 133-157.

Testik F.Y., A.P. Barros, and L.F. Bliven, Field Observations of Multimode Raindrop Oscillations by High-Speed Imaging. American Meteorological Society, 2006. 63: p. 2663-2668.

Thiessen, D. B. and K.F. Man, Surface Tension Measurement. The Measurement, Instrumentation and Sensors Handbook on CD-ROM, CRC Pres, 1999.

Thongyai, N., Study of Stainless Steel Surface Cleanability. Thesis. (MS). King Mongkut's Institute of Technology North Bangkok, 2005.

Thoroddsen, S.T., T.G. Etoh and K. Takehara, High-Speed Imaging of Drops and Bubbles. The Annual Review of Fluid Mechanics, 2008. 40: p. 257-85.

Thurai, M. and V.N. Bringi, Drop Axis Ratios, from a 2D-Video Disdrometer, J. Atmos. Ocean. Technol., 2005. 22: p. 963-975.

Thurston, G. B., The Viscoelasticity of Human Blood. Biophysical Journal, 1972. 12: p. 1205-1217.

Thurston, G.B., Theory of Oscillation of a Viscoelastic Fluid in a Circular tube, J. Acoust. Soc. Amer., 1960. 32: p. 210-213.

Tong, A.Y. and Z. Wang, Relaxation Dynamics of a Free Elongated Liquid Ligament. Physics of fluids, 2007. 19: p. 092101-1-11.

Trinh, A. and T.G. Wang, Large-amplitude Free and Driven Drop-shape Oscillations: Experimental Observations, 1982

Tritton, D. J., Physical Fluid Dynamics, 2nd ed., Oxford, England: Clarendon Press, p. 58, 1988.

Trudnowski, R.J., and R.C. Rico, Specific Gravity of Blood and Plasma at 4 and 37 °C. Clinical Chemistry, 1974. 20(5): p. 615-616.

Tsamopoulos, J. and R.A. Brown, Non-linear Oscillations of Inviscid Drops and Bubbles. Journal of Fluid Mechanics, 1983. 127: p. 519-537.

Turgeon, M.L., Clinical Hematology: Theory and Procedures. Lippincott Williams & Wilkins., 2004, p. 100.

Tyler, E., Instability of Liquid Jets. The London, Edinburgh and Dublin Philosophical Magazine and Journal of Science, 1933. 16(105): p. 504-519.

Uplinger, W.G., A New Formula for Raindrop Terminal Velocity. Preprints 20th Radar Metheorology Conference, Am. Meteor. Soc. Boston, 1977, p. 389-391.

van Boxel, J.H, Numerical Model for the Fall Speed of Raindrops in a Rainfall Simulator. Workshop on Wind and Water Erosion, November 17-18, 1997, Ghent Belgium, p. 77-85.

Van de Sande, E., and J.M. Smith, Jet and Air Entrainment by Low-Velocity Turbulent Jets. Chemical Engineering Society, 1976. 31(3): p. 219-224.

van Oss, C.J., The Properties of Water and their Role in Colloidal and Biological Systems. Interfacial Science and Technology, 16, Elsevier Ltd., 1st ed., 2008.

Vlastos, G., D. Lerche, and B. Koch, The Superposition of Steady on OIscillatory Shear and its Effect on the Viscoelasticity of Human Blood and a Blood-Like Model Fuid. Biorheology, 1997. 34: p. 19-36.

Wagner, C., Y. Amarouchene, D. Bonn and J. Eggers, Droplet Detachment and Satellite Bead Formation in Viscoelastic Fluids. Physical Review Letters, 2005. 95: p. 1645041-4.

Warshay, M., E. Bogusz, M. Johnson, and R.C. Kintner, Ultimate Velocity of Drops in Stationary Liquid Media, Canadian.Journal of Chemical Engineering, 1959. 37: p. 29.

Weast, R.J., Handbook of Chemistry and Physics, 51st Ed. Chem Rubber Co., Cleveland, 1970/71.

Weber, C., Zum Zerfall eines Flüssigkeitsstrahles. Z. angew. Math. Mech., 1931. 11: p. 136-154.

Weissenborn, P.K., and R.J. Pugh, Surface Tension of Aqueous Solutions of Electrolytes: Relationship With Ion Hydration, Oxygen Solubility, and Bubble Coalescence. Journal of Colloid and Interface Science. 1996, 184: p. 550-563.

Wells, J.K., Investigation of Factors Affecting the Region of Origin Estimate in Bloodstain Pattern Analysis. MSc. dissertation, Mechanical Engineering Department, University of Canterbury, 2006.

Wells, R., and H. Schmid-Schijnbein, Redcell Deformability and Fluidity of Concentrated Cell Suspensions. Journal of Applied Physiology, 1969. 27: p. 213-217.

Wells, R.E., R. Denton and E.W. Merrill, Measurement of Viscosity of Biologic Fluids by Cone Plate Viscometer. Journal of Laboratory and Clinical Medicine, 1961. 57(4): p. 646-656.

Wenzel, R.N., Resistance of Solid Surface to Wetting by Water. Industrial & Engineering Chemistry, 1936. 28: p. 988-994.

Wierzba, A., Deformation and Breakup of Liquid Drops in a Gas Stream at Nearly Critical Weber Numbers. Experiments in Fluids, 1990. 9: p. 59-64.

Williams, E. and M.C. Taylor, The Development and Construction of a Motorized Blood Droplet Generation Device (BDGD) for Detailed Analysis of Blood Droplet Dynamics, Technical Paper, Journal of Bloodstain Pattern Analysis, 2013. 29(1): p. 14-29.

Williams, E., Cast-Off, but not out. Crime Scene Reconstruction using an Integrated Approach, PhD Thesis, University of Auckland, 2014.

Winnikow, S., and B.T. Chao, Droplet Motion in Purified Systems. Physics of Fluids, 1966. 9(1): p. 50-61.

Wonder, A.Y., Blood Dynamics. 2001, London: Academic Press. viii, 168.

Yamashita B. Validation of the BackTrack™ Suite of Programs for Bloodstain Pattern Analysis. J.

Young, T., An Essay On the Cohesion of Fluids. Phil. Trans. R. Soc. Lond., 1805. 95: p. 65–87. see also Young T., Miscellaneous Works, G. Peacock, Ed. Murray, London, 1855. 1: p. 418.

Yunus, A.C. and J.M. Cimbala, Fluid Mechanics: Fundamentals and Application, McGraw-Hill Science Engineering, 2005.

Zapryanov Z.D., S.Tabakova, Dynamics of Bubbles, Drops and Rigid Particles, Kluwer Academic Publishers: New York, London, Dordrecht, 1998, 514p.

Zhang, D. and H.A. Stone, Drop Formation In Viscous Flows at a Vertical Capillary Tube. Physics of Fluids, 1997. 9: p. 2234-2242.

Zhang, X. and O. A. Basaran, An Experimental Study of Dynamics of Drop Formation. Physics of Fluids, 1995. 7: p. 1184-1203.

Zhang, X., Dynamics of Drop Formation in Viscous Flows. Chemical Engineering Science, 1999. 54: p. 1759-1774.

Zhu J., Zheng F., Laucks M.L., and Davis E.J., Mass transfer from an oscillating microsphere, Journal of colloid and interface science, 2002, 249(2), p: 351-358.

Zozaya, J.A., Physicochemical Study Of Blood Sera II : Analysis of 500 cases. Journal of Physical Chemistry, 1938. 42(2): p. 191-207.

Zozaya, J.A., Physicochemical Study of Blood Sera. Journal of Experimental Biology, 1935. 12(1): p. 65-79.